The Dissertation Committee for Wen-Jong Chang Certifies that this is the approved version of the following dissertation:

Development of an In Situ Dynamic Liquefaction Test

Committee:

Ellen M. Rathje, Supervisor

Kenneth H. Stokoe

Clark R. Wilson

Eric B. Williamson

Stephen G. Wright

Development of an In Situ Dynamic Liquefaction Test

by

Wen-Jong Chang, B.S., M.S.

Dissertation

Presented to the Faculty of the Graduate School of

The University of Texas at Austin

in Partial Fulfillment

of the Requirements

for the Degree of

Doctor of Philosophy

The University of Texas at Austin

August, 2002

Dedication

To my parents, wife, and daughter

Acknowledgements

This work would not have been possible without the help, dedication, and support of Professor Ellen M. Rathje. It is a great fortune for me to work for her and I will be forever grateful.

During the research process, Professor K. H. Stokoe has been very generous and is great help to us. He also provides many precious opinions and useful suggestions in the instrumentation designs and data interpretations. I really appreciate his assistances in this research. Also, I am very thankful to my committee members, Professor Wilson, Professor Williamson, and Professor Wright for their constructive opinions and valuable time.

In addition, I am very grateful many faculty members at UT-Austin. The list includes: Professor Olson, Professor Gilbert, Professor Rauch, and Professor Wright. I have learned so much from all of you, and I appreciate all you have done to prepare me for the future.

Mostly, I would like to thank my wife Pei-Shan and daughter Alison for their tremendous patient during my preparation of this dissertation. My wife in particular has had to carry more than her fair share of the duties taking care of our daughter. Also, to my incredible parents, I am so lucky to have you.

I am indebted to many former and current graduate students in geotechnical engineering group at UT-Austin. They had been help me preparing the specimen, conducting field and laboratory tests, encouraging me in bad days, and sharing joys in good days.

I would also like to thank all the people at Capitol Aggregates for providing a test site and concrete both essential to this work.

Development of an In Situ Dynamic Liquefaction Test

Publication No._____

Wen-Jong Chang, Ph.D.

The University of Texas at Austin, 2002

Supervisor: Ellen M. Rathje

An in situ dynamic liquefaction test has been developed at the University of Texas at Austin. The distinct characteristics of this testing procedure are the simultaneous in situ measurement of ground response and pore water pressures. The in situ liquefaction test directly measures pore pressure generation in the field and avoids many of the laboratory testing limitations related to sample disturbance, boundary conditions, and small sample size.

The essential components of in situ dynamic liquefaction test are a dynamic loading source and an embedded instrumentation array for simultaneously monitoring the ground response and pore pressure generation. The dynamic loading system consists of a vibroseis truck that applies dynamic loads to the ground surface and generates waves propagating through the instrumented test area. An instrumentation system and associated data reduction procedures were developed to monitor the coupled behavior between the soil skeleton and the pore

water pressure. The measured response to dynamic loading was used to evaluate the pore pressure generation characteristics of the soil in terms of the induced shear strains and excess pore pressures.

The developed in situ dynamic liquefaction test was used to dynamically load reconstituted test specimens located near the ground surface. For the first time, pore pressure generation curves that describe the relationships between excess pore pressure, shear strain amplitude, and number of cycles were measured in situ. These curves are similar to those previously measured in the laboratory. The developed testing technique represents a new testing alternative for the study of liquefaction and potentially will have a significant impact in the field of geotechnical earthquake engineering. The test results indicate that the proposed testing technique can capture the coupled response of the induced shear strain and the excess pore pressure generation during and after dynamic loading.

Table of Contents

List of Tables

List of Figures

Chapter 1. Introduction

1.1 LIQUEFACTION HAZARD

Liquefaction of saturated granular soil deposits due to seismic loading is one of the most dramatic threats to the safety of structures during earthquakes. Liquefaction-induced damage includes sand boiling, excessive settlement of buildings, lateral spreading, landslides, and failure of retaining structures. Observations of soil liquefaction both in natural and artificial deposits have been found in almost all major earthquakes. Some recent reminders include the 1999 Kocaeli (Turkey) earthquake (EERI 2000), and the 1999 Chi-Chi (Taiwan) earthquake (EERI 2001).

Although the term "liquefaction" has been used historically to describe a variety of phenomena that involve soil deformations caused by static or dynamic loading under undrained conditions, the generation of excess pore water pressure plays a key role in all liquefaction-related phenomena. In general, liquefaction occurs in loose, saturated granular materials. These materials tend to contract when sheared under drained conditions, but generate positive excess pore water pressures when sheared under undrained conditions, such as during earthquake shaking. These positive pore pressures reduce the effective stresses in the soil, causing the stiffness and strength of the soil to be reduced. These changes to the soil lead to excessive deformation and/or soil failure.

Starting with the 1964 Niigata earthquake in Japan (M_s=7.5), liquefaction has been extensively studied by researchers around the world. Specifically, research has focused on the evaluation of liquefaction potential (e.g., Seed and Idriss 1971, Martin et al. 1975, Kayen and Mitchell 1997), site response during and after liquefaction (e.g., Seed and Idriss 1967, Finn et al. 1977, Ishihara and Towhata 1980, Prevost 1981, Zienkiewicz et al. 1990), and the application of remediation and mitigation techniques (e.g., Seed and Booker 1977, Mitchell et al. 1995, Pestana et al. 1997). Although significant progress has been made both in fundamental research and practical applications over the past three decades, liquefaction remains a highly challenging issue because of the complexities of the phenomenon and the uncertainties associated with liquefaction evaluation.

1.2 RESEARCH SIGNIFICANCE

Soil liquefaction is a complicated phenomenon involving the coupled response of the soil skeleton and the pore water. Although soil liquefaction has been observed under monotonic or static loading conditions, often the most interesting cases are those caused by seismic or cyclic loading. Simplified procedures using results from in situ tests and laboratory tests have been proposed and used in academic research and practical applications to predict liquefaction behavior (Youd et al. 2001). However, these procedures all face intrinsic limitations such as the uncertainties in the measured in situ test parameters, the accuracy of empirical correlations, the heterogeneity of a field site, the size of laboratory soil specimens, and sample disturbance. An approach that uses an in

situ testing technique that directly measures pore pressure generation and soil response is highly preferred to overcome many of the existing limitations of current techniques.

Few in situ measurements of both site response and pore pressure generation have been reported (e.g., Holzer et al. 1989, Ishihara et al. 1981, Shen et al. 1989, Charlie, et al. 1992, Gohl et al. 2001). Additionally, the accuracy of some of the recorded data has been questioned because of the durability, installation, and setup of the instrumentation. The difficulties associated with previous research regarding in situ pore pressure measurement during earthquakes include the unknown occurrence of future earthquakes, the durability and maintenance of instrumentation during the long time between earthquakes, the triggering and recording of high-speed data acquisition, the design and installation of sensors, and appropriate site characterization before and after liquefaction. The proposed testing technique will address each of these issues.

The main goal of this research is to develop a testing procedure that can evaluate liquefaction potential and study the liquefaction mechanism in situ. Previous research (e.g., Dobry et al. 1982) reveals that the liquefaction phenomenon derives from the coupled response between the cyclic shear strain and excess pore water pressure. The proposed testing procedure will attempt to measure the relationship between the induced cyclic shear strain and excess pore pressure in situ. A vibroseis truck is used to generate strong surface waves propagating through an instrumented test area. The strong surface waves induce cyclic shear strains, which in turn generate excess pore water pressure. To

evaluate shear strain and pore water pressure in situ, a new sensor has been developed and embedded below the ground surface to simultaneously monitor both the dynamic soil particle velocity and the pore water pressure generation. Shear strain time-histories are calculated systematically from the measured ground velocities. The excess pore water pressure-time histories are measured at the location where the shear strains were calculated using a miniature pore water pressure transducer. Therefore, the full process of soil liquefaction is captured. Also, seismic testing techniques are used in this research to characterize the soil conditions before and after liquefaction. The following chapters will describe the details of the testing design, the associated analytical background, the data reduction procedures, and results from several field test series performed on large-scale reconstituted test specimens that have been constructed in a test pit.

1.3 SCOPE OF RESEARCH

This dissertation describes the details of the development of an in situ soil liquefaction testing procedure at the University of Texas at Austin (UT). The research consists of five main components: (1) the setup and testing procedures for the in situ liquefaction test; (2) the analytical framework regarding the ground response due to dynamic surface loads, the numerical simulation of the testing setup, and the data processing procedures; (3) issues regarding the sensors and data acquisition systems; (4) test results and validation; and (5) the implementation in fundamental soil liquefaction research.

The in situ soil liquefaction testing procedure under development at UT is one of the pioneering studies in this field. The unique feature of this testing procedure is the in situ real-time measurement of ground response, which is used to calculated shear strain, and pore water pressure. To measure these parameters, a new in situ instrumentation system with an associated data processing procedure was developed. To date, the testing procedure has been used to dynamically load a reconstituted test site. However, this testing procedure can be applied to natural soil deposits with only minor modifications.

Because the dynamic loading source used in this research is different from an earthquake, special considerations and reasonable assumptions are required to analyze the dynamic response. The current vibroseis at UT only vibrates vertically, therefore surface waves are the major seismic components propagating in the test area. It is essential to understand surface wave propagation behavior to appropriately interpret the measured results. Field validation tests were performed to study surface wave propagation through the test area, and these field data were compared with simplified analytical solutions and numerical simulation.

Based on different assumptions, the shear strains can be numerically computed from the particle velocities recorded by geophones measuring velocity in two directions. Different strain evaluation techniques have been adopted, compared, and verified through the in situ test results. The induced shear strains combined with the recorded pore water pressures allow the liquefaction potential to be characterized. These results are critically reviewed and compared with other data from the laboratory testing of other soils. Current results show good

agreement with previous research. Additionally, laboratory testing programs are underway to test the soil used in this research (Valle 2003, Hazirbaba 2004). The results from the laboratory studies will be compared with the field test results.

For this research, the testing procedure was used to dynamically load a reconstituted test specimen prepared in a test pit in the field. This test can be viewed as a full-size model test under one-g (g = gravitationally acceleration) conditions. However, the testing procedure can be extended widely for fundamental soil liquefaction research. This testing procedure can be used in the future to study pore pressure generation and dissipation behaviors, changes in soil properties due to pore pressure generation, and the liquefaction of special soil types (i.e., silts, gravels, and low-plasticity soils).

1.4 ORGANIZATION OF DISSERTATION

This dissertation focuses on the development process of the in situ dynamic liquefaction testing procedure and the results from initial testing. The dissertation consists of 12 chapters:

Chapter 1 includes a brief discussion of the significance of the in situ soil liquefaction test, the general testing procedure, and an organizational description of the dissertation.

Chapter 2 summarizes the current understanding of soil liquefaction and describes the current liquefaction evaluation techniques and their limitations. The difficulties and problems regarding previous attempts at in situ liquefaction

measurement are discussed. The goals of this research, as related to previous research, are also presented.

Chapter 3 describes briefly the in situ soil liquefaction test, including the vibration source, the layout of the test pit, the sensors and associated instrumentation systems, and the collected data. Detailed descriptions of the components of the instrumentation system are provided in Chapter 6.

Chapter 4 discusses the wave field due to a cyclic vertical load on the surface of an elastic half space, which represents the physical model of the current field test setup. Numerical simulations using the finite element method and a simplified elastic constitutive model are conducted to gain insight into the dynamic behavior of the test setup.

Chapter 5 addresses the data analysis techniques involved in this research. Signal processing algorithms in the time and frequency domains are reviewed. Additionally, different shear strain evaluation methods are described and compared in this chapter.

Chapter 6 describes the details and design considerations regarding the sensors and data acquisition systems.

Chapter 7 depicts the preparation and configuration of the reconstituted test specimen. Testing procedures and data reduction procedures are also presented.

Chapter 8 presents the testing results from the initial test series using preliminary designs of the sensors. This test series was used to verify the pore

pressure generation using the loading source and led to the redesign of the test sensors.

Chapter 9 discussed results from test series T2, which incorporated the newly designed liquefaction sensors. This test series also incorporated small-strain seismic testing to characterize the test specimen.

Chapter 10 discusses results from test series T3. This test series incorporated a longer duration of loading, providing data on pore pressure generation over a large number of loading cycles.

Chapter 11 includes a discussion of specific test results. The measured data are qualitatively assessed regarding the particle velocities, and hydrodynamic pore pressure. A comparison of shear strain-time histories computed by different shear strain evaluation methods using the field measured data is also presented. Experimental observations from the testing results are also discussed. Also, suggestions for a future laboratory test plan are addressed.

Chapter 12 includes a summary of this dissertation, future refinements of the developed testing technique, and applications of the proposed testing technique in soil dynamics and earthquake engineering.

Chapter 2. Liquefaction Background

2.1 INTRODUCTION

This chapter briefly describes the soil liquefaction phenomenon and reviews current techniques for liquefaction evaluation. In addition, previous in situ measurements of pore pressure generation during earthquake shaking are presented. Concerns regarding the accuracy of these measurements are discussed. Motivated by the limitations of current liquefaction evaluation techniques and the problems with previous in situ measurements of pore pressure generation, the main objectives of this research are to: 1. overcome many of the shortcomings of current liquefaction evaluation procedures, 2. improve the in situ measurement of pore pressure generation during dynamic shaking, and 3. improve our understanding of variables affecting soil liquefaction.

2.2 SOIL LIQUEFACTION PHENOMENON

The term "liquefaction" has been used frequently to describe various phenomena associated with excessive soil deformations caused by static, transient, or cyclic disturbances of saturated granular soils under undrained conditions. The key aspect for all of these phenomena is the generation of excess pore water pressure. Under undrained conditions, the buildup of excess pore water pressure results in a decrease in effective stress, and hence a reduction in the soil

strength and stiffness. The following sections review the basic concepts of granular soil behavior as related to liquefaction, the factors affecting the initiation of liquefaction, and the consequences of liquefaction.

2.2.1 Critical-state soil mechanics and liquefaction

Critical-state soil mechanics provides a useful framework to describe the liquefaction phenomenon. Critical state is defined as an ultimate condition in which plastic shearing continues indefinitely without changes in volume or effective stress (Wood 1990). This theory provides a foundation to qualitatively explain soil behavior under different loading conditions.

Critical-state soil mechanics started from the hypothesis that a critical void ratio exists for soils tested at a specific effective confining pressure (Casagrande 1936). Casagrande (1936) observed that initially loose and dense soils tested in drained triaxial shear at the same effective confining pressure tended to reach the same density or void ratio at large strains. Casagrande (1936) termed this constant void ratio as the critical void ratio (CVR), which is uniquely related to the effective confining stress. The locus of CVR and effective confining stress was called the CVR line. Castro and Poulos (1977) extended the concept of the CVR line by performing undrained triaxial tests. The results from these tests also indicated a unique relationship between void ratio and effective confining pressure, but the line did not agree with the CVR line developed from drained testing. It was postulated that under undrained conditions liquefied soil develops a "flow structure" that cannot be replicated in drained testing (Casagrande 1976).

This flow condition was termed steady state deformation (Castro and Poulos 1977). A steady-state line (SSL) can be defined that describes the values of void ratio (e), effective confining stress (σ'), and shear stress (τ) that occur at steady state. The projection of this line into e-σ' space is similar to the CVR line and is shown in Figure 2-1(a). Contractive soils initially plot above the SSL, while dilative soils initially plot below it.

As shown in Figure 2-1(b), initially loose soils (point A in Figure 2-1(b)) tend to contract (i.e., decrease in volume) during drained shearing. Under monotonic and cyclic undrained loading, positive excess pore water pressures are generated. In contrast, initially dense soils (point B in Figure 2-1(b)) tend to dilate (i.e., increase in volume) during drained shearing, and generate negative excess pore water pressure under monotonic undrained loading. However, under cyclic undrained loading, dense soil can generate positive excess pore pressures. These pore pressures soften the soil, but do not reduce its ultimate strength because sustained shear stresses will cause the soil to dilate (i.e., increase effective stresses through negative pore pressures) to the steady state line (Figure 2-1(b)). Therefore, softening of dense soils under undrained conditions may cause some deformation, but the strength of the soil is not reduced.

2.2.2 Types of liquefaction

Liquefaction phenomena are generally categorized into two major groups: flow liquefaction and cyclic mobility (Kramer 1996). Flow liquefaction occurs in cases where there is a static driving shear stress in the soil necessary for static

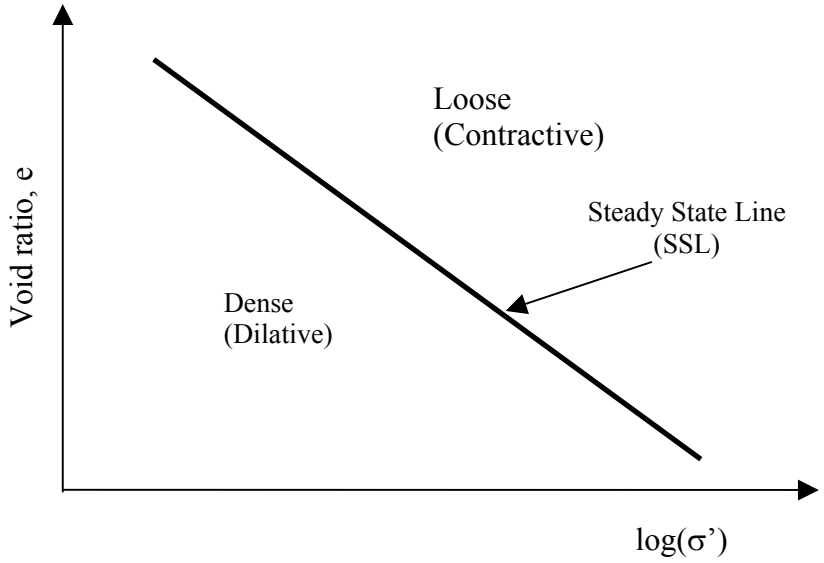

Figure 2-1(a) Steady state line (SSL) in e-log(σ') plane

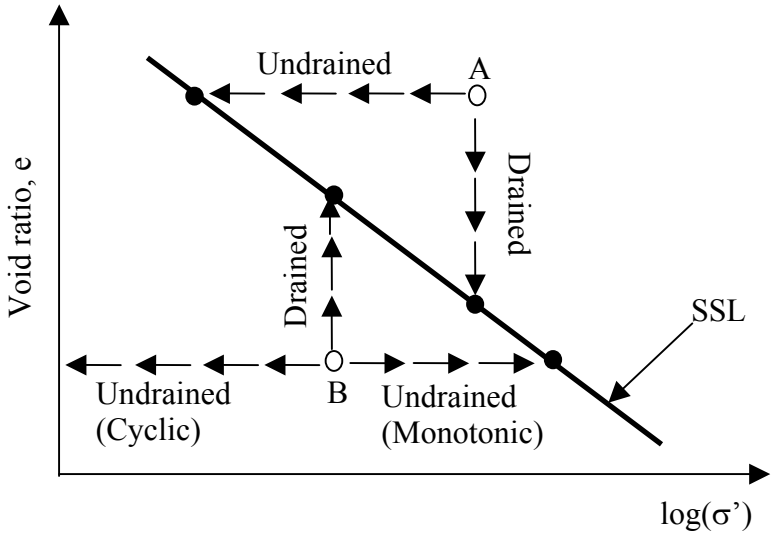

Figure 2-1(b) Soil behavior under different shearing conditions

Figure 2-1 Conceptual illustration of soil behavior under different shearing conditions using the steady state line (modified from Kramer 1996)

equilibrium and this static shear stress is greater than the undrained steady state strength of the soil (S_{SU}). Positive excess pore pressures generated during cyclic loading cause the structure of the soil to collapse and the strength to be reduced to S_{SU}. Because this reduced strength is smaller than the static shear stress needed for equilibrium, a flow failure occurs.

Cyclic mobility occurs in level ground, which has no driving shear stresses or in cases where the static shear stresses are smaller than S_{SU}. The generation of excess pore pressures during cyclic loading results in a reduction in stiffness, large volumetric strains, and lateral spreading. Cyclic mobility can occur in both loose and dense soils.

In addition to these two mechanisms, many field cases of flow liquefaction failures are the result of the flow of water after an earthquake as excess pore pressures in liquefied soil layers dissipate. The flow of water generates positive pore pressures in other layers, hence reducing the soil strength over a large volume. This redistribution of pore water pressure explains the failure of some dams after the end of earthquake shaking, such as the failure of the Lower San Fernando Dam during the 1971 San Fernando earthquake (Seed 1979).

2.2.3 Factors affecting the initiation of liquefaction

The potential occurrence of liquefaction is determined by two conditions: the level of undrained disturbance and the liquefaction resistance of the soil. Hence, factors related to each of these conditions will directly influence the liquefaction potential. The following discussions address these two conditions.

Based on laboratory investigations and field observations, it is well recognized that the intensity and duration of the cyclic loading are the two major factors related to the undrained loading required to trigger liquefaction (Seed and Idriss 1971). In an earthquake, the intensity of the cyclic loading is characterized by the intensity of ground shaking (i.e., peak ground acceleration, PGA), as this influences the magnitude of the induced shear stresses and shear strains. The duration of earthquake shaking is important because it influences the number of cycles of significant shear stress and shear strain applied to the soil. Generally, the ground motions expected at a site can be characterized either by site specific ground response analysis or by a simplified approach.

The liquefaction vulnerability of a soil element subjected to a dynamic disturbance is determined by its liquefaction resistance and the initial state of stress. The five key soil properties affecting liquefaction potential, as discussed by Seed (1979) and summarized by Ladd et al. (1989), are: 1. relative density, 2. soil fabric, 3. prior seismic straining, 4. stress history, and 5. aging. Among the five properties, relative density was considered the main soil property affecting liquefaction potential, as this property indicates the pore pressure generation behavior of the soil (e.g., Figure 2-1). Laboratory studies (Pyke et al. 1974, Mulilis et al. 1975) revealed that specimens prepared at the same relative density, but by different sample preparation methods, show different liquefaction characteristics. This difference was attributed to the different soil fabrics created by each sample preparation procedure. Prior strain history, without significantly densifying the sand, was observed in the laboratory to increase the liquefaction

resistance of a soil by a factor of 1.5 (Seed et al. 1975). Cyclic simple shear test data showed that specimens with a higher overconsolidation ratio, and therefore a larger lateral earth pressure coefficient (K_0), displayed a higher liquefaction resistance (Seed and Peacock 1971, Ishihara and Sherif 1974). A comparison between the laboratory measured liquefaction resistance of undisturbed samples and freshly deposited samples of the same sand indicates a 75% increase in liquefaction resistance due to aging.

In addition to the aforementioned five factors, laboratory investigations have shown that a decrease in the degree of saturation increases the liquefaction resistance (Chaney 1976, Ishihara et al. 2001).

2.2.4 Consequences of liquefaction

Depending on the initial site conditions and the relevant liquefaction mechanism, the consequences of liquefaction will be different. Possible consequences of liquefaction include flow failure, lateral spreading, foundation failure, and other soil stability problems.

Flow liquefaction occurs when the shear strength of the liquefied soil is smaller than the shear stress required for static equilibrium. The result is a massive flow slide, such as the Lower San Fernando Dam failure (Figure 2-2) during the 1971 San Fernando earthquake (Seed et al. 1975). Other flow failures include bearing capacity and tilting failures of buildings, such as observed during the 1964 Niigata, Japan earthquake (Seed and Lee 1966).

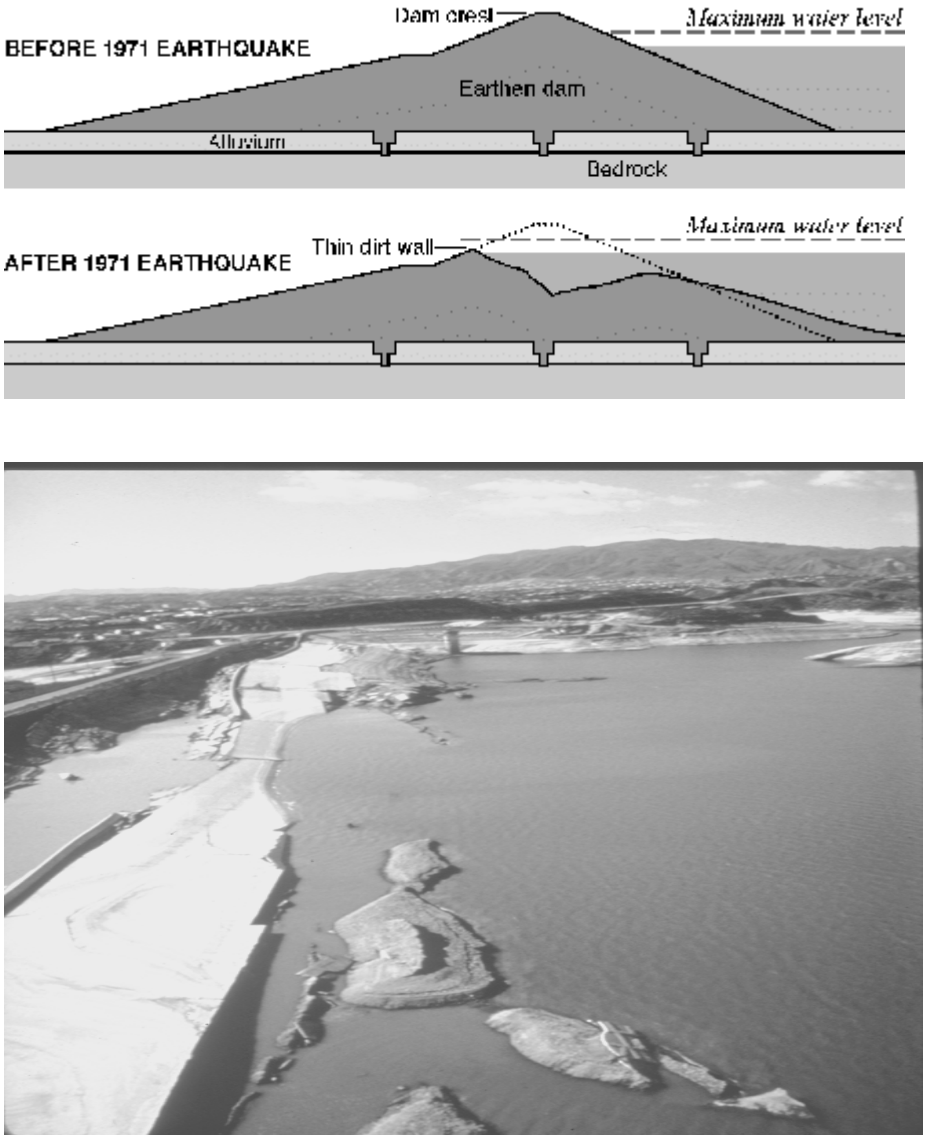

Figure 2-2 Flow liquefaction failure of the Lower San Fernando Dam (Page et al. 1995)

Unlike flow liquefaction, which involves large unlimited deformations, lateral spreading is the result of seismically induced, incremental, permanent deformation of liquefied soil. Lateral permanent movement of the liquefied soil can cause ground cracking, ground fissures, underground shear zones, and buckled soil. Lateral spreading experienced along Izmit Bay during the 1999 Kocaeli, Turkey earthquake is shown in Figure 2-3. Lateral spreading is commonly seen near river channels and can cause damage to bridges and pipelines.

Figure 2-3 Lateral spreading failure at the Seymen-Tea Garden during the Kocaeli, (Turkey) earthquake (EERI 2000)

Another common liquefaction-induced phenomenon is sand boils, which generally occur when a liquefied sand stratum is overlain by a less permeable or non-liquefiable layer. After the lower layer liquefies, the upward flow of water carries soil up to the ground surface through localized cracks or channels in the non-liquefied layer. Sand boils do not always have a large engineering significance, except for the associated volume change and settlement, but they are a good indication of high excess pore water pressures in the field.

Liquefaction-induced settlement is the result of volumetric strain and is responsible for the distress of shallow foundations, piles, and lifelines. Factors affecting the magnitude of settlement include the initial density of the sand, the maximum shear strain induced by an earthquake, and the level of excess pore pressure.

2.3 EXISTING LIQUEFACTION EVALUATION PROCEDURES

There are several available techniques for the evaluation of liquefaction potential. Simplified procedures (e.g., Seed and Idriss 1971, Dobry et al. 1982, Law et al. 1990, Kayen and Mitchell 1997) have been developed to predict the initiation of liquefaction and are commonly used in engineering practice. More complicated constitutive models (e.g., Finn et al. 1977, Prevost 1981, Zienkiewicz et al. 1990) have been proposed and employed in finite element programs to predict pore pressure generation, stiffness degradation, and permanent deformations during seismic events.

2.3.1 Cyclic stress approach

Seed and Idriss (1967) proposed a general approach for evaluating liquefaction potential, known as the cyclic stress approach, which addresses three major factors influencing the initiation of liquefaction: (1) the characteristics of the earthquake loading, including the intensity and duration of shaking, (2) the initial stress state of the soil, and (3) the liquefaction resistance of the soil. For the earthquake loading, the equivalent cyclic shear stress induced by the earthquake is computed from ground response analysis or estimated from the peak acceleration expected at the site. The duration of shaking is expressed as the number of equivalent, uniform stress cycles and is estimated from the earthquake magnitude. The cyclic strength or liquefaction resistance of the soil is defined in terms of the cyclic stress ratio required to reach a zero effective stress state in the number of loading cycles expected from the earthquake. Originally, it was proposed that the cyclic strength could be evaluated from a series of undrained cyclic, stress-controlled triaxial tests on reconstituted samples that replicate the field relative density and effective stresses. If the equivalent cyclic stress ratio induced by the earthquake is larger than the cyclic strength ratio of the soil, liquefaction is predicted. This laboratory evaluation of liquefaction potential has a significant shortcoming related to sample preparation. Different sample preparation techniques produce different soil fabrics, which significantly affects the measured cyclic strength (Seed 1979). Additionally, prior seismic straining and aging are difficult to replicate in laboratory testing.

To overcome the limitations with the laboratory evaluation of soil liquefaction, Seed and Idriss (1971) developed a simplified procedure that is based on the empirical evaluation of field observations. This procedure is widely used in engineering practice. The most updated version of this procedure is in the summary report of 1996 NCEER and 1998 NCEER/NSF workshops (Youd et al. 2001).

In the simplified procedure, the liquefaction potential of a site is evaluated based on the estimation of two variables: (1) the cyclic stress ratio (CSR) induced by the expected seismic loading; and (2) the cyclic liquefaction resistance ratio (CRR) representing the cyclic stress ratio required to initiate liquefaction in a given number of loading cycles. If the CSR is greater than the CRR, the soil layer is expected to liquefy.

Considering one-dimensional upward propagation of shear waves in a soil deposit, Seed and Idriss (1971) proposed the following equation to calculate the cyclic stress ratio:

$$CSR = \frac{\tau_{av}}{\sigma'_{vo}} = 0.65 \frac{a_{\max}}{g} \frac{\sigma_{vo}}{\sigma'_{vo}} r_d \quad \text{.......................................} (2\text{-}1)$$

where τ_{av} = equivalent uniform cyclic shear stress; σ'_{vo} and σ_{vo} are the initial effective and total vertical stresses, respectively; $a_{\max}$ = peak horizontal acceleration at the ground surface; g = acceleration of gravity; and r_d = stress reduction factor at the depth of interest, accounting for the flexibility of the soil column.

Although engineers have acknowledged that the theoretically best way to evaluate the CRR is to retrieve undistributed soil specimens for laboratory testing,

this is generally not done because of the difficulties associated with obtaining undisturbed specimens of potentially liquefiable soil. These soils tend to be loose and most sampling procedures will densify the soil, making any laboratory results unreliable and unconservative. As an alternative, empirical correlations between in situ test parameters and the CRR have been proposed from post liquefaction investigations and widely used in engineering practice. Several empirical correlations between the CRR and various in situ test parameters have been established. These in situ test parameters include the corrected Standard Penetration Test (SPT) blow count ($N_{1,60}$; Seed et al. 1985), the stress-corrected Cone Penetration Test (CPT) tip resistance (q_{c1n}; Robertson and Wride 1998), the stress-corrected shear wave velocity (V_{s1}; Andrus and Stokoe 2000), and the Becker penetration test (BPT, Harder 1997).

Figure 2-4 shows the SPT empirical curves for CRR. These curves are for a magnitude 7.5 earthquake and soils with different fines contents. Other empirical correlations are similar to Figure 2-4, but with different values of in situ test parameters on the abscissa. These types of correlations are very useful in practice and perform well when sites are predicted to definitely liquefy (i.e., CSR>>CRR) or definitely not liquefy (i.e., CSR<<CRR). However, there is more uncertainty with these correlations for borderline predictions (i.e., CSR~CRR) and for sites with high fines content.

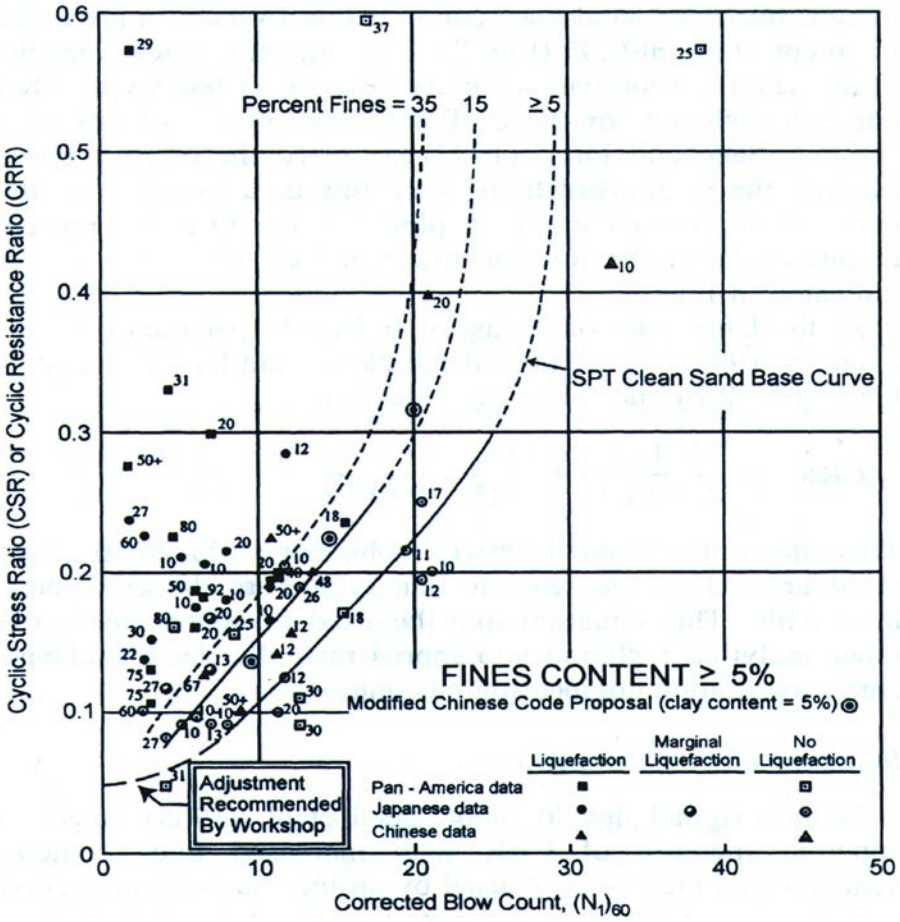

Figure 2-4 CRR versus corrected SPT-N values for magnitude 7.5 earthquakes (Reproduced from Youd et al. 2001)

2.3.2 Cyclic strain approach

In the simplified cyclic stress approach, it was assumed that the CRR of a soil is mainly a function of the relative density and the initial effective confining

pressure. However, later research found that other factors, as discussed previously, also have significant influences on the liquefaction resistance. Dobry et al. (1982) proposed the cyclic strain approach based on the strong relationship between excess pore pressure ratio ($r_u = \frac{\Delta u}{\sigma'}$, where Δu=excess pore pressure, and σ'=effective confining pressure) and cyclic strain amplitude, as observed in undrained, cyclic, strain-controlled triaxial tests (Figure 2-5). In this approach, shear modulus, rather than relative density, is the main parameter that controls pore pressure buildup.

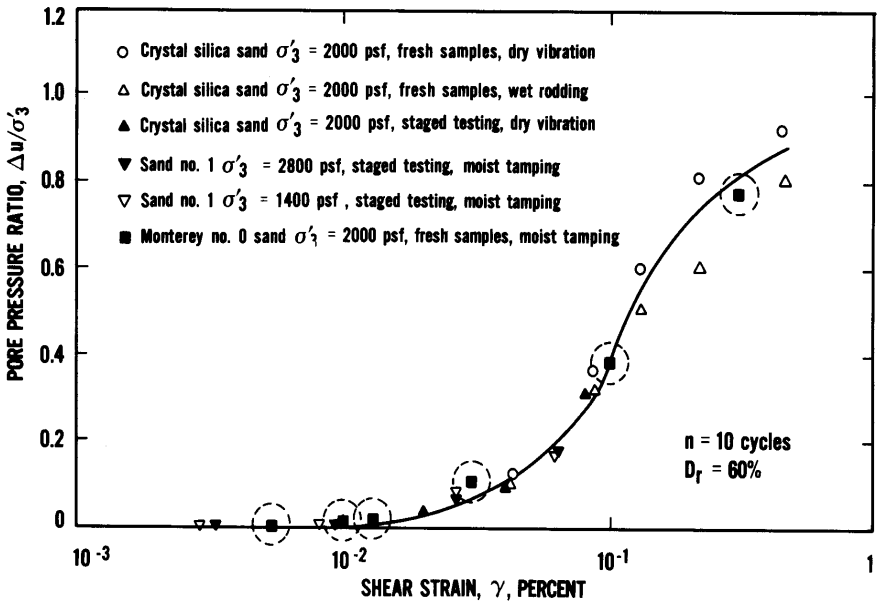

Figure 2-5 Excess pore pressure ratios versus cyclic shear strains from strain-controlled cyclic triaxial tests (n=10 cycles, D_r=60%) (from Dobry et al. 1982)

Similar to the simplified cyclic stress approach, the loading condition for the cyclic strain approach is characterized in terms of cyclic shear strain, γ_c, calculated by:

$$\gamma_c = \frac{\tau_{av}}{G(\gamma_c)} = 0.65 \frac{a_{\max}}{g} \frac{\sigma_{vo}}{G(\gamma_c)} r_d \quad \text{..... (2-2)}$$

where $G(\gamma_c)$ is the shear modulus of the soil with respect to the shear strain level γ_c , and the other parameters are the same as defined in Equation (2-1).

The liquefaction potential of the soil is determined by evaluating the excess pore pressure ratio from the earthquake-induced cyclic shear strain and the expected number of strain cycles. The major problem with the cyclic strain approach is the difficulty in estimating the cyclic shear strain level induced by the earthquake, because the shear modulus needed in Equation (2-2) is a function of the shear strain and effective stress (excess pore pressures). Consequently, the cyclic strain approach is used less often in engineering practice.

2.3.3 Other approaches

Law et al. (1990) proposed an energy dissipation approach that is based on the unique relationship between the cumulative dissipated energy and the excess pore pressure leading to liquefaction. This relationship was observed in cyclic triaxial and simple shear tests. This approach is unique in that it accounts for both cyclic stress and cyclic strain, it is related to the inherent stochastic nature of earthquake ground motions, and it is related to fundamental earthquake parameters. Nevertheless, the energy dissipation approach is less popular in engineering practice because of the lack of independent verifications.

With the advances in computing technologies, numerical modeling of soil response under cyclic loading has been a major research subject in geotechnical earthquake engineering. To accurately model the full response of a saturated soil under undrained cyclic loading, several factors must be incorporated in the finite element procedure. These factors include nonlinear stress-strain behavior, pore pressure generation and subsequent stiffness degradation, and pore pressure redistribution during and after dynamic loading. Finn et al. (1977) used a nonlinear strain hardening constitutive model with a pore pressure generation model proposed by Martin et al. (1975) to analyze the dynamic response of level ground. Prevost (1989) used an advanced constitutive model to more rigorously predict the generation, redistribution, and dissipation of excess pore pressure during and after seismic loading. Zienkiewicz et al. (1990) used a more advanced constitutive model with a densification model to solve the simplified Biot's equations (1955) that govern the deformation and flow of porous media. The complexities and difficulties in the evaluation of the model parameters used in these constitutive models have limited their use in geotechnical earthquake engineering practice.

2.4 PREVIOUS IN SITU LIQUEFACTION MEASUREMENTS

In situ pore pressure measurements have been made at several liquefiable sites around the world during previous earthquakes. Recently, research has been conducted using various dynamic loading sources (e.g. explosion, drop-weight) other than earthquakes to study in situ pore pressure generation and soil

liquefaction behavior. A summary of selected published results of in situ pore pressure measurements is listed in Table 2-1.

Table 2-1 Summary of previous in situ liquefaction measurements

Site	Soil Type	Collected Data	Source	Reference
Owi Island (Japan)	Silty fine sand	SPT, CPT, pore pressure, surface acceleration	Mid-Chiba earthquake a_{max}=0.1 g	Ishihara et al. (1981)
Sunamachi (Japan)	Fine sand	SPT, Vs, pore pressure, downhole acceleration	Chiba-Toho-Oki earthquake, a_{max}=0.12 g	Ishihara et al. (1989)
Lotung site (Taiwan)	Sand	Vs, CPT, pore pressure, Downhole acceleration	18 earthquakes during 1985-1986	Shen et al. (1989)
Wildlife site (USA)	Silty sand	SPT,CPT, Vs, pore pressure, downhole acceleration	Superstition Hills earthquake, a_{max}=0.21 g	Youd et al. (1994)
South Platte River (USA)	Coarse sand	SPT, CPT, Vs, pore pressure, particle velocity, settlement	Downhole explosions	Charlie et al. (1992)
Boundary Bay (Canada)	Sandy silt	CPT, Vs, pore pressure, surface acceleration, settlement	Downhole explosions	Gohl et al. (2001)

Among those sites measuring pore pressures during earthquake shaking, only the Wildlife site during the 1987 Superstition Hills earthquake in Imperial Valley, CA fully liquefied. The acceleration and pore pressure-time histories recorded at the Wildlife site during the 1987 Superstition Hills earthquake are shown in Figure 2-6 (Holzer et al. 1989). The maximum acceleration recorded in

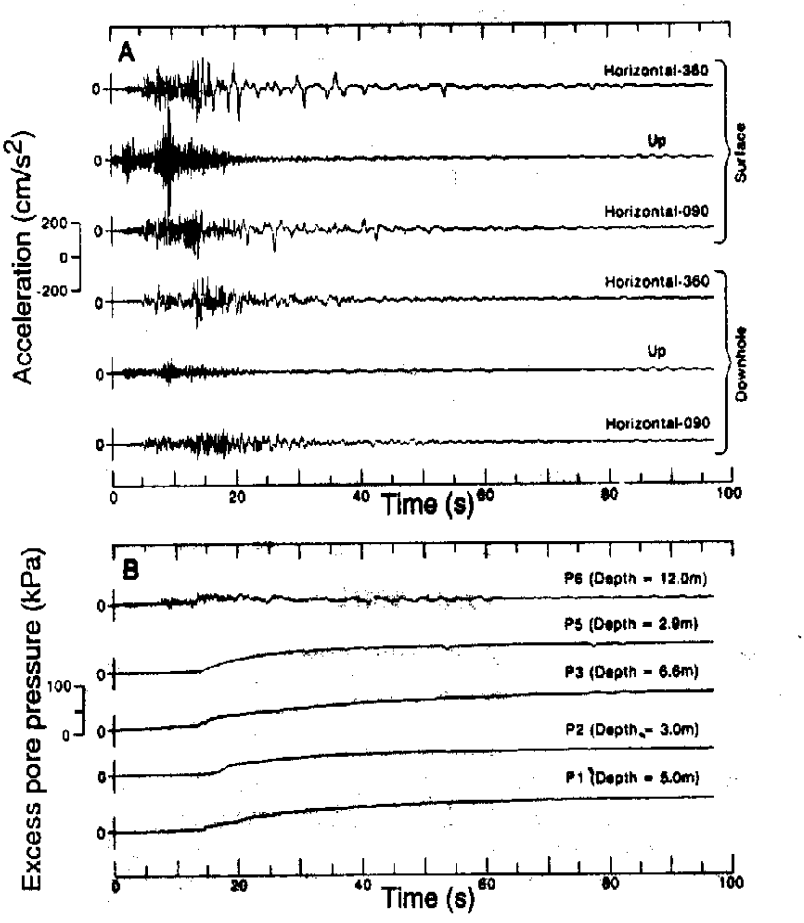

Figure 2-6 Acceleration-time histories and pore pressure records at the Wildlife site during the 1987 Superstition Hills earthquake (Holzer et al. 1989)

the soil below the liquefied layer was 0.17 g and the maximum horizontal acceleration recorded at the ground surface was 0.21 g. The four piezometers (pore pressure transducers) within the liquefied silty sand layer all reached a pore pressure ratio (r_u) greater than 0.87. However, the pore pressure data show a long rise time and a time lag between the strongest ground shaking and the maximum

pore pressure. These observations raised concerns regarding the credibility of the data (Hushmand and Scott 1992).

Youd and Holzer (1994) reviewed the Wildlife site data and concluded that the piezometer response was correct based on several reasons. The recorded acceleration-time histories at the ground surface displayed some acceleration pulses that were coincident with pore pressure pulses (Zeghal and Elgamal 1994). Additionally, the average shear strain-time histories calculated from downhole accelerations (Zeghal and Elgamal 1994) showed that the average shear strain-time histories are closely parallel to the rise in recorded pore pressure. Because shear strain amplitude is closely related to excess pore pressure generation, the parallel behavior between the induced shear strains and pore pressure has lead some researchers to conclude that the pore pressure data at the Wildlife site are accurate.

However, pore water pressure records from Owi Island in Japan (Ishihara et al. 1981, Ishihara et al. 1989) and data from the Lotung site in Taiwan (Shen et al. 1989) reveal different pore pressure generation patterns than those from the Wildlife site. The Owi Island data from the 1980 Mid-Chiba earthquake (Figure 2-7) indicated that the maximum excess pore pressure was closely coincident with the peak ground acceleration. Additionally, when the strong ground shaking was no longer intense enough to generate further excess pore pressures, the pore pressure declined exponentially back to the static condition. However, the horizontal surface ground shaking at Owi Island during this earthquake was less than 0.1 g, and only generated a excess pore pressure ratio of 0.2. The records at

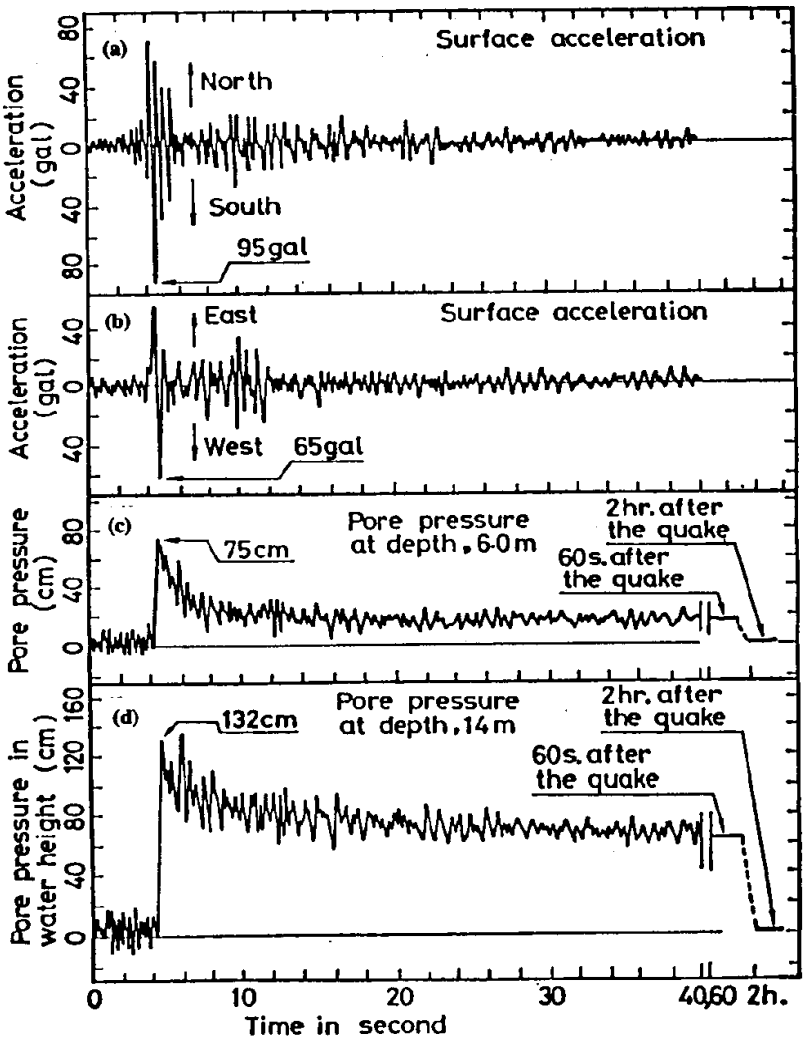

Figure 2-7 Surface acceleration histories and pore pressure records at Owi island site during the Mid-Chiba earthquake (Ishihara et al. 1981)

the Lotung site during an earthquake in 1986 (Event 16 in the SMART1 catalog) also show a pore pressure response coincident with the acceleration data, this site did not fully liquefy, only experiencing a PGA at the ground surface of 0.17g and an excess pore pressure ratio of 0.25.

Pore pressure records from seismic centrifuge tests (Hushmand et al. 1993) are similar to the Owi Island and Lotung site measurements, indicating a short response time for pore pressure generation. Scott and Hushmand (1995a) performed several in situ tests at the Treasure Island site in San Francisco to evaluate the response of the USGS piezometers that had previously been installed there. The USGS piezometers at the Treasure Island site are similar to those at the Wildlife site. The results showed that the USGS piezometers were less sensitive, both in time and magnitude, than the reference piezometers installed by Scott and Hushmand (1995a). Scott and Hushmand (1995b) questioned the performance of the USGS piezometers on the basis of clogging, the calibration procedure, durability, and partial saturation of the piezometer. To address the questions raised, a better and standardized piezometer for dynamic pore pressure measurements is necessary.

Gohl et al. (2001) conducted an in situ liquefaction test using controlled, sequential detonation of explosives in British Columbia, Canada. The testing array includes downhole 3D accelerometers, “fast speed” piezometers monitoring the hydrodynamic pore water pressure from blast-induced shock waves, and “low speed” piezometers monitoring the residual excess pore pressure from blast-induced shear strains. The strain levels estimated using small strain solid

mechanics theory and differential displacements over the test volume ranged from 0.3% to 7%, depending on the distance from the source. The measured excess pore water pressure ratio was about 0.48. The test provided a new direction for in situ soil liquefaction measurement, using explosives as a seismic source. However, questions regarding the high frequency motions induced by blasting, estimation of the shear strain level, difficulties in monitoring high pore pressures due to the shock front, and validation of the test results indicate more efforts are required in this field.

Hryciw et al. (1990) studied a unique case history in which a flow slide of an embankment was induced by liquefaction during seismic exploration (Figure 2-8). The failure was triggered by six vibroseis trucks that were being used as sources for a reflection survey in the upper peninsula of Michigan. Field tests after the slope failure indicated the existence of loose sand within the embankment. The seismic waves generated by the vibroseis trucks initiated liquefaction in the loose sand zone, causing a flow slide into the lake. Post-failure analyses conducted by Hryciw et al. (1990) estimated the maximum induced shear strain in the liquefaction zone as 0.055 %, which is larger than the threshold strain for pore pressure generation (0.01%) proposed by Dobry et al. (1982). This case demonstrates that a vibroseis truck is capable of generating large shear strains and significant excess pore pressure.

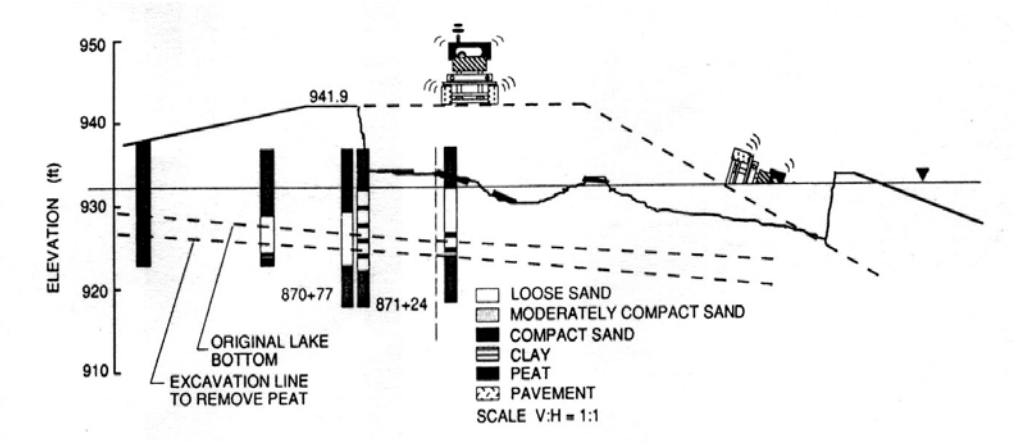

Figure 2-8 Cross section of embankment failed by vibroseis truck (Hryciw et al. 1990)

2.5 MOTIVATION FOR RESEARCH

Dynamic laboratory tests, including cyclic triaxial tests, cyclic simple shear tests, shaking table tests, and cyclic torsional shear tests, provide useful information for understanding the mechanism of liquefaction. However, when they are applied to the field, problems with sample disturbance or reconstituted test specimens make the results less reliable. The semi-empirical relations between liquefaction resistance and in situ testing parameters provide alternative solutions. However, due to their simplicity and the assumptions imposed, the results are not always accurate, especially near the boundary lines. Effective-stress based finite element analysis provides the most detail regarding the development of excess pore pressures and deformations during a seismic event. However, difficulties in evaluating the input constitutive model parameters and the variation of soil properties across a site limit the use of these methods. Also,

to validate these complicated numerical models, high quality field measurement data are required.

To overcome the shortcomings of existing liquefaction evaluation and testing techniques, an in situ dynamic liquefaction test is highly desired. The in situ dynamic liquefaction testing procedure developed at UT measures the pore pressure generation and ground response simultaneously in the field. Therefore, sample disturbance is minimized. Also, by monitoring the full process of pore pressure generation and dissipation in the time domain, the collected data can be applied not only to the identification of initial liquefaction, but also to cases where partial liquefaction occurs. In both of these cases, the consequences of liquefaction can be studied. In addition, the testing procedure can be used to evaluate the effectiveness of various liquefaction remediation techniques. Furthermore, the testing data can be utilized in validation of dynamic numerical analysis. The testing procedure under development will benefit engineering practice, as well as advance the state knowledge regarding liquefaction.

Chapter 3. In Situ Dynamic Liquefaction Test

3.1 INTRODUCTION

Unlike a conventional laboratory cyclic liquefaction test that applies a cyclic loading to a relatively small reconstituted specimen or undisturbed specimen, the in situ dynamic liquefaction test uses embedded sensors to monitor the coupled behavior between the soil skeleton and pore water pressure in saturated granular soils. This measured response to dynamic loading is used to evaluate the liquefaction characteristics of the soil. In situ dynamic liquefaction testing minimizes sample disturbance (when testing natural deposits), avoids the boundary conditions found in all laboratory tests, and allows complicated soil strata to be studied. These features address some of the problems associated with the laboratory evaluation of liquefaction resistance.

The essential components for in situ dynamic liquefaction testing are the dynamic loading source and the instrumentation system for simultaneously monitoring the ground response and pore pressure generation. Most previous studies (e.g., Ishihara et al. 1981, Ishihara et al. 1989, Youd et al. 1994) that measured in situ pore pressure generation installed instrumentation systems and waited for an earthquake to dynamically load the site. Surface and downhole array accelerometers were used to monitor the ground response and pore pressure transducers were utilized to measure pore pressure generation. The major

limitations of these studies include the unknown recurrence of earthquakes, the durability of the sensors after long periods waiting for an earthquake, assumptions regarding the calculation of strains, and validation of the recorded data. Although using controlled sequential explosions (Charlie et al. 1992, Gohl et al. 2001) can be an alternative dynamic loading source, the high blast pressures and the high frequency components of the blast loading are different from earthquakes. These two issues make blast loading difficult to compare with earthquake shaking.

The in situ dynamic liquefaction test under development at UT is designed to measure pore pressure generation in situ without having to wait for an earthquake. The cyclic loading for the proposed test will be similar to earthquake shaking, unlike the dynamic loading induced by blasting. Also, very importantly, it can perform tests over a wide range in strains as the cyclic threshold strain can be evaluated. In the developed testing procedure, a vibroseis truck is used to generate Rayleigh waves that propagate through the test area and induce controlled number of cycles of shear strain and shear stress. The shear strains at specific locations can be systematically evaluated using recorded particle velocity data. Pore pressure buildup and dissipation is recorded using miniature pore pressure transducers capable of recording both hydrodynamic and residual pore pressure. Therefore, the coupled behavior between the dynamic response of the soil skeleton, represented by shear strain, and the excess pore water pressure can be measured. Also, the pore pressure generation characteristics of the soil, expressed as excess pore pressure ratio versus mean shear strain amplitude for a specific number of loading cycles, can be measured in the field. This is analogous

to the technique developed by Dobry et al. (1982) from cyclic strain-controlled laboratory tests and shown in Figure 2-5.

In this chapter, the general framework of the in situ liquefaction testing technique is described. Details regarding each specific aspect of the test are presented in Chapters 6, 7, and 8 for data analysis, instrumentation system, and field setup and data reduction, respectively.

3.2 DYNAMIC SOURCE

One of the major distinctions between this research and previous in situ liquefaction measurements is the dynamic source. A well-controlled dynamic loading system is used that is capable of generating loads of uniform amplitude at a specific frequency for a specific number of cycles. The dynamic loading system includes a vibroseis truck, a 222-kN (50-kips) load cell, a loading frame, and a rigid circular concrete footing. The vibroseis truck is used as a vertical vibrator that dynamically loads the rigid footing located at the ground surface. The vertical vibration of this rigid footing generates surface waves that propagate through the test area and induce shear strains and excess pore pressure.

Vibroseis trucks have been widely used in seismic exploration as a wave source. The vibroseis truck owned by the University of Texas at Austin has been modified for dynamic pavement testing (Bay 1997, Bay et al. 1999, Bay and Stokoe 1999, Stokoe et al. 2000) and in situ nonlinear soil property studies (Phillips 2000, Axtell 2001). A photo and schematic drawing of the UT vibroseis truck are shown in Figure 3-1. The main components of the vibroseis truck

include the hydraulic ram (vibrator) and the control system. Limited by the servo valves of the hydraulic system, the UT vibroseis truck can generate sinusoidal waves within a frequency range of 15 Hz to 100 Hz. The maximum applied force is controlled by the weight of the truck, which is 178 kN (40 kips), and the output of the hydraulic ram. An electronic function generator is used to control the loading amplitude, frequency, and number of loading cycles.

The setup of the load cell, loading frame, and rigid footing is illustrated in Figure 3-2. The load cell is used to monitor the force applied to the loading frame, as well as to provide a point load to the loading frame. The loading frame then transfers the load to the rigid footing. The loading frame is made of I-beam steel in a T-shape, with three circular plates in contact with the footing to ensure a uniform distribution of load from the load cell. The 30-cm (1-foot) thick circular concrete footing was epoxied in the field with the top of the footing near the original ground surface for good contact with the soil and to provide enough clearance for the load cell and loading frame to fit beneath the vibroseis truck.

3.3 INSTRUMENTATION SYSTEM

The major instrumentation for the in situ dynamic liquefaction test consists of 2D-geophones, accelerometers, pore pressure transducers (PPT), associated signal conditioners, and high-speed data acquisition systems. Two data acquisition systems are employed in this research for different recording lengths. A general description of each component is presented below.

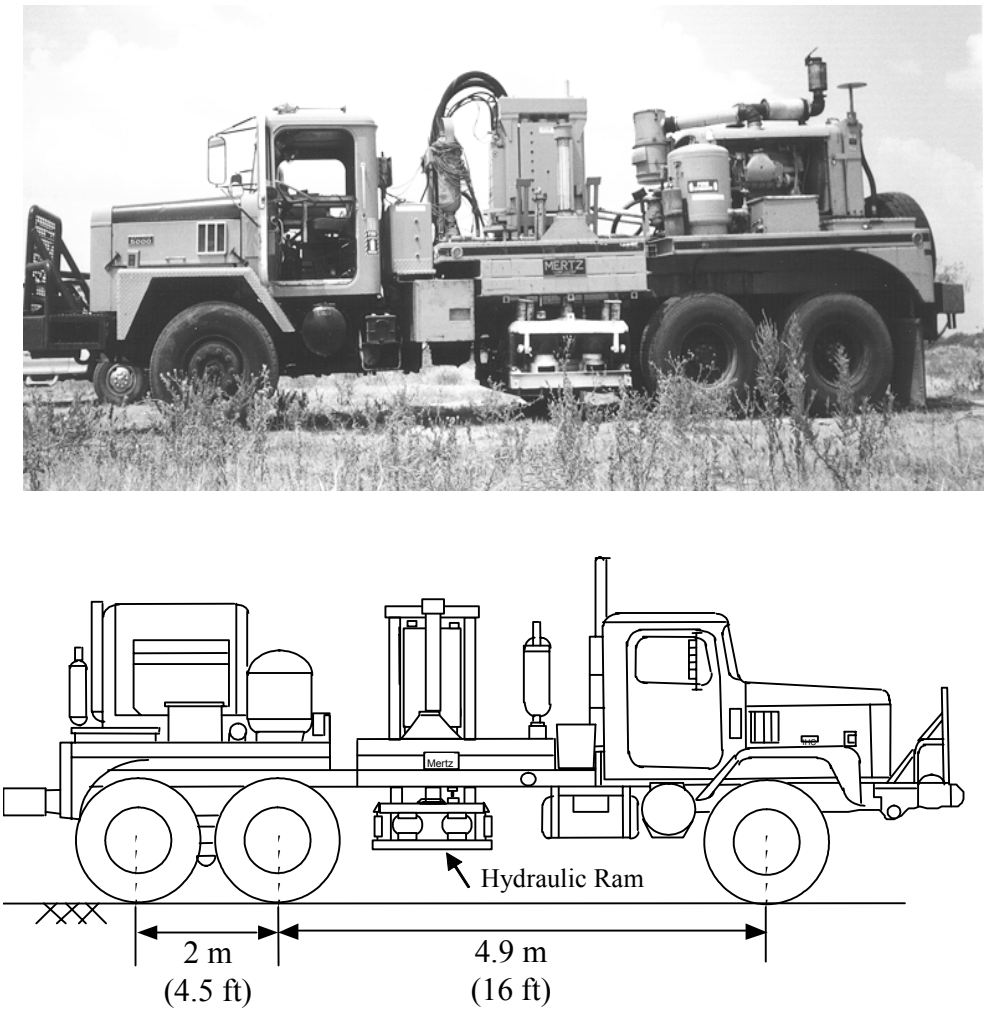

Figure 3-1 Schematic drawing of vibroseis truck (Bay 1997)

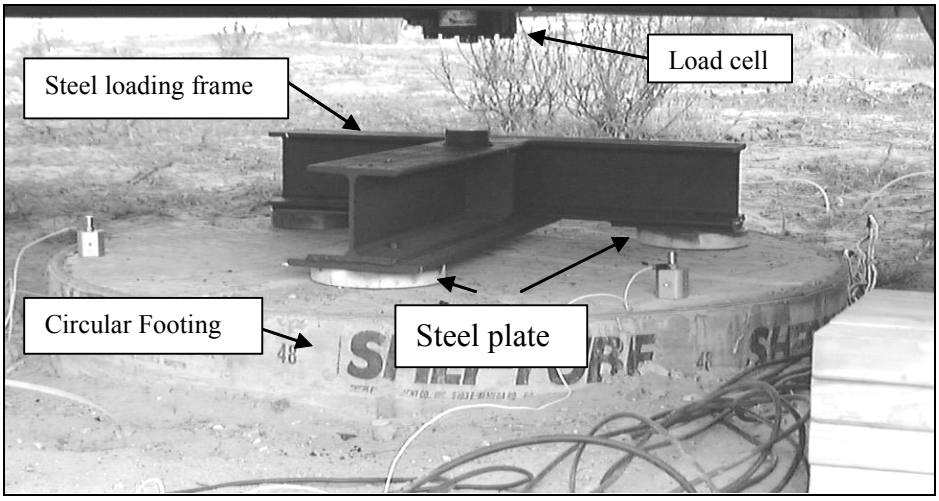

Figure 3-2 Setup of load cell, loading frame, and circular footing (Phillips 2000)

3.3.1 2D-geophone

Geophones are velocity transducers, which are used to measure particle velocity. In the developed in situ dynamic liquefaction test, the geophones are embedded beneath the ground surface. To measure the particle motion generated by the vibrating footing, a special acrylic case was built to combine two perpendicularly oriented geophones. These cases allow both the velocities in the vertical and radial (horizontal) directions to be measured. Additionally, these cases provide waterproofing for the geophones. A small steel shoe is attached to the bottom of each case for easy installation and maintenance of orientation and verticality during the test. In addition to the geophones, a pore pressure transducer is also included in the acrylic case for pore pressure measurements. This combined sensor that includes both geophones and a pore pressure transducer has

been named the liquefaction sensor. A detailed description of the liquefaction sensor is presented in Chapter 6. Because geophones generate significant voltage signals during dynamic movements, no signal conditioners are required. All geophones were calibrated before installation and after testing as discussed in Section 6.3.2.

3.3.2 Pore pressure transducer

Pore pressure transducers (PPT) are used for dynamic pore pressure measurements in this study. To measure pore water pressures in soil, a filter is essential to separate the soil from the pressure-sensing element. Sources of error for general purpose PPTs include hydrodynamic time lag, gas or air bubbles in the system or in the vicinity of the filter, clogging of the filter, temperature variation, and change in calibration characteristics (Dunnicliff 1988). The main concern for the measurement of transient pore pressures is time lag. A time lag may be caused by a relatively low permeability filter, air trapped inside the filter, or air trapped in the chamber between the filter and the pressure-sensing diaphragm. A low permeability filter can be avoided by proper filter design. Air in the system will cause the PPT to become partially saturated, and this can be caused by improper saturation and installation procedures. An additional problem may arise if the filter becomes clogged with soil particles. All of these issues can lead to a time lag in the pore pressure-time histories and measured pore pressures that are smaller than the actual pore pressure.

In the early stages of this research, a modified push-in Geokon-3400 piezometer was used. This push-in piezometer was designed to accurately measure dynamic pore pressures by alleviating previously stated concerns. A standard procedure for saturation was developed for this piezometer. Details regarding the push-in piezometer are presented in Chapter 6. At the later stages of this research, a miniature pore pressure transducer (Drucker PDCR 81-8317), which has been widely used in centrifuge experiments, was integrated into the liquefaction sensor to replace the separate push-in piezometer. This sensor is discussed further in Chapter 6. Because the pore pressure transducers used in this research are electrical resistance type sensors, a DC power supply and a signal amplifier are required.

3.3.3 Accelerometer

Accelerometers are acceleration sensors used to measure the acceleration of adjacent media. Due to difficulties in waterproofing, they were used only on the ground surface in this study. Wilcoxon-736T accelerometers with a built-in microelectronic amplifier inside the transducer that converts electric charge to DC voltages were used in this research. The built-in amplifier needs a constant current, which was provided by an in-line current source operated by batteries. Triaxial mounting cubes with a threaded stud were used to mount the accelerometers on the footing and on the top of the reconstituted test pit.

3.3.4 Data acquisition system

A data acquisition system (DAQ) is used to convert continuous analog signals from various sensors into discrete digital data and to store them for later processing. Two data acquisition systems, called the transient response data acquisition system (TRDAQ) and the long-term data acquisition system (LTDAQ), are employed in this study. To synchronize the two systems, the function generator signal is used as a reference channel that is recorded by both systems.

The TRDAQ records sensors that are only active during dynamic loading. These sensors are typically the geophones. The main features of the TRDAQ are no interchannel delay, a high sampling rate, an input analog signal trigger, and high resolution. The HP 3567A multichannel dynamic signal analyzer (DSA) is employed as the TRDAQ to record data during dynamic loading. The current configuration of the DSA has ten input channels. A notebook with a PCMCIA version of the GPIB card is employed to control the DSA.

The LTDAQ is composed of an analog-to-digital (A/D) board, which converts continuous analog signals to discrete digital data, a storage device that saves the digitalized data, and software that controls the process. A multifunction National Instruments A/D board (PCI-6035E) and *LabView*® software are employed with a high performance PC as the LTDAQ. The current configuration has 8 channels for differential input signals.

3.3.5 Seismic testing equipment

To characterize the dynamic soil properties of the instrumented test area, in situ seismic testing was performed. Specifically, crosshole testing was performed prior to and after each dynamic loading. Also, the measurement of P-wave velocity between sensors was used to verify the saturation of the reconstituted test specimen.

The embedded geophones were used to conduct the crosshole tests. By selecting the appropriately oriented geophones and using an appropriate source, S-wave and P-wave velocities were measured. The crosshole source was placed in a previously installed PVC pipe and was operated at the same elevation as the selected geophones. A portable dynamic signal analyzer was used to acquire and process the signals from the geophones. Because seismic testing is a small-strain test, it can be repeated without changing the soil properties. Generally, several crosshole tests were performed and the recorded signals were stacked in the time domain to effectively reduce background noise.

3.4 FIELD SETUP

Currently, the in situ dynamic liquefaction test was conducted only on reconstituted soil specimens prepared in a 1.8-m^3 test pit. The reconstituted test specimens were used for following reasons. First, reconstituted specimens can be reconstructed many times at the same site, which makes the process repeatable. Second, the physical properties of the testing soil, such as relative density, unit weight, and degree of saturation, can be better controlled and more accurately

measured using reconstituted test specimens. Third, it is easier to install sensors at designated locations without disturbing the soil.

Although analytical studies (presented in Chapter 4) revealed that the largest strains would be generated at locations close to the footing, the reconstituted test pit was placed 3.3 m (11 ft) away from the edge of the footing. This distance was chosen because of safety considerations for the vibroseis truck, such as overturning of the truck when the test pit loses strength and liquefies. A general schematic of the dynamic liquefaction test is shown in Figure 3-3. The test pit is lined with a waterproof liner and backfilled soil is deposited under water table in the test pit to prepare the specimen. As the soil is deposited, four sensors are placed in a square array, with another sensor placed at the center of the array. An accelerometer is placed at the top of the test pit. Each test performed in this study had a layout similar to that shown in Figure 3-3.

To establish the liquefaction characteristics of the test soil, each test series starts from a low-loading amplitude level. The loading level is gradually increased until significant excess pore pressures are observed or the capacity of vibroseis truck is reached.

3.5 COLLECTED DATA

With the current configuration of the test pit and testing sequence, several types of data are collected to determine the dynamic soil properties and pore pressure generation characteristics of the instrumented site. The fundamental data are listed as follows:

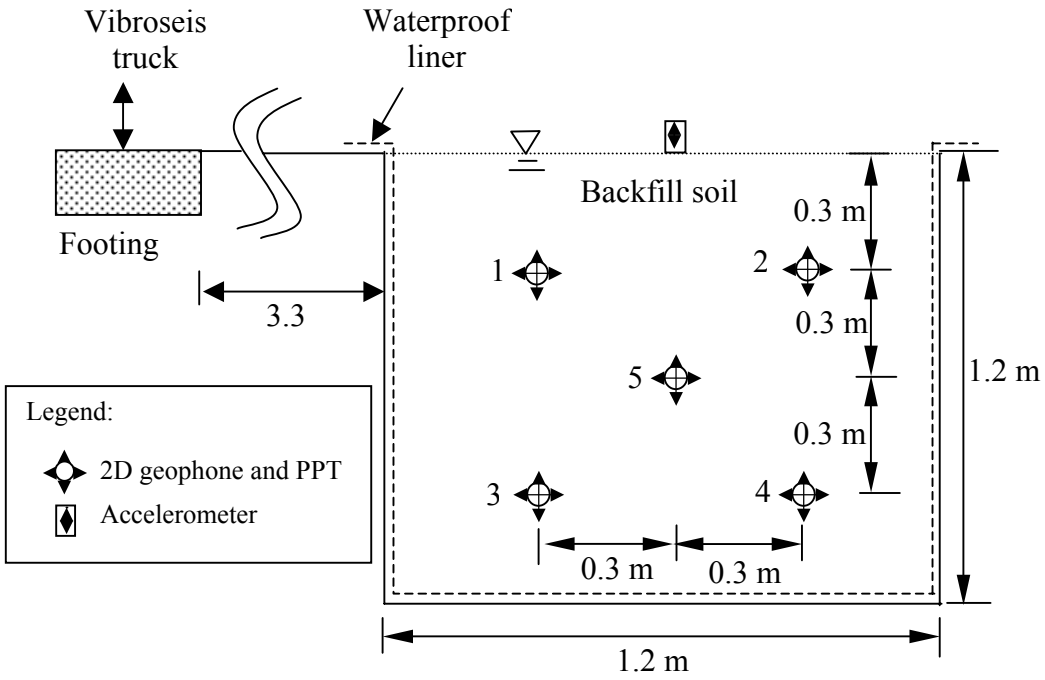

Figure 3-3 Schematic illustration of in situ dynamic liquefaction test

1. The shear strain-time histories are evaluated using the geophone records. The geophone data also provide information about the stress waves propagating through the test area.
2. Pore water pressure-time histories are obtained. The pore water pressure-time histories contain both hydrodynamic and residual components. Combined with the shear strain-time histories, the coupled behavior between the induced shear strain and pore pressure generation is measured.

3. The phase velocity of the stress waves is obtained from the vertical geophones.
4. The pore pressure generation curve of the site is established by compiling the dynamically induced shear strain level and generated excess pore water pressure with respect to a specific number of loading cycles.

3.6 SUMMARY

This chapter provides a general description of the in situ dynamic liquefaction test developed at UT. The testing procedure uses a vibroseis truck as a dynamic loading source that generates stress waves that shear the soil and induce excess pore water pressures.

The dynamic loading system in this study consists of a vibroseis truck, load cell, loading frame, and circular concrete footing. Detailed descriptions of the dynamic loading system are presented in section 3.2. Section 3.3 provides a general description of the instrumentation system used in the in situ liquefaction test. The instrumentation system is composed of sensors, including geophones, accelerometers, and pore pressure transducers, and two data acquisition systems that convert the analog signals to digital form and store them. The field setup of the liquefaction test performed on a reconstituted test specimen is described in Section 3.4. The reasons why reconstituted test specimens were used in these initial studies are addressed. The collected data using the current testing configuration are listed in Section 3.5. The fundamental data types include shear

strain-time histories, pore pressure-time histories, and particle velocity data. The collected data allow the pore pressure generation characteristics of the reconstituted test specimen, expressed as the excess pore pressure ratio versus the induced shear strain amplitude, to be measured in the field.

Chapter 4. Analytical Framework and Numerical Simulation

4.1 INTRODUCTION

In this chapter, the analytical framework for the developed testing technique and results from numerical simulation of the testing procedure are described. The theoretical wave field generated by the vertically vibrating vibroseis used in the current experimental setup is described. The applicability of this theoretical solution to the proposed test setup is also discussed. This analytical solution provides the basis for interpreting the recorded particle motions, as well as providing the theoretical background for wave propagation-based methods for evaluating shear strain. In addition, field vibration tests, which were performed to verify the performance of the loading system and to characterize the wave propagation properties of the native soil at the test site, are presented.

Numerical simulations using the finite element method were conducted in the early stages of this research to predict the shear strains induced by the test setup described in Chapter 3. These finite element analyses provide useful information regarding the expected shear strain levels and the general shear strain field within the test area.

4.2 WAVE PROPAGATION FOR PROPOSED TEST SETUP

In the in situ dynamic liquefaction test, the cyclic or dynamic strains are induced by stress waves generated by the vertically vibrating vibroseis and propagating through the test area. The particle motion during the test is governed predominately by surface wave propagation theory. A proper understanding of the wave propagation due to dynamic surface loads is essential for proper interpretations of the collected data.

4.2.1 Theoretical wave field due to dynamic vertical surface loads

A dynamic circular load acting normal to the surface of a half space will generate two types of body waves, compression waves (P-wave) and shear waves (S-wave), one type of surface wave, Rayleigh waves, and one secondary wave, head waves (Foinquinos and Roesset 2000). Analytical solutions for different loading conditions applied to the surface of an isotropic, homogeneous, and elastic half-space have been developed by various researchers. Solutions for a point load source (Lamb 1904), a uniform impulse on a circular area (Mitra 1961), and a harmonic uniform circular load (Miller and Pursey 1954) have all been developed. Analytical solutions for a layered system subjected to vertical surface loads have been presented by Haskell (1953), and Kausel and Roesset (1981) present a numerical solution for the same problem. A detailed review of the soil response due to dynamic surface loads can be found in Foinquinos and Roesset (2000).

The wavefronts for a homogeneous, isotropic, elastic half-space subjected to a uniform impulsive pressure exerted on a circular area are shown in Figure 4-1 (Foinquinos and Roesset 2000). There are four types of waves propagating in the half-space: compression waves (P-waves), shear waves (S-waves), head waves (Von Schmit waves), and Rayleigh-waves. P-waves and S-waves are body waves. Head waves are secondary disturbances generated by incident P-waves at the surface and propagating with the S-wave velocity. Rayleigh-waves are surface waves. Analytical solutions (Mitra 1961) reveal that the displacements in the near field (i.e., within 4 wavelengths from the source) are generally due to a mixture of P-, S-, head, and Rayleigh-waves. In the far field (i.e. greater than 4 wavelengths), the arrivals of the different wavefronts separate and the displacements due to Rayleigh waves dominate.

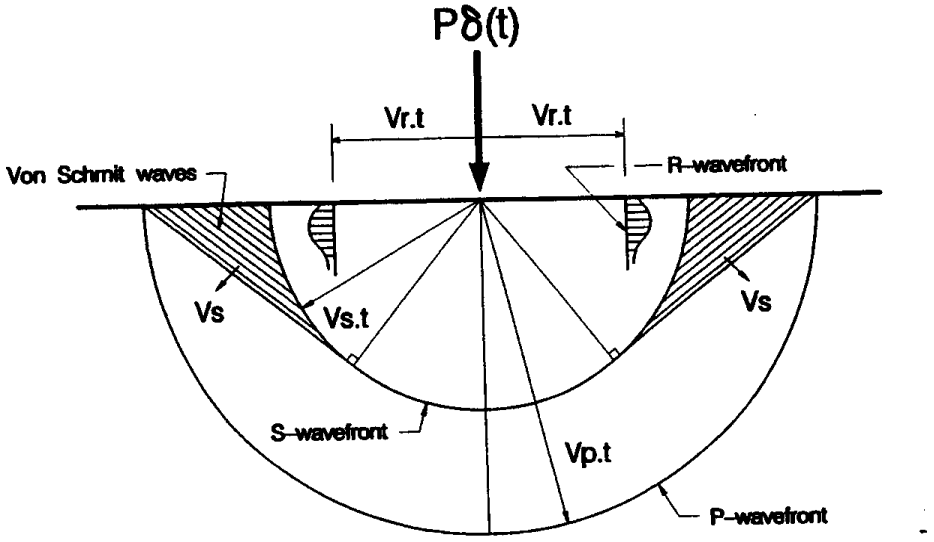

Figure 4-1 Wavefronts in the elastic half space due to an impulsive point load (Foinquinos and Roesset 2000)

The far-field displacement field for a harmonic surface load on an elastic half space with Poisson's ratio (ν) equal to 0.25 is shown in Figure 4-2 (Woods 1968). From the energy perspective, Rayleigh waves carry the majority of energy (67 %), while shear waves and compression waves carry less energy (26% and 7%, respectively). From the attenuation perspective, Rayleigh waves decay with one over the square root of distance from the source ($1/R^{0.5}$), while body waves decay more quickly, both within the mass (1/R) and along the surface ($1/R^2$). Although the current configuration is in the near-field range, it is still dominated by Rayleigh waves. Consequently, the Rayleigh wave should be the dominant wave that shears the soil in the current test configuration.

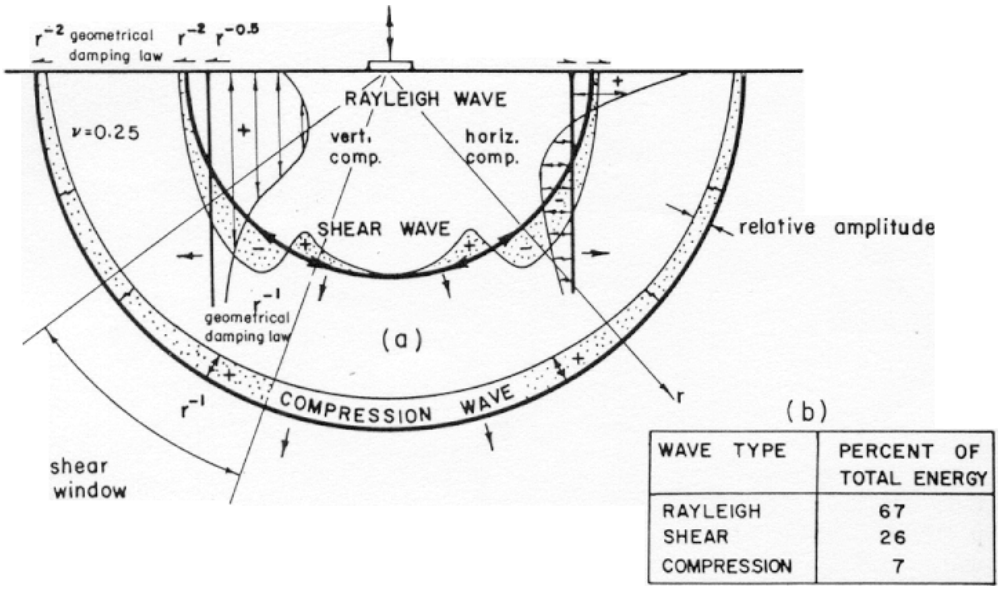

WAVE TYPE	PERCENT OF TOTAL ENERGY
RAYLEIGH	67
SHEAR	26
COMPRESSION	7

Figure 4-2 Far field displacement field for dynamically loading circular footing on an elastic half space with ν=0.25 (after Woods 1968)

4.2.2 Properties of Rayleigh waves

There are several important properties of Rayleigh waves that are of interest in field exploration and earthquake engineering. Three properties are discussed here for their applications to site characterization and validation of recorded geophone data in the field.

Rayleigh wave velocity is closely related to S-wave velocity. The ratio of Rayleigh wave velocity to S-wave velocity, as a function of ν, is shown in Figure 4-3. In engineering practice, Rayleigh wave velocity is commonly taken as about 90% of the S-wave velocity. Using the velocity relationship between Rayleigh waves and S-waves, measured Rayleigh wave velocities can be used to determine the average S-wave velocity of soil within about one wavelength of the ground surface (Stokoe and Nazarian 1985)

The displacement solution for Rayleigh wave propagation can be expressed in the horizontal and vertical components. Considering a half cylindrical coordinate system with an x-coordinate positive to the right, and a z-coordinate positive downward, the Rayleigh wave displacement solution in the far field can be expressed as (Rayleigh 1885):

$$u_x = iA_1 k_R \left(-e^{-qz} + \frac{2qs}{s^2 + k_R^2} e^{-sz}\right) e^{i(\omega t - k_R x)} \quad \text{..... (4-1)}$$

$$u_z = A_1 q \left(-e^{-qz} + \frac{2k_R^2}{s^2 + k_R^2} e^{-sz}\right) e^{i(\omega t - k_R x)} \quad \text{..... (4-2)}$$

where u_x, u_z = horizontal and vertical displacements, respectively, A_1=amplitude constant, $k_R = \omega / V_R$ (wave number), ω= circular frequency, $q = k_R \sqrt{1 - (V_R / V_P)^2}$,

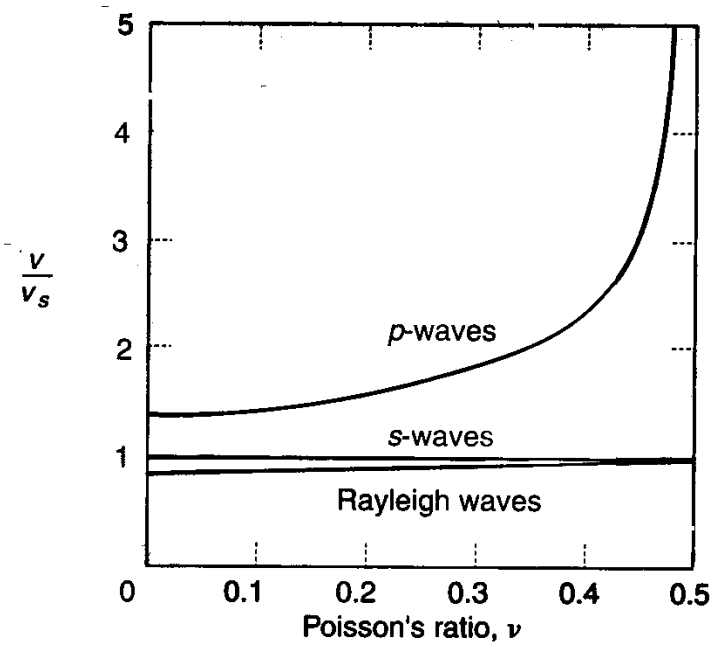

Figure 4-3 Variation of wave velocity ratios (wave velocity normalized by shear wave velocity) with Poisson's ratio (after Richart et al. 1970)

$s = k_R\sqrt{1-(V_R/V_S)^2}$, V_R, V_P, V_s = wave propagation velocities of Rayleigh, S-waves, and P-waves, respectively.

The displacement amplitudes are a function of distance from the source, depth, wave velocities of the subsoil, Poisson's ratio, and frequency. The variation of normalized vertical and horizontal displacement amplitudes with depth for different values of Poisson's ratio are shown in Figure 4-4. Figure 4-4 shows that at all depths the vertical motion is in the positive direction, while the horizontal motion changes from negative to positive motion at a depth of

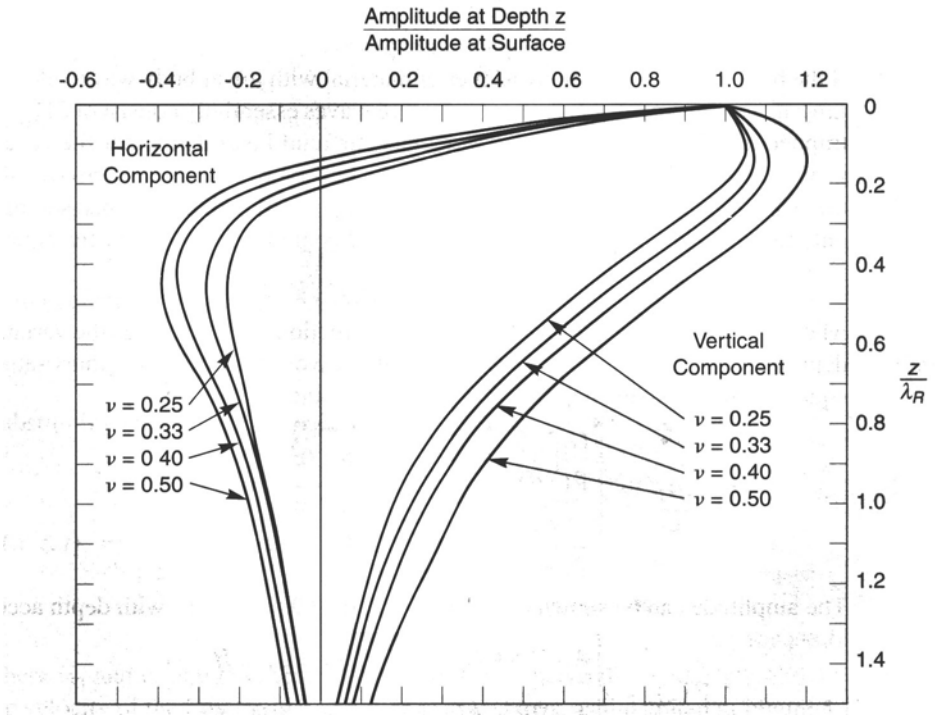

Figure 4-4 Variation of horizontal and vertical displacement amplitudes of Rayleigh waves (after Richart et al. 1970)

about 0.2 wavelengths. The analytical solution (Equations 4-1 and 4-2) also shows that there is a 90° phase difference between the horizontal and vertical components of motion. The result is retrograde elliptical motion near the surface and prograde elliptical motion at depth.

Another important characteristic of Rayleigh waves is their dispersive behavior in a non-homogeneous half space. Dispersive waves propagate at different velocities at different frequencies. Using this dispersive property and the velocity ratio between Rayleigh waves and S-waves, stiffness properties of different soil layers can be determined. The Spectral-Analysis-of-Surface-Waves

(SASW) method (Stokoe et al. 1994) is one method that uses Rayleigh waves to evaluate shear wave velocity profiles of the subsurface. In the SASW method, the Rayleigh wave velocity is measured at different frequencies to create a dispersion curve, which shows the relationship between Rayleigh wave velocity and frequency. Subsequently, a forward modeling technique is used to develop a theoretical dispersion curve for a layered system with a given shear wave velocity profile. The shear wave velocity profile that produces a theoretical dispersion curve that best matches the field measured dispersion curve is taken as the in situ velocity profile.

4.3 FIELD VIBRATION TEST

Field vibration tests were performed to verify the performance of the loading system and to characterize the wave propagation properties of the native soil at the test site. A schematic of the field vibration test is shown in Figure 4-5. Four vertical accelerometers were placed at four locations: on top of the footing, and 1.2 m (4 ft), 2.1 m (7 ft), and 3 m (10 ft) away from the edge of the footing. These accelerometers measured the vertical accelerations generated by the vibroseis.

A linear swept sine forcing function with a frequency span of 10 to100 Hz and a constant input voltage amplitude was applied to the hydraulic ram to determine the response of the footing. The acceleration spectrum measured by the accelerometer on the footing and the applied load amplitude spectrum measured by the load cell are shown in Figure 4-6. The maximum acceleration of the

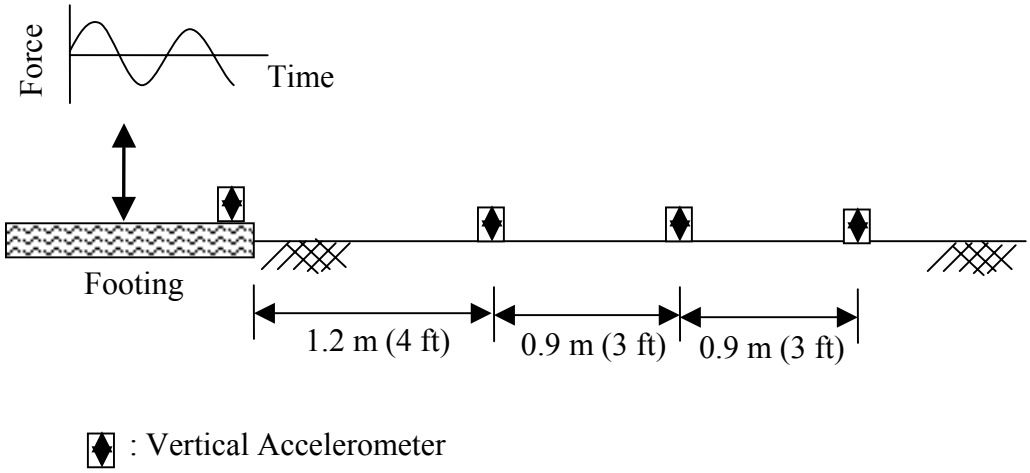

Figure 4-5 Schematic illustration of field vibration test

footing occurred close to 50 Hz, indicating a resonant frequency of the system at about 50 Hz. A relatively constant output of force occurs in the 20 to 50 Hz range. The accelerometer and load cell data at frequencies below 20 Hz show a large peak at 15 Hz, and a sharp drop off at frequencies below 15 Hz. These spurious data may be a result of poor performance of the hydraulic system at frequencies below its designed operating range. Alternatively, the peak between 10 and 20 Hz may represent a rocking mode of the footing, because the footing was not placed exactly level.

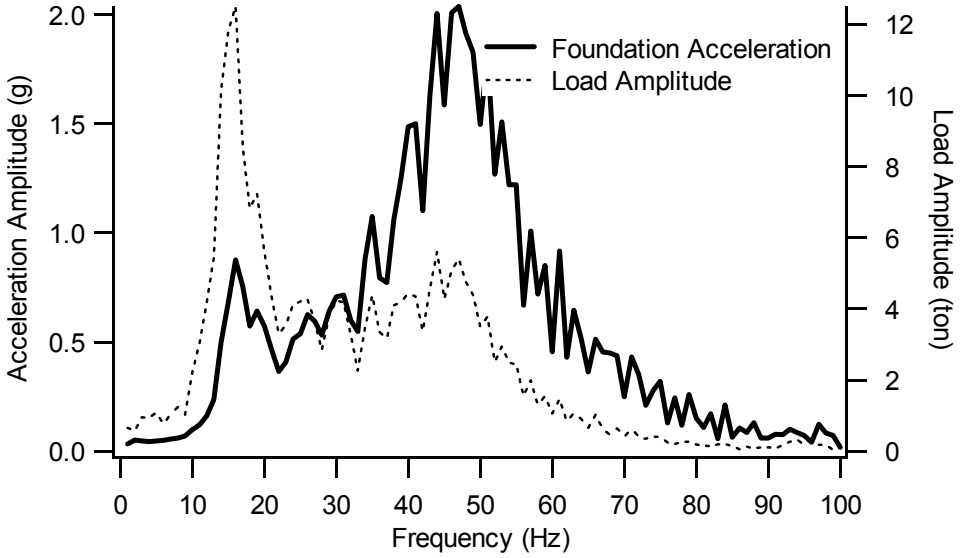

Figure 4-6 Measured vertical footing acceleration spectrum and measured footing load spectrum from swept sine vibration test

Three frequencies were selected (20, 40 and 50 Hz) to conduct steady-state vibration tests, where the footing was vibrated at a constant frequency. Various input voltage amplitudes were used to characterize the loading response of the hydraulic vibrator with respect to the input voltage. Additionally, the steady-state vibration tests evaluated the similarity between the output force and the footing motion, and the propagation behavior of surface waves in the native soil. The results from each loading frequency were similar and only the 20 Hz data are shown here. It should be noted that the in situ liquefaction test was performed at 20 Hz in this study. Although this frequency is higher than the typical frequency content of earthquake ground motions, it was chosen because it is the lowest frequency at which the vibroseis generates clear sinusoidal waves.

The vertical load and the vertical footing acceleration amplitudes with respect to various input voltages are shown in Figure 4-7. The results reveal that the output force of the vibrator is relatively linear with respect to the input voltage. These results will assist in specify loading levels for the in situ liquefaction test.

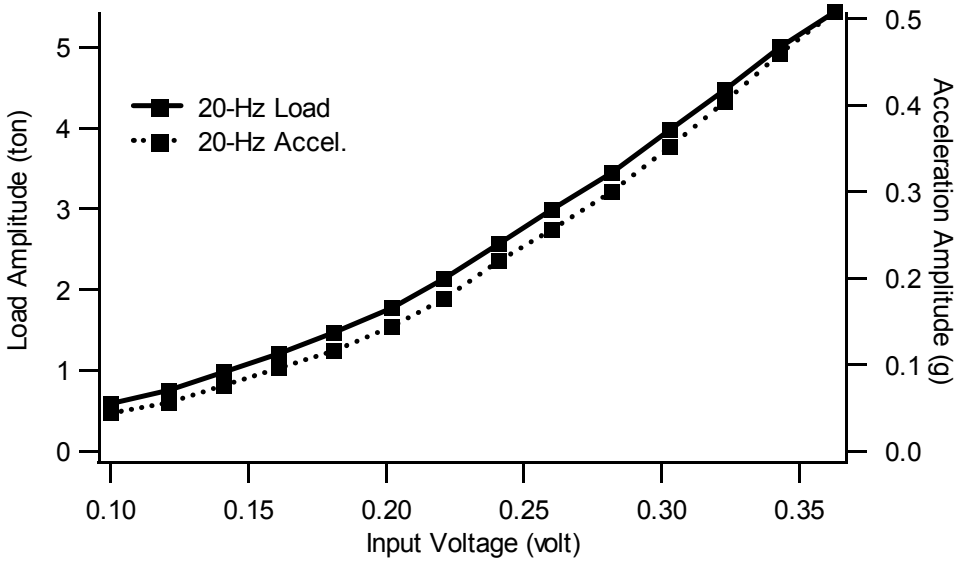

Figure 4-7 Load and acceleration response of the loading system at 20 Hz

The acceleration amplitudes recorded by the vertical accelerometers located on top of the footing and at different distances from the footing are shown in Figure 4-8. The largest accelerations are always recorded at top of the footing and the recorded acceleration amplitudes decay with distance from the footing. The accelerations at each location increase linearly with the applied load amplitude, indicating that the native soil is still in the linear elastic range.

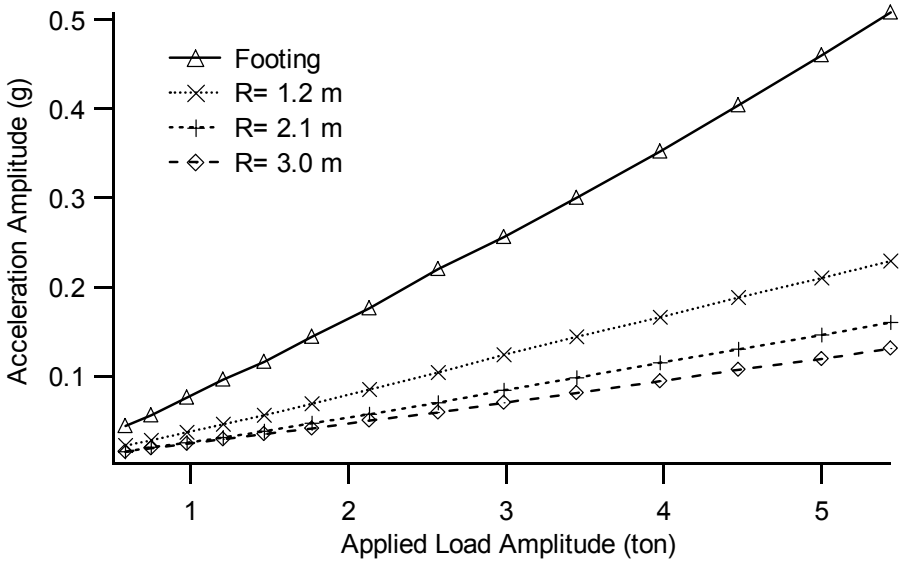

Figure 4-8 Acceleration amplitude versus applied footing load amplitude for the vertical accelerometers at different radial distances from the footing

The attenuation of the wave amplitudes with distance was considered by computing the normalized acceleration ($a_{max}/a_{max,footing}$) for each accelerometer at each loading level. The normalized acceleration with respect to $1/R^{0.5}$ (where R= distance from footing) is shown in Figure 4-9. Attenuation with $1/R^{0.5}$ is expected for surface waves (Richart et al. 1970) and Figure 4-9 indicates that the measurements in the field decay in this manner. Consequently, the dominant wave generated by the vertical vibration of the footing is a Rayleigh-type surface wave.

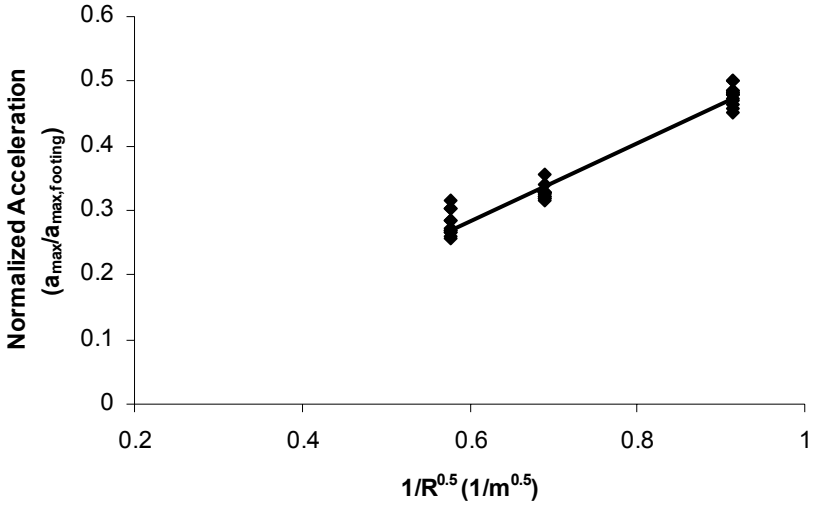

Figure 4-9 Attenuation of normalized surface vertical acceleration with $1/R^{0.5}$ for native soil under 20 Hz loading

The phase velocity between the recorded accelerations at 2.1 m (7 ft) and 3.0 m (10 ft) from the footing was computed as 150 m/s (500 ft/s). This velocity corresponds to the Rayleigh wave velocity of the subsurface profile within about one wavelength from the ground surface. Considering the loading frequency of 20 Hz, the wavelength ($\lambda_R = \frac{V_R}{f}$, where λ_R and V_R are the wavelength and velocity of Rayleigh waves, respectively, and f is frequency) is about 7.5 m (25 ft). Rayleigh wave velocity is typically 90% of the S-wave velocity of the medium. Therefore, the measured Rayleigh wave velocity indicates that the average S-wave velocity of the native material is about 165 m/s over the top 7.5 m. Similar wave velocities

were measured at loading frequencies of 40 Hz and 50 Hz, indicating the soil in the top 7.5 m is relatively uniform.

4.4 NUMERICAL SIMULATION

Because of the complexity of the field conditions, the finite element method (FEM) was employed to simulate the field behavior and collect more insight into the dynamic soil response for the proposed testing technique. FEM analyses were also conducted to validate the strain calculation from measured nodal displacements, as well as to evaluate the appropriateness of the instrumentation array size and the effects of a layered system. These results are presented in Chapter 5. Details of the numerical models and major findings are presented here.

4.4.1 Finite element analysis

With advances in computational technologies, finite element methods have become important parts of engineering analysis and design. Many finite element programs have been developed and widely used in different engineering disciplines. The framework for finite element procedures can be found throughout the literature (e.g., Bathe 1996, Zienkiewicz et al. 1995). The analyses presented here address the soil response under sinusodial loads and the simplified assumptions to be incorporated in analyzing the field data.

The governing equation of motion for a dynamic system is:

$$M\ddot{U}(t) + C\dot{U}(t) + KU(t) = R(t) \quad \text{..... (4-3)}$$

where M= the mass matrix, C=damping matrix, K=stiffness matrix, R=load vector, and $\ddot{U},\dot{U},U$ =vectors of nodal accelerations, velocities, and displacements, respectively. To solve a complex system, the system is discretized both in the spatial and time domains, and the approximate solution is obtained numerically through element by element calculations at each time step.

A general-purpose finite element program, ABAQUS, is used in this study. A general direct integration method, the Hilber-Hughes-Taylor operator, is employed in an implicit analysis. The principal advantage of the operator is unconditionally stable for linear systems. To simplify the analysis, the soil and circular footing are modeled as linear elastic materials. Four-node axisymmetric elements were used to model both the footing and soil. Infinite elements were utilized around the finite element boundaries to minimize the effects of wave reflection. At the contact area between the footing and soil, nodes are constrained in the horizontal direction, which models a rough contact between the footing and soil.

In wave propagation analyses, two of the primary concerns are the stability and accuracy of the direct time integration scheme. The stability depends on the increment of the time step in an explicit integration scheme and the accuracy depends on the mesh dimensions. In the time domain, improper temporal discretization will cause instability and frequency aliasing (Valliappan and Murti 1984). In the spatial domain, large element dimensions remove high frequency components of motion resulting in spurious oscillations and velocity dispersion.

Because the employed numerical integration scheme is unconditionally stable, no stability constraint in the time step is imposed. However, to achieve an accurate solution, a reasonably small time step is required. A time step less than 0.002 seconds was used for all analyses because it provides over 100 time steps per 20 Hz loading cycle. The element size was taken as less than 15.2 cm because this size will provide about 60 elements per wavelength, allowing the displacement field to be fully characterized. Two finite element meshes were generated for different analyses. Details about the element size, time step, and material properties for these models are tabulated in Table 4-1.

Table 4-1 Summary of finite element models

Model	**Element Size (cm)**	**Δt (sec)**	**V_S (m/s)**	**ν**	**ρ (kg/m^3)**	**Purpose**
M1	7.6	0.001	183	0.25	197	Model Calibration
M2	15.2	0.002	183	0.25	197	Calculate maximum strain level in field

4.4.2 Finite element model calibration

The purpose of model M1 is to calibrate the finite element model with respect to recorded data from the field test site. The recorded data comes from testing performed by Phillips (2000) at the field test site. This testing involved embedding geophones in the native soil and measuring the particle motions during footing vibration. The soil is modeled as a homogeneous, isotropic, elastic material with elastic shear modulus $G = 6.6 \times 10^6$ kPa (i.e., V_S=183 m/s) and Poisson's ratio $\nu = 0.25$. The Poisson's ratio was taken from the measured S-

wave and P-wave velocities at the field test site by Chen (2001). The shear modulus was estimated from several sources, including the in situ seismic field tests performed by Axtell (2001) and Chen (2001), P-wave velocities measured by Phillips (2000), and the vibration test described previously. Although the shear wave velocity of the field test site may increase with depth, the measured data seem to indicate that it is relatively constant. Axtell (2001) measured a constant shear wave velocity of about 180 m/s in the top 0.75 m of the site, while the Rayleigh wave testing previously discussed indicates an average shear wave velocity of 165 m/s over the top 7.5 m of the site. These values are relatively close, therefore a single value of V_S (or G) was used throughout the finite element model. In addition, the circular footing is modeled as 1000 times stiffer than the soil and infinite elements are used in underground boundaries to reduce the reflected waves from these boundaries.

The numerical results are compared with the test data collected by Phillips (2000). The loading frequency for this test was 40 Hz with various dynamic loading levels. The finite element model and the relative locations of the geophones in the test are shown in Figure 4-10. The three geophones beneath the center axis of the footing are vertical geophones, while others are 2D geophones oriented vertically and horizontally. A comparison of the measured and computed vertical and horizontal displacement-time histories at geophone C4 is shown in Figure 4-11. The favorable agreement between measured and predicted displacement amplitudes indicates that the simplified finite element model can properly simulate the wave propagation behavior of the native soil.

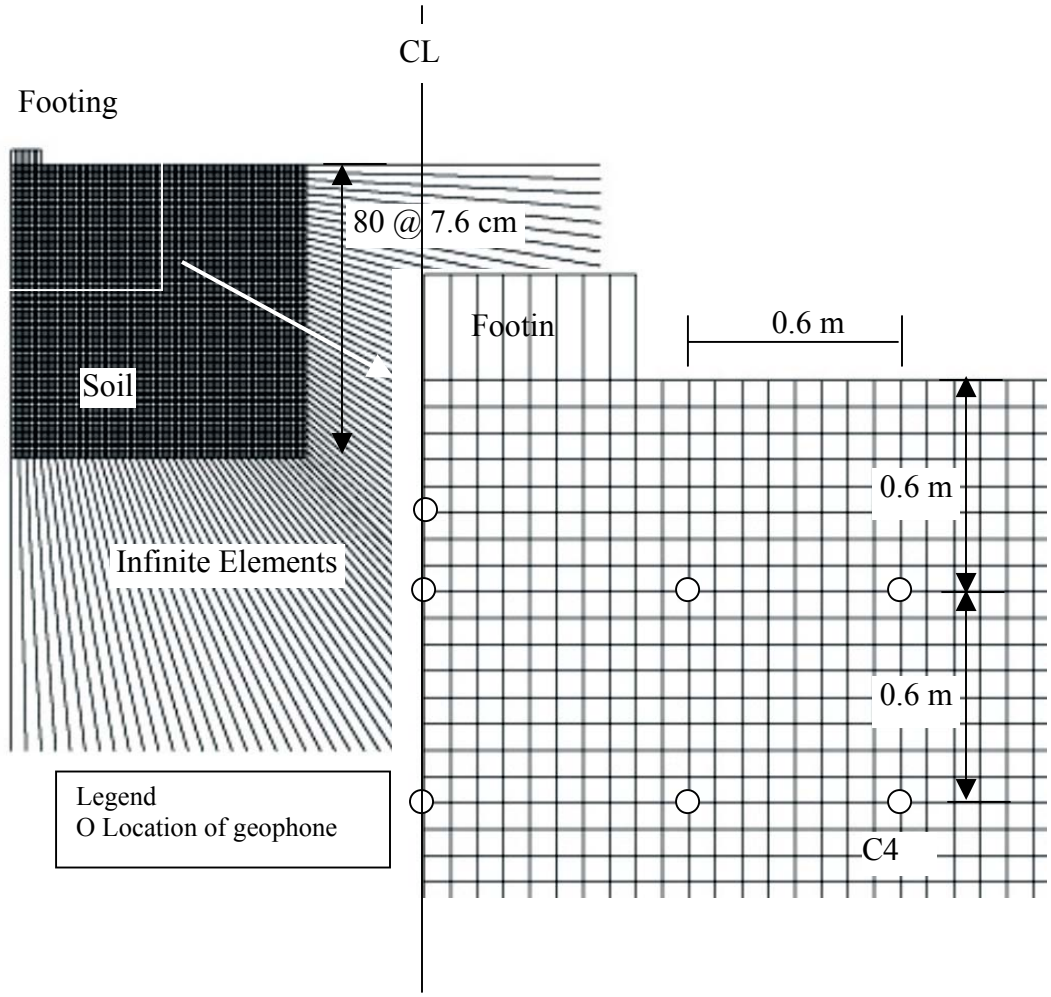

Figure 4-10 Finite element model M1 and testing layout of the in situ dynamic test by Phillips (2000)

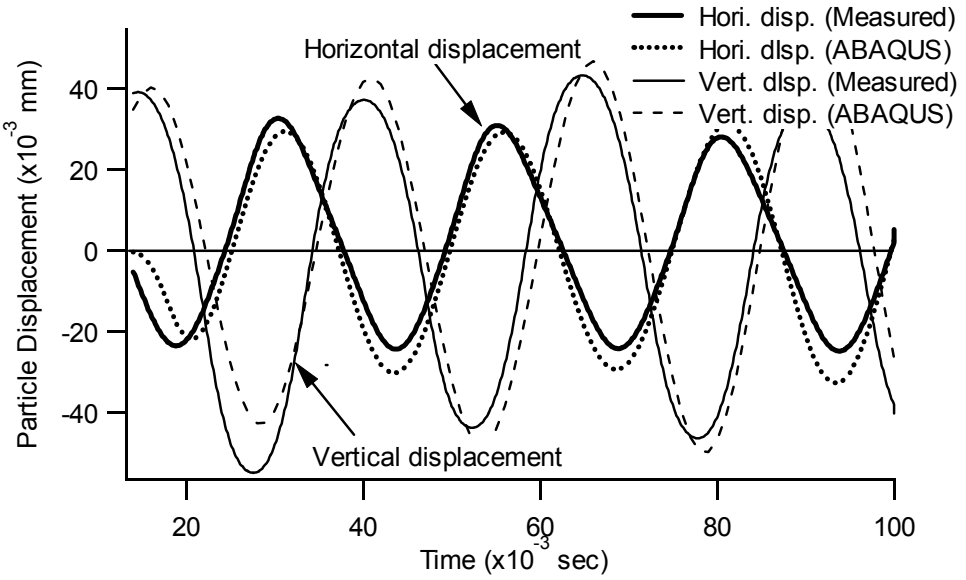

Figure 4-11 Comparison of measured and predicted transient displacement time histories at the location of C4 (loading frequency= 40 Hz, dynamic load amplitude= 35 kN)

4.4.3 Expected strains induced in an homogeneous, elastic soil deposit

To generate significant excess pore water pressure, the dynamic shear strains induced in the soil should be larger than the conventional threshold shear strain of around 0.01%. The purpose of model M2 is to evaluate the shear strain level expected in the field under a specific loading level applied by the vibroseis truck. Model M2 is similar to M1, except that a larger element size (15.2 cm) is used to cover a larger area and a lower loading frequency (20 Hz) is used. To simulate the loading conditions used in the in situ liquefaction test, a sinusoidal load with a frequency of 20 Hz and a dynamic load amplitude of 53.3 kN (12 kips) was applied uniformly to the footing.

Contours of shear strain amplitude are shown in Figure 4-12, along with the relative locations of the Phillips (2000) array and the proposed reconstituted test pit. The largest shear strain (0.12%) occurs in the area near the Phillips (2000) array. Although this seems to be the best place to build the test pit, there are concerns regarding the stability of the vibroseis truck if the test pit was placed here. When the test pit loses strength and liquefies, the vibroseis may tilt or overturn, damaging the equipment. Therefore, the proposed test pit was shifted to a location approximately 3.3 m (11 ft) away from the edge of the footing. The maximum shear strain in the test pit area is expected to exceed the conventional threshold shear strain (0.01%). Additionally, the results indicate that the shear strain field inside the proposed test pit is relatively uniform, as evidenced by the small gradient in shear strain contours.

It should be noted the largest load amplitude applied in the field is 89 kN (20 kips), which is almost twice the load used in the analysis. A larger induced shear strain level in the native soil is expected.

4.5 SUMMARY

The theoretical wave field due to vertical sinusoidal surface loads was presented. These analytical solutions are useful in qualitatively assessing the measured particle motion data. Displacements in the near field are due to a mixture of P-, S-, head, and Rayleigh waves. In the far field, displacements are dominated by Rayleigh waves.

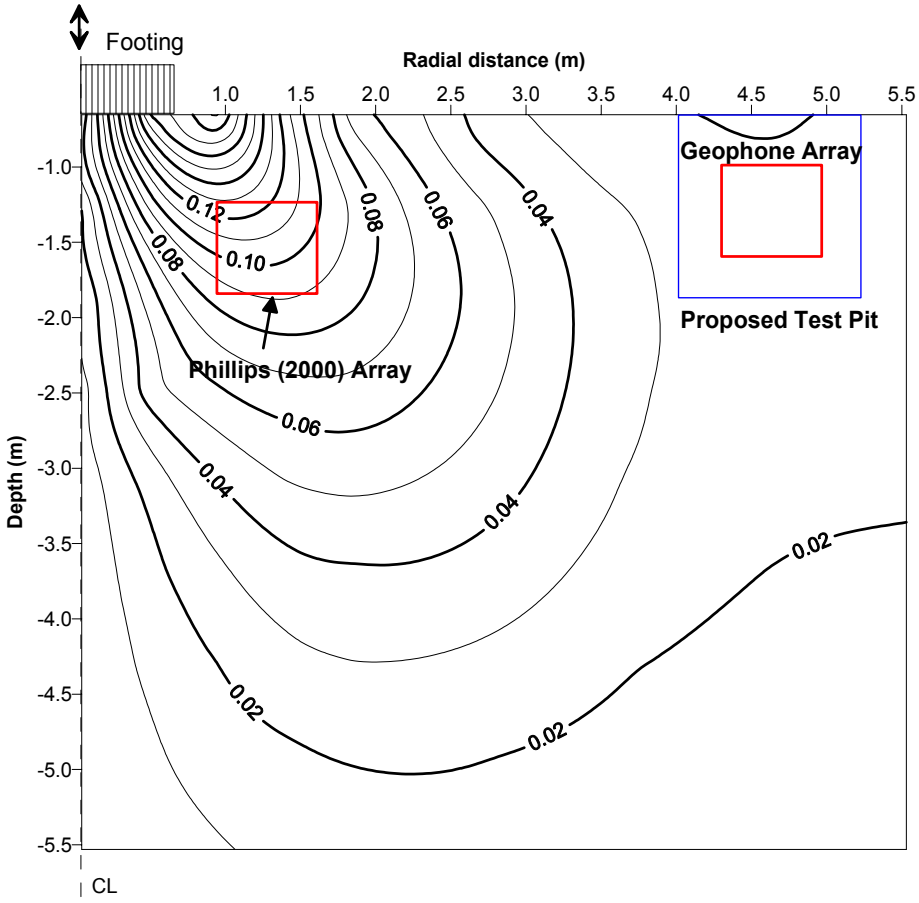

Figure 4-12 Contours of shear strain amplitude from model M2 for sinusoidal loading frequency of 20 Hz and loading amplitude of 53.3 kN

The Rayleigh wave properties associated with this research, such as the velocity relationship between Rayleigh waves and body waves and dispersion of Rayleigh waves in a layered system, were discussed. Rayleigh wave velocity is commonly taken as about 90% of the S-wave velocity. The displacement solution reveals that Rayleigh waves display retrograde elliptical motion near the surface

and prograde elliptical motion at depth. Rayleigh waves are dispersive in a layered system with waves propagating at different velocities at different frequencies. The dispersive behavior of Rayleigh waves is the basis of the SASW technique.

The field vibration test, which verified the performance of the loading system, and the wave propagation properties of the native material were also presented. The vibration tests revealed that the dominant wave type in the native soil is the Rayleigh wave and the average Rayleigh wave velocity for the top 7.6 m of native soil is around 150 m/s.

The finite element method was employed to simulate the field behavior of the developed testing technique and collect more insight into the dynamic soil response. Two finite element models were created. Model M1 was used to calibrate the finite element model using field test data collected previously. Model M2 was used to predict the expected shear strain levels induced by the proposed field testing configuration. The numerical results from model M2 indicate that the induced shear strains will be greater than the conventional threshold shear strain of 0.01%.

Chapter 5. Data Analysis

5.1 INTRODUCTION

The data analysis techniques used in this research are presented in this chapter. The two important parameters in this study are the induced shear strain and the generated excess pore pressure. The induced shear strains are computed from the geophone data and the generated excess pore pressures are processed from the pore pressure transducer signals. The signal processing and numerical algorithms involved in converting the data from the sensor signals (i.e., voltages) to physical properties (e.g., velocities, displacements, and pore water pressures) are described. Numerical techniques performed in the time and frequency domains are discussed.

The methods used to evaluate shear strain-time histories from measured ground velocity-time histories are presented. Four distinct methods are proposed and used to calculate shear strains. These methods are classified into two categories: displacement-based methods and wave propagation-based methods.

The techniques presented in this chapter provide the background knowledge for the data reduction procedures presented in Chapter 7.

5.2 SIGNAL PROCESSING AND NUMERICAL ALGORITHMS

Signal processing is an important issue for dynamic measurements. In the current testing configuration, the intended engineering parameters are rapidly acquired using electronic transducers and are stored in discrete digital form. To interpret the results, signal processing techniques are used to either enhance dynamic signals with respect to noise or to highlight specific signals. The purpose of this section is to provide a brief description of the signal processing techniques employed in this study. Additionally, some numerical algorithms used to compute displacement-time histories from recorded velocity data are presented.

For most data processing, the main mathematical operations are convolution, Fourier transformation, and correlation (Sheriff and Geldart 1995). The discussions in this chapter will focus on time domain and frequency domain analyses using these mathematical operations. Time domain analyses are operations that are performed using the discrete time series as they were originally recorded. For frequency domain analyses, the recorded time signals are transformed into frequency spectra, which show the distribution of wave amplitudes across different frequencies.

5.2.1 Time domain analysis

Three types of analysis are performed in the time domain: numerical integration, baseline correction, and signal stacking. Numerical integration of the geophone data, along with a baseline correction algorithm, were used to compute the transient displacements at the geophones for the displacement-based method

of strain calculation presented in Section 5.3.1. The stacking techniques are used in crosshole tests to reduce background noise.

Due to the small time step used to record the geophone signals, a simple trapezoidal rule is employed in the numerical integration of the velocity data to obtain the displacement-time history. The displacement-time history is calculated as:

$$s_j = s_{j-1} + \frac{1}{2}(v_j + v_{j-1}) \cdot \Delta t \quad \text{..... (5-1)}$$

where s_j = displacement at $t = j \cdot \Delta t$, v_j = velocity at $t = j \cdot \Delta t$, and Δt= time step in the geophone signals. The initial displacement is set to zero (i.e., $s_0 = 0$) and the successive displacements are calculated until the end of the velocity record. The displacement-time history calculated using Equation (5-1) has a 90° phase shift with respect to the original velocity-time history. From the point of view of digital filters, the trapezoidal rule integration can be expressed as an autoregressive moving average filter with respect to a specific impulse response (Oppenheim et al. 1999).

Because of the existence of noise and the recorded wave signals not being perfectly sinusoidal, the displacement time-histories computed using the original velocity-time histories show a drift from zero at the end of shaking (Figure 5-1). To eliminate the drift in each displacement-time history, a baseline correction is applied before the strain calculation. A baseline correction finds a best fit curve to the displacement drift using least squares regression, then subtracts the best fit curve from the drift displacement-time history. A 6^{th} order polynomial was used for the baseline correction. From the viewpoint of digital filtering, a baseline

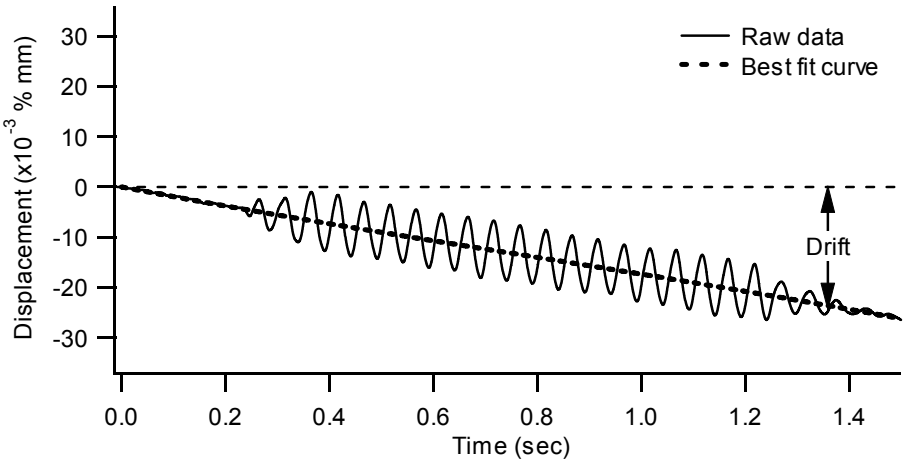

Figure 5-1 Drift error in computed displacement-time history and the corresponding best fit curve (Test T1-2, Case-1 horizontal)

correction is similar to filtering out the DC or low frequency components in a signal. Because filtering can be performed more easily and quickly than a baseline correction in the time domain, a high-pass filter with a cut-off frequency of 4 Hz was used prior to numerical integration using Equation (5-1) to eliminate the drift error.

Because of the small signal amplitudes generated in seismic testing techniques, noise reduction is often required to gather a clear signal. Signal stacking is an effective technique to increase the signal-to-noise ratio (SNR). The SNR is defined as the variance of the signal divided by the variance of the noise. Assuming noise behaves as Gaussian noise with zero mean, averaging multiple measurements in the time domain cancels the random noise and enhances the correlated signals. The SNR can be reduced by 1/N when N measurements are

averaged (Santamarina and Fratta 1998). In the field, signal stacking is performed by the dynamic signal analyzer.

5.2.2 Frequency domain analysis

For frequency domain analysis, dynamic signals are separated into sinusoidal waves of different frequency, amplitude, and phase (Sheriff and Geldart 1995). Transforms between the frequency and time domain are advantageous, especially for filtering. The major computations performed in the frequency domain in this research are digital filtering using a linear filter and cross-spectral analysis.

In the current data reduction framework, frequency filters are used to eliminate noise, process the frequency dependent calibration factors for the geophones, and highlight desired signals. The output from a frequency filter is then used to reconstruct the filtered signal in the time domain. Because the data are in discrete form, only discrete representations in both the time and frequency domains are considered. For data analysis, cross-spectral analysis is used to compute the apparent phase velocity at a specific frequency between two receivers.

5.2.2.1 Transform theory and the fast Fourier transform

The reason for conducting domain transformation in signal processing is that some processes can be performed more easily in one domain than another. There are different transforms used in signal processing in different disciplines.

The most common transform is the Fourier transform, which represents signals as a combination of sinusoids. Because the recorded signals in this research are discrete, the transform is conducted in discrete form and is called the discrete Fourier transform (DFT). For a discrete time signal with a time step Δt, the transform from the time domain to the frequency domain can be represented by:

$$X_k = \frac{1}{N}\sum_{j=0}^{N-1} x_j \cdot e^{-i(\omega_k \cdot t_j)} \quad \text{..... (5-2)}$$

where X_k = Fourier coefficient at frequency ω_k, k=0 ... N/2,

x_j = digital signal in the time domain at $t_j = j \cdot \Delta t$, j=0 … N-1,

$t_j = j \cdot \Delta t$,

N = number of data points,

$\omega_k = \frac{2\pi}{N \cdot \Delta t} \cdot k$, circular frequency, and

$i = \sqrt{-1}$.

The time and frequency intervals are related by:

$$\Delta f = \frac{1}{N \cdot \Delta t} \quad \text{.....(5-3)}$$

The summations in the X_k calculation can be reduced to (N/2+1) by taking advantage of symmetry and periodicity. The maximum non-repeated frequency represented in the Fourier spectrum is $1/(2 \cdot \Delta t)$, which is equal to the Nyquist frequency. The Nyquist frequency is defined as half of the sampling frequency. When sampling continuous signals, no frequency above the Nyquist frequency is allowed.

The inverse discrete Fourier transform (IDFT) reconstructs x_j in the time domain from the Fourier coefficients, X_k. This transformation is computed by:

$$x_j = \sum_{k=0}^{N-1} X_k \cdot e^{i(\omega_k \cdot t_j)} \quad \text{..... (5-4)}$$

Equations (5-2) and (5-4) form a Fourier transform pair, which allows the signals to be transferred from one domain to the other.

The discrete Fourier transform requires a large computation effort. A more effective algorithm was published by Cooley and Turkey (1965), which decomposes the DFT calculation into successively smaller DFT calculations. This fast algorithm is applicable when N (i.e., the number of data points) is a power of 2. The algorithm is known as the fast Fourier transform (FFT). The FFT and the inverse FFT (IFFT) are widely used and are standard built-in functions in all signal processing software.

5.2.2.2 Filters in the frequency domain

The major use of the FFT in this research is to incorporate frequency filters. Utilizing a digital frequency filter, background noise or unwanted signals can be subtracted from the raw data. Also, a digital frequency filter can be used to highlight signals at certain frequencies. Furthermore, it is easier to incorporate frequency dependent geophone calibration factors in the frequency domain.

Frequency filters are generally classified into three types: low-pass, high-pass, and band-pass filters. These names are based on the frequency components preserved after filtering. The three types of filter are represented schematically in Figure 5-2.

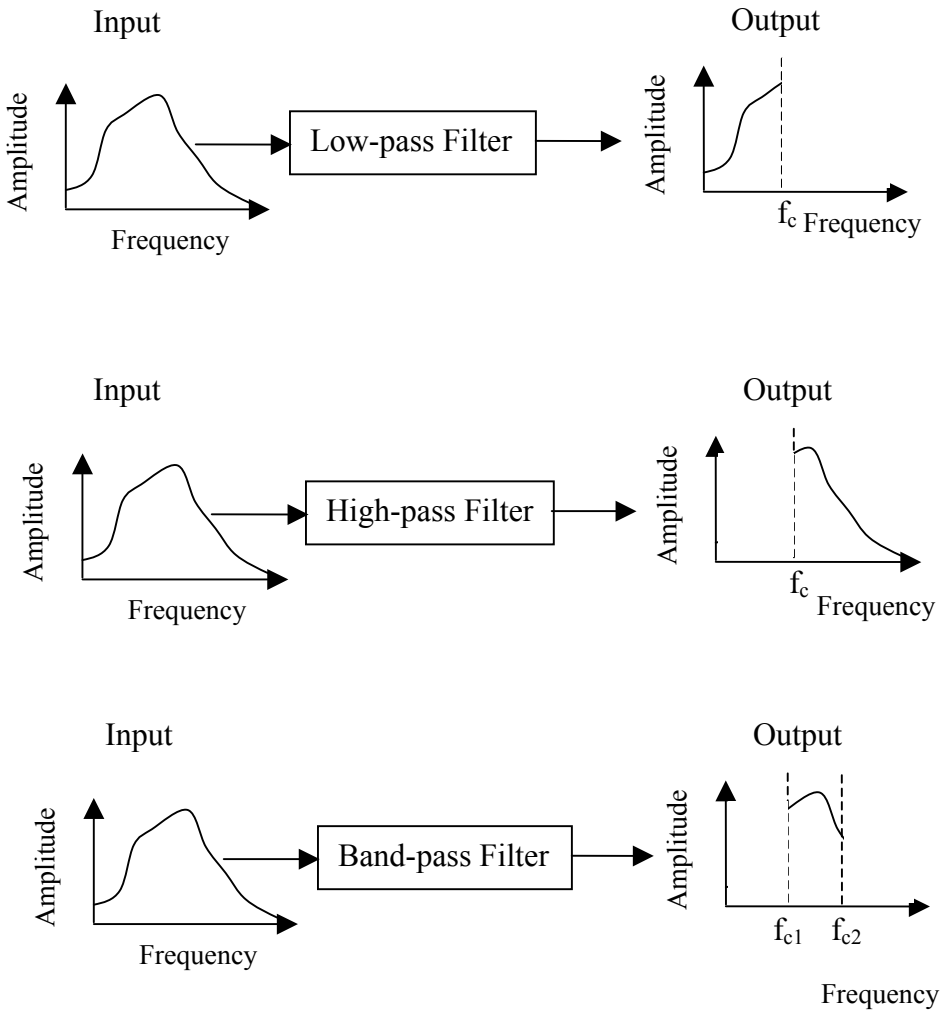

Figure 5-2 Schematic illustration of frequency filters

Low-pass filters preserve the frequency components below the cut-off frequency and remove the frequency components above the cut-off frequency by setting these Fourier coefficients to zero. Low-pass filters are used to remove high frequency noise from sources such as power lines, vehicle engines, etc. In this research, low-pass filters are used to remove high-frequency background noise from geophone data and pore water pressure records.

In contrast to low-pass filters, high-pass filters keep the frequency components above the cut-off frequency and reject the frequency components below the cut-off frequency. The purpose of high-pass filters is to remove a static value (DC component) and low frequency noise from recorded signals. The implementation of this type of filter in this research is to remove the displacement drift from integrated velocity data.

Band-pass filters preserve the frequency components between two specified frequencies and reject the frequency components outside this range. Band-pass filters are used in this research to investigate the hydrodynamic excess pore water pressure at 20 Hz.

A frequency filter can be represented as a window spectrum (W_k), which is an array of zeros and ones that represents the window of the filter. The output of the frequency filter is computed by applying the window spectrum to the input Fourier spectrum. The process for low-pass filtering is schematically illustrated in Figure 5-3. Numerically, the process is easily performed through element by element multiplication of the two spectra, expressed as:

$$Y_k = X_k \cdot W_k \quad \text{..... (5-5)}$$

where X_k = Fourier coefficient at frequency ω_k, before filtering,

W_k = filter "window" in the frequency domain at frequency ω_k, and

Y_k = Fourier coefficient at frequency ω_k, after filtering.

For example, low-pass filtering is performed by applying a window with zero amplitude above the cut-off frequency and unit amplitude below the cut-off frequency (Figure 5-3). After filtering, the filtered data are transformed back to the time domain using the IFFT.

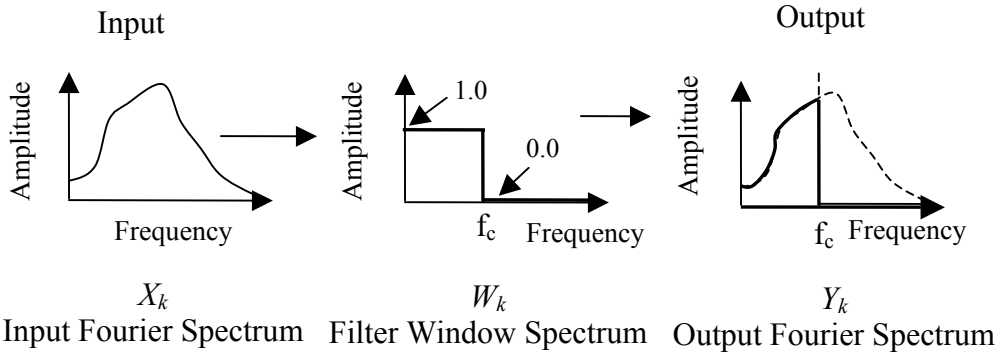

Figure 5-3 Schematic illustration of low-pass filtering using a window spectrum with a cut-off frequency f_c

A frequency filter can also be used to process the calibration factors for frequency dependent sensors, such as geophones. The calibration factors convert the electrical signal (i.e., voltage) generated by the geophone to the physical property (i.e., velocity) measured. These calibration factors for the geophones are

frequency dependent when the measured frequencies are below the resonant frequency of the geophone. Therefore, a calibration spectrum must be developed, rather than defining a single calibration factor for the geophone. When converting measured signals to a physical property, the calibration spectrum can be considered a special filter in the frequency domain. In this process, the measured data are transformed into the frequency domain and the calibration spectrum is applied through element by element multiplication of the calibration spectrum and the measured data spectrum. The measured physical properties can then be presented in the time domain using the IFFT.

A major concern when transforming data between the two domains is losing information due to truncation of the data. This error can be reduced by increasing the length of the time series by padding zeros at the end of the series, increasing the sampling frequency, and carefully selecting the filter window.

5.2.2.3 Selection of cut-off frequency

When applying the frequency filters, a critical issue is the selection of the cut-off frequencies. The selection is somewhat subjective depending on the signal processing techniques, the instrumentation characteristics, and the physical properties being studied (Wilson 1998). The selection of cut-off frequencies for different aspects of this research are discussed below.

A cut-off frequency of 4 Hz was selected for the high-pass filter applied to the velocity data to avoid drifts in displacement calculations. This cut-off frequency was chosen because the predominant frequency in the velocity data is

20 Hz, which corresponds to the loading frequency, and frequencies below 20 Hz are attributed to background noise. To check the displacements computed from the filtered velocity data, displacement-time histories were computed using a baseline correction with no filtering and using a high-pass filter (f_c=4 Hz) on the velocity data without a baseline correction. The displacement-time histories were similar, indicating that the 4 Hz cut-off frequency was appropriate. Although the comparison was favorable, a baseline correction was still applied after filtering to remove any remaining small drift error.

It should be noted that the true permanent displacements in the field computed from velocity or acceleration data are obscured by noise. Using a high-pass filter removes these true permanent displacements. Therefore, the shear strains calculated from the computed displacements only represent the dynamic components.

The cut-off frequencies selected for pore pressure processing depend on the data of interest. When investigating the residual excess pore pressure at the end of shaking, a low-pass filter with a cut-off frequency of 2 Hz is applied. The 2 Hz cut-off frequency is based on the observed variation of pore pressure over the entire record. When studying the hydrodynamic components of pore pressure, a band-pass filter with a lower bound of 15 Hz and an upper bound of 25 Hz is used to highlight the 20 Hz dynamic response. To present the combined residual and hydrodynamic pore pressure, a 28 Hz low-pass filter is applied to eliminate noise from the AC power and the computers used in data collection.

In summary, the selection of an appropriate filter with a specific cut-off frequency helps to investigate the recorded data. The cut-off frequency must be carefully chosen based on the sources of noise, the dominant frequency in the recorded data, the properties that need to be highlighted, and the overall fit to the results.

5.2.2.4 Cross-power spectral analysis

A cross-power spectrum is the representation of the cross-correlation in the frequency domain. Cross-correlations and cross-power spectra are used to identify similarities between two signals. The phase of the cross power spectrum is the phase difference between two signals. The computation of the cross power spectrum is more efficient than the computation of the cross-correlation because fewer multiplications are involved. Only the cross-power spectrum are discussed here.

Consider two time signals, x_j and z_j, recorded at two locations separated by a distance S. These signals are recorded waves traveling from location X to location Z. The cross-power spectrum for the two receiver records, x_j and z_j, is computed by:

$$G_k^{<xz>} = Z_k \cdot \overline{X_k} \quad \text{……..…….. (5-6)}$$

where $G_k^{<xz>}$ = cross-power spectrum coefficient at frequency ω_k,

$\overline{X_k}$ = conjugate Fourier coefficient of the time series x_j at frequency ω_k,

Z_k = Fourier coefficient of the time series z_j at frequency ω_k, and

$\omega_k = \dfrac{2\pi}{N \cdot \Delta t} k$, circular frequency.

The phase spectrum, which defines the phase difference between the two time series, is expressed as:

$$\phi_k = \tan^{-1}\left[\frac{\mathrm{Im}(G_k^{<xz>})}{\mathrm{Re}(G_k^{<xz>})}\right] \quad \text{..... (5-7)}$$

where ϕ_k = phase difference for frequency ω_k,

$\mathrm{Re}(G_k^{<xz>})$ = Real part of the cross-power spectrum coefficient $G_k^{<xz>}$, and

$\mathrm{Im}(G_k^{<xz>})$ = Imaginary part of the cross-power spectrum coefficient $G_k^{<xz>}$.

The travel time of a wave of frequency ω_k traveling from location X to location Z is calculated by:

$$\Delta t_k = \frac{\phi_k}{\omega_k} \quad \text{..... (5-8)}$$

where t_k = the travel time for a wave with a frequency of ω_k

The apparent phase velocity of a wave at a given frequency can be calculated using the travel time and spacing between X and Z:

$$V_{ah,k} = \frac{S}{t_k} \quad \text{..... (5-9)}$$

where $V_{ah,k}$ = apparent phase velocity of a wave with a frequency of ω_k and

S = distance between the two receivers.

In this research, cross-power spectral analysis is used to evaluate apparent wave velocities for the waves traveling through the test area. These apparent wave velocities are used in one of the strain evaluation methods that are discussed in the next section.

5.3 SHEAR STRAIN EVALUATION METHODS

An attractive feature of the in situ dynamic liquefaction test is the evaluation of shear strain-time histories during dynamic loading. Four distinct methods for shear strain computation are considered, and the results from these methods are compared. These methods can be categorized into two groups: (1) displacement-based methods and (2) wave propagation-based methods. The theoretical background of each of these methods, as well as the advantages and disadvantages of each approach, are presented here. A comparison of the shear strains computed by each method using in situ test data is also presented.

5.3.1 Displacement-based method for strain calculation

For the displacement-based strain calculation method, the instrumentation array is designed as a 4-node finite element. Similar to the displacement approach in the finite element method procedure, the displacement-based method utilizes nodal displacements measured in the field to calculate the strain components inside the element. Detailed mathematical derivations for the finite element can be found in general finite element textbooks (e.g., Bathe 1995, Reddy 1984, Zienkiewicz and Taylor 1989). The associated mathematical formulation for the strain calculation is described in this section.

The analytical framework used for the strain calculation is the isoparameteric finite element formulation, which describes the element geometry and the variation of displacements across an element with the same interpolation functions. These interpolation functions, or shape functions, describe the variation

of parameters (i.e., locations, displacements) in terms of a simplified natural coordinate system. Consider a 4-node element in a global coordinate system (Figure 5-4(a)) and its simple, square representation in the natural coordinate system (Figure 5-4(b)). Points within the element in the natural coordinate system (r,s) can be related to points within the element in the global coordinate system (x, y) using:

$$x = \sum_{i=1}^{4} N_i(r,s)x_i \quad \text{..... (5-10a)}$$

$$y = \sum_{i=1}^{4} N_i(r,s)y_i \quad \text{..... (5-10b)}$$

where x, y are the global coordinates for a point inside the element; x_i, y_i are the coordinates of each node in the global coordinate system; $N_i(r,s)$ is the shape function for node i, expressed in the natural coordinate system of the element.

The fundamental property of the shape functions (N_i) is that it is equal to unity at node i and equal to zero at all other nodes in the natural coordinate system. Using the Lagrange polynomials in two dimensions yields the following shape functions for the element shown in Figure 5-4(b):

$$N_1 = \frac{1}{4}(1-r)(1-s) \quad \text{..... (5-11a)}$$

$$N_2 = \frac{1}{4}(1+r)(1-s) \quad \text{..... (5-11b)}$$

$$N_3 = \frac{1}{4}(1+r)(1+s) \quad \text{..... (5-11c)}$$

$$N_4 = \frac{1}{4}(1-r)(1+s) \quad \text{..... (5-11d)}$$

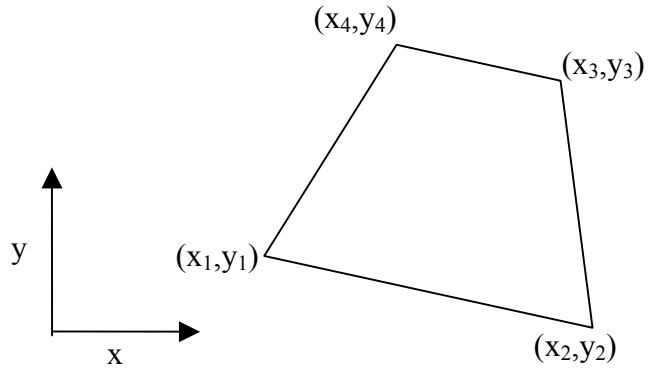

(a) Representation of 4-node element in the global coordinate system

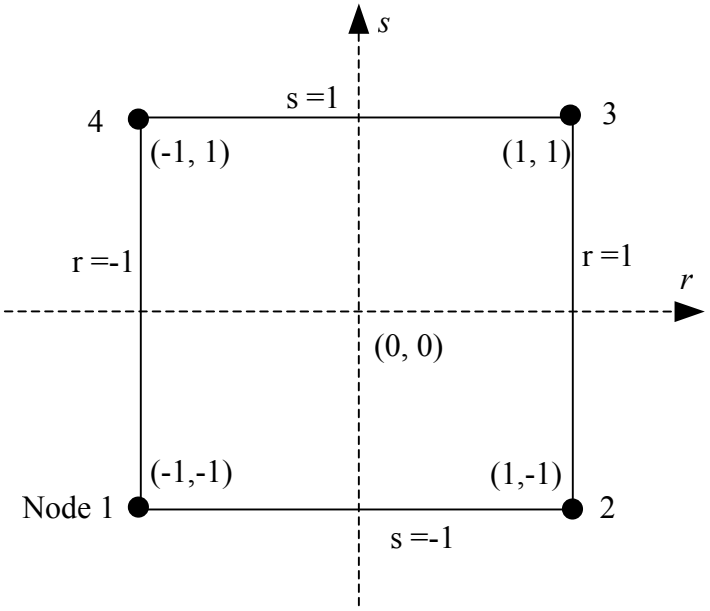

(b) Representation of 4-node element in the natural coordinate system

Figure 5-4 Representation of 4-node element in (a) the global coordinate system and (b) the natural coordinate system

The displacements inside an element are interpolated from the nodal displacements using the same shape functions, which yields:

$$u = \sum_{i=1}^{4} N_i(r,s)u_i \quad \text{(5-12a)}$$

$$v = \sum_{i=1}^{4} N_i(r,s)v_i \quad \text{(5-12b)}$$

where u, v are the displacements in the x and y directions, respectively, at location (r,s) in the natural coordinate system and the corresponding location (x,y) in the global coordinate system; and u_i, v_i are the nodal displacements at node i in the x and y directions, respectively. Using Equation (5-12), the displacement at any point (x,y) within the element can be computed from the nodal displacements and the corresponding natural coordinates of the point of interest.

The element strain vector, $\underline{\varepsilon}^T = [\varepsilon_x \quad \varepsilon_y \quad \gamma_{xy}]$, in the global coordinate system can be obtained from the derivatives of the element displacements with respect to the global coordinates:

$$\varepsilon_x = \frac{\partial u}{\partial x} \quad \text{(5-13a)}$$

$$\varepsilon_y = \frac{\partial v}{\partial y} \quad \text{(5-13b)}$$

$$\gamma_{xy} = \frac{\partial u}{\partial y} + \frac{\partial v}{\partial x} \quad \text{(5-13c)}$$

Using Equations (5-12) and (5-13), the element strain vector can be expressed in matrix form as:

$$\underline{\varepsilon} = \underline{\underline{\boldsymbol{B}}} \cdot \underline{\boldsymbol{u}} \quad \text{(5-14)}$$

where $\underline{\boldsymbol{u}}^T = \begin{bmatrix} u_1 & v_1 & u_2 & v_2 & u_3 & v_3 & u_4 & v_4 \end{bmatrix}$

u_i = horizontal displacement at node i, i=1 to 4,

v_i = vertical displacement at node i, i=1 to 4, and

$\boldsymbol{B}$= strain-displacement transformation matrix.

The explicit form of $\boldsymbol{B}$ is:

$$\boldsymbol{B}=\begin{bmatrix} \frac{\partial N_1}{\partial x} & 0 & \frac{\partial N_2}{\partial x} & 0 & \frac{\partial N_3}{\partial x} & 0 & \frac{\partial N_4}{\partial x} & 0 \\ 0 & \frac{\partial N_1}{\partial y} & 0 & \frac{\partial N_2}{\partial y} & 0 & \frac{\partial N_3}{\partial y} & 0 & \frac{\partial N_4}{\partial y} \\ \frac{\partial N_1}{\partial y} & \frac{\partial N_1}{\partial x} & \frac{\partial N_2}{\partial y} & \frac{\partial N_2}{\partial x} & \frac{\partial N_3}{\partial y} & \frac{\partial N_3}{\partial x} & \frac{\partial N_4}{\partial y} & \frac{\partial N_4}{\partial x} \end{bmatrix} \quad \text{..... (5-15)}$$

Because the shape functions, $N_i(r,s)$, are defined in terms of r and s, a relationship between the natural coordinate derivatives and the global coordinate derivatives is needed. This relationship is the Jacobian operator. In 2-dimensional formulations, the Jacobian operator is a 2-by-2 matrix and is defined as:

$$\begin{Bmatrix} dx \\ dy \end{Bmatrix} = \mathbf{J}^T \begin{Bmatrix} dr \\ ds \end{Bmatrix} \quad \text{..... (5-16)}$$

where $\mathbf{J} = \begin{bmatrix} \partial x/\partial r & \partial y/\partial r \\ \partial x/\partial s & \partial y/\partial s \end{bmatrix}$ (Jacobian matrix)

The derivatives of the shape functions with respect to the global coordinate system (i.e., entries in Equation (5-15)) can be calculated by:

$$\begin{bmatrix} \frac{\partial N_i(r,s)}{\partial x} \\ \frac{\partial N_i(r,s)}{\partial y} \end{bmatrix} = \mathbf{J}^{-1} \begin{bmatrix} \frac{\partial N_i(r,s)}{\partial r} \\ \frac{\partial N_i(r,s)}{\partial s} \end{bmatrix} \quad \text{..... (5-17)}$$

Using Equations (5-14) and (5-15), and the corrected displacement-time histories at the nodal points, the strain-time history at any point inside the field array can be computed. In the developed testing procedure, the shear strain-time histories were calculated in order to take into account equally the recordings from each nodal points.

Several assumptions are incorporated in this strain computation method. A linear variation of displacement between nodes is assumed and the principal of superposition is assumed when combining displacements interpolated from different nodes. All nodes must be aligned in the same vertical plane to satisfy the 2D formulation. The inverse of the Jacobian operator must exist to map the element in the global coordinate system to the natural coordinate system. Finally, the strain levels must be relatively small to satisfy the Lagrangian strain formulation in Equation (5-13).

For these assumptions to be valid, the arrangement of the array in the field must satisfy the following four constraints. First, for a linear variation of displacements between adjacent nodes to be assured, the size of the experimental array in the direction of wave propagation should be less than about one-quarter of the wavelength of the highest significant frequency (i.e., the shortest wavelength). Second, excessively large nodal displacements will violate the principle of superposition and the Lagrangian strain definition; therefore, the method will be most suitable for relatively small strain levels (i.e., less than about 0.1%). Third, all of the arrayed geophones must be aligned in the same plane for the 2D formulation. And, finally a square array is preferred to simplify

calculations and to avoid problems regarding the mapping between the two coordinate systems.

The advantages of the displacement-based method are that it provides a systematic approach to evaluate all strain components in the field, no assumptions regarding wave propagation are required, and no wave velocities are needed. The disadvantages of this method are that more sensors are required, point measurements of strain are not possible, the results are sensitive to any error from a single sensor, and the method is not applicable for relatively large deformations.

Because of the complicated wave field in the current configuration, the displacement-based method is used as the principal method for the strain calculation. The results from the displacement-based method are also used to compare with the wave propagation-based methods. Because the strain is computed using the strain-displacement matrix, this method is called the "Strain-Displacement Matrix" (SDM) method hereafter.

5.3.2 Evaluation of the displacement-based strain calculation method in layered soil

Because the reconstituted test specimen is near the ground surface, the mean effective stress varies significantly from the top of the test pit to the bottom. Hence, the stiffness variation in the reconstituted test specimen is significant. To study the effects of the stiffness variation inside the experimental array, finite element analyses were performed to evaluate whether the 0.6 m by 0.6 m (2 ft by 2 ft) experimental array is small enough to accurately compute shear strains using the SDM method. Essentially, these analyses were aimed at evaluating if the

assumption of a linear variation of displacement over a 0.6 m by 0.6 m element is appropriate in a layered system, where displacements may vary more dramatically.

A layered system model (M3), as shown in Figure 5-5, was generated to analyze the effects of a layered system on the shear strain calculation. Model M3 has 40 element layers in the mesh and elements are 7.5 cm by 7.5 cm in size. Within this finite element mesh, a hypothetical 0.6 m by 0.6 m geophone array is defined. This hypothetical geophone array is used to compute strain and evaluate the accuracy of the SDM method for a 0.6 m by 0.6 m element.

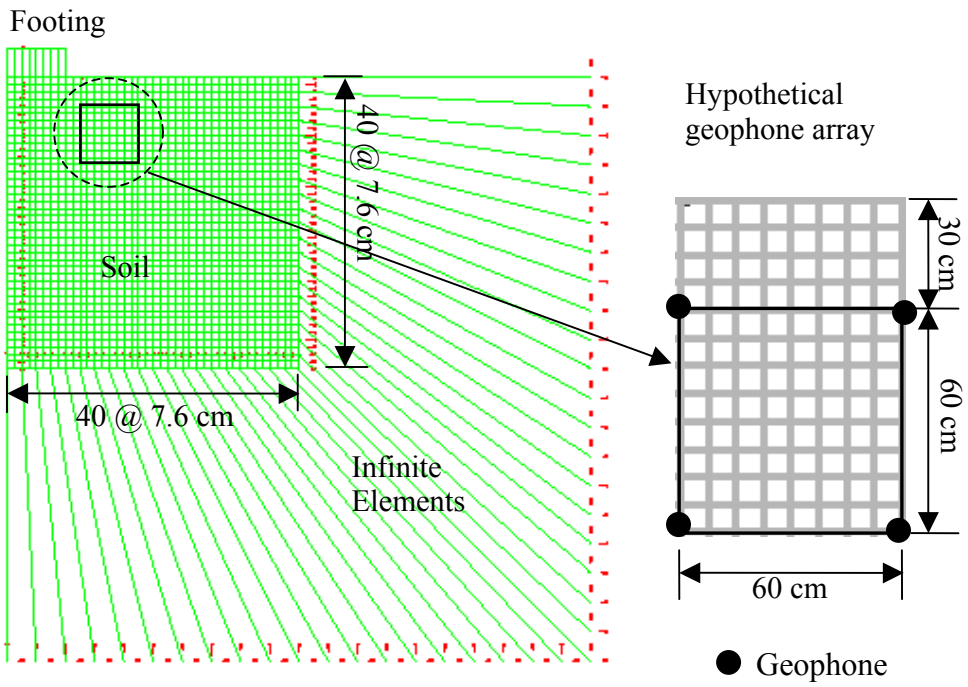

Figure 5-5 FEM model M3 used to study the layered system effects in shear strain calculation

In the model M3, the Poisson's ratio of the soil is υ=0.25 and the mass density ρ= 197 kg/m^3. The elastic shear moduli of the soil layers are inferred from the empirical relationship proposed by Seed and Idriss (1970):

$$G_{\max} = 1000 K_2 (\sigma_m^{'})^{0.5} \quad \text{..... (5-18)}$$

where G_{max}= maximum shear modulus (psf) ; K_2=empirical coefficient determined from relative density, (K_2=43 for D_r=43%); and $\sigma_m^{'}$ = mean effective stress (psf). Equation (5-18) is used to compute the G_{max} of each soil layer. The shear wave velocity of each layer is computed from:

$$G = \rho \cdot V_S^2 \quad \text{.....(5-19)}$$

where V_S= shear wave velocity and ρ= soil mass density. The resulting Vs profile varies from 65.2 m/s (214 ft/s) at a depth on 7.5 cm (0.25 ft) to 163 m/s (534 ft/s) at a depth of 3.0 m (9.75 ft). Within the hypothetical geophone array, the shear wave velocity varies between 91 m/s (300 ft/s) and 122 m/s (400 ft/s). The layered soil is modeled as linear elastic.

Based on the shear strain level contours from model M2 presented in Chapter 4, the largest shear strain gradient occurs near the footing. Also, the variation in the shear modulus is most dramatic near the ground surface. To consider the worst case scenario for shear strain variations, an area located close to the footing and close to the ground surface (Figure 5-5) is selected for the hypothetical geophone array.

To verify the shear strain calculation using the hypothetical 0.6 m by 0.6 m geophone array in the layered system, the nodal displacements computed by ABAQUS at the 4 corners of the hypothetical element were extracted. These

displacements were used to calculate the shear strain at the center of the hypothetical element using the SDM method described in Section 5.3.1. This computation assumes a linear variation of displacement across this hypothetical 0.6 m by 0.6 m element. In model M3, the 0.6 m by 0.6 m array element consists of 64 finite elements in the mesh, allowing a nonlinear variation of displacement to be modeled within the 0.6 m by 0.6 m element, if warranted. The strain computed at the center of the array from the extracted displacements is compared with the shear strain computed at the same location by ABAQUS.

For a 20-Hz loading with a dynamic loading amplitude of 53.4 kN (12 kips), the shear strain-time histories at the center of the 0.6 m by 0.6 m element are shown in Figure 5-6. Although a slight phase shift is observed, there is still favorable agreement in both the amplitude and phase of the results. It should be noted that the field experimental array is located further from the footing, where the shear strain gradient is less dramatic. The comparison is expected to be better than the selected hypothetical geophone array in Figure 5-5. Therefore, using a 0.6 m by 0.6 m element to estimate shear strains from nodal displacements is appropriate, without losing significant accuracy.

5.3.3 Wave propagation-based methods for shear strain calculation

Wave propagation-based methods for calculating dynamic strains have been used in the earthquake engineering and the seismic exploration fields (e.g., White 1965, Robertson et al. 1985). Because of the surface loading and the generated wave field, three different wave propagation-based methods are

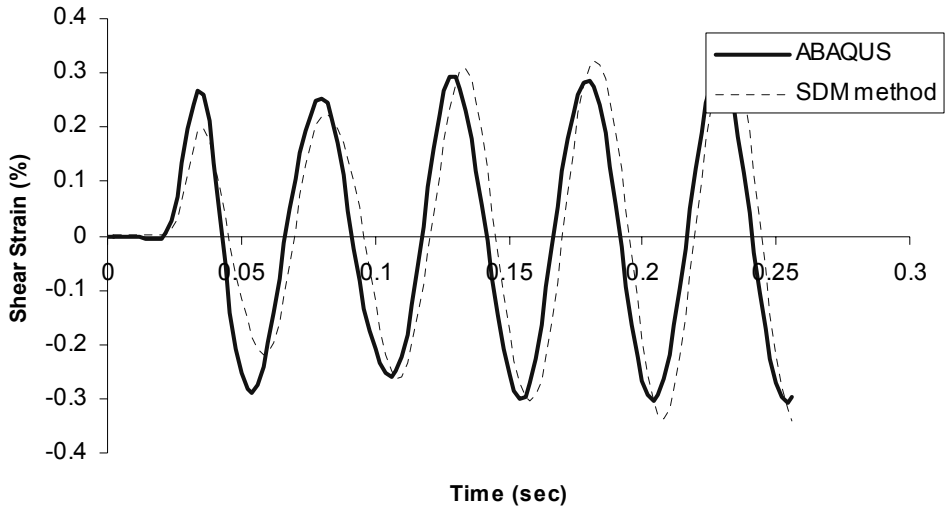

Figure 5-6 Comparison of the shear strain at the center of the 0.6 m by 0.6 m evaluated from SDM method and direct ABAQUS calculation

employed to calculate shear strain: (1) plane shear wave propagation, (2) plane Rayleigh wave propagation, and (3) apparent wave propagation. Details regarding these methods are presented in the following sections.

5.3.3.1 Shear strain induced by a plane shear wave

For a plane shear wave propagating in an elastic half space, the shear strain can be computed as:

$$\gamma_{xz} = -\frac{PV}{V_s} \quad \text{..... (5-20)}$$

where PV= particle velocity measured perpendicular to the direction of wave propagation, and V_S=shear wave velocity. The minus sign in Equation (5-20)

represents a phase shift of 180° between the particle velocity and the shear strain. Assuming the shear wave velocity is constant during dynamic loading and assuming the shear wave propagates horizontally in the test specimen, shear strain can be evaluated by measuring the vertical particle velocity and using the shear wave velocity ($V_{S,hv}$) measured prior to testing. This method is termed the "Plane Shear Wave" (PSW) method, hereafter.

The main advantage of this method is that it is simple and easy to use. However, there are several reasons why the PSW method may be inaccurate for the current testing configuration. First, shear waves propagate in a hemispherical pattern from the center of the footing, rather than just in the horizontal direction (Figure 4-2). Therefore, the shear waves are not plane shear waves propagating in the horizontal direction. Also, different waves interfere with each other close to the footing, as indicated in the theoretical wave field (Figure 4-1). The reflection of waves at the interface between the native soil and the reconstituted test specimen may also affect the measured signals. Additionally, during dynamic testing, the shear wave velocity may vary significantly because of soil nonlinearity and the generation of excess pore pressure. Finally, and perhaps most importantly, shear waves may not be the dominant waves shearing the soil.

5.3.3.2 Shear strain induced by a plane Rayleigh wave

Because of the configuration of the surface loading, Rayleigh waves are the dominant waves propagating through the test area. Therefore, the shear strain relationship given in Equation (5-20) will not be valid. However, the theoretical

solution for Rayleigh wave propagation can be used to develop a relationship for the shear strain induced by Rayleigh waves that has a form similar to Equation (5-20). The newly developed relationship incorporates the measured particle velocity and various wave velocities.

Equations (4-1) and (4-2) in Chapter 4 showed the displacement solution for a plane Rayleigh wave in the far field. Incorporating Equations (4-1) and (4-2) into the definition for the Lagrangian shear strain (Equation 5-13c) yields:

$$\gamma_{xz} = -ik_R(k_R A_1)\left[\eta(\xi_t^2 - 1)e^{sz}\right]e^{i(\omega t - k_R x)} \quad \text{..... (5-21)}$$

where γ_{xz} = shear strain

$$\eta = -\frac{2\xi_l}{(1+\xi_t^2)}$$

$$\xi_t = \sqrt{1-(V_R/V_S)}$$

$$\xi_l = \sqrt{1-(V_R/V_P)}$$

$$k_R = \frac{\omega}{V_R} \text{ (wave number)}$$

$$s = k_R\sqrt{1-(V_R/V_S)^2}$$

A_1 = amplitude constant

V_R, V_S, V_P = wave propagation velocities of Rayleigh, S-,and P-waves, respectively

$$i = \sqrt{-1}$$

The vertical particle velocity normalized by the Rayleigh wave velocity can be determined from Equation (4-2), which describes the vertical displacement induced by a Rayleigh wave. The resulting normalized vertical particle velocity is:

$$\frac{\dot{u}_z}{V_R} = -i\frac{\omega}{V_R}(k_R A_1)\left[\xi_l e^{-qz} + \eta e^{-sz}\right] e^{i(\omega t - k_R x)} \quad \text{..... (5-22)}$$

where $\dot{u}_z = \dfrac{\partial u_z}{\partial t}$ =vertical particle velocity

$$q = k_R\sqrt{1-(V_R/V_P)^2}$$

The ratio between the shear strain and the normalized vertical particle velocity (α_v) can then be calculated as:

$$\alpha_v = \frac{\gamma_{xz}}{(\dfrac{\dot{u}_z}{V_R})} = \frac{\left[\eta\left(\xi_t^2 - 1\right)e^{-sz}\right]}{\left[\xi_l e^{-qz} + \eta e^{-sz}\right]} \quad \text{..... (5-23)}$$

This shear strain ratio (α_v) allows the induced shear strain to be computed from the measured vertical particle velocity and the known Rayleigh wave velocity. To define α_v , estimates of the P-wave and S-wave velocities are needed, and the loading frequency and measurement location (i.e., depth) must be specified. The variation of shear strain ratio with depth for a material with V_s=166 m/s (545 ft/s), V_P=288 m/s (945 ft/s) (i.e., V_R=152 m/s (500 ft/s) and ν=0.25), and a loading frequency of 20 Hz is shown in Figure 5-7.

Figure 5-7 indicates α_v varies from -2.0 at the ground surface to about -0.9 at a depth of 7.6 m (25 ft). The negative values indicate that the shear strain is 180° out of phase with the normalized vertical particle velocity. The most significant observation from Figure 5-7 is that α_v is significantly larger than 1.0 near the ground surface. These large values occur because the displacement profile for surface waves varies significantly with depth near the ground surface

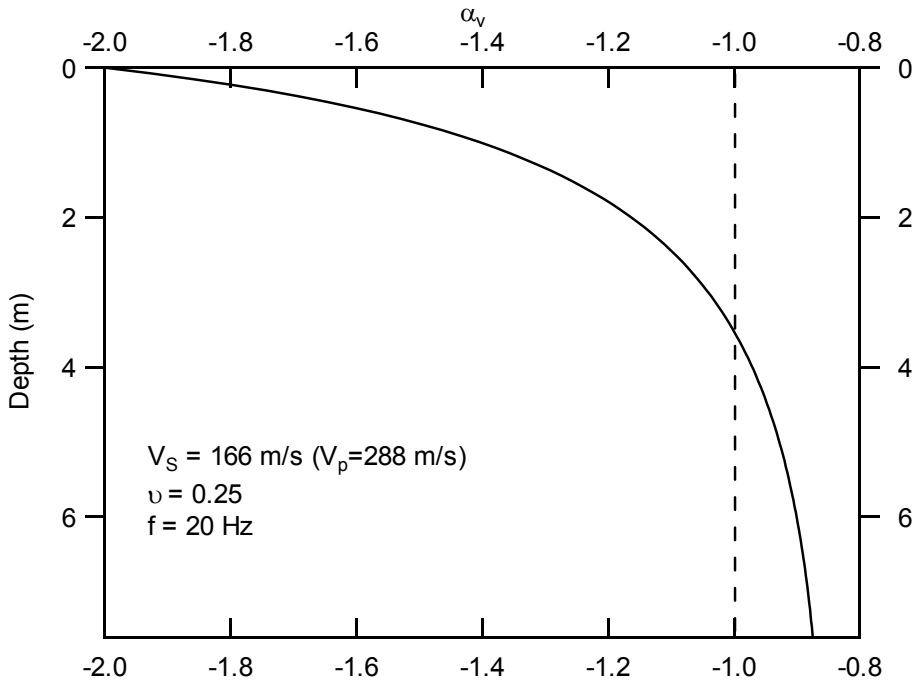

Figure 5-7 Variation of shear strain ratio (α_v) using far field displacement solution for plane Rayleigh waves

(Figure 4-4). Rearranging Equation (5-23), the shear strain can be calculated as:

$$\gamma_{xz} = \frac{\dot{u}_z}{V_R} \cdot \alpha_v \quad \text{..... (5-24)}$$

No minus sign is contained in Equation (5-24) because α_v is always negative.

In Equation (5-23), the ratio between the shear strain and the normalized vertical particle velocity (α_v) is a function of shear wave velocity, Poisson's ratio, frequency, and depth. In the current test configuration, the loading frequency is always 20 Hz. The parameters affecting α_v at a certain depth are shear wave

velocity and Poisson's ratio. Sensitivity analyses were conducted to study the effect of shear wave velocity and Poisson's ratio on computed values of α_v. The results are shown in Figure 5-8. To study the effect of shear wave velocity, the α_v values were computed with shear wave velocities ranging from 90 m/s to 180 m/s (300 ft/s to 600 ft/s) with a constant Poisson's ratio of 0.25 (Figure 5-8(a)). Another analysis was conducted by varying the Poisson's ratio from 0.1 to 0.4 with a constant shear wave velocity of 150 m/s (500 ft/s) (Figure 5-8(b)). The sensitivity analyses revealed that the Poisson's ratio has little effect on α_v. However, shear wave velocity has a more significant effect. Figure 5-8(a) shows that smaller values of shear wave velocity result in smaller absolute values of α_v. The effect is most significant between depths of 0.5 m to 3 m. In this zone, α_v may vary by as much as 20%.

In the current test setup, vertical particle velocities are measured in the field during dynamic testing. It is difficult to choose a value of V_R for Equation (5-24) for the liquefaction test because the Rayleigh waves are propagating in the reconstituted test specimen and the native soil beneath the test pit. The Rayleigh wave velocity of the native soil was estimated from the field vibration test (Section 4.3) as V_R=152 m/s (500 ft/s) at 20 Hz. The corresponding wavelength is 7.6 m (25 ft), indicating that Rayleigh waves travel mainly through the native soils, even with the reconstituted test specimen in place. Therefore, an initial estimate of the V_R used to calculate shear strain for the liquefaction test is 152 m/s (500 ft/s). After choosing a V_R, the shear strain ratio (α_v) at a specific depth is determined using Equation (5-23), and the shear strain-time histories are

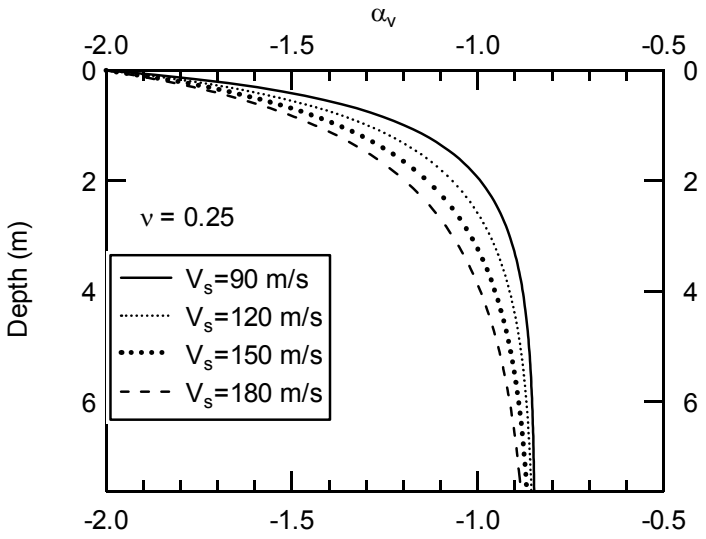

(a) Variation of computed α_v for varied shear wave velocities

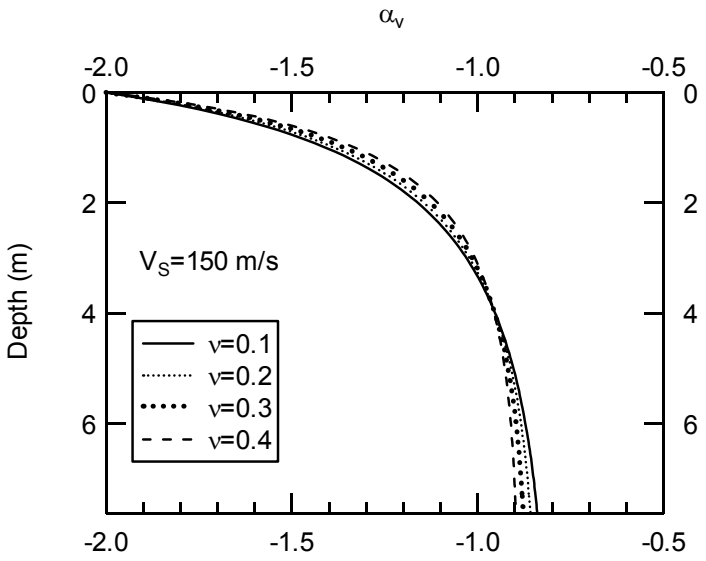

(b) Variation of computed α_v for varied Poisson's ratios

Figure 5-8 Effect of Poisson's ratio and shear wave velocity on computed α_v

computed from the measured vertical particle velocity, the Rayleigh wave velocity, and Equation (5-24). Because this method is based on plane Rayleigh wave propagation, it is called the "Plane Rayleigh Wave" (PRW) method, hereafter.

Similar to the other wave propagation-based methods, this method is simple and easy to use. Theoretically, only one vertically oriented geophone is required to evaluate the shear strain. However, prior Rayleigh wave velocity measurements of the native soil are needed.

Possible errors in the PRW method come from several sources. In the near field, the vertical ground displacements can not be accurately described by Equation (4-2) because of the close arrivals of body waves and surface waves. Also, reflected waves from the interface between the native soil and the reconstituted test specimen are inevitable. Due to the existence of the reconstituted test pit, the plane wave assumption may not be valid. Data collected in the liquefaction test show a phase difference between geophones at the same radial distance but different depths, indicating a curved wavefront. Finally, in liquefiable soil, the soil stiffness will decrease due to excess pore pressure generation and soil nonlinearity, resulting in a change in the Rayleigh wave velocity. This makes it difficult to choose a Rayleigh wave velocity for Equation (5-24).

5.3.3.3 Shear strain induced by an apparent wave

As previously discussed, the wave propagation behavior in the test pit is complicated and it is difficult to be described by a single wave type or analyzed by a single analytical technique. Another approach is proposed using the vertical particle motion and an apparent wave propagation velocity. The apparent wave propagation velocity is measured from the phase difference measured between two embedded geophones at the same elevation during dynamic testing. Similar to Equation (5-20), the shear strain can be evaluated by:

$$\gamma_{xz} = -\frac{PV_v}{V_{ah}} \quad \text{..... (5-25)}$$

where PV_v= vertical particle velocity and V_{ah}= apparent wave velocity propagating in the horizontal direction, as measured by the embedded geophones. Again, the minus sign is for the phase shift.

The apparent wave velocity propagating in the horizontal direction (V_{ah}) is obtained from the phase difference between two adjacent sensors separated by a distance, *S*. The cross-spectral analysis described in Section 5.2.2.4 is used for this measurement. The apparent wave velocity is computed by:

$$V_{ah} = \frac{2\pi f \cdot S}{\phi_f} \quad \text{..... (5-26)}$$

where *f*= loading frequency in Hz, *S*=distance between the two sensors, and ϕ_f=phase difference at the loading frequency, in radians.

In the near field, particle motion is induced by body waves, head waves, and Rayleigh waves, rather than just one wave type. Because the wave velocity used in the shear strain computation cannot be attributed to a single wave type, it

is called the apparent wave velocity, and this shear strain calculation method is called the "Apparent Wave" (AW) method.

There are several benefits to use the AW method. No prior shear wave velocity measurements are required because the wave velocity is measured using the vertical particle motion recorded during dynamic loading. The complexity of the near field effects and nonhomogeneity are rationally taken into account and only two sensors, rather than the four needed for the SDM method, are required in this method. Additionally, the variation of wave velocity during dynamic testing can be measured through a phase difference calculation for each load cycle. Finally, the pore pressures and shear strains are evaluated from sensors located at the same point.

In the AW method, horizontal wave propagation is assumed and the validity of this assumption for the proposed test setup must be assessed. The vertical particle motion in the test area is mainly from Rayleigh waves and shear waves; therefore, only these two wave types will be discussed. Rayleigh waves always propagate horizontally in level ground. Therefore horizontal propagation of Rayleigh waves is a valid assumption. For shear waves, the geometry of the test setup, with the geophones located close to the ground surface, will minimize the effect of the hemispherical wave front (Figure 4-2). Therefore, horizontal wave propagation for shear waves is also a reasonable assumption.

Because of the advantages described, the AW method is preferred over the other two wave propagation-based methods.

5.4 IN SITU COMPARISON OF SHEAR STRAIN EVALUATION METHODS

In this research, four shear strain evaluation methods were proposed and used in the data analysis. Data from test series T2 (Chapter 9) is used to compare these shear strain evaluation methods for the current test configuration. Because the wave propagation-based methods evaluate the shear strain at the location where the sensor was installed and the SDM method is best at the center of the array, the induced shear strain at the center of the array is used to compare these methods. Details of the methodology used in the comparison are discussed below.

5.4.1 Comparison methods

In order to equally weight the measured data from the four sensors of the field array, the SDM method calculates the shear strains at the center of the array. However, all of the wave propagation-based methods (i.e., PSW, PRW, and AW methods) calculate shear strains at the sensor points, which are the locations of the geophones. Therefore, the induced shear strains at the center of the array are used for comparison of these four methods. Additionally, because of the aforementioned advantages and the minimum assumptions employed, the SDM method is used as the reference method for comparison with the three wave propagation-based methods.

To estimate the shear strain at the center of array by wave propagation–based methods, an averaging technique is used. The proposed averaging technique is based loosely on the SDM strain calculation method. Because the SDM method

implicitly takes an arithmetic average of the displacement values at the four nodal points, an analogous averaging method is proposed. The averaging technique takes the arithmetic average in the time domain of the shear strain-time histories computed by the wave propagation-based methods at the sensor points to represent the induced shear strain at the center of the array. The averaging is performed in the time domain to take into account the phase difference between the geophones at the four sensor points. For an additional comparison, the vertical velocity recorded by the vertical geophone installed at the center of the array is used to directly compute the shear strain at the center of the array using the wave-propagation-based methods.

For the PSW method, the shear wave velocities used in the shear strain calculation were obtained from crosshole S-wave velocity measurements conducted before dynamic loading (see Table 9-3 in Chapter 9). The shear wave velocity at the center of the array is interpolated from the measured shear wave velocities at the other sensor depths and the variation of effective stress within the test specimen. Generally, the shear wave velocity at the center of the array is about 105% of the measured shear wave velocity at 0.3 m.

For the PRW method, the Rayleigh wave velocity was taken as 152 m/s (500 ft/s) for 20 Hz loading, based on the field vibration tests. The α_v values were calculated based on the depth of the geophones, a V_R of 152 m/s and ν=0.25. At the center of the array, α_v equals -1.62 for test series T2.

For the AW method, the apparent phase velocities at the geophone depths were computed from the phase difference between the two vertical geophones

spaced 0.6 m apart (see Table 9-3 in Chapter 9). For the center geophone, the apparent wave velocity was interpolated from those measured at 0.3 m and 0.9 m.

5.4.2 Comparison of mean shear strain from different shear strain evaluation methods

The data collected in test series T2 are used to compare the shear strains computed by the different shear strain evaluation methods. This test series is used because it has the required parameters to compute shear strains using all of the shear strain evaluation methods. A detailed description of test series T2 is presented in Chapter 9.

Figure 5-9 compares the mean shear strain amplitudes (over the entire shear strain-time histories) at the center of the array computed by the wave propagation-based methods and the SDM method. For the wave propagation-based methods, this figure shows the shear strains averaged from the 4 sensor points. A comparison of the mean shear strains at the center of the array computed from the wave propagation-based methods using the measured vertical particle velocity at the center of the array is shown in Figure 5-10. Both figures indicate that the AW method matches very well with the SDM method, especially for shear strain levels less than 0.01%. In general, the error for the AW method with respect to the SDM method is less than 10%. The shear strain amplitudes calculated by the PSW and PRW methods have similar values and are 40% to 80% larger than the shear strain amplitudes computed by the SDM method. Based on these comparisons, the AW and SDM methods are chosen as the two principal methods for shear strain evaluation.

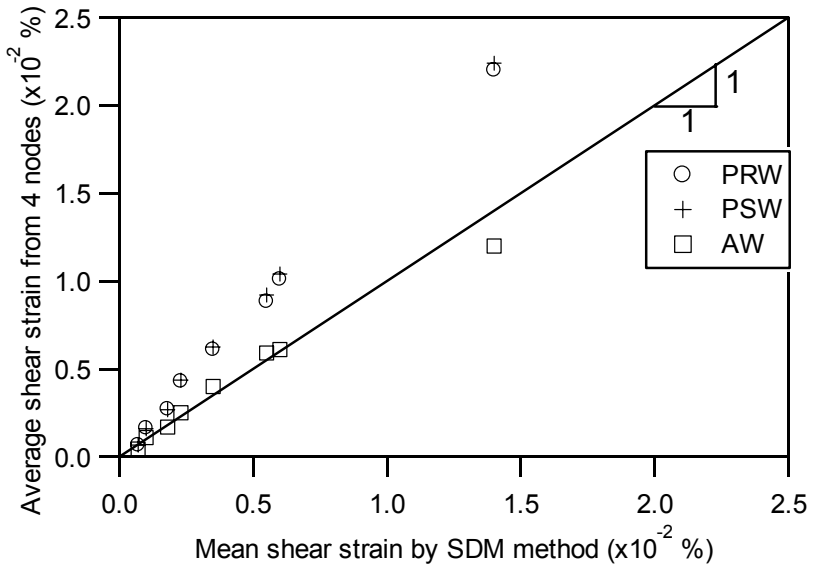

Figure 5-9 Comparison of the shear strain at the center of the array using average of 4 nodes computed by wave propagation-based methods (T2)

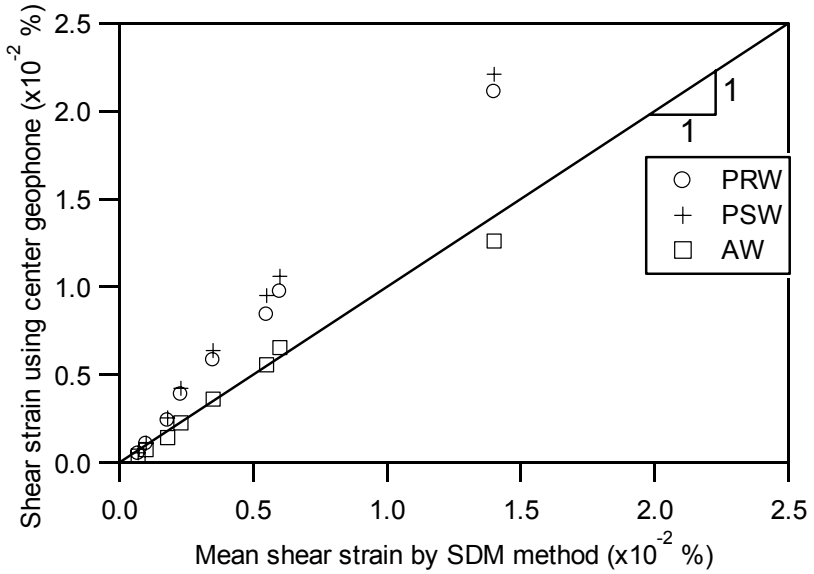

Figure 5-10 Comparison of the shear strain at the center of the array using center geophone data in wave propagation-based methods (T2)

5.5 SUMMARY

The analytical techniques involved in this research were presented in this chapter, including signal processing techniques, numerical algorithms, and computational methods for shear strain evaluation. The contents are summarized here.

To correctly interpret the collected data, signal processing techniques are used to either enhance dynamic signals with respect to noise or to highlight a specific signal. The signal processing procedures for collected particle velocity and pore water pressure data are presented in Section 5.2. Three types of analysis are performed in the time domain: numerical integration, baseline correction, and signal stacking. The major computations performed in the frequency domain are digital filtering using linear filters and cross-spectral analysis for calculation of phase velocity between two receivers.

Different cut-off frequencies are chosen for frequency filters. A cut-off frequency of 4 Hz was selected for the high-pass filter applied to the velocity data to avoid drifts in displacement. When investigating the residual excess pore pressure, a low-pass filter with a cut-off frequency of 2 Hz was applied. When studying the hydrodynamic components of pore pressure, a band-pass filter with a lower bound of 15 Hz and an upper bound of 25 Hz was used to highlight the 20 Hz dynamic response.

The shear strain evaluation methods were introduced in Section 5.3. These methods are classified into two categories: displacement-based methods and wave propagation-based methods. The four shear strain evaluation methods are

summarized and tabulated in Table 5-1. This table compares the fundamental relationships used in each method, the number of required geophone sensors, the underlying assumptions, the necessary prior information, and the location of the calculated strain for each method.

The displacement-based method uses the strain-displacement matrix to calculate strain components at the center of the experimental array and is called the SDM method. Three wave propagation-based methods are presented: the plane shear wave (PSW) method, the plane Rayleigh wave (PRW) method, and the apparent wave (AW) method. These wave propagation-based methods calculate the shear strain at the sensor location using particle velocity and wave velocity data.

A comparison of the shear strain evaluation methods using in situ test data collected in this research was also presented. The comparisons of the mean shear strain at the center of the array indicate that the AW method matches very well with the SDM method, especially for shear strain levels less than 0.01%. The PSW and PRW methods compute shear strain 40% to 80% larger than the SDM and AW methods. Based on these comparisons, the AW and SDM methods are chosen as the two principal methods for shear strain evaluation.

Table 5-1 Summary of shear strain evaluation methods

	SDM method	**PSW method**	**PRW method**	**AW method**
Fundamental relationship	$\underline{\varepsilon} = \underline{\underline{B}} \cdot \underline{u}$	$\gamma_{xz} = -\frac{PV}{V_S}$	$\gamma_{xz} = \frac{\dot{u}_z}{V_R} \cdot \alpha_v$	$\gamma_{xz} = -\frac{PV_v}{V_{ah}}$
Number of sensors needed	8	1	1	2
Underlying assumption	Axisymmetric	Plane wave	Plane wave	Plane wave
Prior information needed	None	Shear wave velocity	Rayleigh wave velocity	None
Calculation location	Center of square array	Sensor location	Sensor location	Sensor location

Chapter 6. Instrumentation System

6.1 INTRODUCTION

This chapter presents a detailed description of the instrumentation system for the developed in situ dynamic liquefaction test. The instrumentation system includes sensors, such as geophones, accelerometers, and pore pressure transducers, and two automatic data acquisition systems. Other instrumentation tools used to characterize the reconstituted specimen and to measure settlements are also introduced here.

6.2 FRAMEWORK FOR INSTRUMENTATION SYSTEM

For the proposed in situ dynamic liquefaction test, the instrumentation system is one of the essential elements of the research. The instrumentation system consists of hardware components and software programs. The hardware components include sensors, an analog-to-digital (A/D) converter board, computers, a dynamic signal analyzer, DC power supplies, and signal conditioners. The software components are programs for controlling and communicating with the equipment.

Dunnicliff (1988) provides a systematic approach for the planning of in situ geotechnical measurements. The guideline consists of eight issues that should be considered when designing an instrumentation system. The eight

considerations are listed in Table 6-1 and the appropriate expectations for the proposed in situ testing technique are also listed. The instrumentation system used in this study has been developed to meet the requirements listed in Table 6-1.

Table 6-1 Considerations for planning of field instrumentation system

Consideration	**Project expectations**
Site conditions	Loose, saturated, reconstituted granular soils near the ground surface
Mechanism that controls behavior	Interaction between pore water pressure buildup and induced shear strains
Questions that need to be answered	Site liquefaction characteristics
Purpose of the instrumentation	1. Monitor induced shear strains 2. Monitor generation of excess pore water pressure
Parameters to be monitored	1. Particle velocity 2. Transient pore water pressure 3. Wave velocity 4. Settlement
Predicted magnitudes	1. Particle velocity <3.0 cm/s (0.1 ft/s) 2. u< 70 kPa (10 psi), Δu< 27 kPa (4 psi) 3. Wave velocities ≅ 200 m/s (600 ft/s) 4. Settlement < 10 cm (0.3 ft)
Devise remedial action	Not applicable to this research
Tasks for design, construction, and operation	1. Fast response 2. High speed automatic data acquisition 3. Long duration recording 4. Waterproof, noise reduction 5. Accurate installation

The framework for the instrumentation system is illustrated schematically in Figure 6-1. A new sensor called the liquefaction sensor was designed to measure particle velocities and pore pressure at the same location. It consists of 2 perpendicularly oriented (horizontally and vertically) geophones and a miniature pore pressure transducer (PPT) integrated in an acrylic case. A signal distributing connector was built to distribute signals from different liquefaction sensors to different paths for signal conditioning, digitizing, and storing. Two data acquisition systems are employed in the test because each is capable of different recording lengths. The function generator used to drive the vibroseis is recorded by each system and used to synchronize the systems after the test. Other equipment, such as DC power supplies and signal conditioners, are connected to the associated sensors. The following sections provide details and design considerations for the sensors, sensor calibration and implementation, and data acquisition. Also, the devices for seismic testing and settlement measurements are described.

6.3 PARTICLE VELOCITY SENSOR- GEOPHONES

There are several types of motion transducers available. The selection of motion transducers depends on the following factors: (1) the frequency content of the motion to be recorded, (2) the magnitude of the motion, (3) the measured motion types, (i.e., acceleration, velocity, displacement), (4) the interface with the signal conditioning and data acquisition, (5) the cost of the transducers, and (6) the size of the transducers.

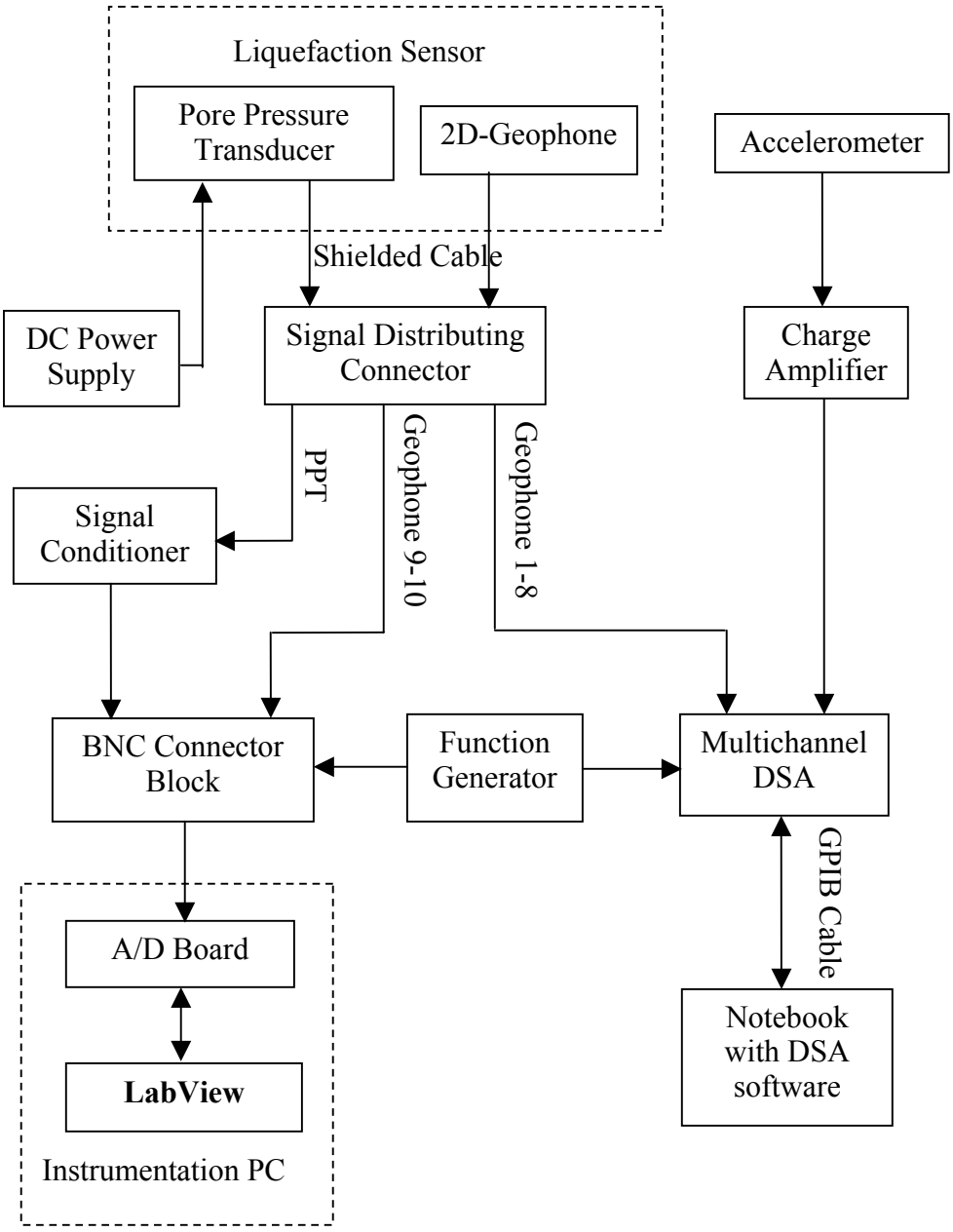

Figure 6-1 Framework for instrumentation system

Geophones, rather than accelerometers, are used in this research as motion transducers based on the following criteria:

1. Geophones are velocity transducers and velocity will be used directly in wave propagation-based method for shear strain calculation.
2. Computation of displacement from velocity requires only a single numerical integration, which is simpler and will introduce fewer errors than double integration from acceleration.
3. No signal conditioner or power supply is needed for geophones.
4. The frequency of interest in the developed test technique is less than 100 Hz. Therefore, no high frequencies need to be measured and geophones typically work well at frequencies above a few Hertz.
5. The cost of geophones is only a fraction of accelerometers.

6.3.1 Geophone features

A geophone consists of a permanent magnet fixed to a geophone case, and a coil suspended by a spring, as shown in Figure 6-2. The magnet generates a magnetic field and a voltage is generated by the relative movement between the magnet and the coil. This voltage is proportional to the relative velocity between the magnet and the coil (Pieuchot 1984).

Because of the dynamic response of the mass-spring system in the geophone, geophone output is frequency dependent. The output calibration

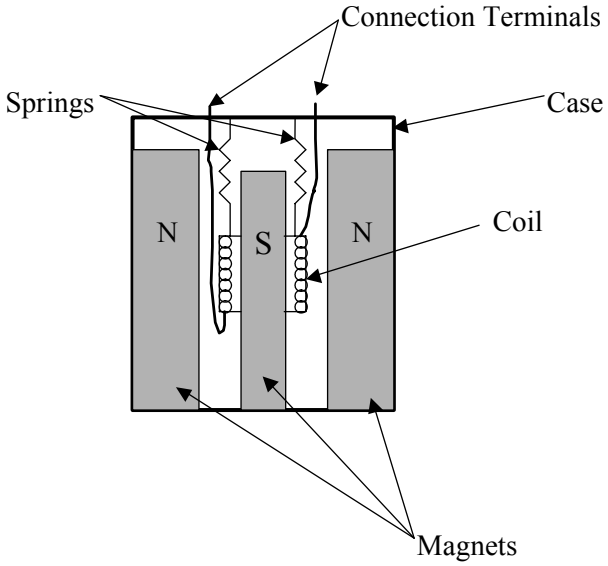

Figure 6-2 Schematic cross section of vertical geophone (Pieuchot 1984)

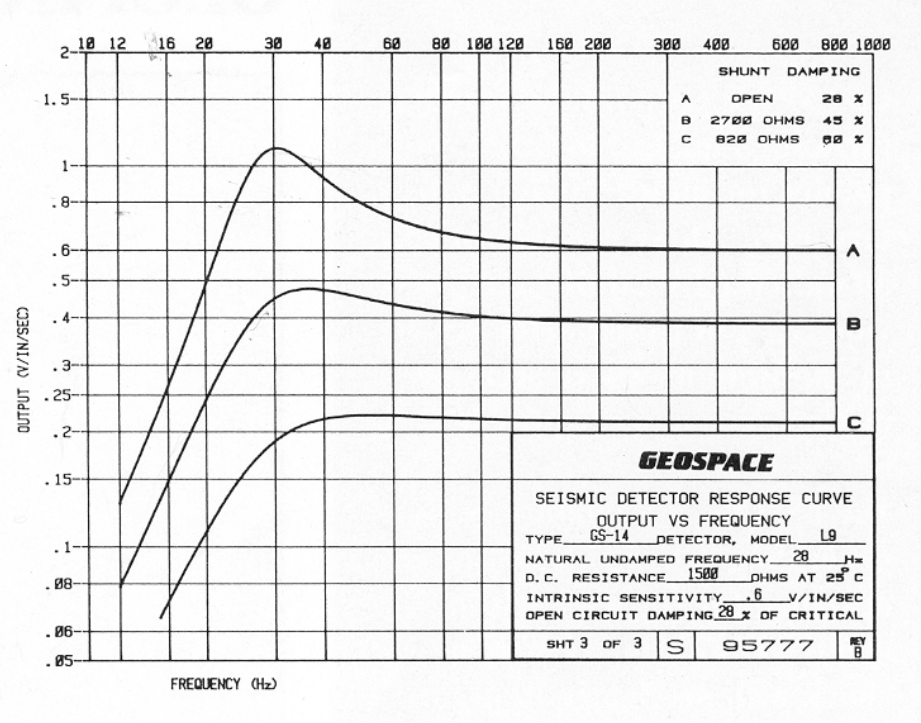

Figure 6-3 Calibration spectrum for 28-Hz geophone (Geo Space 2000)

spectrum for a 28-Hz geophone is shown in Figure 6-3. Figure 6-3 indicates that if a geophone is used above its natural frequency, a single calibration factor can be used.

There are three calibration curves shown in Figure 6-3 for the 28-Hz geophone. Curve A is the calibration curve for a 28-Hz geophone without any additional damping resistance, which has 28% damping ratio and a large peak near the natural frequency (28 Hz). Curves B and C are the calibration curves for the same geophone, but with damping ratios of 45% and 50%, respectively, due to the addition of a 2700 and 820 ohms electrical resistor, respectively. Curve B and C show a larger frequency range with a constant calibration factor, but a smaller output voltage over all frequencies. Electrically damped geophones (Curve B and C) are beneficial when monitoring motions near the natural frequency. Additionally, the shape of Curve B and C is simples and easier to fit by a higher-order polynomial. This simplicity aids in using the geophone at frequencies below its natural frequency.

A geophone with a lower natural frequency has a more flexible mass-spring system, resulting in a different output calibration curve, or even malfunctions, when vertical geophones are tilted from vertical. Additionally, low natural frequency geophones need a larger mass, which results in a larger size and higher cost. These factors need to be taken into account when selecting an appropriate geophone.

Initial testing in this research used 4.5-Hz geophones. Although the 4.5-Hz geophones have higher output voltages and a lower natural frequency, they were

not ideal in this research because of orientation constraints, their size, and their cost. Instead, 28-Hz geophones (Geo Space GS-14-L9) with a 2700 ohms electrical resistor are used in the liquefaction test sensors (Curve B). These geophones are much smaller than the 4.5-Hz geophones and the same geophone can be used in both the horizontal and vertical directions due to the higher stiffness spring. Additionally, 28-Hz geophones are less expensive than 4.5-Hz geophones. To accurately measure the particle velocity below the natural frequency of the 28-Hz geophone, the full calibration spectrum for the geophone is used instead of a constant calibration factor. Hereafter, the discussion will focus on 28-Hz geophones.

6.3.2 Geophone calibration

All transducers used in this research need to be carefully calibrated prior to installation, as well as after testing for post-testing assurance. Although the manufacturer often provides a reference calibration curve, careful calibration in the laboratory is still required because the operational environment is different and the instrumentation system connected to the sensor varies. Because the geophones used in the liquefaction sensor are epoxied in an acrylic case with a pore pressure transducer, the calibration might change due to the assembly details and the existence of the case. Therefore, a dedicated procedure is employed to calibrate the geophones in the acrylic case. The laboratory calibration is performed using an electromagnetic shaker and a proximeter. A proximeter is a displacement transducer and the response of a proximeter is frequency

independent. The calibration procedure is briefly reviewed, followed by the calibration results.

The basic principle of the calibration is to use the amplitude and phase relation between displacement amplitude and velocity amplitude for sinusodial motion. This relationship can be expressed as:

$$\dot{u}_{peak} = u_{peak} \cdot \omega \quad \text{.....} \quad (6\text{-}1)$$

where $\dot{u}_{peak}$ = velocity amplitude, u_{peak} = displacement amplitude, $\omega = 2\pi f$ (circular frequency, rad/s), and f= frequency (Hz). The phase difference between velocity and displacement is $\pi / 2$. The displacement amplitude of the plate mounted on electromagnetic shaker is monitored by a proximeter and converted to velocity amplitude using Equation (6-1). This velocity is compared with the output voltage of the geophone that is being calibrated. The velocity amplitude measured by the proximeter is calculated as:

$$\dot{u}_{prox} = v_{prox} \cdot CF_{prox} \cdot \omega \quad \text{.....} \quad (6\text{-}2)$$

where $\dot{u}_{prox}$ = velocity amplitude measured by proximeter, v_{prox} = output voltage of proximeter, and CF_{prox} = calibration factor of proximeter (= 0.007018 in./volt). The output calibration factor for the calibrated geophone at the circular frequency, ω, is:

$$Output_{geo}(\omega) = \frac{v_{geo}}{\dot{u}_{prox}} \quad \text{.....} \quad (6\text{-}3)$$

where $Output_{geo(\omega)}$= output calibration factor for geophone (volt/(in/s)) at frequency ω and v_{geo} = output voltage from geophone. The complete output calibration spectrum, which represents the output calibration factor at different

frequencies, can be generated by varying the shaking frequency of the electromagnetic shaker.

The electromagnetic shaker was driven by a Dynamic Signal Analyzer, which generates a constant amplitude swept sine signal. The frequency was varied between 200 to 4 Hz. The cross-power spectrum of the peak signals between the geophone and the calibrated proximeter is computed. Using Equation (6-3) and the cross-power spectrum of the peak signals, the output calibration spectrum of the geophone is established. The calibration data for the horizontal geophone in case 1 is shown in Figure 6-4. The output calibration curve in Figure 6-4 is similar to the manufacturer curves shown in Figure 6-3 (Curve B). The resonant frequency of the geophone is the frequency of zero phase in the cross-power spectrum. Based on the calibration data, the natural frequency of the geophone is 25.6 Hz, rather than the specified 28 Hz.

It should be noted that the geophones are calibrated with the cables, connectors, and the signal distribution block all assembled, because these components are used in the field. Therefore, the output calibration spectrum should represent the response of the entire system, rather than just the geophone itself.

6.3.3 Implementation of full calibration spectrum in velocity measurement

The loading frequency of the proposed dynamic liquefaction test is 20 Hz, which is below the natural frequency of the 28-Hz geophones. Therefore, the nonlinear portion of the output calibration spectrum needs to be taken into

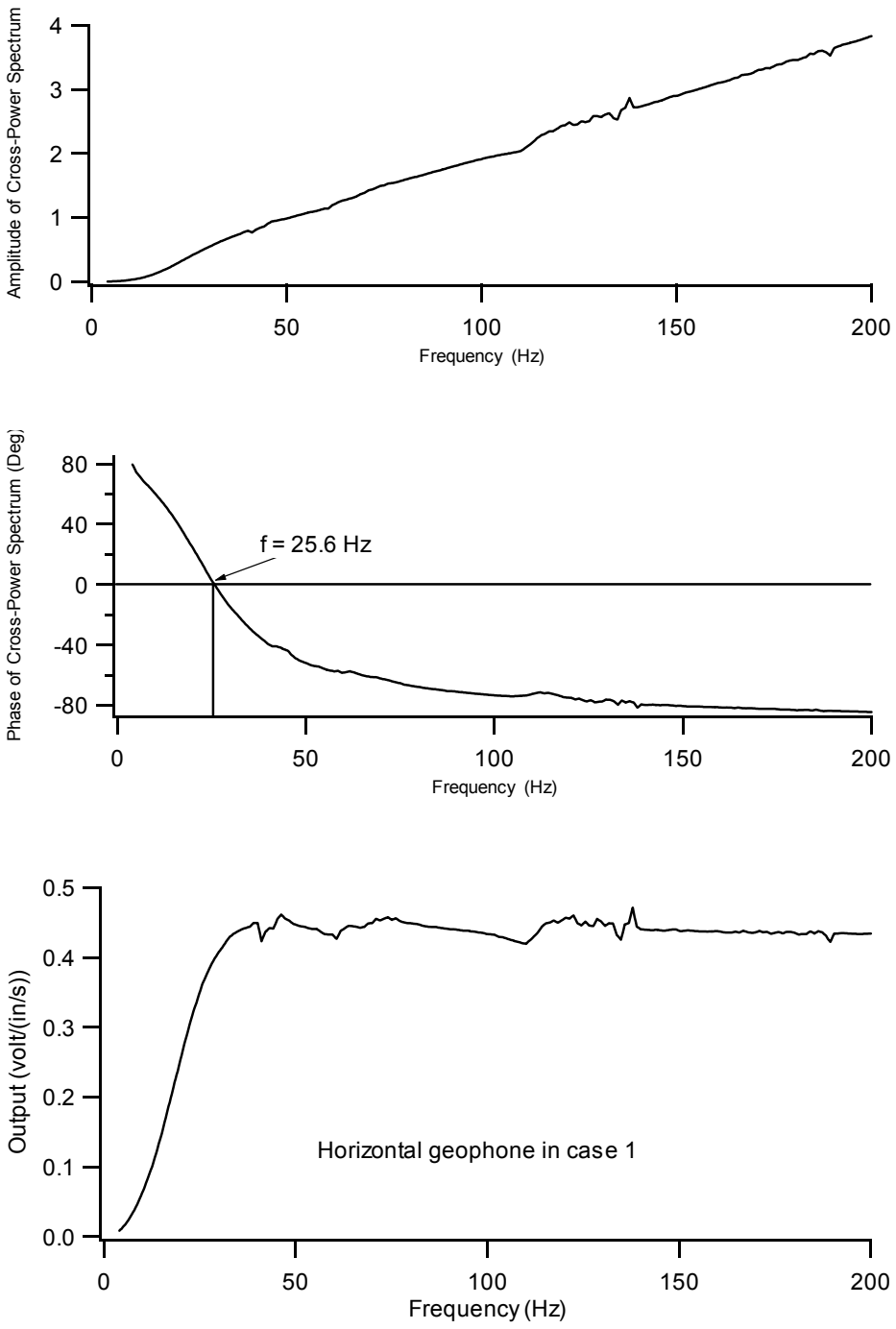

Figure 6-4 Calibration result for horizontal geophone in case 1

account to accurately represent the measured particle velocity. This process can be conducted easily in the frequency domain because it is a frequency-dependent property.

As mentioned in Chapter 5, the calibration spectrum is similar to a filter window. The recorded signal is transferred to the frequency domain using the FFT and each component is multiplied by the corresponding calibration factor, which is the reciprocal of the calibration factor from the output calibration spectrum, using Equation (5-5). The resulting spectrum is transferred back to the time domain using the inverse FFT. However, two problems need be addressed in order to use this processing technique. First, the frequency points in the calibration spectrum are different from the frequency points in the field data; therefore, they cannot be multiplied directly. A simple procedure was developed which uses high-order polynomials to fit the output spectrum. As a result, the calibration factor can be computed for each frequency point in the field data. A 5th-order polynomial was employed to fit each curve over the frequency range of 4 to 38 Hz. The coefficients of the polynomials were determined using the least squares method.

The second issue is related to the smaller output calibration factors for frequencies below the natural frequency. Because the recorded signal is divided by the output calibration factors, these smaller values result in larger values of the signal amplitude. From the filter viewpoint, these small values amplify low frequency signals, which mostly represent noise. In addition, calibration factors at low frequencies are less reliable because of the limitations of the electromagnetic

shaker and the proximeter. The proposed solution is to set a minimum value in the output calibration spectrum. The output calibration factor at the dominant frequency, 20 Hz, is selected as the minimum value. The output calibration factors above 38 Hz are constant and set to the same value as at 38 Hz. The output calibration spectrum used for data processing for the horizontal geophone in case 1 is shown in Figure 6-5, along with the laboratory output calibration spectrum.

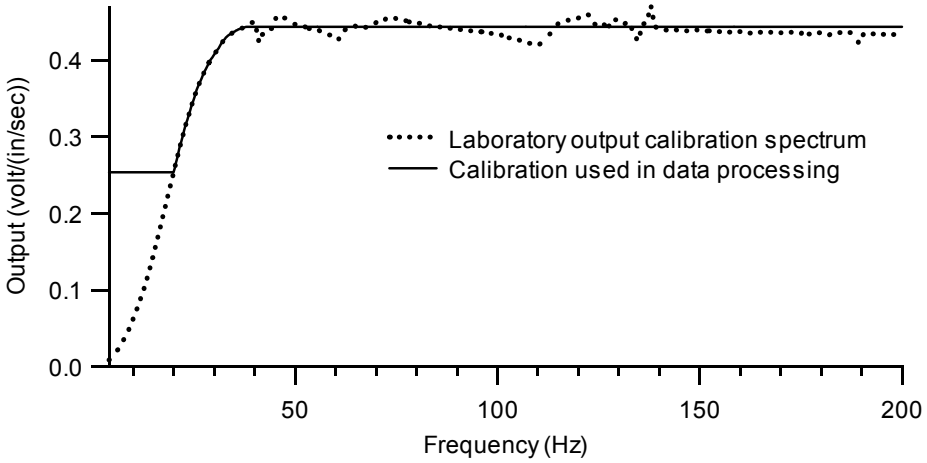

Figure 6-5 Calibration spectrum used in data processing and the laboratory calibration spectrum

6.4 PORE PRESSURE TRANSDUCERS AND PIEZOMETER

A pore pressure transducer (PPT) is used to measure the static and dynamic response of the excess pore water pressure in the developed testing technique. In geotechnical engineering practice, a pore pressure transducer is

often called a piezometer. These transducers are sealed within the ground so they respond only to the surrounding water pressure (Dunnicliff 1988).

Several types of piezometers have been used in engineering practice. These piezometers include open standpipes, pneumatic piezometers, vibrating wire piezometers, and electrical resistance strain gage piezometers. To measure the dynamic response of excess pore pressure at a specific location, the electrical resistance strain gage piezometer is the only option because it is the only piezometer that has a fast response and can be integrated with the automatic data acquisition system. Hereafter, the discussions focus on the electrical resistance strain gage piezometers.

6.4.1 Issues for pore pressure measurement

A pore pressure transducer consists of a pressure-sensing diaphragm that converts pressure to an electric signal, a porous filter that separates the pressure-sensing diaphragm from the surrounding soil, and a metal case. The pressure-sensing diaphragm is a precisely machined metal membrane with bonded strain gages attached to the metal membrane. Fluid pressure causes deformation of the metal membrane and the deformation is measured by the bonded strain gages. The major distinction between a PPT and a general purpose pressure transducer is the existence of the filter that separates the pressure-sensing diaphragm from the surrounding soils and allows water to flow through. A cavity between the diaphragm and the porous filter(s) is necessary to avoid direct contact between the

pressure-sensing diaphragm and the filter(s). Also, a metal case is required to protect the sensing element and to fix the porous filter in place.

Sources of error for general purpose PPT include hydrodynamic time lag, air bubbles in the system or in the vicinity of the filter, clogging of the filter, temperature variation, and change in calibration characteristics (Dunnicliff 1988). The hydrodynamic time lag is the time required for water to flow into or out of a piezometer to equalize pressure (Hvorslev 1951). For electrical resistance piezometers, the hydrodynamic time lag depends primarily on the response of the filter, the volume of the cavity between the filter and the pressure-sensing diaphragm, and the volume change due to deflection of the diaphragm. Also, the existence of air inside the piezometer can cause a time lag and reduced the magnitude of the pore pressure measurement (Hvorslev 1951, Terzaghi and Peck 1967). The main concern for the measurement of dynamic pore pressures is the time lag caused by a relatively low permeability porous filter, a partially saturated porous filter, or air trapped in the space between the metal membrane and the filter.

The improper design of the piezometer, the saturation procedure, or the installation procedure can cause the piezometer to become partially saturated, which results in a time lag and a small pore pressure response when making dynamic pore pressure measurements. In this research, these issues are seriously considered and special procedures are developed to ensure the PPT can accurately measure the hydrodynamic and residual excess pore pressures.

6.4.2 Signal conditioning for pore pressure transducers

The operation of a PPT is similar to other strain gage type sensors (e.g., load cell), which uses the linear relationship between the electric resistance and the length of the conductor. Details of the theory can be found in instrumentation literature (Dunnicliff 1996, Figliola and Beasley 2000). The PPT measures the strain of the pressure-sensing diaphragm, which is related to the pressure applied to the diaphragm, using bonded strain gages. The strain gages are wired into a circuit and the voltage drop across the circuit is related to the strain. To power this circuit, a constant excitation voltage must be supplied. Also, it is often necessary to amplify the signal from a PPT due to the small voltages being measured (Figliola and Beasley 2000). A DC power supply (Lambda LL903 power supply) is used in this research to provide the constant excitation voltage. Also, a DC analog amplifier (Neff 128 DC Amplifier) is employed to amplify the signal.

It should be addressed that the calibration factor for the PPT depends on the excitation voltage and the amplifier employed. When calibrating the PPT in the laboratory, the entire system, including the sensor, DC power supply, analog amplifier, and associated cables and connectors, must be used. Because the natural frequency of a PPT generally is much higher than the operation frequency, a constant calibration factor is used in the data processing. In addition, the expected range of field pressure should be considered when choosing a PPT. A PPT with a range closer to the expected measured pressure will have a larger signal-to-noise ratio and higher resolution.

6.4.3 Push-in piezometer

Several dynamic piezometers had been developed and installed in the field (e.g., Youd and Wieczorek 1984, Scott and Hushmand 1995). Scott and Hushmand (1996) designed and fabricated a new pore water pressure measuring probe, named the "Caltech Piezometer", for dynamic pore pressure measurements in the field. The Caltech Piezometer has many attractive features, including: being retrievable for periodic inspection, easy installation with conventional drilling equipment, being capable of maintaining saturation prior to and during installation, quick response time, and high accuracy. The test results conducted at Treasure Island showed that the Caltech Piezometer had performed better than the other types of piezometers previously installed at Treasure Island by the USGS (Scott and Hushmand 1995).

Based on the design of the Caltech Piezometer, a modified version was developed in the early stages of this research. This piezometer, called the push-in piezometer, is shown in Figure 6-6. The main component of the push-in piezometer is the Geokon 3400 piezometer. The Geokon 3400 piezometer has a built-in amplifier inside the piezometer, therefore it only needs an external DC power supply. The major modifications made to the Geokon 3400 piezometer are the addition of an outer sleeve to function as a sealing device and a drilling rod connection. The outer sleeve seals the section of the piezometer that contains the porous filters so that saturation can be maintained during transportation to the field and the installation process. This seal is maintained by four O-rings (Figure 6-6). The drilling adapter is located at the top of the outer sleeve and is used to

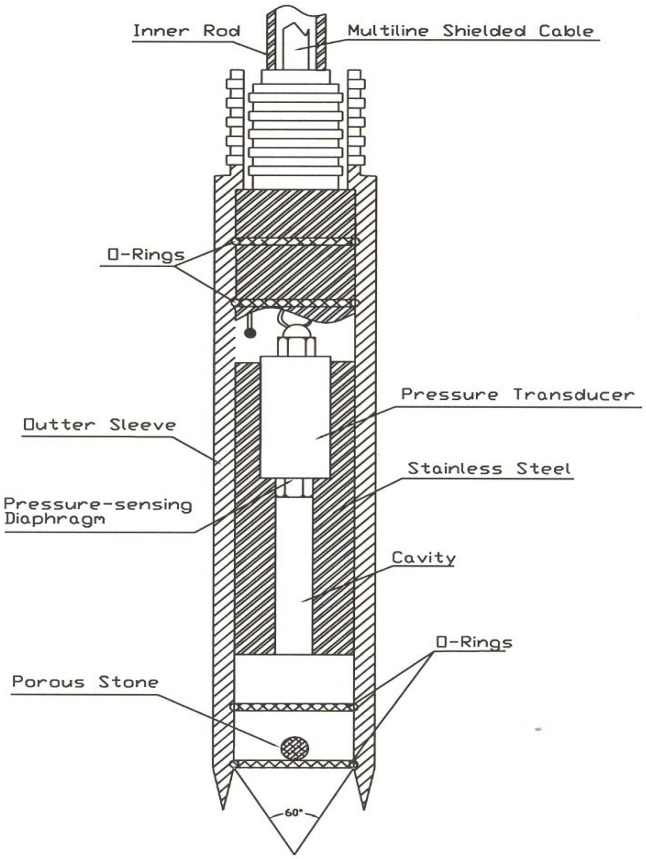

Figure 6-6 Cross-section of the push-in piezometer

connect with standard EW rods.

6.4.3.1 Saturation and calibration procedure

Full saturation of a piezometer is the key step in making accurate pore water pressure measurements. Saturation in this study means keeping air out of

the zone between the surrounding soil and the pressure-sensing diaphragm. The two crucial components that need to be saturated are the filter and the cavity in front of the diaphragm.

A special chamber was designed for calibration and saturation of the push-in piezometer, as shown in Figure 6-7. The three outlets in the chamber are connected to a pressure supply, vacuum, and a separate Validyne pressure transducer without a filter. When filling the chamber with water, the pore pressure transducer is removed and the side outlet is connected to a deaired water tank. An adjustable reaction frame is used to fix the sleeve and the piezometer in the chamber. The Validyne pressure transducer with its pressure-sensing diaphragm directly in contact with the water in the chamber is used as a reference transducer in calibrating the piezometer and evaluating any possible time lag due to the porous filters. The detailed saturation procedure used in this study is described below:

1. The piezometer is assembled with the sleeve and inserted into the chamber as shown in Figure 6-7. The porous filter is exposed from the outer sleeve for saturation and calibration. The pressure-sensing diaphragm inside the cavity of the piezometer must be below the top cap of the chamber to ensure that it will be submerged after filling with water. The bottom outlet of the chamber is connected to the deaired water tank.

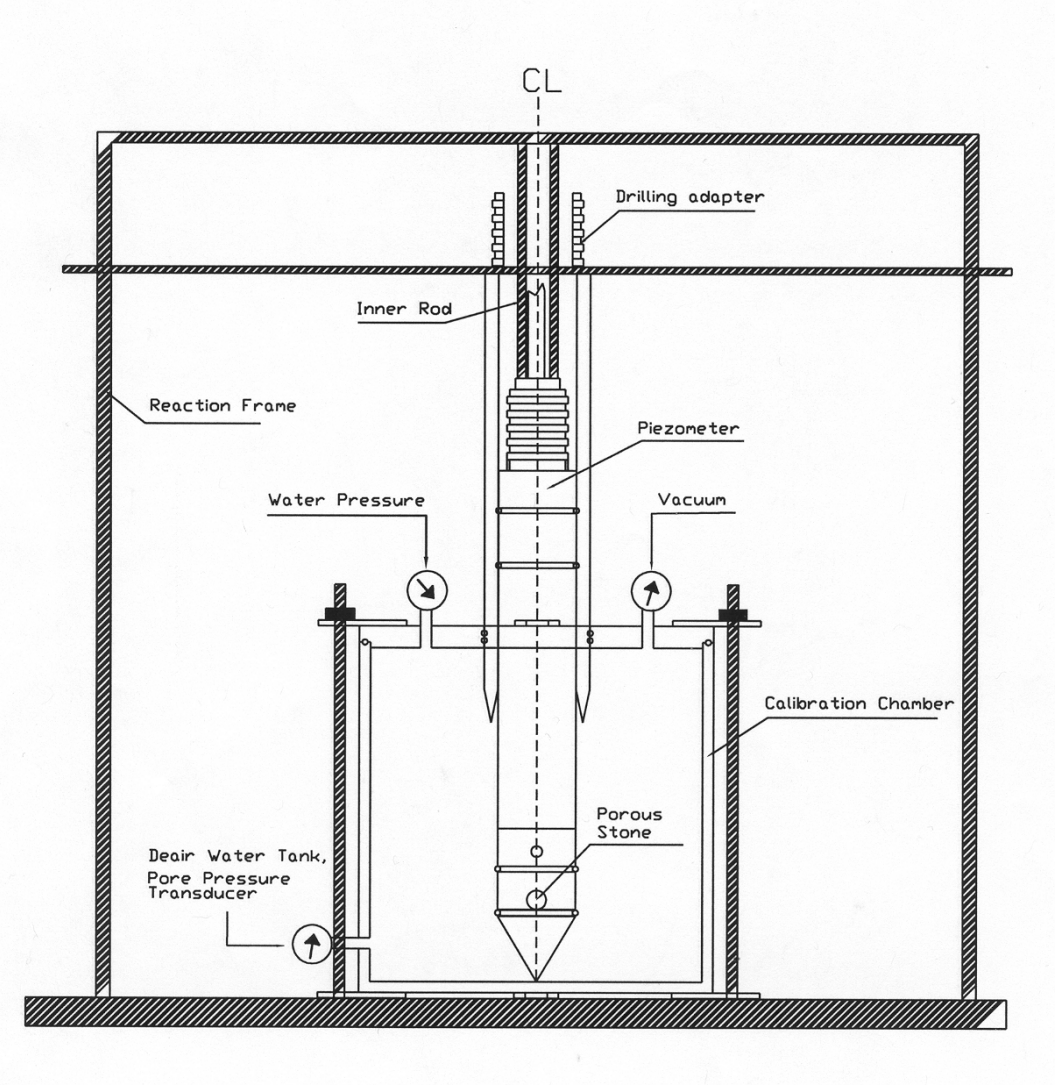

Figure 6-7 Setup of calibration and saturation chamber for the push-in piezometer

2. A vacuum is slowly applied to the chamber. By monitoring the vacuum pressure, sealing of the system is checked. After sealing is ensured, the vacuum pressure is increased to –0.8 atm for 5 minutes to remove air

from the system. After application of the vacuum, the amount of air in the chamber, the porous filter, the cavity in front of the diaphragm, and the plastic pipes connected to the chamber is reduced significantly.

3. While maintaining the same vacuum pressure, the valve to the deaired water tank is opened. The deaired water enters the chamber due to the gradient generated by the pressure difference between the vacuum and atmospheric pressure.
4. When the chamber and piezometer are filled with deaired water, the side outlet is closed and the vacuum is disconnected. Before applying the water pressure, the sleeve and piezometer are fixed to the reaction frame to prevent movement. The deaired water tank is disconnected and the side outlet is connected to the reference pressure transducer. A water pressure of 68.5 kPa (10 psi) is applied to the chamber and sustained for at least 24 hours to dissolve any remaining air.
5. To ensure that the piezometer is saturated, the time lag and pore pressure magnitude difference between the piezometer and the reference transducer are evaluated. If the time lag and pore pressure magnitude difference between the piezometer and the reference transducer are zero, saturation is complete.
6. The rod used to fix the piezometer is removed and pressure is applied to the chamber. This pressure pushed the piezometer into the outer sleeve and the piezometer is completely sealed.

7. After sealing, the remaining pressure in the cavity is used as an index of sealing and saturation. Theoretically, the pressure should be constant inside the piezometer. However, the pressure tends to drop slightly because of some dissolution of the air.
8. The sealed piezometer with its sleeve is disassembled from the chamber and ready for transportation and installation.

6.4.3.2 Effect of saturation on pore pressure measurement

To study the effects of air inside the piezometer on the pore pressure measurement, a series of tests using the push-in piezometer and the calibration and saturation chamber were conducted to study the time lag and magnitude reduction issues.

To evaluate the time lag of the push-in piezometer, a general-purpose pressure transducer, Validyne DP15, is used as a reference sensor in the calibration chamber. The pressure-sensing diaphragm of the Validyne transducer is exposed directly to the water, so the time lag due to air in the filter(s) and the cavity is eliminated. An impact type test is used to measure the time lag between the push-in piezometer and the Validyne sensor. To be more realistic, the calibration chamber was filled with air dry sand before insertion of the push-in piezometer.

A dynamic pressure is applied to the chamber over a short time interval and the pore pressure response of both the piezometer and the reference sensor are recorded simultaneously with a multichannel analyzer sampling at 8192

samples/sec. The time lag between the signals was calculated using the cross-correlation algorithm (Chapter 5). Tests were performed on the push-in piezometer in two conditions: (1) after saturation using the procedure previously discussed and (2) after insertion into the calibration chamber with no saturation procedure.

Measured pressures from tests performed on the saturated piezometer are shown in Figure 6-8. No time lag is observed between the piezometer and the reference transducer and the pore pressure magnitudes are the same. Similar results were observed for all tests that used the saturation procedure. Measured pressures from tests performed on the piezometer with no saturation procedure are shown in Figure 6-9. For this test, a time lag of 0.054 sec is indicated and the pressure measured by the push-in piezometer is about 5% smaller than that measured by the reference transducer.

To further study this issue, the dynamic pressure tests on the partially saturated push-in piezometer were conducted at different peak pressure levels. A summary of the results regarding the time lag and percent pressure difference ($\frac{\Delta p_{peak}}{p_{peak}}$, where p_{peak} is the peak pressure measured by the reference transducer) are presented in Figure 6-10. The time lag tends to decrease slightly as the peak pressure increases. The percent pressure difference remains approximately constant as the peak pressure increases. The time lag indicated in Figure 6-10 is not acceptable for this project because the loading is so quick. For a loading frequency of 20 Hz, one cycle of loading occurs in 50 ms, which is approximately

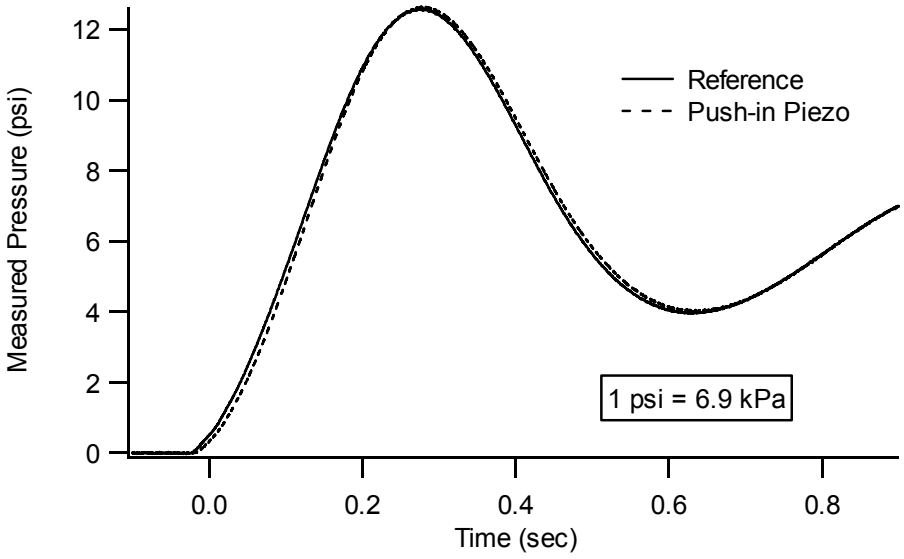

Figure 6-8 Pore pressure response for fully saturated push-in piezometer

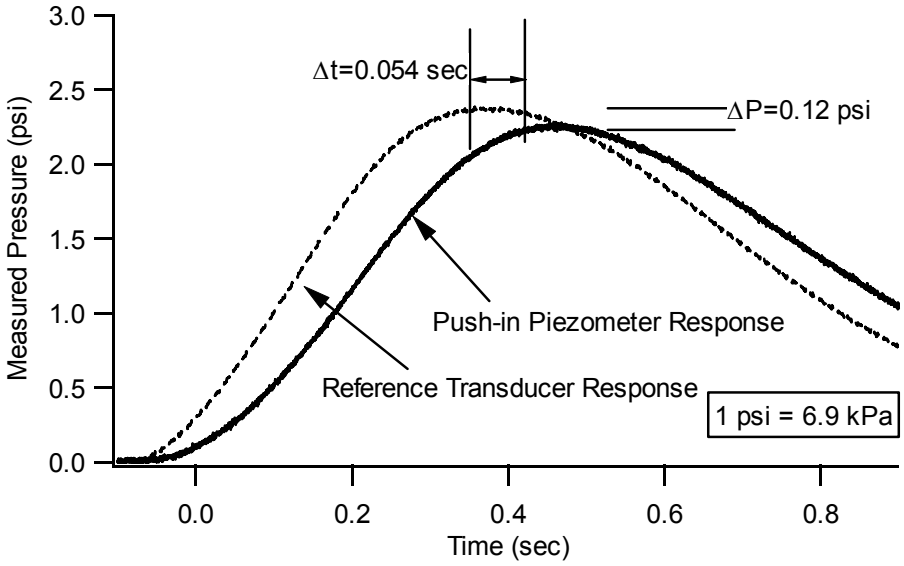

Figure 6-9 Pore pressure response for partially saturated push-in piezometer

equal to the time lag in Figure 6-10. As a result, a partially saturated piezometer can cause almost a 1 cycle delay in the measured pore pressure.

Based on this experimental study, a partially saturated piezometer will cause a time delay and slightly smaller pressures will be measured. It should be noted that the time lag and pressure difference presented here is only for the push-in piezometer. The quantitative errors for different piezometers should be determined through further experimental studies.

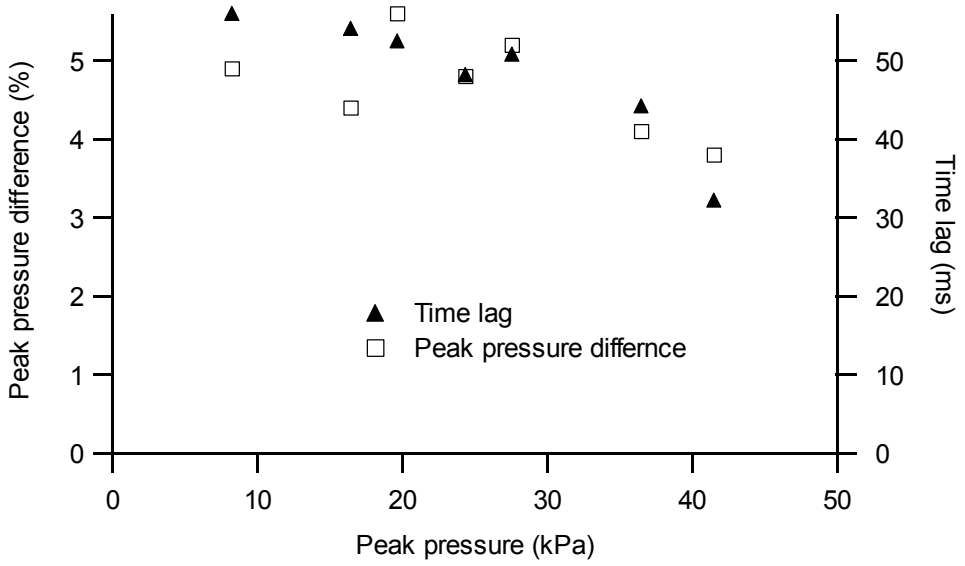

Figure 6-10 Summary of pore pressure response for partially saturated push-in piezometer

6.4.4 Miniature pore pressure transducer

After the first test series, it was decided that a smaller pore pressure transducer should be used. A miniature pore pressure transducer (Drucker PDCR 81-8317), which has been widely used in centrifuge experiments, was used to replace the push-in piezometer. This miniature PPT was integrated into the liquefaction test sensor for subsequent experiments. The miniature PPT is shown in Figure 6-11. Porous bronze is used as the filter to replace the ceramic filter provided by the manufacturer. Because the miniature PPT is an electrical resistance strain gage transducer, a DC power supply and a signal conditioner are required. The signal conditioner provides signal amplification and real-time filtering. The Drucker miniature PPTs are used in four of the five liquefaction sensors. One of the liquefaction sensors incorporates a miniature PPT manufactured by Entran (Entran EPX-V01). Both the Drucker and the Entran miniature PPTs show similar pressure responses.

There are several advantages regarding the miniature PPT. First, the miniature PPT has a smaller pressure-sensing diaphragm, so less volume change due to the deflection of the diaphragm occurs. Second, the smaller cavity between the diaphragm and the porous filter reduces the possibility of trapping air in the cavity. Third, the small dimension of the miniature PPT allows it to be integrated with the geophones into one small acrylic case.

The major concern for the miniature PPT is its durability in the field. These sensors are designed for use in the laboratory over a relatively short time. In the field, special care must be taken with respect to the cable integrity, stress

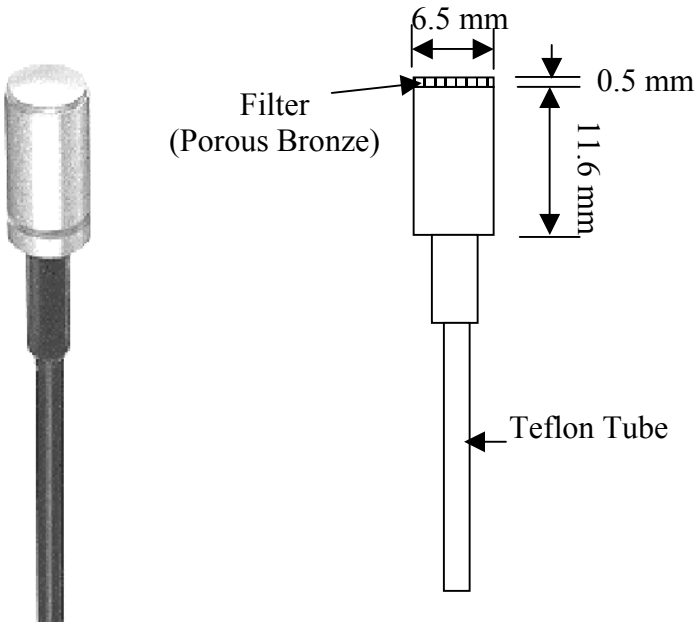

Figure 6-11 Miniature pore pressure transducer (Drucker PDCR81-8317)

levels, and water resistance. For use in the field, the miniature PPTs are epoxied in an acrylic case for protection and water resistance.

To saturate and calibrate the miniature PPT after it is epoxied in the acrylic case of the liquefaction sensor, another saturation chamber was constructed (Figure 6-12). Each PPT is first statically calibrated using a mercury manometer. For saturation, the procedure used for the push-in piezometer was again used. Impact testing was performed on the miniature PPT, but the testing revealed that the miniature PPT is less affected by the saturation procedure. A

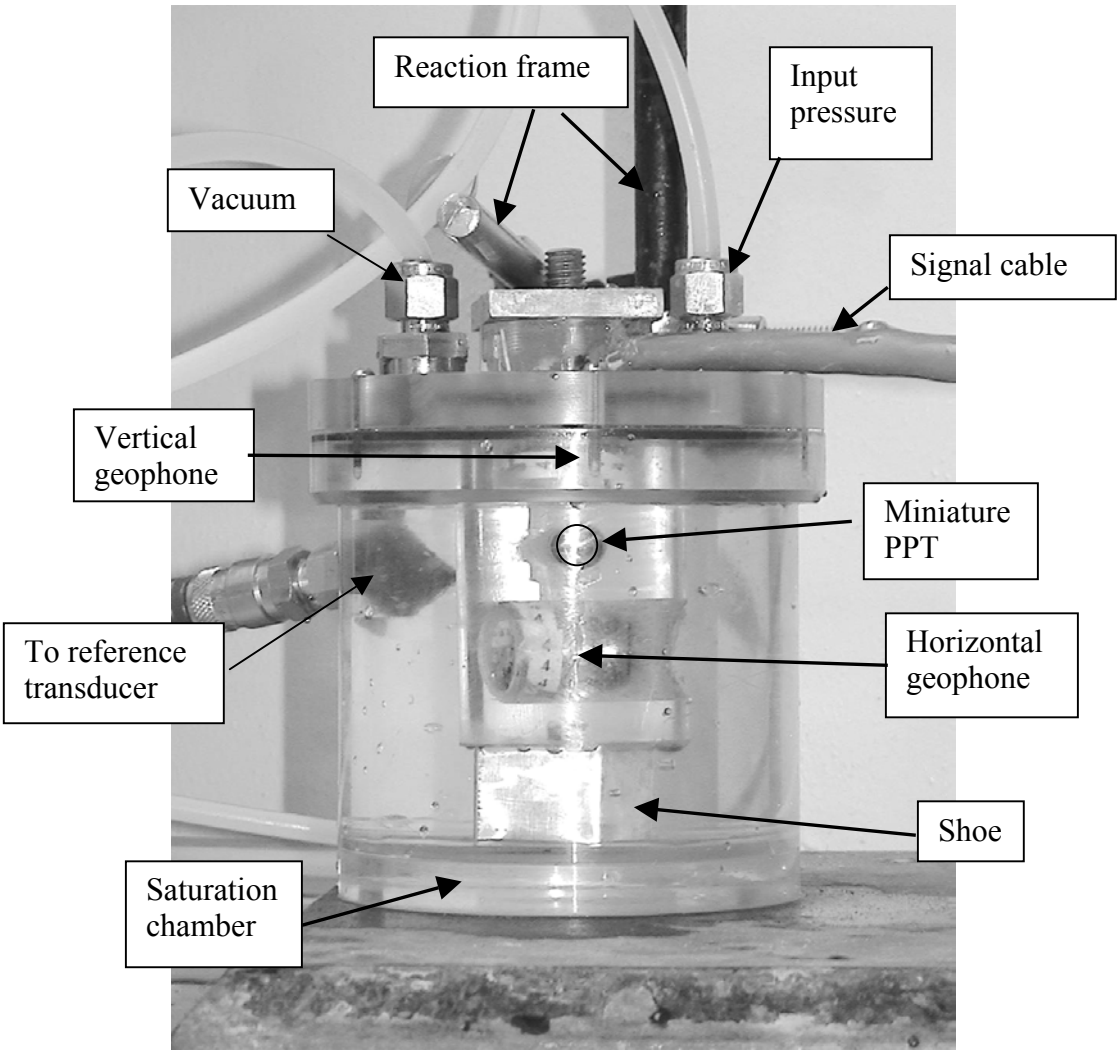

Figure 6-12 Calibration and saturation chamber for miniature PPT

time lag is rarely observed and the percent pressure difference is less than 1% of the applied pressure. The absence of the time lag and pressure difference are most likely due to the smaller cavity and smaller pressure-sensing diaphragm of the miniature PPT.

To ensure the best performance of the PPT, the miniature PPTs are still saturated using the saturation procedure. After saturation, the entire liquefaction sensor is placed inside a plastic bag filled with deaired water and submerged in a bucket filled with water. During installation, the PPT is always kept submerged. The testing results revealed that the miniature PPTs successfully captured both hydrodynamic and residual pore water pressure. Also, the signals from the miniature PPTs contain less noise than the push-in piezometer.

6.5 DEVELOPMENT OF THE LIQUEFACTION SENSOR

A new sensor, called the liquefaction sensor, was developed that integrates two geophones and a miniature PPT inside a single acrylic case. This sensor is smaller than the sensors previously discussed (4.5 Hz geophone, push-in piezometer) and allows simultaneous measurement of particle velocities and pore pressure at the same point. Five liquefaction sensors were installed in the liquefaction test pit (Chapter 3). Details are given below.

The goal for the liquefaction sensor is to measure particle motion and excess pore pressure at the same location. Because particle motion and pore pressure are measured by geophones and PPTs, respectively, these two types of sensors must be combined. There are several issues that must be considered in the

design. First, the sensor must be small enough to avoid significant interference with the surrounding soils. Second, the unit weight of the sensor must be similar to the total unit weight of the surrounding soil to avoid floating or sinking of the sensor after significant excess pore water pressure generation. Third, the stiffness of the sensor must be large enough to withstand the stresses during installation and the dynamic loading. Fourth, the noise level needs to be small for seismic testing and data reduction. Fifth, the sensor must be able to be installed vertically. Finally, the sensor and cable must be waterproof.

A schematic of the liquefaction sensor is shown in Figure 6-13. A cylindrical acrylic case was machined with holes to install two perpendicularly oriented 28-Hz geophones and one miniature PPT. The acrylic case is waterproof and provides protection for the sensors. A "shoe", made of thin metal plate, was attached to the bottom of the sensor to provide stability of the sensor during installation. A square aluminum plate with a threaded rod at the center was attached to the top of the sensor to provide a connection with the placement tool. Epoxy was used to fix the sensors within the case and at the correct orientations. The epoxy also was used to fill all voids. An individually shielded, four-pair cable was used to provide DC power to the miniature PPT and to connect the two geophones and the PPT with the data acquisition systems.

Because the miniature PPT is a relative pressure transducer, which measures the pressure difference between the two sides of the pressure-sensing diaphragm, the side opposite to the water contact surface needs to be vented to the

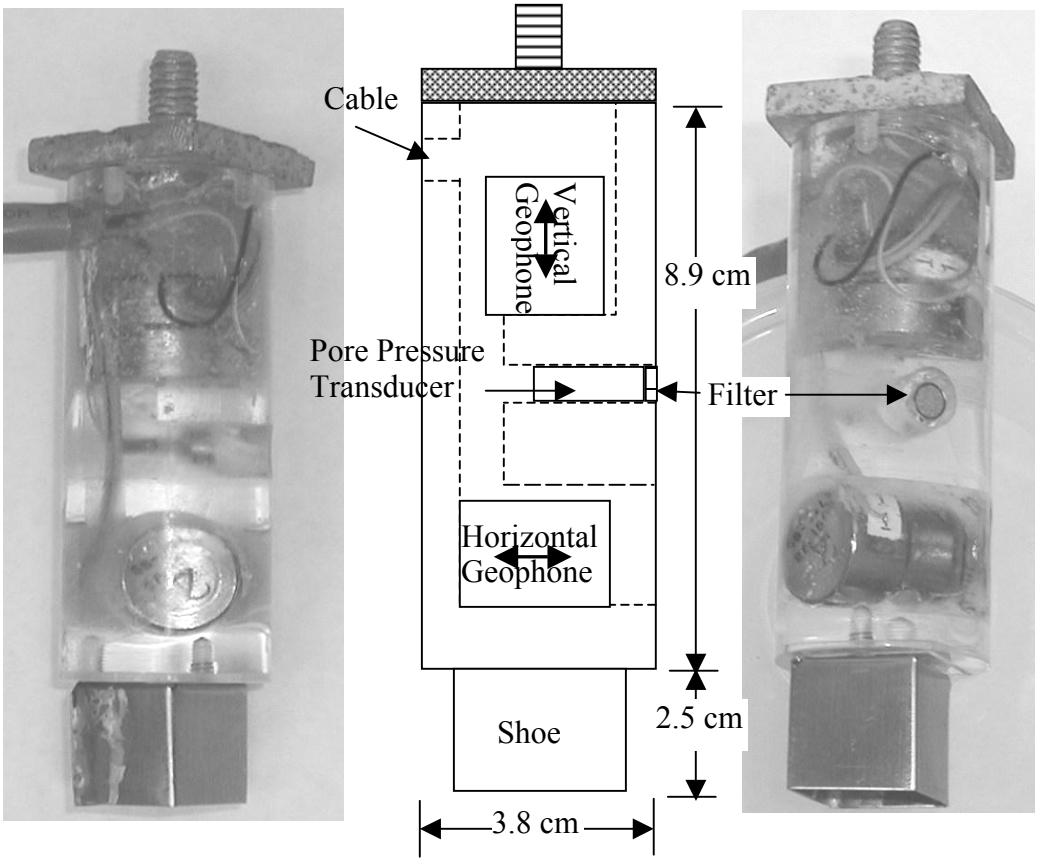

Figure 6-13 Schematic of liquefaction test sensor

atmosphere to eliminate any pressure difference due to minor changes in atmosphere pressure. A tiny Teflon tube was used to vent the PPT. This tube extends from the back of the PPT to the electrical cable. Venting is achieved through the voids inside the electrical cable, which is open to the air at the end. The estimated unit weight of the liquefaction sensor is 2.24 g/cm^3 (140 pcf),

which is quite close to the total unit weight of the surrounding saturated sand, which is about 2.0 g/cm^3 (130 pcf).

To install the liquefaction sensor at a certain depth with the appropriate orientation, a placement tool was used to hold the sensor during installation and to detach the sensor after placement. The placement tool is a modified version of that used by Phillips (2000) and a schematic is shown in Figure 6-14. Two tilt switches, oriented in perpendicular directions, were attached to the metal plate on top of the liquefaction sensor to monitor the verticality of the sensor. When the

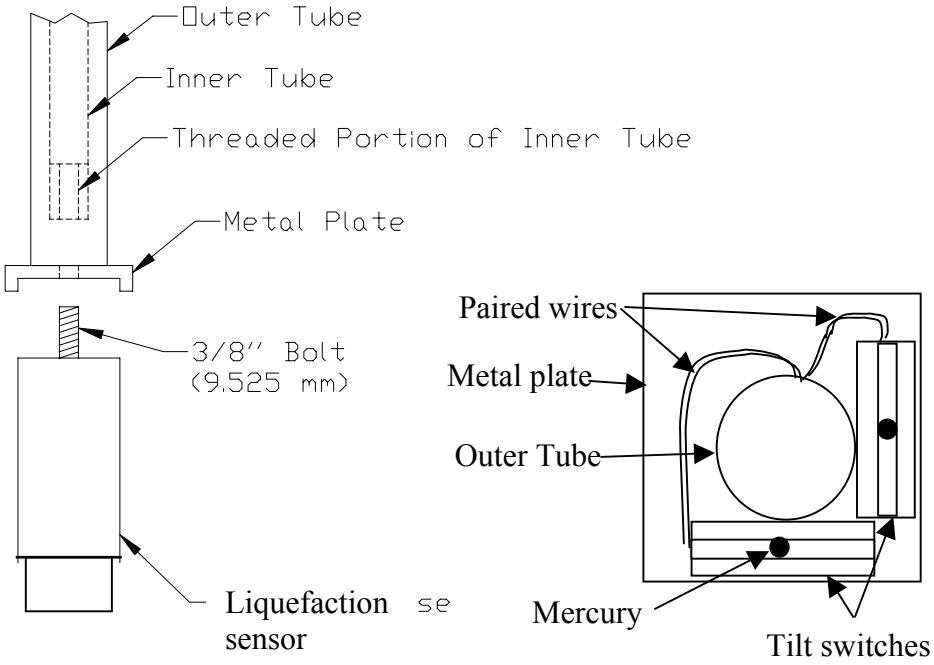

Figure 6-14 Schematic diagram of placement tool (Modified from Phillips 2000)

inclination on either side of the metal plate exceeds 3°, an error signal is triggered.

In the field, the liquefaction sensor was attached to the placement tool through the threaded rod on top of the sensor and the threaded portion of the inner tube (Figure 6-14). After the liquefaction sensor was placed in the test pit, the inner tube was unscrewed from the threaded rod. The outer tube with a square metal plate that fits over the metal plate on top of the liquefaction sensor, holds the sensor still while unscrewed the inner tube. The inner tube then is pulled out, inverted, and re-inserted into the outer tube. The other end of the inner tube is closed and placed in contact with the threaded rod. Using the inner tube as a reaction, the outer tube is pulled up and detached from the liquefaction sensor. Details regarding the placement tool and placement procedure can be found in Phillips (2000).

6.6 ACCELEROMETER

Accelerometers, which measure acceleration, were used in this research to measure the motion of the footing and the acceleration at the top of the test pit during dynamic testing. Piezoelectric accelerometers were used in this study. A piezoelectric accelerometer consists of three basic elements: the case, the piezoelectric sensing element (piezoelectric crystal), and the mass attached to the piezoelectric crystal (Figure 6-15). Piezoelectric materials produce an electrical charge when a mechanical load is applied. Therefore, the electrical charge is used to measure the force acting on the piezoelectric crystal. When an accelerometer is

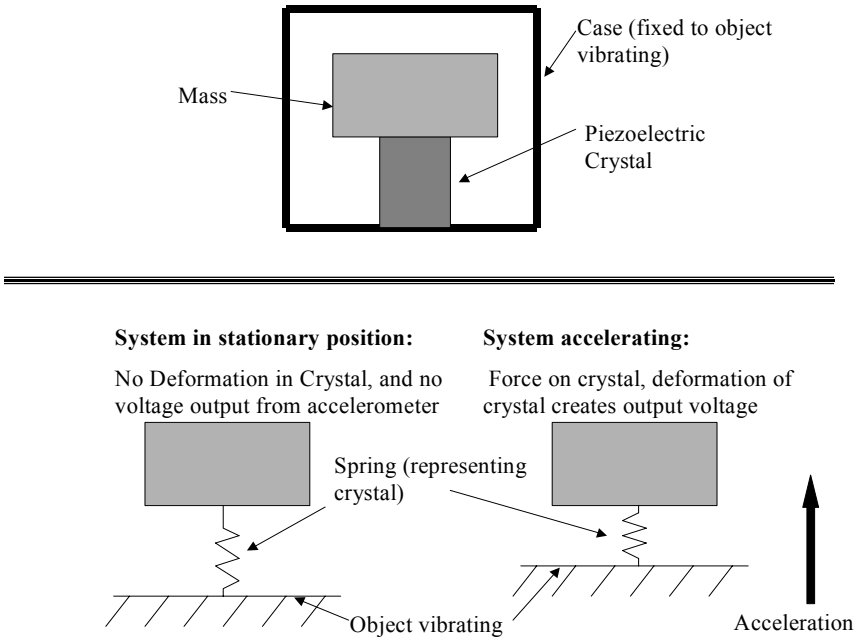

Figure 6-15 Schematic diagram of a piezoelectric accelerometer

moving, the force acting on the piezoelectric crystal is proportional to the acceleration of the mass, in accordance with Newton's first law. Therefore, the acceleration is measured by measuring the generated electrical charge.

A piezoelectric accelerometer needs a signal conditioner to convert the electrical charge to a voltage and to amplify the output voltage. The design of the signal conditioning varies between manufacturers. The accelerometers used in this research were the Wilcoxon-736T. The Wilcoxon accelerometer has a built-in microelectronic amplifier inside the accelerometer that converts electrical charge to voltage. The built-in amplifier needs a constant current, which is provided by an external in-line current source operated by 9-volt batteries.

For accurate measurement of acceleration, the accelerometer must be properly coupled with the moving object. The mounting must be rigid over the frequency and magnitude ranges of interest. Triaxial mounting cubes, with threaded studs, were used to mount accelerometer for vertical and horizontal measurements. On the concrete footing, the mounting cube was directly adhered to the leveled concrete surface with epoxy. On top of the test pit, a metal spike was attached to the bottom of the mounting cube to maintain proper coupling with the soil.

When using an accelerometer, the frequency of the measured acceleration should be well below the natural frequency of the accelerometer to ensure a linear response. The natural frequency of the Wilcoxon-736T accelerometers is 60 kHz. The high natural frequency is due to the high stiffness of the piezoelectric crystal and the small mass. Additionally, because an accelerometer is basically an AC coupled device, it is not suitable to measure very low frequency vibrations. The accelerometer used in this test can measure down to 2 Hz. The loading frequency in the field was 20 Hz, which will ensure a linear response.

6.7 SMALL-STRAIN SEISMIC TESTING EQUIPMENT

Small-strain seismic testing techniques, specifically crosshole and downhole tests, were used in this research to characterize the reconstituted test specimen, as well as to monitor the stiffness variation of the test specimen before and after dynamic loading. Additionally, these testing techniques were used to check the saturation of the reconstituted test specimen. The small-strain seismic

tests were performed in accordance with typical crosshole and downhole testing procedures, using the embedded array sensors as receivers and a variety of sources. Details regarding the theory, signal processing, and testing procedures used in small-strain seismic testing can be found in other literature (e.g., Stokoe and Woods 1972, Stokoe and Hoar 1975, ASTM D4428/D4428M). The equipment for the small-strain seismic testing is introduced here. The seismic testing procedures are discussed in Chapter 9 and specific testing results are presented in the chapters for the individual test series.

6.7.1 Crosshole seismic source

The source used in the seismic crosshole tests is shown in Figure 6-16 (Chen 2001), along with a schematic illustration of the layout of the crosshole test. The source was placed in a vertically oriented PVC pipe located at the edge of the reconstituted test pit. This source was used to generate both horizontally propagating shear waves with vertical particle motion (S_{hv}-waves) and horizontally propagating constrained compression waves (P_h-waves). The S_{hv}-wave velocity was measured from the travel time between the two geophone receivers, as indicated by recordings from the vertically oriented geophones inside the embedded liquefaction sensors. The P_h-wave velocity was determined in a similar way using the horizontally oriented geophones as receivers.

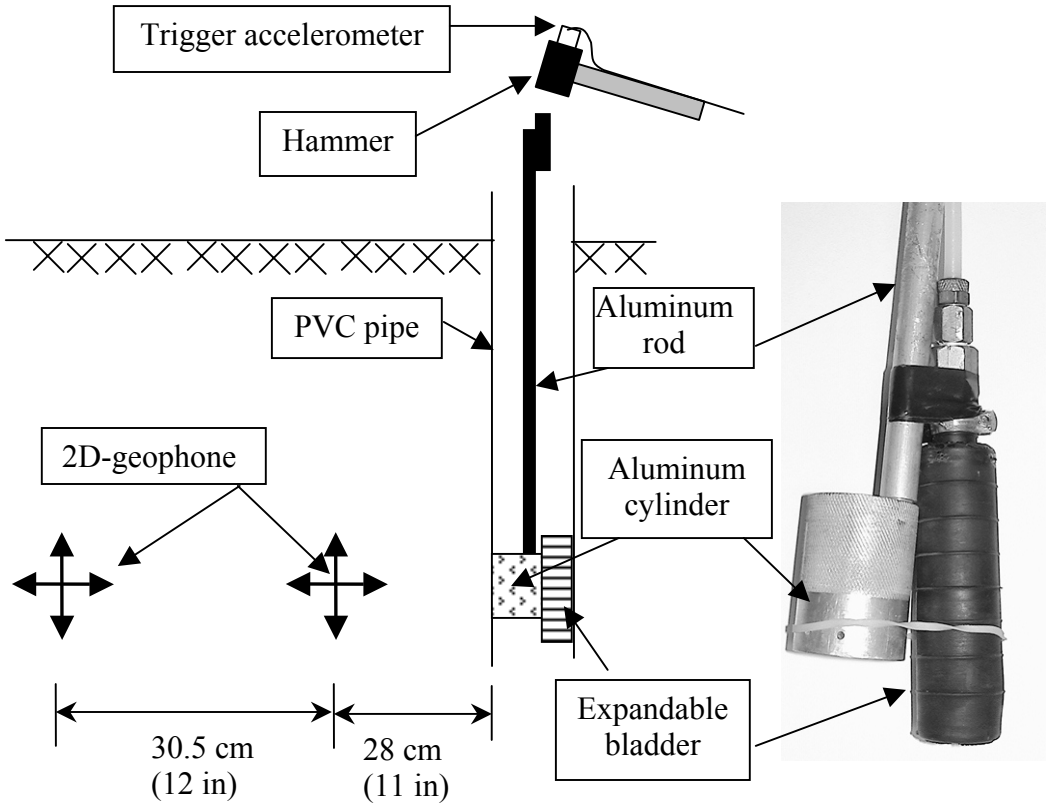

Figure 6-16 Seismic crosshole source and crosshole testing layout (Chen 2001)

The crosshole source used to generate the S_{hv}- and P_h-waves consists of a roughly surfaced aluminum cylinder attached to an expandable, thick-walled rubber bladder, and an extendable aluminum rod. The rubber bladder was attached to the aluminum cylinder with electrical tape at the top of the bladder and a rubber band at the lower part of the bladder. Once attached, the aluminum cylinder and bladder were lowered into the PVC pipe to a depth that coincided with the depth of the embedded receivers. Next, the bladder was inflated using a

bicycle pump to obtain good contact between the aluminum cylinder and PVC pipe. A metal hammer was used to impact the top of the aluminum rod to generate stress waves. An accelerometer (PCB-303A02) was mounted at the top of the hammer to serve as an external trigger.

Because the wave velocity measurement was an interval measurement between two receivers, no time delay due to the wave traveling from the top of the aluminum rod to the aluminum cylinder was considered.

6.7.2 Crosshole test for saturation verification

The cyclic resistance of sand will increase as the degree of saturation decreases. The degree of saturation can be quantified by the B-value in laboratory tests (e.g., Chaney 1978, Yoshimi et al. 1989) and P-wave velocity in the field (e.g., Ishihara 1998). For saturated soil, the theoretical P-wave velocity is about 1524 m/s (5000 ft/s), which is the P-wave velocity of water. Field P-wave velocity measurements in Japan disclosed that soil several meters below the ground water table may not be fully saturated (Ishihara et al. 2001). To verify saturation for the proposed field tests, P-wave velocity measurements of the reconstituted test specimens were conducted.

Initially, P_h-wave measurements were attempted with the crosshole source, using the horizontal geophones inside the liquefaction sensors at the same elevation. The results were not successful because the source does not generate significant P_h-wave energy, resulting in small signals that were overwhelmed by noise. An alternative is to conduct downhole seismic tests to measure vertically

propagating P-waves (P_v-waves) using the vertical geophones inside two liquefaction sensors aligned vertically as receivers. An aluminum rod attached to a square aluminum plate and located at the top of the reconstituted test specimen was used as the seismic source for these downhole measurements. Three travel times were recorded: (1) from the aluminum plate to the first receiver, (2) from the aluminum plate to the second receiver, and (3) from the first receiver to the second receiver. These measurements give the average P_v-wave velocities in the top 1 m of the test pit.

To obtain more localized measurements of P-wave velocity, so that small pockets of partially saturated material can be identified, a new testing configuration was developed. This testing configuration includes an aluminum rod source and a small, push-in geophone receiver that can be positioned at various locations within the soil for crosshole tests. Tests using this instrumentation must be performed after liquefaction testing, because insertion of the instrumentation disturbs the soil. The source is a 1.5 m aluminum rod, 0.7 cm in diameter. A hammer with a trigger accelerometer was used to hit the top of the source rod to generate P_h-waves. The receiver consists of a horizontally oriented 28-Hz geophone epoxied in a mini acrylic cone connected to an aluminum rod, as shown in Figure 6-17. A portable digital oscilloscope was used to record the trigger and wave arrival. Before conducting the field test, the travel time for wave traveling down the source rod was measured in the laboratory and denoted t_r. When conducting the test in the field, the source rod and receiver were pushed to the same depth, approximately 30.5 cm (1 ft) apart. The travel time from the top

of the source rod to the receiver was measured using the digital oscilloscope and denoted t_m. The P-wave velocity is computed as

$$V_P = \frac{0.3048 \quad m}{t_m - t_r} \quad \text{..... (6-4)}$$

with t_m and t_r in seconds and V_P in m/s. Measurements were taken every 2.54 cm (1 inch) until a consistent P-wave velocity above 1524 m/s (5000 ft/s) was measured. The variation of Vp with depth can be used to define zones of partial saturation. The same procedure can be conducted in different locations to measure the spatial variation in saturation. The measurement results, particularly the saturation within the instrumentation array, are presented in Chapter 9.

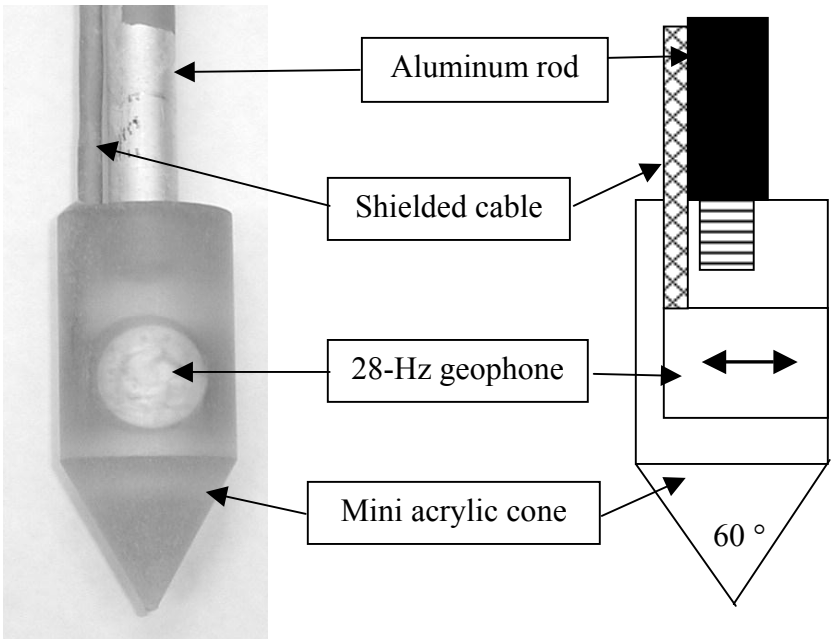

Figure 6-17 Push-in P-wave velocity measurement receiver

6.7.3 Dynamic signal analyzer and digital oscilloscope

In the seismic testing mentioned above, a portable dynamic signal analyzer (DSA) is required for signal acquisition, signal processing, and storage of signals. The DSA used in this test is an Agilent-35670A 4-channel DSA. The features of this DSA include FFT-based spectrum analysis, a frequency span of up to 51.2 kHz, 16-bit A/D conversion, different averaging modes in the frequency or time domain, and windowing in the frequency and time domain. The features used in the crosshole testing are time domain signal capturing, analog pre-triggering, time domain averaging, and data storage. In the field, the noise was effectively reduced by averaging 5 test results in the time domain. The DSA is used for the crosshole S_{hv}-wave velocity measurements.

The DSA is not appropriate for measuring the P-wave velocity of the saturated soil because the sampling rate is not fast enough to capture the short travel time of the P-wave. Instead, a digital oscilloscope (Tektronix 2220) is used to capture the time domain signals because of its high sampling rate. Unfortunately, this digital oscilloscope can not store data for future analysis and has limited triggering levels. Additionally, the digital oscilloscope cannot perform frequency domain analysis and has a limited recording length. To improve these drawbacks, a new digital oscilloscope with a built-in disk drive and larger memory is recommended.

6.8 OTHER INSTRUMENTATION

Besides the previously discussed electronic instrumentation equipment, other tools were used in this research for settlement and in situ density measurements. Details of the design and operation of these tools are described here.

6.8.1 Settlement platform

Settlement platforms were used in this research to monitor the settlement of the reconstituted test specimen at different depths. The settlement data will be used to construct the settlement profile of the reconstituted test pit, to calculate the permanent vertical stain, and to estimate the in situ density after dynamic loading.

The settlement platform consists of a square aluminum plate (10 cm by 10 cm) placed within the soil at the location where settlement is to be monitored (Figure 6-18). An aluminum rod is fixed to the steel plate and extends above the ground surface. A sleeve pipe is placed around the rod to allow the plate to settle freely. Settlement platforms are installed at different depths to measure the variation of deformation with depth (Figure 6-18). Optical leveling measurements of the top of the rod are taken before and after each dynamic test. The vertical settlements for each plate can be obtained by subtracting the original elevation. The accuracy is limited by the resolution of optical leveling equipment, which is 3 mm (0.12 in.).

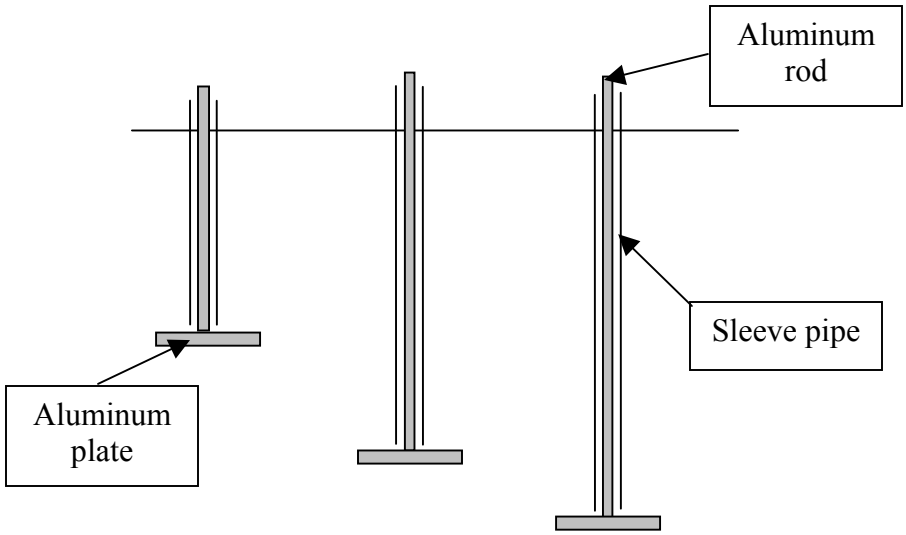

Figure 6-18 Schematic setup of settlement platforms at different depths

The settlement platforms were installed at the desired depth during preparation of the reconstituted test specimen. Care was taken to maintain rod verticality. The elevations of the tops of the rods were measured during and after the preparation of the reconstituted test specimen to evaluate any displacements during sample preparation. The elevations of the tops of the rods were also monitored before and after dynamic testing. In low-strain tests, no settlement should be observed. In large-strain tests, the measured settlements at different depths provide a vertical stain profile, which shows the permanent vertical strain variation with depth. The vertical displacement of the top of the reconstituted test specimen was also used to calculate the change in relative density of the test specimen. The final density calculated from the measured settlement at the top of

the test specimen was compared with the in situ density measured after dynamic testing. In situ density measurement is discussed in the next section.

6.8.2 In situ density measurement tool

For the current testing procedure, the initial in situ density is estimated from the volume of the test pit and the dry weight of the soil backfilled into the test pit. To verify the estimated density, a sampling device was constructed to obtain in situ density measurements of the reconstituted test specimen. The sampling device (Figure 6-19) is essentially a short Shelby tube with an aluminum plate that can be attached to one end of the tube using wing nuts. The tube is 10.3 cm long, with an outside diameter of 8.9 cm and an inside diameter of 8.5 cm, resulting in an area ratio of 9%. A cutting edge was machined at the bottom of the tube with 1% relief (Figure 6-19). A 21.6-cm square aluminum plate is attached to the tube at the opposite end using three wing nuts.

The in situ densities were measured after the test series was finished. The procedure is as follows. The cutting edge of the tube is pushed into the soil below the current ground surface, without the aluminum plate attached. The soil at the top surface of the tube is leveled and removed using a thin cutter, and the aluminum plate is attached using the wing nuts. The entire sampling device is excavated from the test specimen, with extra soil left on top of the sampling device. This extra soil is leveled and removed. The filled tube is placed in a plastic bag, transported back to the laboratory, and placed to dry in an oven for 24

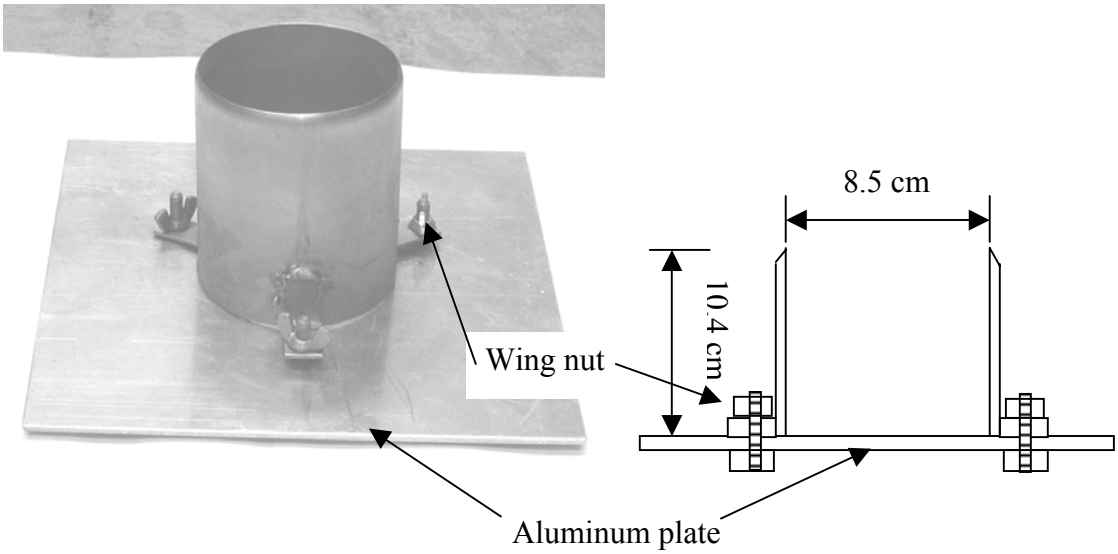

Figure 6-19 In situ density measurement tool

hours. The weight of the dry soil and the volume of the sampling tube are used to calculate the dry density of the soil. The in situ unit weight is estimated by assuming the in situ sand is saturated. The procedure was repeated at different depths.

6.9 DATA ACQUISITION SYSTEMS

For dynamic testing, a high-speed, automated data acquisition system is essential to collect and record signals from the various sensors. The basic functions of an automated data acquisition system are digitization of analog signals and storage of the signals in digital format for future analyses. Selection of an automated data acquisition system is based on the required sampling rate,

desired recording time length, signal type, expected magnitude of the signals, number of sensors, cost, and integration with data reduction procedures. Details regarding the data acquisition systems involved in this study are presented in the following sections.

The major components of an automated data acquisition system are an analog-to-digital processor (A/D board), storage media, and software that connects these two physical devices. The analog-to-digital processor serves to simultaneously sample and digitize continuous, analog signals into discrete, digital signals. The digital signals are then stored in the storage media. The data acquisition software functions as a bridge between the A/D board and storage media. This software configures the A/D board, controls data transfer, and buffers overflow data. The data acquisition program for the DSA also provides signal processing functions.

As shown in Figure 6-1, two automated data acquisition systems were employed in the current testing configuration. The first system is called the transient response data acquisition system, TRDAQ, and it records the dynamic response during and shortly after dynamic testing. The second system is called the long-term data acquisition system, LTDAQ, and it records the dynamic response during dynamic testing and for a significant time after dynamic testing. The major reasons for using two data acquisition systems are: (1) the required recording time lengths for various sensors are different, (2) the cost for expanding the DSA is high, and (3) the data reduction procedures for pore pressures transducers and geophones are different.

Details regarding the two systems are described below. Additionally, the technique used to synchronize the two systems is introduced.

6.9.1 Transient response data acquisition system-TRDAQ

As its name indicates, the TRDAQ only records signals from the transducers for a short length of time. In the current testing configuration, sensors that monitor ground vibration (i.e., geophones and accelerometers) only produce signals during the dynamic testing. These sensors were recoded with the TRDAQ. The HP 3567A Dynamic Signal Analyzer (DSA) was used as the TRDAQ in this research. Basically, the DSA serves as a digital oscilloscope that provides signal conditioning, digitization of analog signals, and storage in one complete setup.

The HP 3567A is a multichannel Dynamic Signal Analyzer (DSA) controlled by a personal computer and associated software with a GPIB/HPIB interface. The GPIB is an acronym for General Purpose Interface Bus and it provides standard commands for automated instrument controls. With the GPIB interface, engineers can communicate and control the instruments through a computer connected with the instruments. The current configuration has ten input channels. Because each channel operates independently, no time skew exists between each channel. This property is important in phase velocity calculations and strain evaluations. In addition, all necessary antialias filtering is automatically performed by the DSA.

Because the HP 3467A is a FFT-based signal analyzer, the number of recorded data points is always a power of 2. The number of data points that are

recorded is determined by the memory available for each channel. The current DSA has 4MB of memory for each channel, resulting in a maximum of 8192 data points. The recording length is determined by the desired sampling rate and the number of data points. For instance, if the sampling rate is 4096 samples/sec, and the memory can record 8192 data points, the recording length is 2 seconds. Because of the limitations in the recording length, the DSA is only used to process the signals from the geophones, accelerometers, and the load cell on the vibroseis. These instruments only need to be monitored during dynamic testing, which typically encompasses less than a few seconds. However, to monitor pore pressure dissipation after dynamic testing, the pore pressure transducers must measure pore pressures for a significant time after dynamic testing. Therefore, the DSA cannot be used to record the pore pressure data.

A notebook with a PCMCIA version of the GPIB card and with the windows-based DSA software is employed to control the DSA. The parameters needed to setup the DSA are the pre-trigger delay, the trigger channel and trigger level, the sampling rate, the recording length, the input analog signal ranges, the measurement type, and the active channel numbers. For the current testing configuration, the signal from the function generator is used as the trigger channel. The pre-trigger delay is -0.25 sec for all channels (slightly more than 10% of the recording length). The input signal ranges are sensor dependent and are adjusted in the field. The sampling rate is determined from the required recording length. For 20-cycles of vibration at 20 Hz, the sampling rate is set to 4096 samples/sec, which results in 2 seconds of recording time. For 60-cycles of

vibration at 20 Hz, the sampling rate is set to 2048 samples/sec, which results in 4 seconds of recording length.

In addition to setting measurement parameters, the DSA software also allows display of selected data and downloading of data from the memory modulus of each channel. The display function is useful in checking the signals and error debugging in the field. The data were stored in the memory modulus of each channel for quick access during acquisition and initial analysis. These data are downloaded and saved for further manipulations.

Currently, the ten channels of the TRDAQ are connected to eight geophones (case 1 to 4), the accelerometer at the top of the test pit, and the function generator.

6.9.2 Long-term data acquisition system-LTDAQ

To capture the full pore pressure response, including generation and dissipation, a long recording length is necessary. Additionally, the current DSA only has ten channels and the testing configuration contains 16 sensors to be recorded. A second automated data acquisition system is adopted to solve these problems. Because it is designed for long recording lengths, it is called the long-term data acquisition system (LTDAQ).

The LTDAQ consists of a high performance personal computer, a multifunction A/D board (NI PCI-6035), and *LabView*® software from National Instruments. The design requirements for the LTDAQ are high speed sampling, small interchannel delay, long recording length, user-friendly interface, high

reliability, and easy incorporation with future analysis. A schematic of the long-term data acquisition system is illustrated in Figure 6-20. A BNC cable connector box is used to connect the input signals with the A/D board. A shielded cable is used between the connector box and the A/D board for noise reduction.

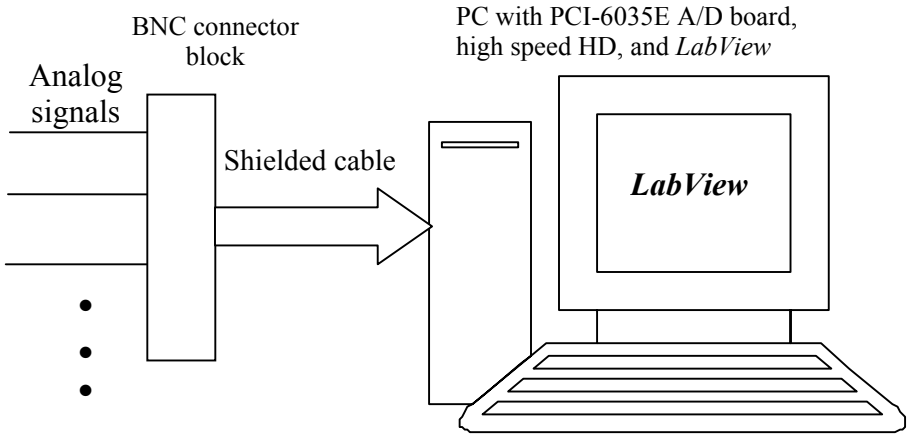

Figure 6-20 Schematic illustration of long-term data acquisition system

The NI PCI-6035E features 16 single-ended or 8 differential-ended analog inputs, 16-bit resolution, 200 kHz sampling rate, and two 24-bit timers. Because this A/D board uses the multiplexing technique, the real sampling rate per channel depends on the number of active channels. As a result, a small interchannel delay exists between channels. The interchannel delay was measured using the function generator and the DSA, and this delay was 15 μs per channel. This delay is relatively small compared with the current sampling rate (maximum 4096

samples/sec) and will be ignored in the analysis. To synchronize the data from the LTDAQ and TRDAQ, the same sampling rate is used for both systems and the signal from the function generator is recorded by both systems as a reference channel. The reference channel data are then used to correct the time difference between two data acquisition systems.

The multifunction A/D board is controlled with a program written in *LabView*®. *LabView*® is a software package that consists of subroutines for system control, data acquisition, memory allocation for buffering, and data storage. To achieve continuous high-speed sampling and to retain the highest accuracy of the system, the signals are scanned and stored continuously to hard disk in binary format during the test. Another program was developed to display and convert the data to ASCII format after the test, which can be manipulated by subsequent data processing programs. A high performance PC with a high-speed processor and hard drive is used to manage the LTDAQ and store the data. Currently, the 8 channels of the LTDAQ are connected to five pore pressure transducers, the function generator, and two geophones. The two geophones are those at the center of the array (case 5) that could not be recorded by the TRDAQ because of channel limitations. It should be noted that the capacity of the LTDAQ can be expanded relatively easily at low cost.

6.9.3 Synchronization of TRDAQ and LTDAQ

Because the NI PCI-6035 has no analog triggering function, the LTDAQ must begin recording before vibration. Therefore, the data recorded by the

TRDAQ and LTDAQ start at different times and it is difficult to synchronize the data. To correct this problem, an A/D board with an analog trigger and a pre-trigger delay is required. An alternative is to record the same signal with both systems at the same sampling rate and use this channel as a reference signal.

Because the signal generated by the function generator that drives the vibroseis is a pure sine wave with a constant amplitude, it is ideal for the reference channel. The time difference between the two DAQ systems is determined by comparing the first peak of the sine wave produced by the function generator. Using this time difference, the data from the LTDAQ can be shifted to match the TRDAQ time scale. This procedure has been programmed in a *MathCad*® worksheet.

6.10 SUMMARY

This chapter describes in detail the instrumentation used in the in situ dynamic liquefaction test. The instrumentation framework for the dynamic liquefaction test was presented in Section 6.2. A summary of the sensors and data acquisition systems is also presented here.

To monitor the coupled response between the particle motion in the soil and the pore water pressure generation, a new sensor was developed called the liquefaction sensor. The liquefaction sensor consists of two perpendicularly oriented geophones, which monitor horizontal and vertical particle velocities, and a miniature pore pressure transducer. All three sensors are epoxied in an acrylic

case for waterproofing and protection. Details regarding the development of the liquefaction sensor and its accessories are presented in Sections 6.3 through 6.5.

Two 28-Hz geophones are used in each liquefaction sensor. The geophones were calibrated in the acrylic case before being used in the field. The calibration procedure for the geophones was presented in Section 6.3.2, followed by a description of the implementation of the full calibration spectrum in the velocity measurement.

Pore pressure transducers and piezometers were discussed in Section 6.4. The issues regarding saturation of the pore pressure transducer are addressed in Section 6.4.1. A partially saturated pore pressure transducer will result in a time delay and smaller magnitudes being measured. The saturation procedure for the miniature pore pressure transducer in the liquefaction sensor is presented in Section 6.4.4. Miniature pore pressure transducers (Drucker PDCR-81 and Entran EPX-V01) were integrated in the liquefaction sensors because of their small size and their easy saturation.

The accelerometers used to monitor the surface acceleration and footing response were discussed in Section 6.6. The small-strain seismic testing equipment for crosshole S_{hv}-wave and P-wave velocity measurements were described in Section 6.7. A new testing configuration for evaluating saturation of the reconstituted test pit was also presented. A push-in P-wave velocity measurement receiver was developed for this purpose. In addition, a description of the settlement platform and the in situ density measurement tool were presented in Section 6.8.

Two data acquisition systems, the transient response data acquisition system (TRDAQ) and the long-term data acquisition system (LTDAQ), were employed in this research for different purposes and different sensors. The main component of the TRDAQ is a dynamic signal analyzer that served for recording short periods of data without a time skew. The TRDAQ is connected to the geophones at the four nodes of the array. The LTDAQ is a computer-based high speed data acquisition system consisting of a personal computer, an A/D board, and *LabView*® software. The LTDAQ is connected to the pore pressure transducers and two of the geophones. Both systems were operated at the same sampling rate for future synchronization and data analyses. The technique for synchronization of the two systems was presented in Section 6.9.3.

Chapter 7. Field Test Setup and Data Reduction

7.1 INTRODUCTION

The proposed in situ dynamic liquefaction test was used to dynamically load reconstituted test specimens located near the ground surface. This chapter provides the details regarding the testing procedure and the sample preparation process for the reconstituted test specimens. Additionally, the Capital Aggregates test site is described in detail and the soil properties of both the reconstituted test specimens and the native soil are presented.

The data reduction procedures using the data analysis algorithms presented in Chapter 5 are also presented here. Specifically, the implementation of these data analysis algorithms in processing the collected data to evaluate the induced shear strains and the excess pore pressures are addressed. Based on the proposed procedures, several programs for data analysis are developed using the *Mathcad*® software. The programs are used to both process and present the collected data.

7.2 DESCRIPTION OF TEST SITE

All tests presented in this dissertation were performed at the Capital Aggregates test site in Austin, Texas. This test site was selected for many reasons. First, the Capital Aggregates test site is located close to the campus of UT and has

easy access due to the courtesy of the managers of Capital Aggregates, Inc. Second, the site has been used by previous researchers (e.g., Kalinski 1998, Phillips 2000, Axtell 2001, and Chen 2001) from the Geotechnical Engineering Group at UT. The relative locations of the research experiments conducted at the Capital Aggregates test site are shown in Figure 7-1. The area encompassed by these research sites is approximately 1000 m^2. The geologic stratigraphy and associated soil properties of the subsoil at this site have been thoroughly investigated by these researchers.

7.2.1 Geologic profile of the test site

The Capital Aggregates test site is located in a flood plain of the Colorado River at east Austin. Historical aerial photographs reveal that 8.8 m of overburden soil have been removed from the test location over the past 30 years (Axtell 2001). The current test location is located on a peninsula. The ground water table is at a depth of about 2.1 m (7 ft) below the current ground surface. The top 0.6 m (2 ft) of soil is a desiccated crust layer containing sand and some traces of gravel. Below the desiccated crust layer is a poorly-graded clean sand.

Although no sample has been retrieved below 1.5 m (5 ft) at the test site, field observations from the excavated slopes and nearby excavations indicate that the thickness of the poorly-graded sand layer is greater than 4.5 m (15 ft) below the current ground surface. The field vibration test results presented in Chapter 3 show low shear wave velocities to at least 7.5 m, indicating that the poorly-graded sand layer may extend to at least this depth.

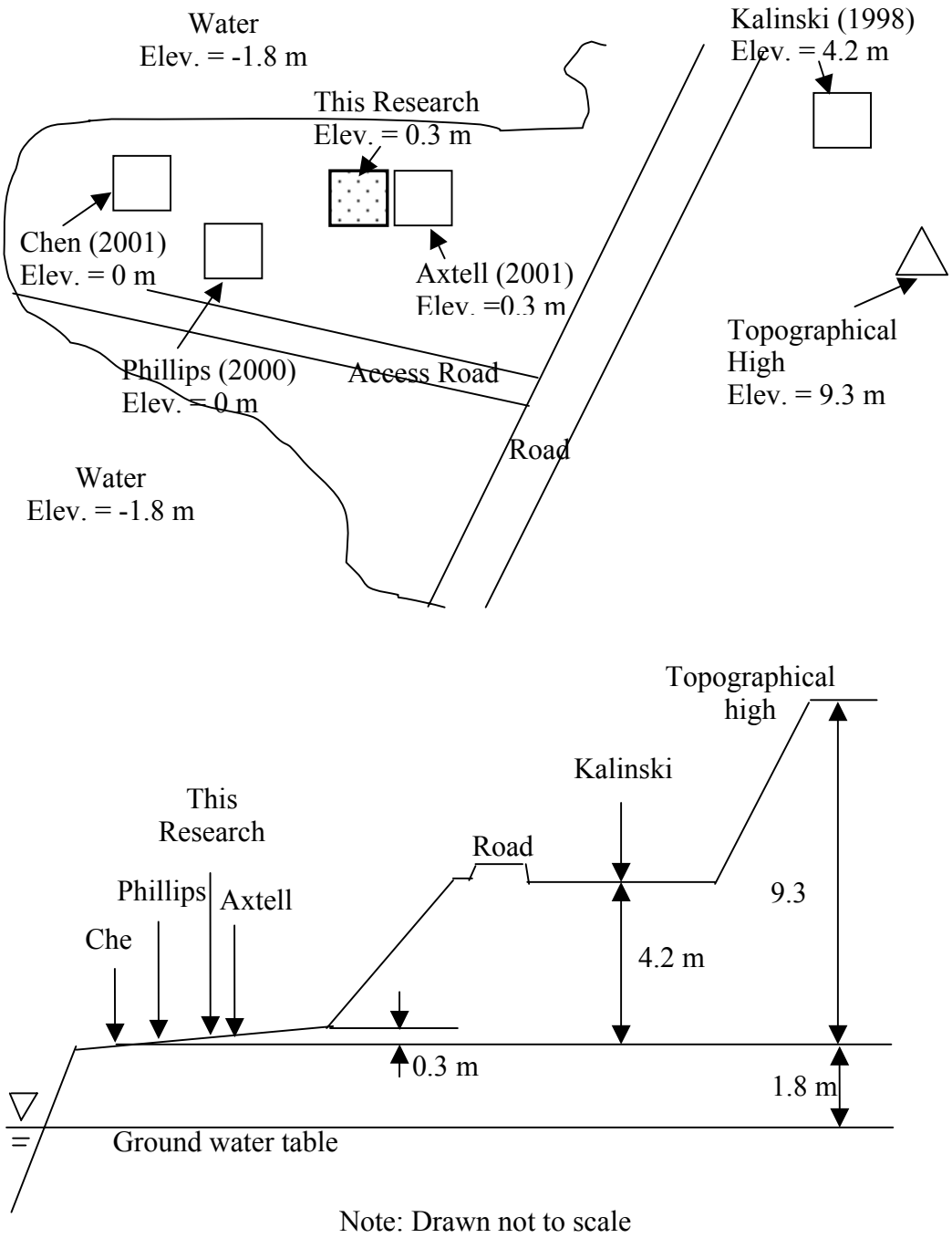

Figure 7-1 Relative locations of tests conducted at Capital Aggregates site (modified from Chen 2001)

7.2.2 Properties of the native soil

Based on the geologic profile, the main stratum at the Capital Aggregates test site is a poorly-graded clean sand. The engineering properties of the native soil between the desiccated crust and the ground water table, as reported by Axtell (2001), are listed in Table 7-1. The dry unit weight, water content, and void ratio were measured in the field using a hand-carved sample obtained from a depth between 0.6 to 0.9 m. The shear wave velocity was measured using embedded geophones at 0.75 m from the ground surface. The Poisson's ratio was calculated from the V_p and V_s measured in the field.

Table 7-1 Native soil properties at the Capital Aggregates test site (Axtell 2001)

Soil Property	**Value**	**Sample Depth from Surface (m)**
Dry unit weight	1.67 ton/m^3 (104.5 pcf)	0.6-0.9 m (2-3 ft)
Total unit weight	1.72 ton/m^3 (107.3 pcf)	0.6-0.9 m (2-3 ft)
Average water content, w	2.5%	0.6-0.9 m (2-3 ft)
Degree of saturation	12%	0.6-0.9 m (2-3 ft)
Void ratio	0.6	0.6-0.9 m (2-3 ft)
USCS classification	SP	0.6-0.9 m (2-3 ft)
Specific gravity, G_s	2.68	0.6-0.9 m (2-3 ft)
Fines content	4.6%	0.6-0.9 m (2-3 ft)
S-wave velocity	195 m/sec (650 ft/s)	0.3 m (1 ft)
Poisson's ratio	0.24	0.75 m (2.5 ft)

The grain size distribution curve of the poorly-graded clean sand is shown in Figure 7-2. The USCS classification is SP and the sand has less than 5% fines content. The effective particle size, D_{10}, of the poorly-graded sand is 0.1 mm, the uniformity coefficient, $C_u = \frac{D_{60}}{D_{10}}$ (where D_{60}, D_{10} are particle sizes with 60% and 10% passing, respectively), is 3.7, and the coefficient of gradation, $C_c = \frac{D_{30}^2}{D_{10} D_{60}}$ (where D_{30} is particle size with 30% passing), is 1.6. Axtell (2001) reported that cementation exists in the poorly-graded clean sand based on the surrounding steep slopes and the competency of the undisturbed sample obtained. The test location for this research is only 3.3 m (11 ft) away from the test location used by Axtell (2001), so the properties of the native soil should be similar.

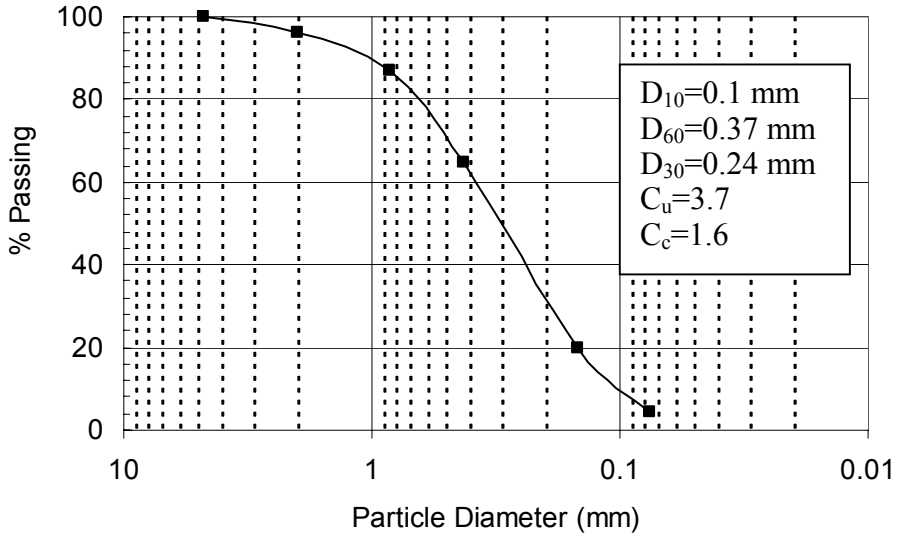

Figure 7-2 Grain size distribution of the poorly-graded, clean sand at Capital Aggregates test site

7.2.3 Properties of the reconstituted test specimen

The material used to build the reconstituted test specimens is a clean aggregate sand that is used in ready-mix concrete. This aggregate sand was provided by Capital Aggregates. The sand obtained from Capital Aggregates was excavated from a quarry close to the test site, so it should have a similar composition as the native soils at the test site. The physical properties of the aggregate sand are given in Table 7-2. The maximum and minimum void ratios are 0.64 and 0.43, respectively. The aggregate sand is classified as an SP material in the USCS classification system. The fines content is less than 0.5%.

Table 7-2 Soil properties for the reconstituted test specimen

Soil Property	Value	Test Method
Specific gravity	2.68	ASTM D854-98
Minimum dry density	1.63 ton/m^3 (102 pcf)	ASTM D4254-00
Maximum dry density	1.87ton/m^3 (117 pcf)	ASTM D4253-00
Maximum void ratio	0.64	ASTM D4254-00
Minimum void ratio	0.43	ASTM D4253-00
USCS classification	SP	ASTM D-2487-00
Fines content	0.43%	ASTM C-136-01

The grain size distribution of the aggregate sand, along with the grain size distribution of the native soil, are shown in Figure 7-3. The effective particle size (D_{10}) of the aggregate sand is 0.21 mm, the uniformity coefficient (C_u) is 3.6, and the coefficient of gradation (C_c) is 1.0. The aggregate sand, which is used for ready-mixed concrete, is coarser than the native soil because the fines had been removed.

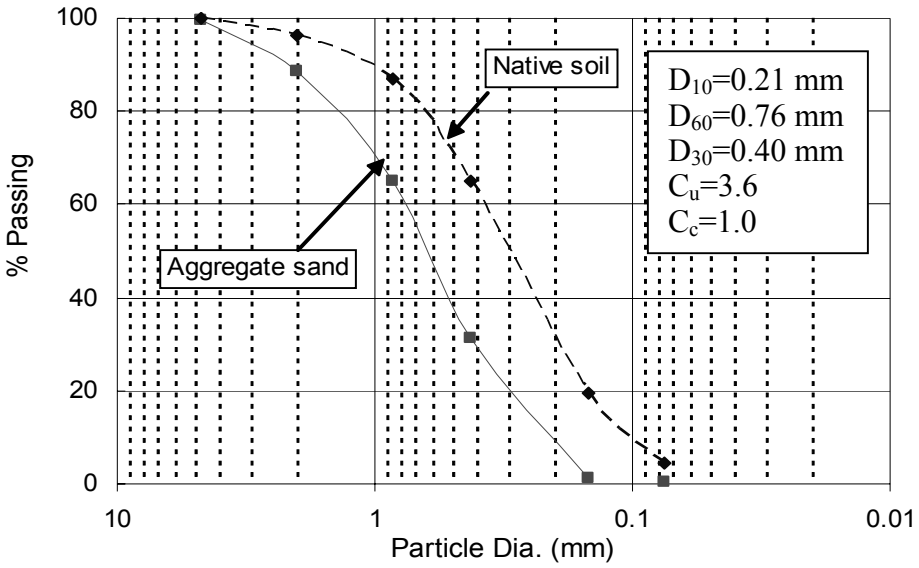

Figure 7-3 Grain size distribution of the native soil and the test specimen aggregate sand

7.3 PREPARATION OF RECONSTITUTED TEST SPECIMEN

Previous research (e.g., Ladd 1974, Mulilis et al. 1977) has shown that the method of sample preparation affects the liquefaction resistance of reconstituted specimens. A sample preparation method that creates the most liquefiable specimen, while still mimicking typical depositional processes, is preferred. Additionally, the specimen preparation method needs to be applicable and repeatable in the field. Other factors regarding the saturation and uniformity of the specimen need also to be taken into account.

Mulilis et al. (1977) investigated the effects of sample preparation on the liquefaction of sand and concluded that for specimens with the same relative

density, specimens prepared by air pluviation showed the lowest cyclic stress resistance (Figure 7-4). Ideally, pluviation through air would be the top candidate for sample preparation because it produces specimens with the lowest liquefaction resistance. However, it would be impossible to fully saturate dry specimens prepared by air pluviation in the field. Water pluviation also provides specimens with low liquefaction resistance (Figure 7-4), and water sedimentation is similar to the alluvial depositional process that creates liquefiable soil deposits in the field. Water sedimentation also allows saturated specimens to be constructed in the field. As a result, this sample preparation procedure was used in this research. Details regarding this sample preparation procedure are described in Section 7.3.2.

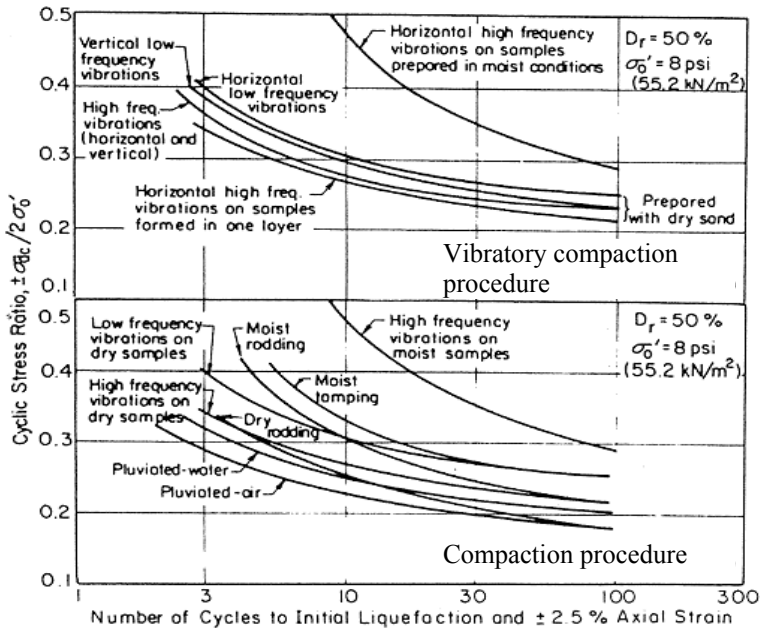

Figure 7-4 Variation of cyclic stress resistance for different sample preparation methods (Mulilis et al. 1977)

7.3.1 Preparation of test pit

The reconstituted test specimens were prepared in a test pit. The test pit configuration is shown again in Figure 7-5 for reference. The test pit is a near cubic hole, about 1.2 m (4 ft) on each side. Because the test pit was excavated using a backhoe, one side of the pit is not vertical. A piece of plywood was placed along this side of the pit and the space behind it backfilled with sand. The other three faces of the test pit were hand-carved to make them as smooth as possible. Because the ground water table is about 1 m (3 ft) below the bottom of the pit, an impermeable liner was placed within the pit to keep water from seeping out of the test specimen. A PVC pipe was placed at the side of the pit furthest from the loading footing to monitor the water level inside the pit and to provide casing for the crosshole source.

To estimate the initial density of the reconstituted test specimen, the volume of the test pit is needed. The volume of the pit was measured by measuring the volume of water needed to fill the test pit. After the pit was filled with water to a height that corresponded to a volume of 1.73 m^3 (64 ft^3), the water level elevation was marked on the liner. At this point, the elevation of the bottom of the pit, the desired height of the specimen, and the ground surface also were measured using an optical level (Nikon AP-3) and a level rod (Mound City SVR-25).

To install the sensors at specific locations that were aligned vertically, the planned horizontal locations of the liquefaction sensors were marked using 3 wires stretched across the test pit (Figure 7-6). The three wires were tied to steel

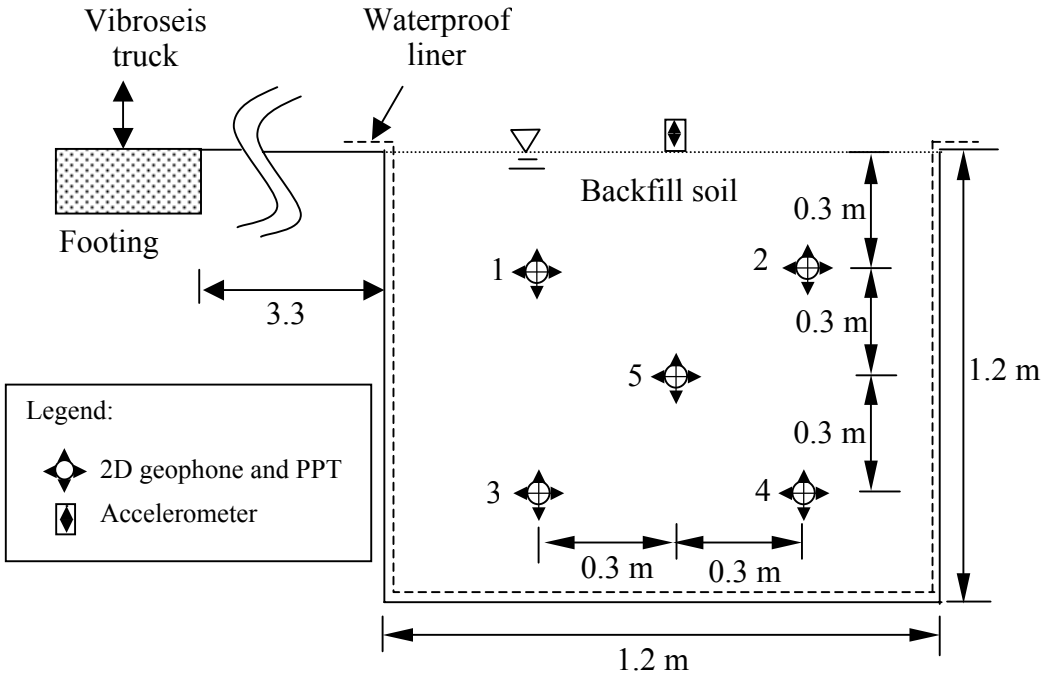

Figure 7-5 Schematic illustration of test pit

posts embedded in the soil outside the test pit and the intersections of these wires indicated the locations of the geophones. The liquefaction sensors were installed along the center line of the specimen to minimize boundary effects. Preparation of the test pit is shown in Figure 7-6. Although all of the reconstituted test specimens were prepared in the same test pit, the volume of the pit was measured each time before preparation of a new specimen, to avoid any error due to deformations of the pit.

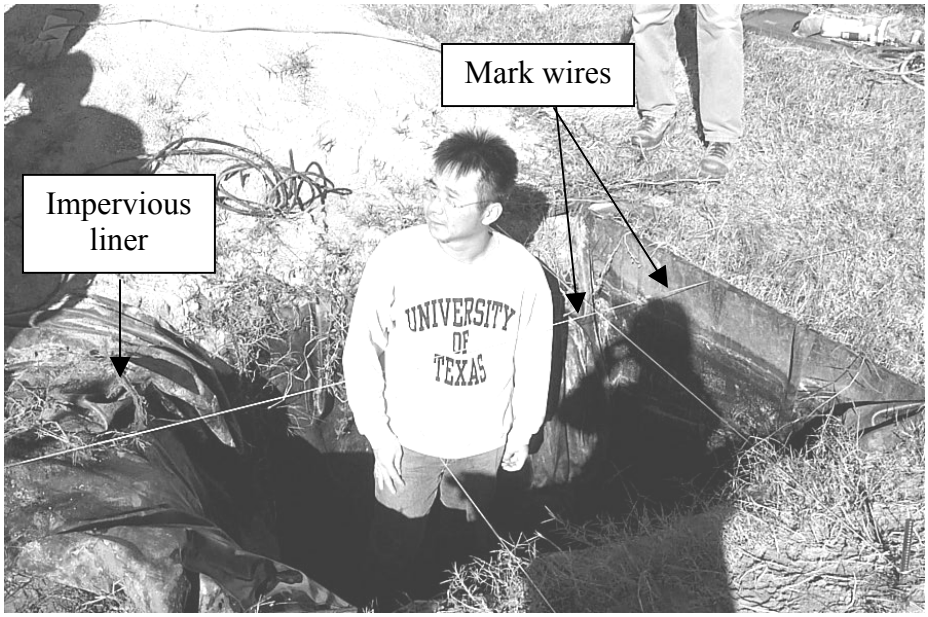

Figure 7-6 Photograph of preparation of test pit

7.3.2 Preparation procedure for reconstituted test specimens

As mentioned before, water pluviation was used to prepare the test specimens. In preparing specimens, the objective is to build loose, uniform, saturated specimens with a known saturated density. First, about 30 cm (1 ft) of water was pumped into the test pit. Throughout sample preparation, the water level was maintained about 30 cm (1ft) above the top of the backfilled sand. The water in the pit allows for water pluviation and minimizes the air trapped in the specimen. The water also allows the sensors to be submerged during the installation process. The water pluviation procedure is schematically shown in Figure 7-7.

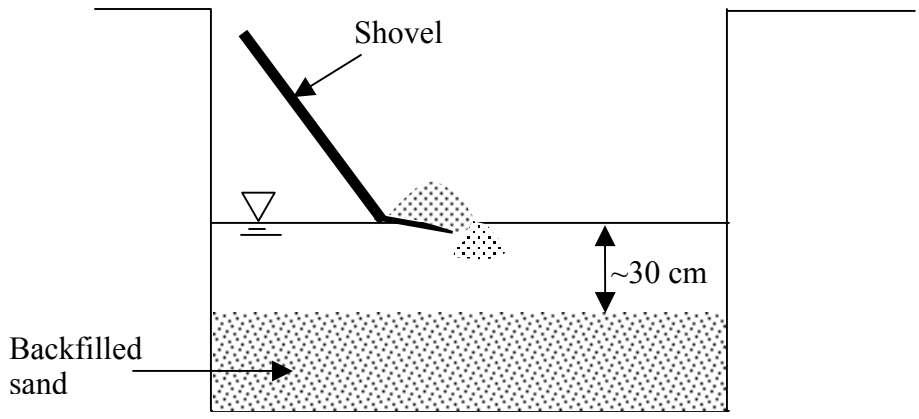

Figure 7-7 Schematic of water pluviation procedure

To start filling the test pit, about 50 kg of air-dried aggregate sand is placed on an electronic scale for weighing. This allows the weight of soil placed in the test pit to be tracked. Samples for water content measurement of the air-dried sand were taken periodically or when a significant moisture change was observed. These samples were sealed in individual plastic bags and weighed in the field. Later, these samples were oven dried in the laboratory for 24 hours to measure the water content. By tracking the total weight and water content of the sand placed in the test pit, specimen properties such as saturated unit weight, void ratio, and saturated water content could be estimated.

After each batch of sand was weighed, it was placed in a container and thoroughly mixed with a large amount of water. This mixing removed air bubbles and produced a nearly saturated condition. The water-sand mixture was then

gently placed inside the test pit and allowed to sediment through the water. A uniform specimen was achieved by maintaining an approximately constant height of water through which the soil was pluviated.

The elevation of the top of the backfilled sand was monitored regularly using optical leveling equipment. When the backfilled sand reached a desired sensor elevation, the backfilling process was halted for sensor installation. Detailed descriptions of the sensor installation process are presented in the next section. Soil placement continued until the soil reached the height indicated on the side of the liner. At this point, the excess water was removed from the surface. A finished reconstituted test specimen is shown in Figure 7-8. To reduce evaporation, a tarp was placed over the entire specimen. Initial testing was performed on specimens that were similar to that shown in Figure 7-8. However, later tests included an approximately 1-m thick layer of dry sand over the saturated test specimen. This sand layer increased the stresses in the test specimen.

7.3.3 Sensor installation

Careful sensor installation is critical to the accurate measurement of data during the in situ dynamic liquefaction test. To implement the strain calculation methods presented in Chapter 5, the liquefaction sensors must be placed at specific locations with specific orientations. Also, the pore pressure transducers in the liquefaction sensors must be submerged during the installation process to

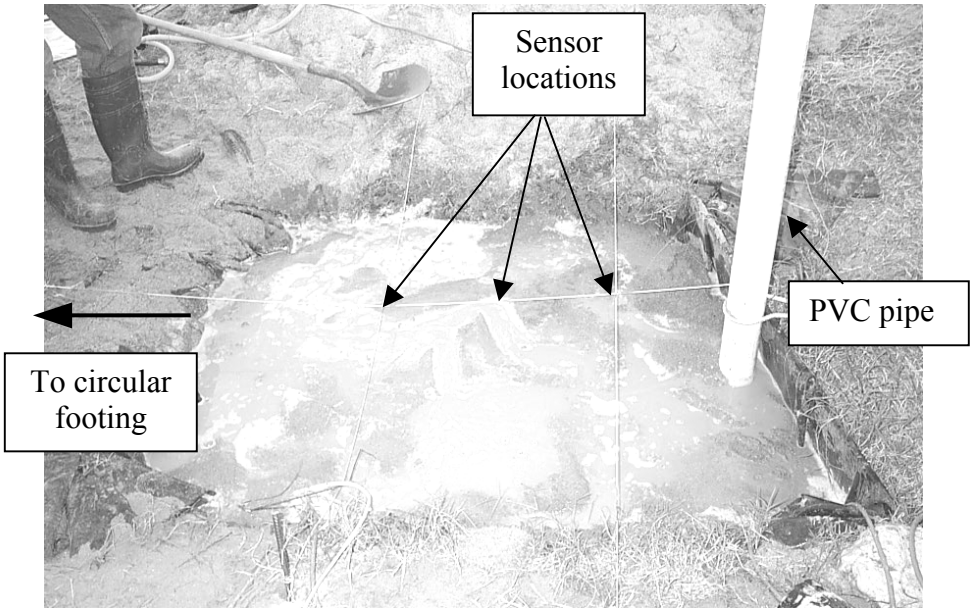

Figure 7-8 Photograph of finished reconstituted test specimen

maintain saturation. In addition, the verticality of the settlement platforms must be assured for accurate measurement of vertical settlement.

When the test pit was filled to about 30 cm (1 ft) above the bottom of the pit, liquefaction sensors case 3 and case 4 (Figure 7-5) were installed. First, the exact elevation of the sensor was measured using the optical level. Then, the placement tool, illustrated in Figure 6-14, was connected to the sensor while it was still covered with a plastic bag and submerged in a bucket. A container filled with water was used to maintain the submerged condition of the liquefaction sensor during transport from the bucket to the test pit. The liquefaction sensor was then placed below the water table in the test pit and the plastic bag was removed.

The sensor was placed on the sand surface at a location below the point indicated by the cross wires and the shoe at the bottom of the sensor was pushed into the sand. The orientation of the sensor was checked from the line on the rod of the placement tool. The verticality of the sensor was verified through the two tilt switches on the placement tool. Some saturated sand was placed around the sensor to stabilize and embed it. When the entire sensor was well surrounded by saturated sand, the placement tool was detached from the sensor and removed from the specimen. All the liquefaction sensors were installed using this procedure.

The settlement platforms were installed near the side of the specimen at approximately same elevations as the liquefaction sensors, as well as at the top of the specimen (Figure 7-9). The verticality of the extended rod of the settlement platforms was verified using the optical level. The elevation of the top of the extended rod was measured at the time of installation and after the specimen was constructed to estimate the settlement that occurred during the sample preparation process. Generally, the settlements due to sample preparation were smaller than the resolution of the level rod (0.3 cm), and therefore, were neglected.

7.4 TESTING PROCEDURE

The developed dynamic liquefaction test measures the liquefaction characteristics of the soil in terms of the shear strain amplitude and the excess pore water pressure ratio for a specific number of loading cycles. To establish this relationship using the reconstituted test specimen, the testing procedure started

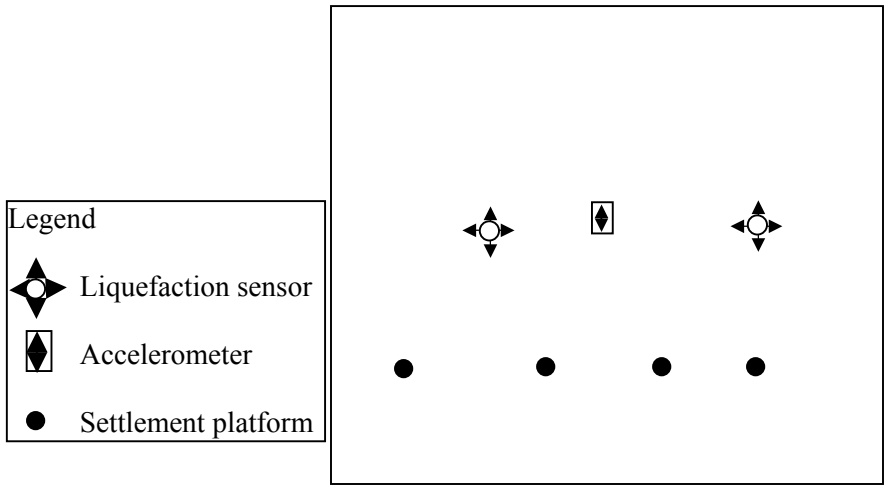

(a) Plan view of locations of settlement platforms

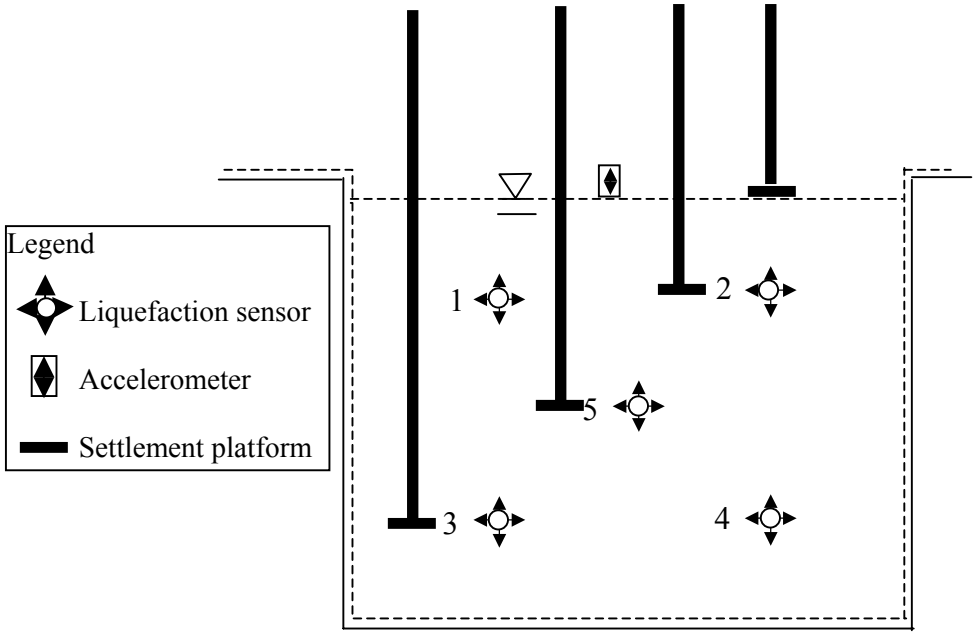

(b) Cross section of locations of settlement platforms

Figure 7-9 Relative locations of settlement platforms

from a small shear strain level and gradually increased to larger shear strain levels. The testing procedure is shown schematically in Figure 7-10 and described as follows:

1. Crosshole tests were performed using the embedded sensors as receivers and the crosshole source described in Chapter 6. These tests were used to characterize the soil properties and to verify the saturation of the specimen. During this testing, the vibroseis was turned off to reduce noise. The elevations of the settlement platforms and the elevation of the overburden were measured using an optical level.
2. A 89-kN (20 kips) static load was applied to the circular footing. The same static load was used for all tests. The static load ensures that all of the applied force is compressive.
3. A 20-Hz sine wave was sent to the vibroseis to vibrate the footing for a specific number of cycles. For the first loading, only a small voltage is applied. The small vibration has two functions. First, it provides a chance to check the integrity of the instrumentation system. Second, it provides information regarding the relationship between the input voltage level and the induced shear strain amplitude. Generally, the induced shear strain level for the first test was about 10^{-4}%, which ensures no excess pore pressure generation and no significant change in the specimen properties

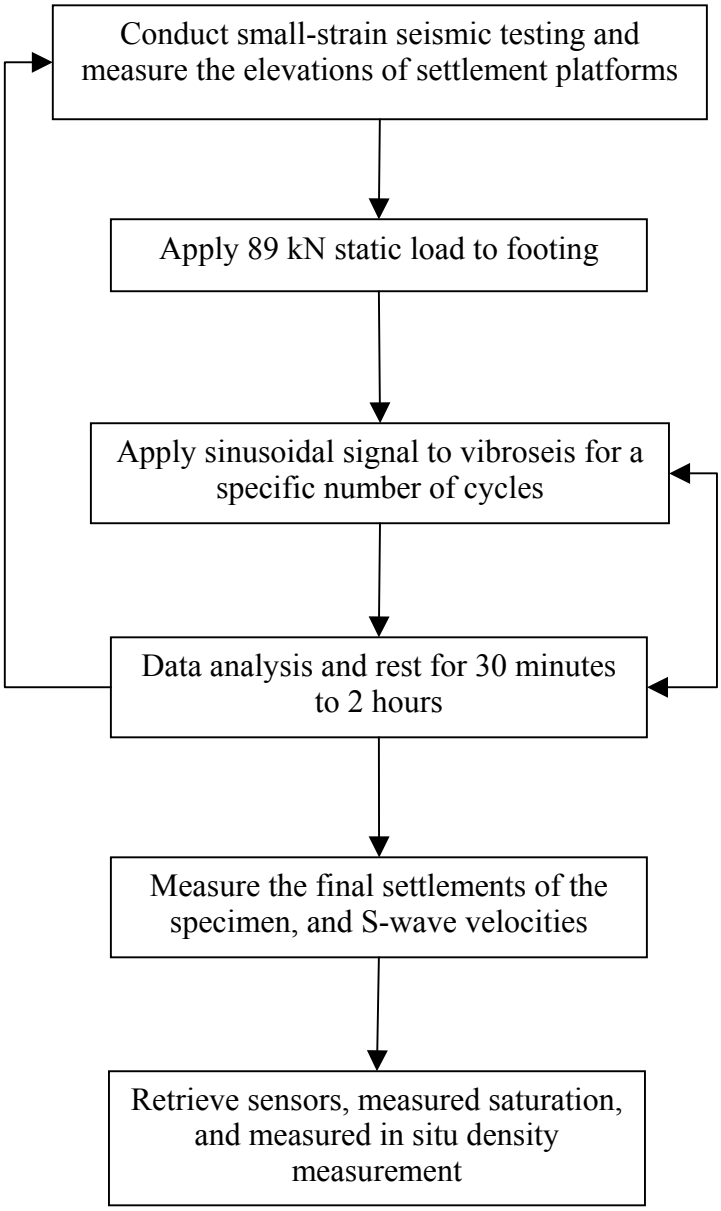

Figure 7-10 Flowchart of liquefaction test procedure

4. The vibroseis was turned off and the test was halted for a certain time period to allow any generated excess pore pressures to dissipate. The length of the time period was chosen based on the magnitude of the generated excess pore pressure. During this rest time, the collected data were analyzed and the induced shear strain amplitude and the excess pore pressure ratio were calculated. The induced shear strain amplitude was used to determine the next loading level.
5. During the rest period, after any excess pore water pressure had dissipated, the elevations of the settlement platforms were recorded. Also, crosshole tests for S-wave velocity measurements were performed to characterize any change in the specimen.
6. Loading increments were increased until the induced shear strain was near the conventional threshold strain (i.e., $\gamma = 10^{-2}\%$) , At this point, the output voltage was set to the maximum value for the vibroseis (e.g., 89 kN for the current vibroseis) for the next loading to induce the largest shear strain amplitude and the largest excess pore pressure.
7. After any excess pore water pressure had dissipated from this final loading, the final elevations of the settlement platforms were recorded. Also, crosshole tests for S-wave velocity measurements were performed to characterize the final shear wave velocity of the specimen.
8. After removal of the overburden sand, saturation was verified using the P-wave velocity measurements as described in Section 6.7.2.

These measurements were performed at several locations within the test pit. Finally, during the sensor retrieval process, in situ density measurements were conducted at different elevations. These data were used to verify the estimated soil properties from the specimen preparation procedure.

7.5 DATA REDUCTION PROCEDURES

In principal, the data reduction procedures are closely related to the design of the instrumentation. For the developed in situ liquefaction testing technique, the two principal measured properties are the induced particle motion and the generated excess pore water pressure. The instrumentation systems are designed to record the real-time measurement of these two properties. The data reduction procedures are developed to calculate the induced shear strain and excess pore water pressure ratio in the time domain. The liquefaction characteristics, as expressed by the induced shear strain and the generated excess pore water pressure ratio for a specific number of cycles, are established by compiling these two data types. The relationship between pore pressure ratio and shear strain for a specific number of cycles is called a pore pressure generation curve.

Because the measurements of particle motion and pore pressure are recorded by two separate data acquisition systems, as described in Chapter 6, the data reduction processes for these data are different. A flowchart describing the separate data reduction procedures is shown in Figure 7-11.

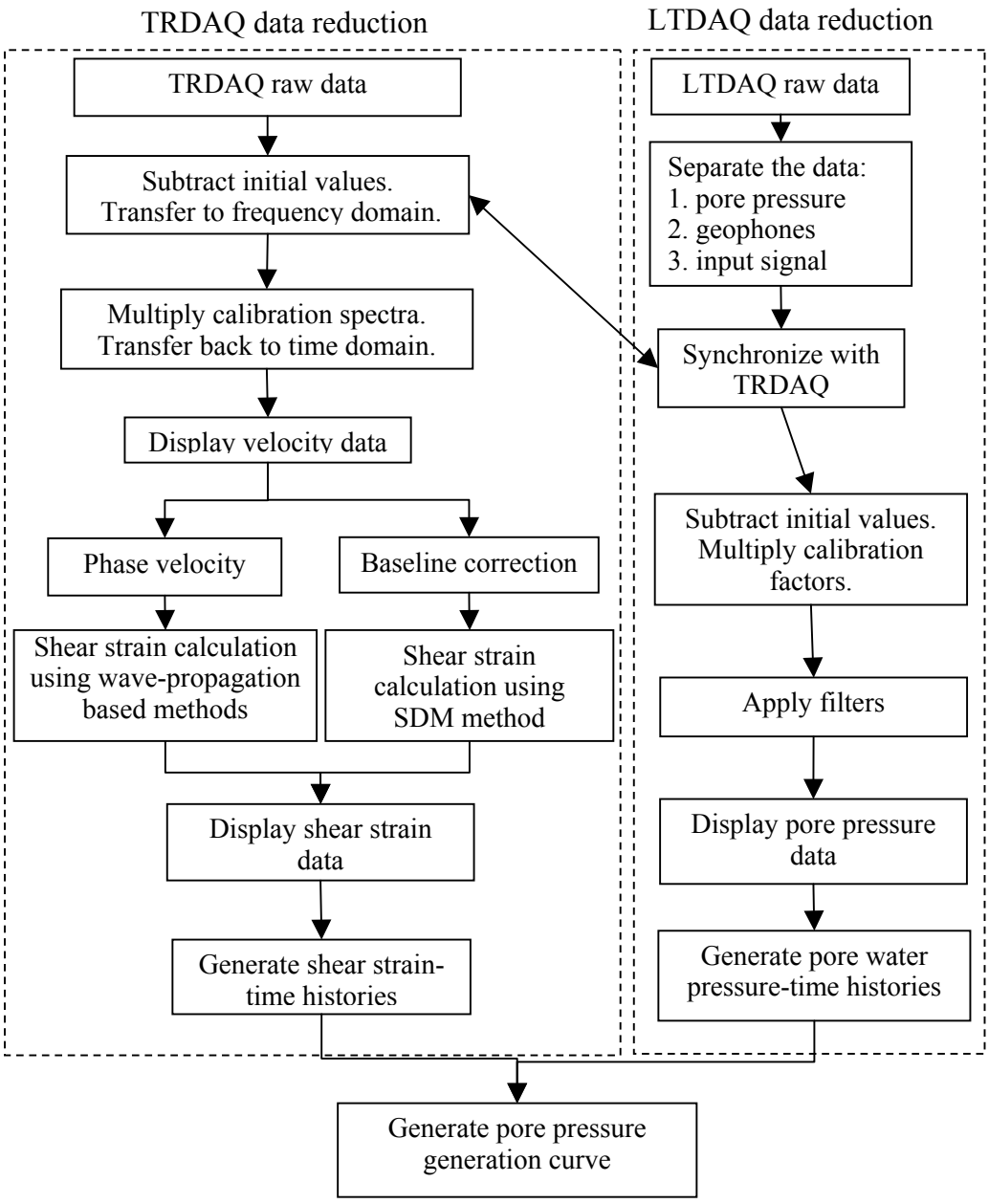

Figure 7-11 Flowchart for the data reduction procedures

Four programs have been developed to process the collected data using the data analysis algorithms presented in Chapter 5. These programs not only process the data, but also display the processed data and generate output files for plotting. Using these programs, the data analysis can be quickly completed in the field and the previous test results can be used to adjust the next test.

Three of the four programs are written in *MathCad*® worksheets. *MathCad*® is a symbolic calculation software, where the programming processes are similar to writing mathematical equations. *MathCad*® also provides many useful functions, such as FFT, IFFT, and polynomial fitting, which are used in the data reduction process. These built-in functions make the data analysis and signal processing quick and easy. Also, the results can be displayed using built in graphics functions. The display function is important in the field because the accuracy and quality of the collected data can be quickly checked. The reduced data are used to determine the next loading level for testing. Another program was written in Fortran to extract data recorded by the TRDAQ. The Fortran program is used for quick computation and it can easily handle formatted input and output.

7.5.1 TRDAQ data reduction

Shear strains are calculated from the particle velocities recorded by the geophones in the liquefaction sensors. The particle velocities used in the shear strain calculation were collected by the TRDAQ. The raw data were downloaded from the multichannel DSA and converted to ASCII format. Next, the initial values caused by noise were subtracted from the raw data and these time domain

velocity signals were transferred to the frequency domain using the fast Fourier transform (FFT) algorithm. No zero-padding is required for the geophone data recorded by the DSA because the DSA always records a power of two data points. The multiplication of the calibration factors was accomplished in the frequency domain using the modified calibration spectrum discussed in Section 6.3.3. The velocity Fourier spectra provide information regarding the dominant frequency of vibration and the relative amplitudes of other frequencies of vibration, which are useful in assessing the quality of the measured data. After calibration, the velocity spectra were transferred back to the time domain using the inverse fast Fourier transform (IFFT) algorithm.

The velocity-time histories were displayed both in the time and frequency domains for preliminary assessment of the data. The apparent phase velocity between sensors at the same elevation was calculated from cross-spectral analysis, as described in Section 5.2.2.4. The obtained apparent phase velocities were used to calculate the shear strain-time histories using the apparent wave (AW) method. The shear wave velocities measured by the crosshole tests were used to calculate the shear strain-time histories by means of the plane shear wave (PSW) method. The Rayleigh wave velocity of the native soil measured in the vibration tests presented in Chapter 3 were used to calculate shear strains in the plane Rayleigh wave (PRW) method.

After being transferred back to the time domain, the velocity-time histories were numerically integrated to displacement-time histories and a baseline correction was applied. The corrected displacement-time histories were

used in the SDM method to calculate shear strain-time histories. The shear strain-time histories calculated by the SDM method were displayed and the mean shear strain amplitude was calculated. Also, a data file was generated and saved for plotting using other software.

Two programs were developed in *MathCad*® for this part of the data processing. The first program was developed to calculate the shear strain-time histories using the SDM method. The second program was developed to calculate the shear strain-time histories using the wave propagation-based methods.

7.5.2 LTDAQ data reduction

The pore water pressure data were recorded by the LTDAQ with the same sampling rate as the DSA, but the recording length was much longer. Due to the long recording length, the data are too big to be edited by any conventional text editors. To process the long pore pressure records, the size of the raw data is reduced by extracting evenly spaced data at a larger sampling interval. The pore pressure data should not be affected by increasing the sampling interval because the dominant frequency in the data is 20 Hz, which does not require the sampling rate of 8192 samples/sec used by the DSA and LTDAQ. The geophone and function generator data are extracted at the same sampling rate that they were collected, but the duration is much shorter than the pore pressure signals because they only produce signals during dynamic loading. A Fortran program was developed for this purpose. The functions of the program include reducing the sampling frequency, dividing data, and extracting a specific time length.

The Fortran program divides the raw data into three files. These files are for the function generator, the pore pressure transducer, and the geophone signals. The function generator signal is extracted at the recorded sampling frequency for at least 4 seconds or until the arrival of the 10th peak of the sinusoidal signal. The time difference between the DSA and LTDAQ is determined from the arrival time of the first peak from the function generator in each recording. The time difference is then used to synchronize the pore pressure transducer data with the particle velocity data. A *MathCad*® worksheet was developed to calculate the time difference, shift the pore pressure data and geophone data to the same time scale as the DSA data, and pad zeros at the end of the PPT data for the FFT calculation.

This research is interested in the excess pore water pressure generated by dynamic loading, therefore the initial hydrostatic pore pressure is subtracted from the recordings. The calibration factors then are multiplied to each PPT in the time domain. The excess pore pressure data are then transferred to the frequency domain for filtering.

Three types of filters are implemented to highlight the different frequency components in the excess pore pressure data. To highlight the residual pore water pressure at the end of dynamic loading, a low-pass filter with a cutoff frequency of 2-Hz is applied to the pore pressure data. The low-pass filter eliminates the hydrodynamic pore pressure, as well as any noise above 2 Hz. The peak of the residual pore pressure is used to calculate the excess pore pressure ratio for the pore pressure generation curve. To highlight the hydrodynamic pore pressure, a

band-pass filter with a frequency range of 15-25 Hz is used. The band-pass filter removes the residual pore pressure, as well as noise outside the bandwidth. To present both the residual and hydrodynamic components, a low-pass filter with a cutoff frequency of 28 Hz is applied to eliminate background noise above 28 Hz. These filters are applied in the frequency domain. The processed signals are transferred back to the time domain after filtering using the IFFT.

A *MathCad*® worksheet was developed to handle the time-corrected pore water pressure data. In addition to the signal processing in the frequency domain, the worksheet also provides data display and generates output data for plotting. This worksheet was also extended to study the pore water pressure dissipation behavior of the specimen.

7.5.3 Pore pressure generation curve

The liquefaction characteristics of the specimen are described by the relationship between the induced shear strain amplitude and the generated excess pore water pressure ratio for a specific number of loading cycles. This relationship is called the pore pressure generation curve. The induced shear strain amplitudes are expressed as mean shear strain amplitudes calculated from the shear strain-time histories. The excess pore water pressure ratios are calculated from the peak residual pore pressures divided by the initial effective vertical stress. The SDM method calculates the shear strain at the center of the array, therefore these data are plotted versus the pore pressure data recorded at the center of the array. For the wave propagation-based methods, shear strain is

calculated at the sensor locations, therefore these data are plotted versus the pore pressure ratio recorded at the appropriate sensor.

7.6 SUMMARY

The specimen preparation and data reduction procedures for the developed in situ dynamic liquefaction test are presented in this chapter. The contents are summarized as follows.

The tests were conducted at the Capital Aggregates test site in Austin, Texas. Previous research conducted at the same site indicates that the site mainly consists of cemented, poorly-graded sand. The S-wave velocity of the native soil at 0.3 m depth is about 195 m/s (650 ft/s). The reconstituted test specimens were constructed with a clean aggregate sand provided by Capital Aggregates.

The sample preparation procedure for the reconstituted test specimens was described in Section 7.3. A test pit with an impervious liner was used to build the test specimens. The reconstituted test specimen was prepared using water pluviation. Embedded sensors were placed at different locations within the test specimen during the sample preparation process. The primary objective of the sample preparation procedure is to prepare a loose, uniform, and saturated specimen.

The test procedure for the in situ dynamic liquefaction test includes staged loading of the test specimen, with the loading level increased in each stage. A main goal of the test is to establish a pore pressure generation curve for the reconstituted test specimen in terms of the induced shear strains and the excess

pore pressure ratios for a specific number of loading cycles. Seismic testing techniques were used to characterize the specimen before and after dynamic loading, as well as to verify saturation. The in situ density of the reconstituted specimen was verified through settlement data and direct in situ density measurements after the test.

The details of the data reduction procedures are presented in Section 7.5. The data from the TRDAQ and The LTDAQ are processed separately. The particle velocity data are processed to obtain the shear strain-time histories. The pore pressure data are manipulated to highlight the residual and hydrodynamic pore pressure responses. The excess pore pressure ratio is calculated from the peak of the residual pore pressure and the initial effective vertical stress. By compiling the induced shear strain levels and the excess pore water pressure ratios for all the tests, the pore pressure generation curve for the specimen is established.

Chapter 8. Results from Initial Test Series

8.1 INTRODUCTION

Three test series have been performed using the proposed in situ dynamic liquefaction test on reconstituted test specimens. This chapter gives an overview of the three test series and presents results from the first test series. Specifically, the labeling system for all test series is introduced, followed by a description of the goals for each test series and the distinctions among the test series. The test results for the initial test series are then presented. The results from subsequent test series are presented in Chapter 9 and 10. Further interpretations and discussions of all of the test results are presented in Chapter 11.

8.2 DESCRIPTION OF FIELD TEST PROGRAM

Three successful test series were performed as part of this research. For each test series, a reconstituted test specimen was prepared by the sample preparation procedure described in Section 7.3, and the staged tests were performed following the testing procedure described in Section 7.4.

The labeling system for the tests conducted in this research is explained in Section 8.2.1. The main goal of each test series is stated in Section 8.2.2. The distinctions between each test series regarding the sensors, sample preparation, and the testing configuration are described in Section 8.2.3

8.2.1 Test series and labeling system

The three test series are named T1, T2, and T3, according to the chronological order that they were performed. In each test series, several dynamic tests were performed to establish the pore pressure generation curve for the reconstituted test specimen. Each test series started from a low dynamic loading level and gradually increased to the largest output load of the vibroseis truck. Each loading within each test series was named according to its chronological order, and this is expressed as an extension after the test series name. For example, the first dynamic loading of test series T1 is expressed as T1-1, the next dynamic loading is T1-2, and so on. A summary of the three test series is tabulated in Table 8-1.

Table 8-1 General information of the three test series

Test series	Number of tests	Date(s)	Goals
T1	T1-1 ~ T1-6	03/08/2001	Verify test method
T2	T2-1 ~ T2-8	01/31/2002 02/01/2002	Validate new sensors and compare shear strain evaluation methods
T3	T3-1~ T3-5	03/13/2002 03/14/2002	Apply larger number of loading cycles

8.2.2 Goals for each test series

The first test series (T1) was used to verify the design of the instrumentation system, establish the data reduction procedures, and evaluate the success of the testing procedure. This test specimen only contained one pore

pressure transducer and 8 geophones. The specimen was dynamically loaded for 20 cycles at a loading frequency of 20 Hz. Because the specimen was prepared near the ground surface and the pore pressure transducer was placed only 0.6 m (2 ft) below the ground surface, the confining pressure was very low (6.4 kPa) at the location of the pore pressure transducer. This provided a unique opportunity to study the pore pressure generation properties of clean sand under very low confining pressures.

The second test series (T2) was tested under more typical confining pressures. This test series incorporated five liquefaction sensors. Each liquefaction sensor includes a horizontal and a vertical geophone and a miniature pore pressure transducer. Dry sand was placed on top of the reconstituted test specimen to increase the confining pressure. This test series was dynamically loaded for 20 cycles at a loading frequency of 20 Hz. The main goals for test series T2 include to: (1) to verify the performance of the liquefaction sensors and the associated data reduction procedures for the new sensors, (2) to induce significant pore pressure generation in the test specimen, (3) to compare the four shear strain evaluation methods using recorded field data, (4) to investigate the degree of saturation of the reconstituted test specimen, and (5) to validate the in situ density calculation using the in situ density measurement tool.

The third test series (T3) was designed to study pore pressure generation patterns and the variation of soil stiffness during a large number of loading cycles. Test series T3 was dynamically loaded for 60 cycles at a loading frequency of 20

Hz. Additionally, the settlement measurement procedure was refined by placing settlement platforms at different depths.

To achieve the desired goals for each test series, minor differences regarding the sensors, the overburden, and the induced number of loading cycles were incorporated. The distinctions among each test series are summarized in Table 8-2. Detailed descriptions of these distinctions are provided in subsequent sections and chapters.

Table 8-2 Summary of test series

	T1	**T2**	**T3**
Sensors	(8) 4.5-Hz geophones (1) push-in piezometer	(5) Liquefaction sensors	(5) Liquefaction sensors
Loading frequency	20 Hz	20 Hz	20 Hz
Number of loading cycles	20	20	up to 60
Overburden	None	~1 m (3 ft)	~1 m (3 ft)
Small-strain seismic testing	None	Yes	Yes
In situ density measurement	None	Yes	None
Settlement platform(s)	No	Top of specimen	Top and inside of specimen

8.3 RESULTS FROM TEST SERIES T1

This section presents the results from the first test series, T1. Because the sensors were installed at locations near the ground surface, the vertical effective stress at the center of the array (i.e., location of PPT) was only 6.4 kPa (0.93 psi). The test results provide unique data to study pore pressure generation behavior

under low confining pressures. Data reduction procedures were developed using the test results from test series T1. Also, many improvements and refinements for the subsequent test series were based on the results from test series T1.

8.3.1 Description of test series T1

The schematic layout for test series T1 is shown in Figure 8-1. Four 2D-geophone cases and a push-in piezometer were used in this test series. The 2D-geophone cases consist of two 4.5-Hz geophones oriented horizontally and vertically. The push-in piezometer described in Section 6.4.3 was installed at the center of the array. No dry sand was placed on top of the specimen to increase the overburden. The depth of the push-in piezometer was approximately 0.6 m (2 ft).

The initial and final physical properties of the reconstituted test specimen for test series T1 are listed in Table 8-3. The aggregate sand was used to prepare the sample. The grain size distribution curve is shown in Figure 7-3. The initial relative density was 38%, which was estimated from the weight of the air-dried aggregate sand placed in the test pit, the water content (4.4%) of the air-dried aggregate sand, the specific gravity (G_s=2.68) of the sand, and the volume of the test pit, assuming the test specimen is saturated. The physical properties after the last dynamic test were estimated from the 4.6 cm (1.8 in) of settlement measured at the top of the specimen. The dynamic loads were applied at a loading frequency of 20 Hz for 1 second. Therefore, 20 cycles of load were applied to the specimen.

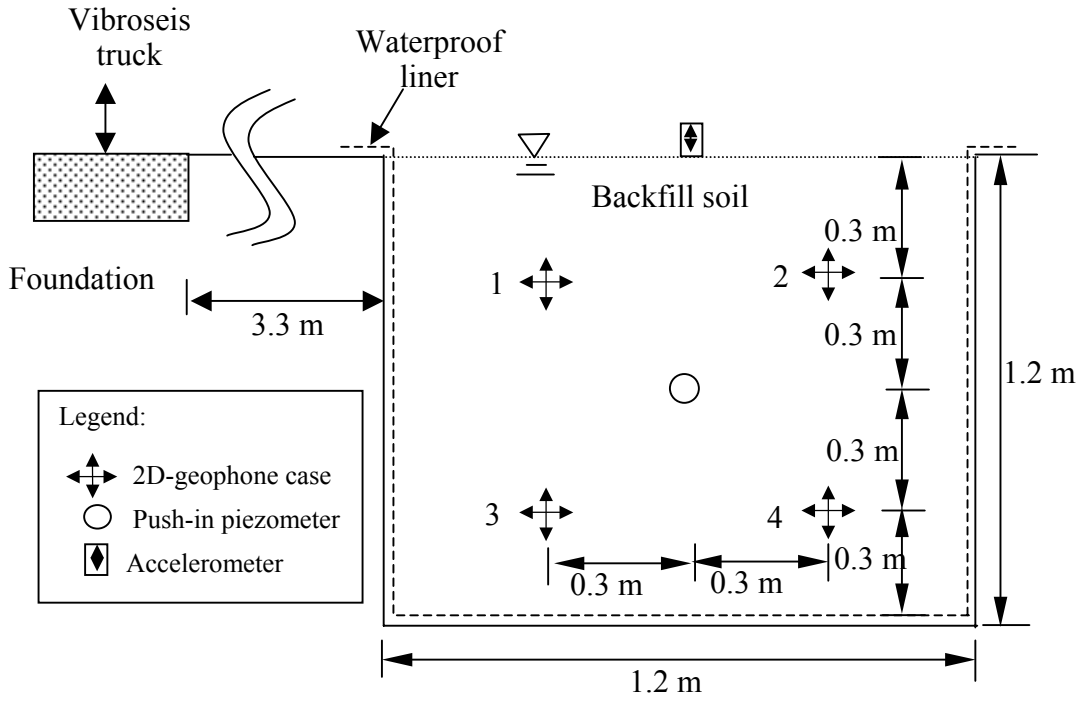

Figure 8-1 Schematic layout of test series T1

Table 8-3 Physical properties of the reconstituted test specimen for test series T1

Soil property		**Value**
Specific gravity (G_s)		2.68
Maximum void ratio (e_{max})		0.64
Minimum void ratio (e_{min})		0.43
Fines content		0.43%
Initial	Relative density (D_r)	38%
	Water content (w)	20.9%
	Total unit weight (γ_t)	20.4 kN/m^3 (129.6 pcf)
Final[(1)]	Relative density (D_r)	65%
	Water content (w)	18.7%
	Total unit weight (γ_t)	20.8 kN/m^3 (132.2 pcf)

Note: [(1)] These values were estimated from the 4.6 cm (1.8 in.) of settlement

8.3.2 Geophone and accelerometer results

The recorded peak particle velocities from the horizontal and vertical geophones for each dynamic loading of test series T1 are summarized in Table 8-4. The reported values are the average of the maximum and minimum values in the time histories. In Table 8-4, the values for H1 represent the peak horizontal velocities measured by the horizontal geophone in case 1 (Figure 8-1). The values for V1 represent the peak vertical velocities measured by the vertical geophone in case 1, and so on. The accelerations measured at the top of the test specimen are also shown in Table 8-4. The maximum recorded vertical surface acceleration was 0.22 g and occurred during dynamic test T1-6.

Table 8-4 Summary of the recorded peak particle velocities and surface accelerations for test series T1

Test #	H1 (cm/s)	V1 (cm/s)	H2 (cm/s)	V2 (cm/s)	H3 (cm/s)	V3 (cm/s)	H4 (cm/s)	V4 (cm/s)	a_{max} (1) (g)
T1-1	0.05	0.06	0.04	0.07	0.02	0.06	0.02	0.06	0.01
T1-2	0.08	0.12	0.07	0.12	0.03	0.11	0.03	0.11	0.02
T1-3	0.18	0.28	0.17	0.27	0.06	0.27	0.05	0.25	0.03
T1-4	0.49	0.73	0.52	0.67	0.13	0.73	0.20	0.67	0.10
T1-5(2)	--	--	--	--	--	--	--	--	0.22
T1-6	1.04	2.68	0.85	1.80	0.64	2.23	0.94	1.65	0.22

Note: (1) Measured at top of the specimen
(2) Array data was inadvertently not recorded

The measured velocity-time histories at the 4 sensor points for the largest strain level test (T1-6) are shown in Figure 8-2. The recorded geophone and surface acceleration data show that the dominant frequency is 20 Hz, which is coincident with the loading frequency. The largest vertical and horizontal

velocities were observed at the location of case 1, which is the closest sensor to the footing. The geophones close to the ground surface (0.3 m depth) were always larger in amplitude than the geophones at 0.9 m. The vertical velocity-time histories show that the vertical velocities slightly increase as the number of the loading cycle increases. For each sensor, the horizontal velocities are smaller than the vertical velocities. Additionally, the wave forms of the horizontal velocities are not as clear as the vertical velocities. These characteristics may be an indication of the complex wave field present in the current testing configuration.

8.3.3 Shear strain and pore pressure ratio-time histories

One of the attractive features of the developed in situ dynamic liquefaction test is the direct estimation of the induced shear strain and excess pore pressure in the time domain. The results are shear strain and pore pressure-time histories. The pore pressure ratio (r_u) is computed from the residual pore pressure (u_r) divided by the initial vertical effective stress ($\sigma_v^{'}$), which was 6.4 kPa for test series T1. Because only one PPT was installed at the center of the array, the shear strain and pore pressure ratio-time histories at the center of the array are presented. Additionally, the shear strain-time histories are evaluated using all available methods. The SDM method is considered the most appropriate for this test series because it computes strain at the center of the array. The PRW and AW wave propagation-based methods are also used to compute strain. However, some assumptions must be made because these methods do not calculate strain at the center of the array. The PSW method was not used because the shear wave

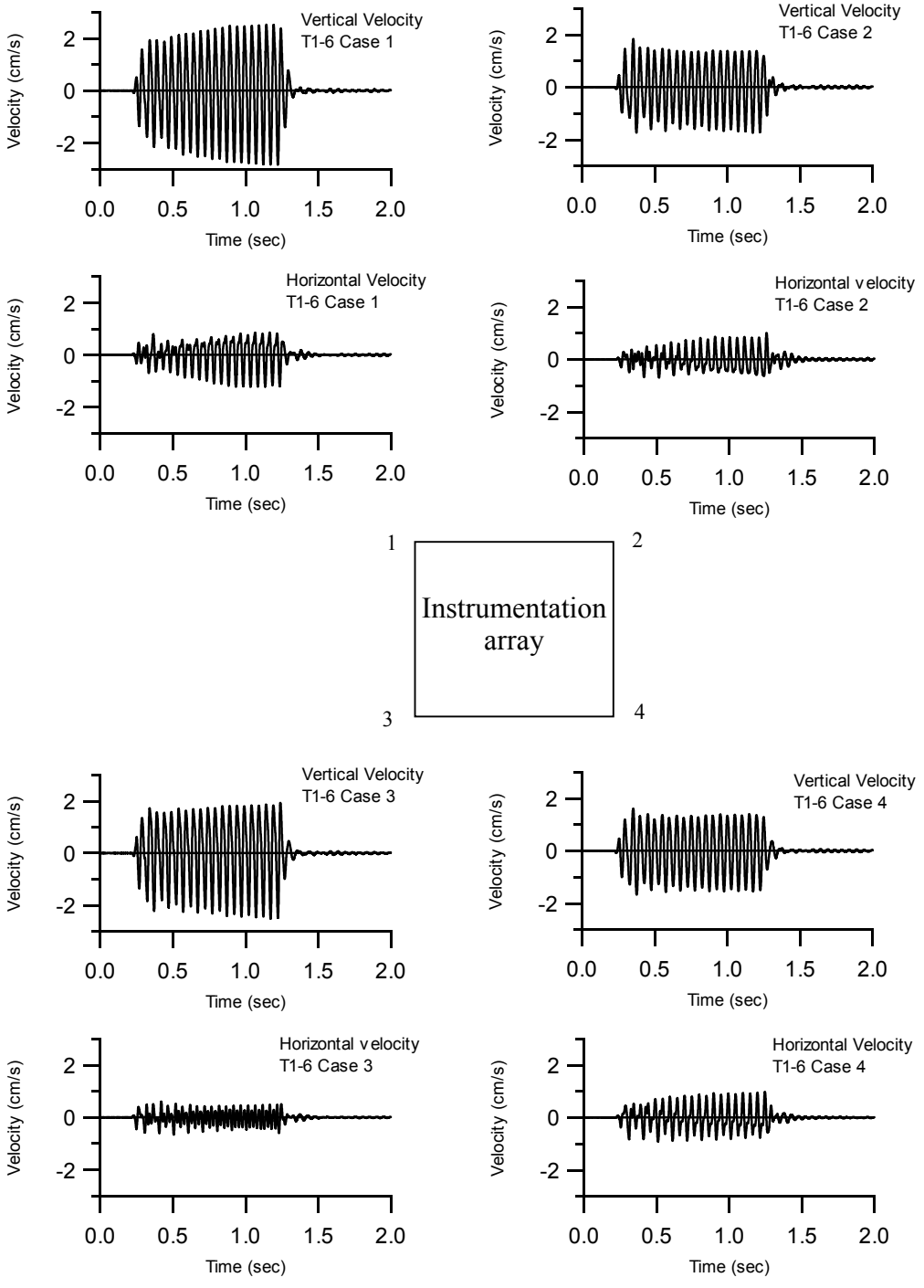

Figure 8-2 Measured velocity-time histories at 4 sensor points during test T1-6

velocity of the test specimen was not measured during this test series.

Based on the induced shear strain level, the shear strain and pore pressure ratio-time histories are presented in two groups: tests at small shear strain levels without residual excess pore pressure buildup and tests at larger shear strain levels with significant residual pore pressure generation. For tests T1-1, T1-2, and T1-3, the induced cyclic shear strain was too small to generate significant excess residual pore pressure. In tests T1-4 through T1-6, the induced shear strain was larger and significant excess pore pressures were observed.

The shear strain and pore pressure ratio-time histories for test T1-3, along with the corresponding Fourier spectra for the signals are shown in Figure 8-3. The cyclic shear strain amplitude is relatively constant at 3.2×10^{-3}% during the dynamic loading (Figure 8-3(a)). The Fourier spectrum of the shear strain–time history (Figure 8-3(a)) indicates that the dominant frequency of the induced cyclic shear strain is 20 Hz, which is the same as the loading frequency. Also, the small, constant shear strain amplitude during test T1-3 indicates that the soil was still in the elastic range without stiffness degradation.

For test T1-3, the recorded excess residual pore pressure ratio was zero, and the hydrodynamic pore pressure ratio oscillated about zero between ± 3%. Again, the Fourier spectrum of the record (Figure 8-3(b)) indicates that the dominant frequency is 20 Hz. However, there is significantly more noise in the pore pressure record than the shear strain record. This noise can be attributed to the small signal-to-noise-ratio (SNR) between the pore pressure signal and the

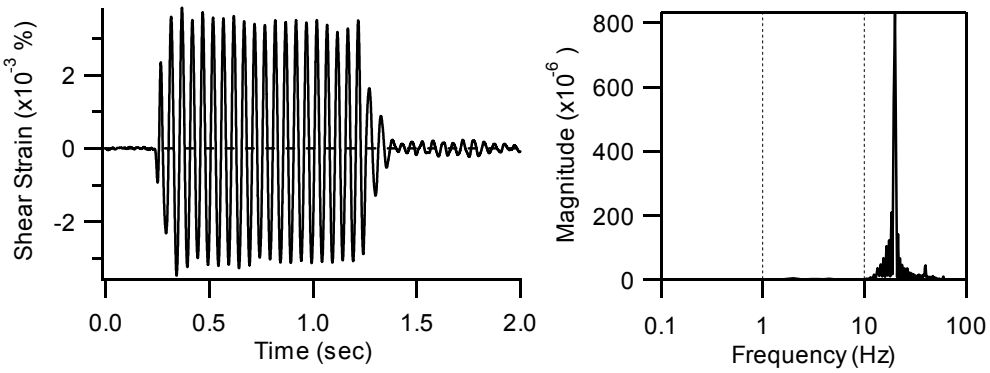

(a) Shear strain response at the center of the array in test T1-3 (SDM method)

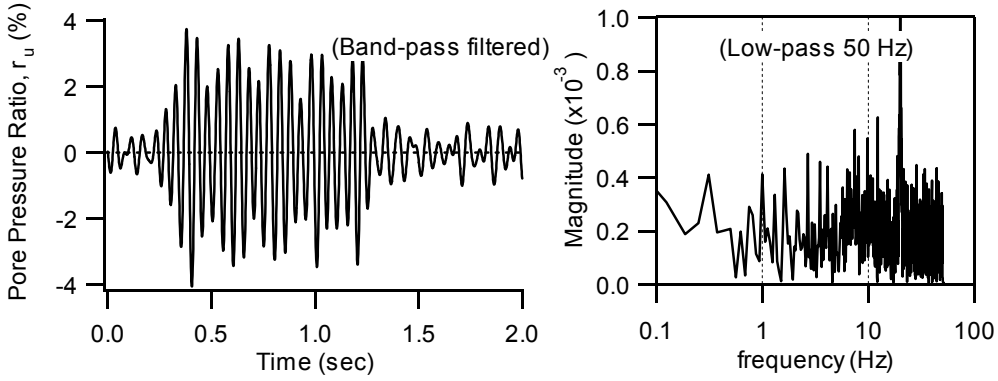

(b) Pore pressure response at the center of the array in T1-3

Figure 8-3 Shear strain and pore pressure ratio response at center of the array for a small strain level test (Test T1-3)

background noise. To improve this problem, a PPT that produces a larger signal in same pore pressure range is used in the subsequent test series.

At larger shear strain levels (Tests T1-4 through T1-6), the characteristics of the shear strain-time histories were different from the characteristics of shear strain-time histories at small loading levels. The shear strain and pore pressure ratio-time histories for test T1-6 are shown in Figure 8-4. The mean shear strain amplitude is about 3×10^{-2}% and increases slightly during the dynamic loading (Figure 8-4(a)).

The recorded pore pressure ratio-time history (Figure 8-4(b)) consists of two components: the hydrodynamic pore pressure and the residual pore pressure. The hydrodynamic pore pressure develops from the wave front propagating through the soil and changing the mean stress. The residual pore pressure is generated by the distortion of the soil skeleton. The hydrodynamic pressure only exists during dynamic loading. The residual pore pressure continually accumulates during dynamic loading and starts to dissipate shortly after the dynamic loading ends. The residual and hydrodynamic pore pressure can be separated using appropriate frequency filters, as described in Chapter 5.

The pore pressure ratio-time history (Figure 8-4) shows a hydrodynamic peak to peak amplitude of about 20%. This amplitude remains approximately constant during the dynamic loading. The residual excess pore pressure reaches at maximum of 65% at the end of the dynamic loading. After this point, the excess pore pressure dissipates back to zero in about 10 to 12 seconds.

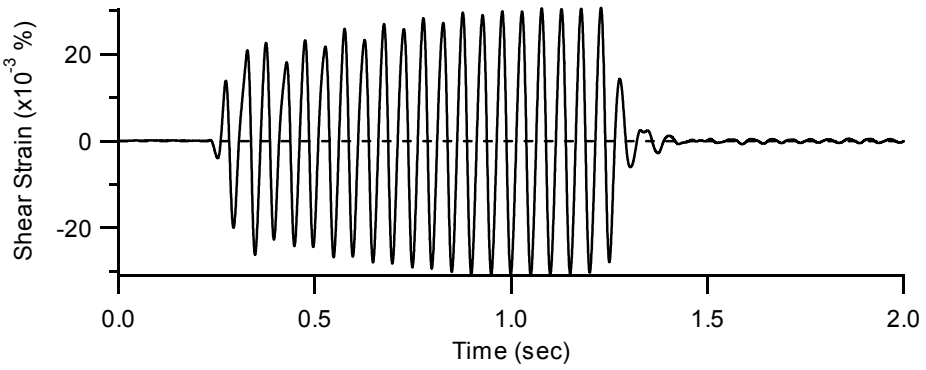

(a) Shear strain-time history at center of array in test T1-6 (SDM method)

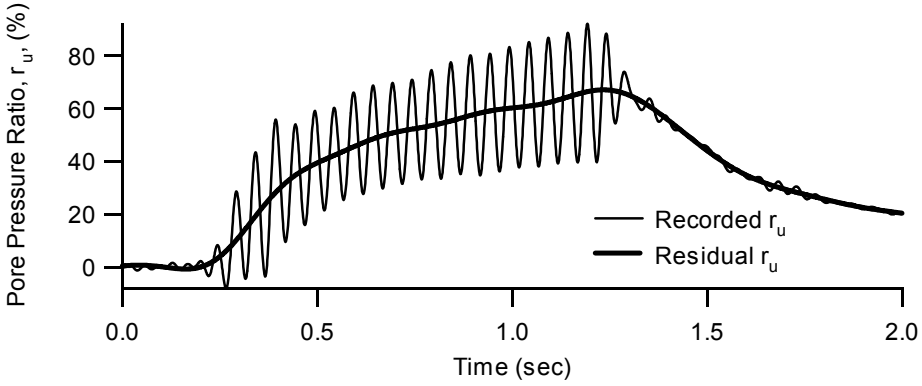

(b) Pore pressure ratio-time history during the dynamic loading in test T1-6

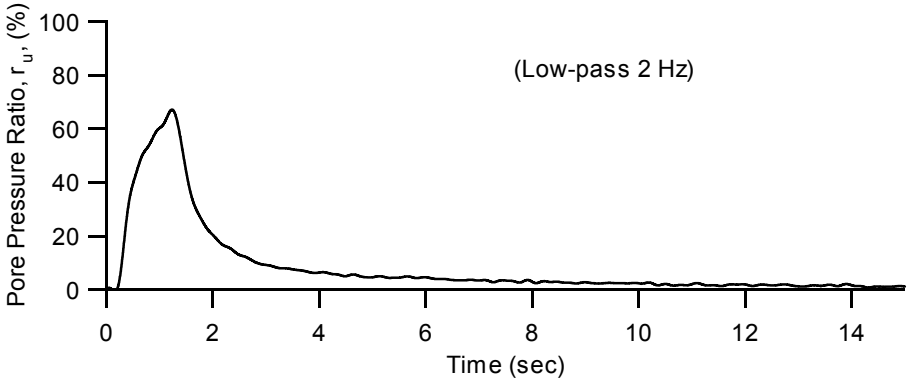

(c) Filtered pore pressure ratio-time history of test T1-6

Figure 8-4 Shear strain and pore pressure ratio response at the center of the array for large strain level tests (Test T1-6)

8.3.4 Pore pressure generation curve

Because only one piezometer was installed at the center of the array, the pore pressure ratio can only be computed at this location. To establish the pore pressure generation curve, the induced shear strain must be evaluated at the location where the pore pressure was measured. The SDM method calculates the shear strain at the center of the array. The wave propagation-based methods calculate the shear strain at the location where the velocities were measured. To calculate the shear strain at the center of the array from the wave propagation-based methods, the averaging technique described in Section 5.4.2 was used. The averaging technique takes the arithmetic average in the time domain of the shear strain-time histories computed by the wave propagation-based methods at the four geophone nodal points to represent the induced shear strain at the center of the array. This averaging technique was shown to produce mean shear strain amplitudes similar to the SDM method. The shear strains at the center of the array using the recorded particle velocities and the PRW and AW methods are processed using this averaging technique.

The Rayleigh wave velocity used in the PRW method was 152 m/s (500 ft/s) and α_v was taken as -1.743 and -1.433 for depths of 0.3 m and 0.9 m, respectively. The apparent phase velocities used in the AW method were calculated from the cross-spectral analysis of the measured vertical geophone data. Because no shear wave velocity measurements were conducted before each dynamic loading in test series T1, the PSW method was not applied.

The shear strain-time histories computed by the SDM method show that the shear strain amplitude varied during dynamic loading (Figure 8-4). The variation is more significant during large strain level tests. The mean shear strain amplitude, which is the average value of the shear strain amplitude during the entire dynamic loading, is used to represent the induced shear strain amplitude. This mean shear strain amplitude is used in the pore pressure generation curve. The calculated mean shear strain amplitudes (γ_{xz}) from the different shear strain evaluation methods, the maximum excess residual pore pressures ($u_{r,max}$), and the excess pore pressure ratios ($r_u = \frac{\Delta u_{r,\max}}{\sigma_v^{'}}$) at the center of the array for each test in test series T1 are summarized in Table 8-5. Table 8-5 indicates the largest shear strain induced was about 0.028% (based on the SDM method) and the corresponding residual pore pressure ratio was 65%. Also, the shear strains calculated from the three different analytical methods agree favorably. The strain calculation methods are compared more thoroughly in Chapter 11.

Using the induced mean shear strain amplitudes and the excess pore pressure ratios listed in Table 8-5, the pore pressure generation curve for the reconstituted test specimen for 20 loading cycles can be established. These data are shown in Figure 8-5. The data show no pore pressure generation up to a shear strain level of about 0.003%. At shear strain levels above 0.007%, residual pore pressure is generated. These data indicate a threshold shear strain for pore pressure generation between 0.003% and 0.007%, which is smaller than the conventional threshold shear strain proposed by Dobry et al. (1982). However,

Table 8-5 Summary results of induced mean shear strains and excess pore pressures at the center of the array for test series T1

Test	SDM γ_{xz} (%)	PRW γ_{xz} (%)	AW γ_{xz} (%)	$\Delta u_{r,max}$ [2] (kPa)	r_u [3] (%)	D_r [4] (%)
T1-1	6.5E-04	4.10E-04	5.90E-04	0	0	38
T1-2	1.4E-03	8.60E-04	1.10E-03	0	0	38
T1-3	3.2E-03	2.30E-03	2.60E-06	0	0	38
T1-4	7.9E-03	6.50E-03	7.00E-03	0.53	8.3	38
T1-5[1]	---	---	---	4.07	63.8	38
T1-6	2.8E-02	1.70E-02	1.90E-02	4.13	64.9	(?)

Note: (1) Array data was inadvertently not recorded.
(2) Does not include the hydrodynamic component
(3) Initial vertical effective stress at center of array = 6.4 kPa
(4) Before loading
? Relative density unknown because surface settlement was not measured

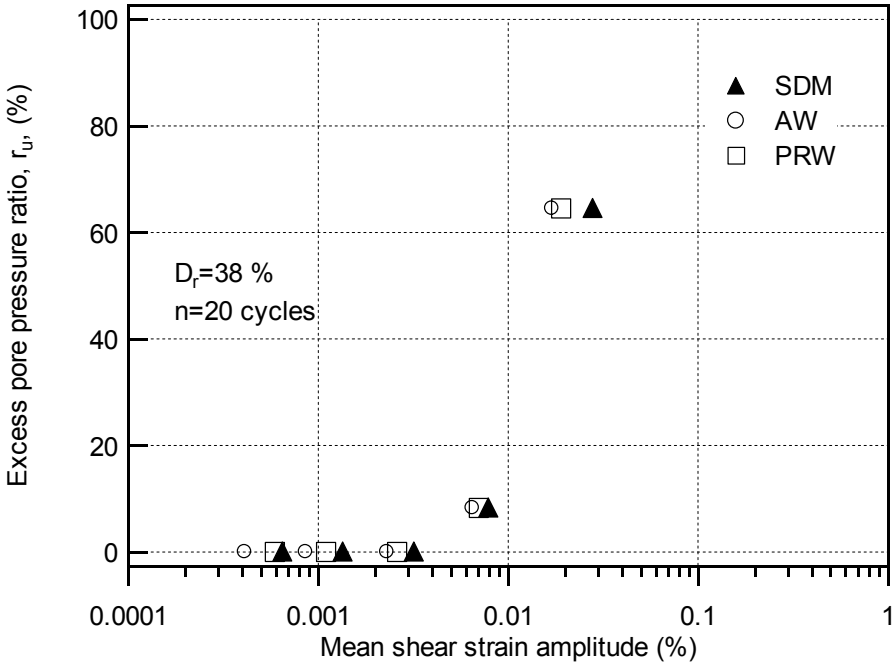

Figure 8-5 Pore pressure generation curves for test series T1

this result may be due to the low stresses in the test pit and is discussed further in Chapter 11.

It should be noted that the data listed in Table 8-5 are corresponding to 20 loading cycles. The family curves that described the relationships between the induced shear strains, excess pore pressures, and numbers of loading cycles can be constructed using the shear strain-time and pore pressure-time histories with respect to different loading cycles. The pore pressure generation curves with shear strain calculated by the SDM method for different loading cycles are shown in Figure 8-6. The results reveal that the excess pore pressure ratio increases for a specific shear strain amplitude greater than the threshold shear strain as the number of loading cycles increases.

Although all of the tests within this test series were conducted on the same reconstituted test specimen, the relative density of the soil before each dynamic loading might be different due to the induced volumetric strain during previous loadings. The relative density of the soil before each loading was estimated from the measured settlement induced by previous tests. However, no settlement was observed until after test T1-5. Unfortunately, due to a data acquisition error, only the pore pressure data were recorded in test T1-5 and no geophone data were recorded. Also, the settlement was not measured after this test. However, significant pore pressure was recorded in the next test (T1-6) and the settlement measured after that test, relative to the initial configuration, was 4.6 cm. This settlement corresponds to a volumetric strain of 3.8%.

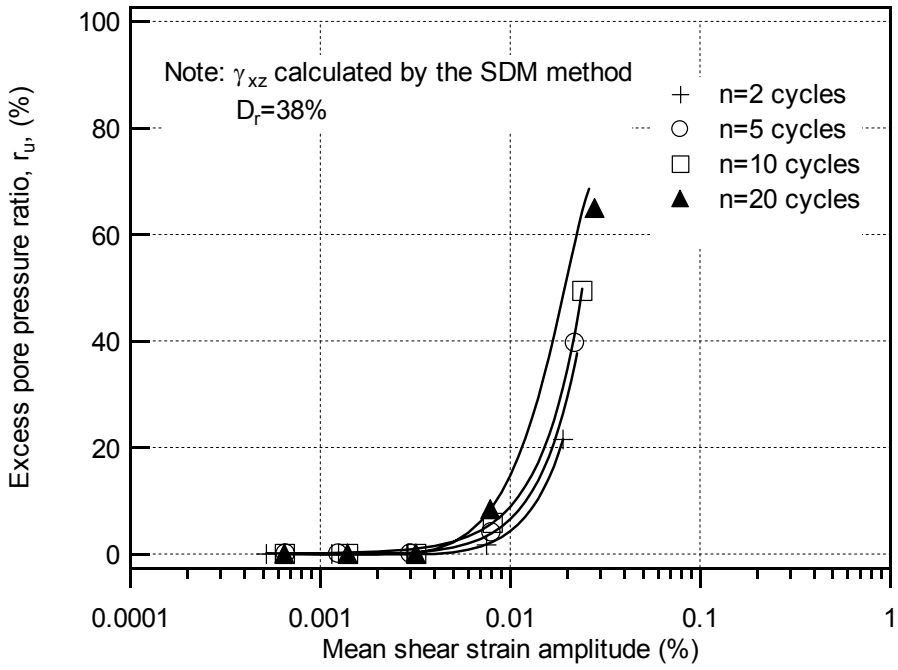

Figure 8-6 Pore pressure generation curves from Test series T1 for different numbers of loading cycles

8.4 SUMMARY

A testing program consisting of three test series was performed using the proposed in situ dynamic liquefaction test on reconstituted test specimens. These test series were labeled according to their chronological order (T1, T2, and T3). In this chapter, the test results from the initial test series (T1) are presented. Further interpretations and discussions of the test results are presented in Chapter 11.

The first test series was performed at a relatively low confining stress. The effective vertical stress at the center of the array where the PPT was installed was only 6.4 kPa (0.93 psi). The test results provide unique data to study pore pressure

generation behavior under low confining pressures. Six tests were performed in test series T1.

The largest velocities were always observed at the location of case 1, which is the closest sensor to the footing. Vertical velocities were larger than the horizontal velocities. The maximum recorded vertical surface acceleration was 0.22 g and occurred during dynamic test T1-6. The vertical velocity-time histories show that the vertical velocities slightly increase as the number of the loading cycle increases. The recorded geophone and surface acceleration data show that the dominant frequency is 20 Hz, which is coincident with the loading frequency.

The shear strain and pore pressure ratio-time histories are presented in two groups: tests at small shear strain levels and tests at large shear strain levels. The Fourier spectra from all the tests show the dominant frequency in the induced shear strain and hydrodynamic pore pressure is 20 Hz, which is the same as the loading frequency. The largest induced mean shear strain in test series T1 was 0.028% and the corresponding residual pore pressure ratio was 65%.

The pore pressure generation curve for test series T1 was established using the mean shear strain amplitudes and the excess pore pressure ratios measured at the center of the array. The test data indicate a threshold shear strain for pore pressure generation between 0.003% and 0.007%, which is smaller than the conventional threshold shear strain proposed by Dobry et al. (1982), which is 0.01%.

Chapter 9. Results from Test Series T2

9.1 INTRODUCTION

After test series T1, there were concerns regarding the size of the sensors, saturation of the test specimen, and characterization of the test specimen. Also, more sensors were needed to compare the shear strain evaluation methods and to monitor excess pore pressure generation and dissipation at different depths. In addition, the stresses within the reconstituted test specimen were increased to be more representative of the in situ stress levels of liquefied sites. Test series T2 was designed to address these concerns.

This chapter presents the results from test series T2. The test data are presented in a manner similar to the data for test series T1 (Chapter 8). This test series was dynamically loaded for 20 cycles at a loading frequency of 20 Hz. In addition, the results for the characterization of the test specimen are presented. Further interpretations and discussions of the test results are presented in Chapter 11.

9.2 TEST RESULTS FROM TEST SERIES T2

The developed liquefaction sensors were used in this test series, as well as in test series T3. Liquefaction sensors measure both particle velocities and pore pressures at the same location. These sensors addressed concerns regarding the

size of the sensors. In addition, small-strain seismic tests were performed to measure the shear wave velocity of the test specimen and to assess the degree of saturation. To increase the stresses within the test specimen, a layer of air-dried sand was placed on top of the test pit. A description of test series T2 and the collected data are presented here.

9.2.1 Description of test series T2

A schematic layout for test series T2 is shown in Figure 9-1. Five liquefaction sensors were installed, four at the corners of a 0.6 m by 0.6 m square array and one at the center of the array. A PVC pipe was installed along the far side of the test pit and in the same vertical plane as the instrumentation array. The PVC pipe was used as an open-end piezometer, which monitoring the water level inside the test pit, and also as casing for the crosshole source. One settlement platform was placed on top of the specimen to measure the settlement of the specimen. A 0.8-m layer of air-dried sand was placed on top of the specimen as overburden to increase the stresses within the test specimen. This overburden increased the vertical effective stress at the center of the array to 19.3 kPa, which is 3 times larger than the vertical effective stress at the center of the array in test series T1. An accelerometer was placed on top of the overburden to monitor the vertical acceleration.

The same soil used in test series T1 was used to prepare the reconstituted test specimen for test series T2. The initial and final physical properties of the reconstituted test specimen for test series T2 are listed in Table 9-1. The final

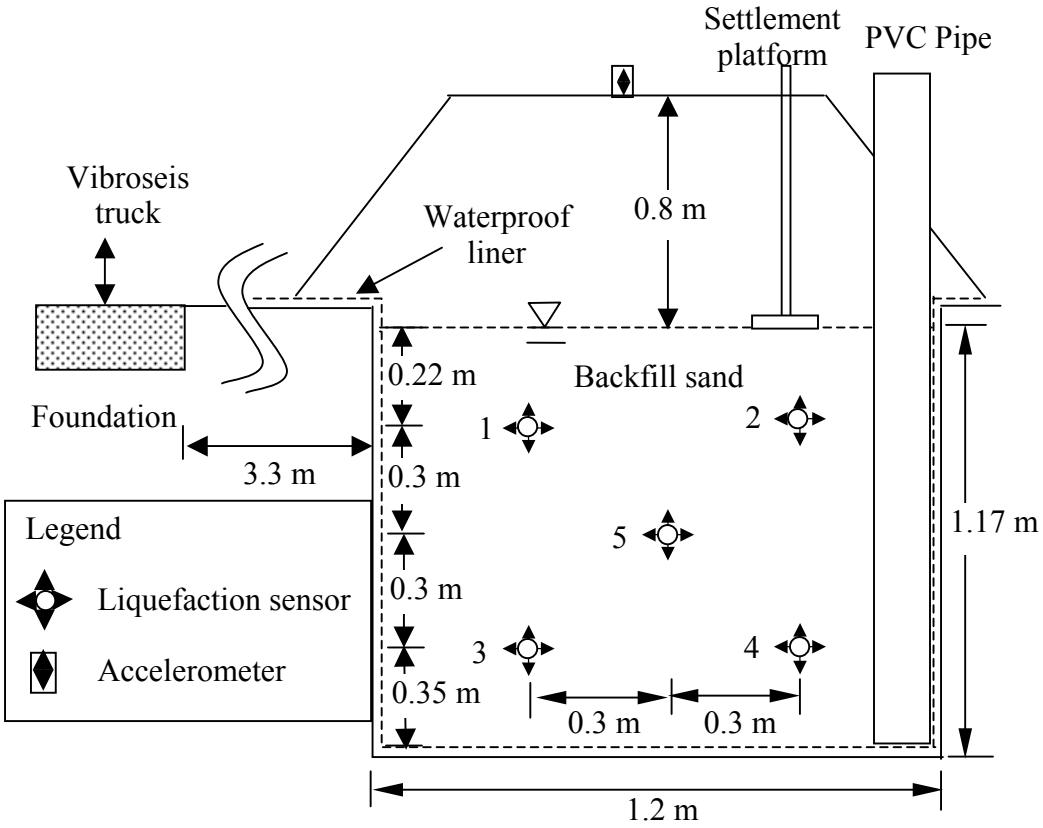

Figure 9-1 Schematic layout of test series T2

Table 9-1 Physical properties of the reconstituted specimen for test series T2

Soil property		**Value**
Specific gravity (G_s)		2.68
Maximum void ratio (e_{max})		0.64
Minimum void ratio (e_{min})		0.43
Fines content		0.43%
Initial	Relative density (D_r)	34.7%
	Water content (w)	21.1%
	Total unit weight (γ_t)	20.4 kN/m^3 (129.3 pcf)
Final[(1)]	Relative density (D_r)	61.2%
	Water content (w)	19.0%
	Total unit weight (γ_t)	20.8 kN/m^3 (132.0 pcf)

Note: [(1)] These values are estimated from 4.3 cm (1.7 in.) of settlement

values are estimated from the 4.3 cm (1.7 in) of settlement measured at the top of the specimen. The dynamic loads were applied to the footing at a loading frequency of 20 Hz for 1 second. Therefore, 20 cycles of loading were generated.

9.2.2 Geophone and accelerometer results

The recorded peak particle velocities for each dynamic loading in test series T2 were processed as discussed in Section 8.3.2. The recorded peak values are summarized in Table 9-2. The listed accelerations were measured at the top of the overburden, as shown in Figure 9-1. The maximum recorded vertical surface acceleration was 0.42 g. This value is twice that recorded in test series T1, but the velocities recorded within the test specimen for test series T2 are similar to those from T1. Therefore, the large acceleration recorded in test series T2 may be a result of the dynamic response of the overburden. Similar to test series T1, the Fourier spectra of the vertical velocity and surface acceleration data show a maximum response at 20 Hz, which is coincident with the loading frequency. However, the horizontal velocities display a second major vibration at a frequency of 40 Hz. The measured velocities for a large strain level test (T2-8) are shown in Figure 9-2. Note that the vertical velocities are greater than the horizontal velocities, and that the waveforms of the horizontal velocities are not as clean as the vertical velocities.

Table 9-2 Summary of the recorded peak particle velocities and surface accelerations for test series T2

Test #	H1 (cm/s)	V1 (cm/s)	H2 (cm/s)	V2 (cm/s)	H3 (cm/s)	V3 (cm/s)
T2-1	0.06	0.06	0.06	0.07	0.02	0.05
T2-2	0.13	0.16	0.13	0.16	0.03	0.14
T2-3	0.18	0.27	0.17	0.26	0.04	0.23
T2-4	0.22	0.43	0.25	0.43	0.06	0.37
T2-5	0.23	0.61	0.30	0.61	0.09	0.52
T2-6	0.25	0.88	0.44	0.88	0.14	0.76
T2-7	0.27	0.98	0.52	1.04	0.17	0.85
T2-8	0.73	2.50	0.85	1.98	0.46	1.89

Test #	H4 (cm/s)	V4 (cm/s)	H5 (cm/s)	V5 (cm/s)	a_{max} (1) (g)
T2-1	0.01	0.06	0.02	0.05	0.01
T2-2	0.03	0.14	0.06	0.10	0.02
T2-3	0.05	0.23	0.08	0.23	0.04
T2-4	0.08	0.37	0.12	0.37	0.08
T2-5	0.12	0.52	0.18	0.55	0.17
T2-6	0.18	0.73	0.24	0.79	0.26
T2-7	0.26	0.85	0.30	0.91	0.36
T2-8	0.58	1.74	0.85	1.98	0.42

Note: (1) Measured at the top of the overburden

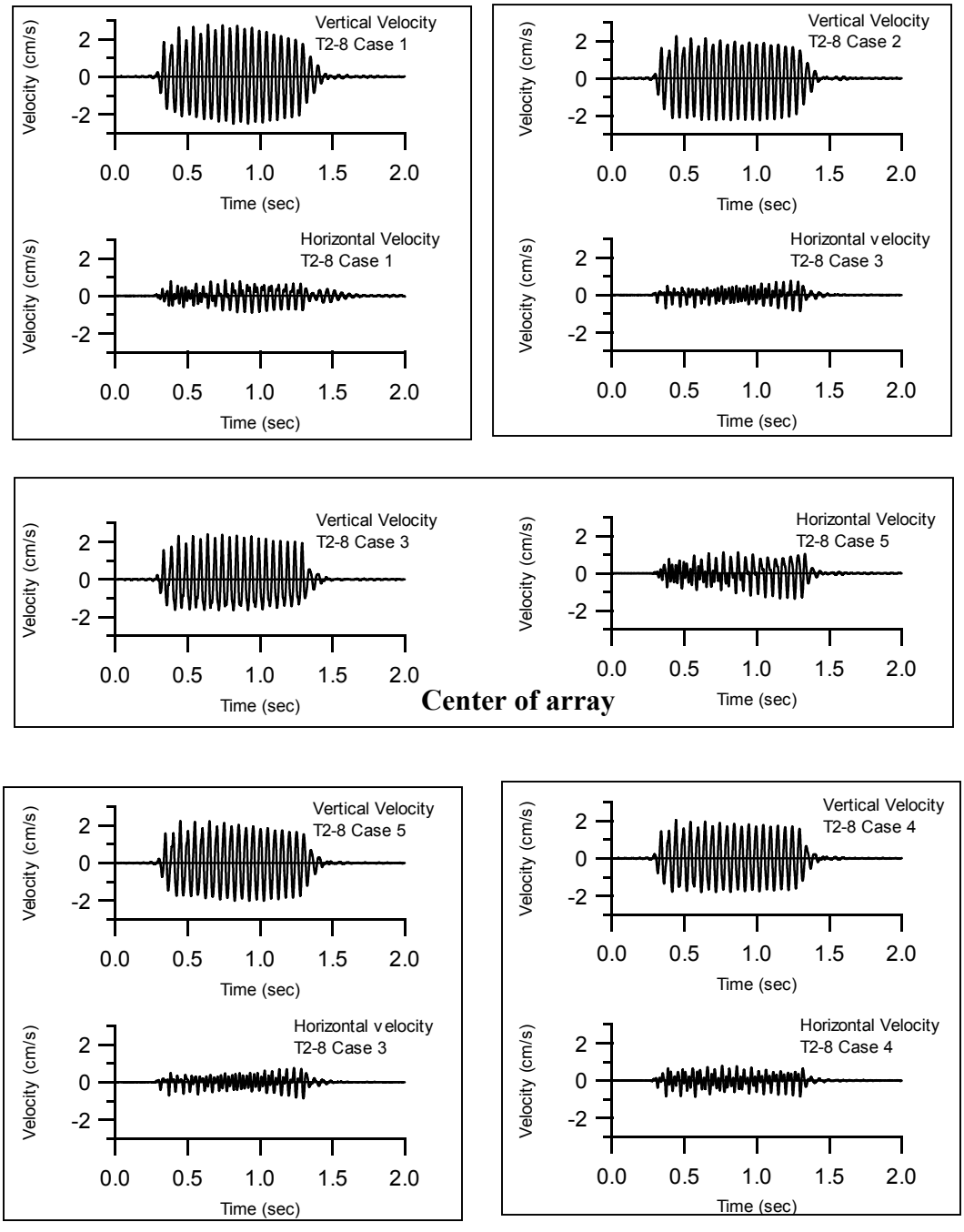

Figure 9-2 Measured velocity-time histories during test T2-8

9.2.3 Shear strain and pore pressure ratio-time histories

The tests conducted in test series T2 are divided into two groups according to their mean shear strain levels. The low shear strain level group includes tests T2-1 through T2-5. These tests displayed no or small excess pore pressure during dynamic loading. Also, the shear strain levels are relatively constant during loading. The large shear strain level group includes tests T2-6 through T2-8. These tests showed significant excess pore pressure generation and the shear strain amplitudes varied during dynamic loading.

To apply the wave propagation-based methods in the shear strain calculation, several parameters must be measured before or during dynamic loading. For the PSW method, the S-wave velocity at the sensor location is required. The S-wave velocities of the test specimen were measured by crosshole seismic tests performed before dynamic loading. The seismic testing results also provided information regarding the change in the soil stiffness due to the dynamic loading tests. The crosshole seismic test results are summarized in Table 9-3. The apparent wave velocities used in the AW shear strain evaluation method were measured from the vertical geophone records during dynamic loading and are also listed in Table 9-3.

Before testing, the S-wave velocity of the soil at the depth of cases 1 and 2 was 83 m/s, while at the depth of cases 3 and 4 the S-wave velocity was 109 m/s. The velocity between cases 3 and 4 is larger due to the larger mean effective stress at this depth. As testing progressed through various loading levels, the mean S-wave velocity did not change significantly, although the velocity between cases

Table 9-3 Measured shear wave velocity and apparent wave velocity for test series T2

Test	Shear wave velocity[1] (m/s)		Apparent wave velocity[2] (m/s)	
	Path 2→ 1[3]	Path 4 → 3	Path 1→ 2	Path 3 → 4
T2-1	83	109	116	127
T2-2	85	108	125	145
T2-3	84	109	121	183
T2-4	82	104	128	192
T2-5	81	104	126	187
T2-6	79	104	119	176
T2-7	81	102	116	170
T2-8	85	98	151	169
Final	83	98	---	---

Note: (1) Measured before each test
(2) Measured during dynamic loading
(3) Sensor number

3 and 4 decreased by about 10%. Based on the change in void ratio, estimated from the measured settlement, a 5% to 7% increase in V_S would be expected at the end of testing. However, this small value is in the range of error for this measurement, and therefore, no significant change in V_S was observed. The S-wave velocity after test T2-8 was 83 m/s between cases 1 and 2, and 98 m/s between cases 3 and 4.

The apparent wave velocities measured between cases 1 and 2, and cases 3 and 4 were larger than the S-wave velocities of the test specimen at the same depths. This larger velocity occurred because the apparent waves represent a combination of waves traveling through both the test specimen and the native soil beneath the test specimen. The variation in the apparent wave velocity from test to test is discussed further in Chapter 11.

The Rayleigh wave velocity used in the PRW method is 152 m/s (500 ft/s). This value is the same as the value measured in the field vibration test and used in test series T1. The ratio between the shear strain and the normalized vertical particle velocity (α_v) for the PRW method is -1.806 and -1.466 for depths of 0.22 m and 0.82 m, respectively.

The shear strain time-histories from a low strain level test (T2-3) are shown in Figure 9-3. At the four sensor points, the shear strains are computed using the AW method. At the center of the array, the shear strains were computed using the SDM method and the average AW shear strains from the four sensor points. The shear strain amplitudes during dynamic loading are relatively constant for each point, except for the shear strain at the center of the array calculated by the SDM method. This difference most likely arises from the fact that the SDM method incorporates horizontal velocity-time histories, which have distinct waveforms and the variation of apparent wave velocity during loading. Note that the AW method only incorporates vertical velocity-time histories. This is discussed further in Chapter 11.

The shear strain-time histories for test T2-8 are shown in Figure 9-4. Test T2-8 has the largest mean shear strain level and the largest excess pore pressure ratio. The shear strain-time histories at the center of the array for test T2-8 are different than those from test T2-3. The strains are much larger for test T2-8, and the shear strain time-history at the center of the array calculated by the SDM method shows significant variation during dynamic loading, indicating a

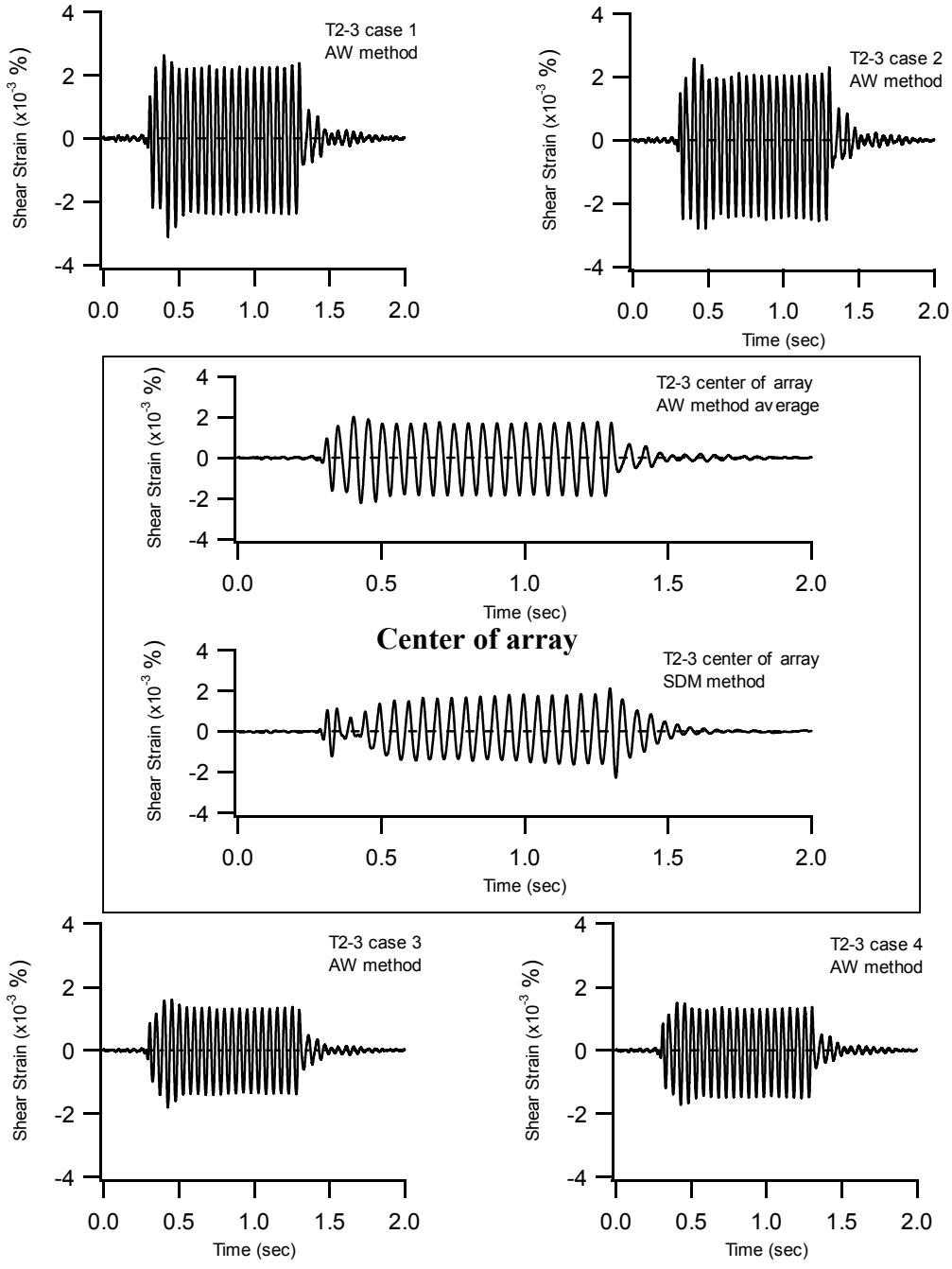

Figure 9-3 Shear strain-time histories at the 4 sensor points and at the center of the array for test T2-3 (low strain level test)

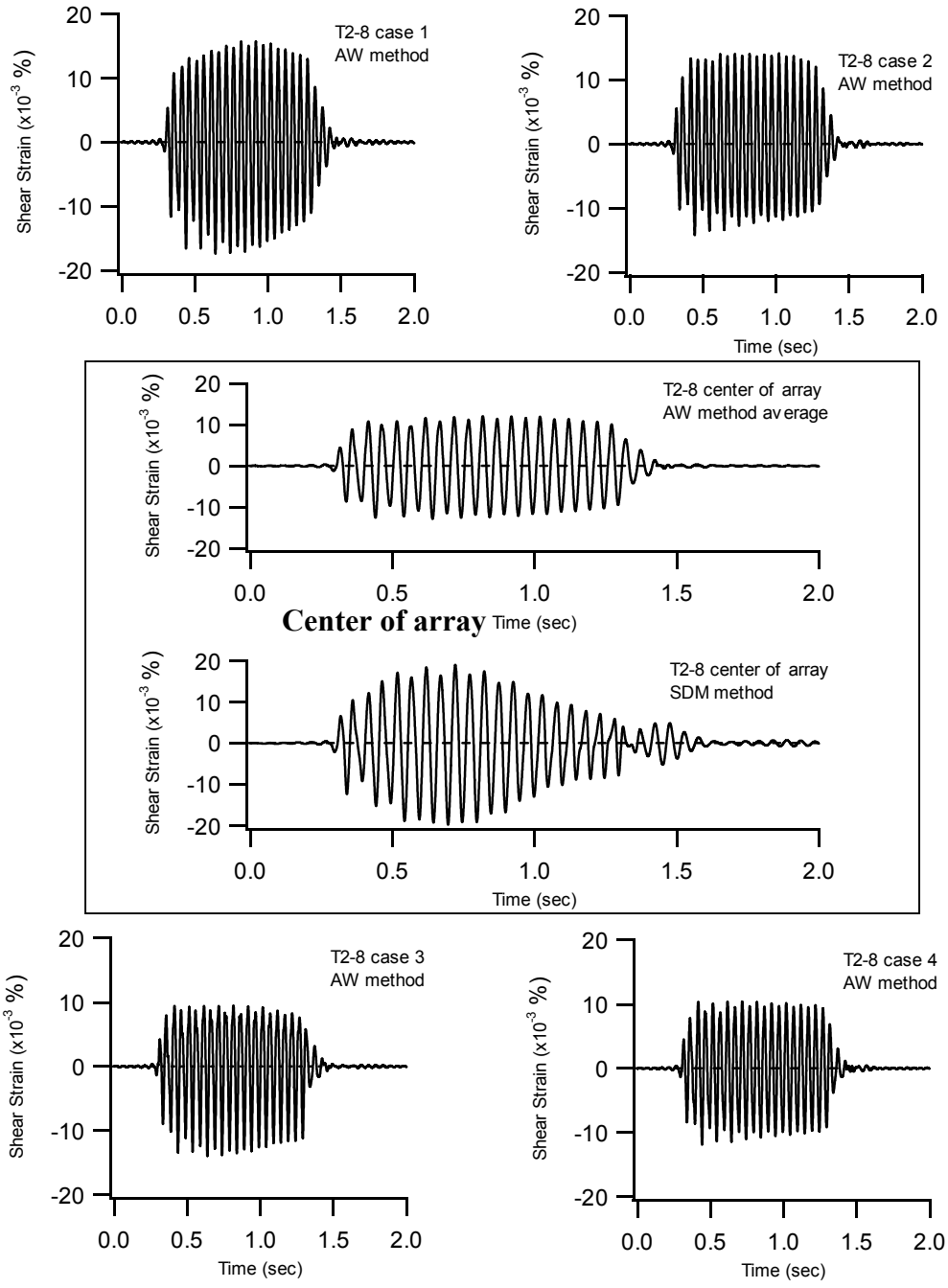

Figure 9-4 Shear strain-time histories at the 4 sensor points and at the center of the array for test T2-8 (large strain level test)

reduction in amplitude during later cycles. This issue is further discussed in Chapter 11.

The pore pressure ratio-time histories from test T2-8 are shown in Figure 9-5. Again, hydrodynamic and residual pore pressures are observed. The hydrodynamic peak to peak amplitude is about 30 % for each recording and remains approximately constant during dynamic loading. The maximum residual excess pore pressure ratio reaches 46% at the center of the array. However, at shallow depths (cases 1 and 2) the pore pressure ratio only reaches 40% and at larger depths (cases 3 and 4) the pore pressure ratio exceeded 50%. For each pore pressure recording, the excess pore pressure dissipated in about 50 seconds. The time for dissipation for test series T2 was longer than for test series T1. Most likely the unsaturated overburden impeded drainage in test series T2 and caused the longer dissipation time.

9.2.4 Pore pressure generation curves

Because five liquefaction sensors were installed within the test specimen for test series T2, a pore pressure generation curve can be established for each sensor location using the recorded residual pore pressure and the shear strain levels evaluated from wave propagation-based methods. However, the SDM method, which is the most rigorously correct strain evaluation method, can only be applied at the center of the array. To compare the pore pressure generation curves generated from the various strain evaluation methods, results are presented the center of the array. The same averaging technique (Section 9.2.3) is used to

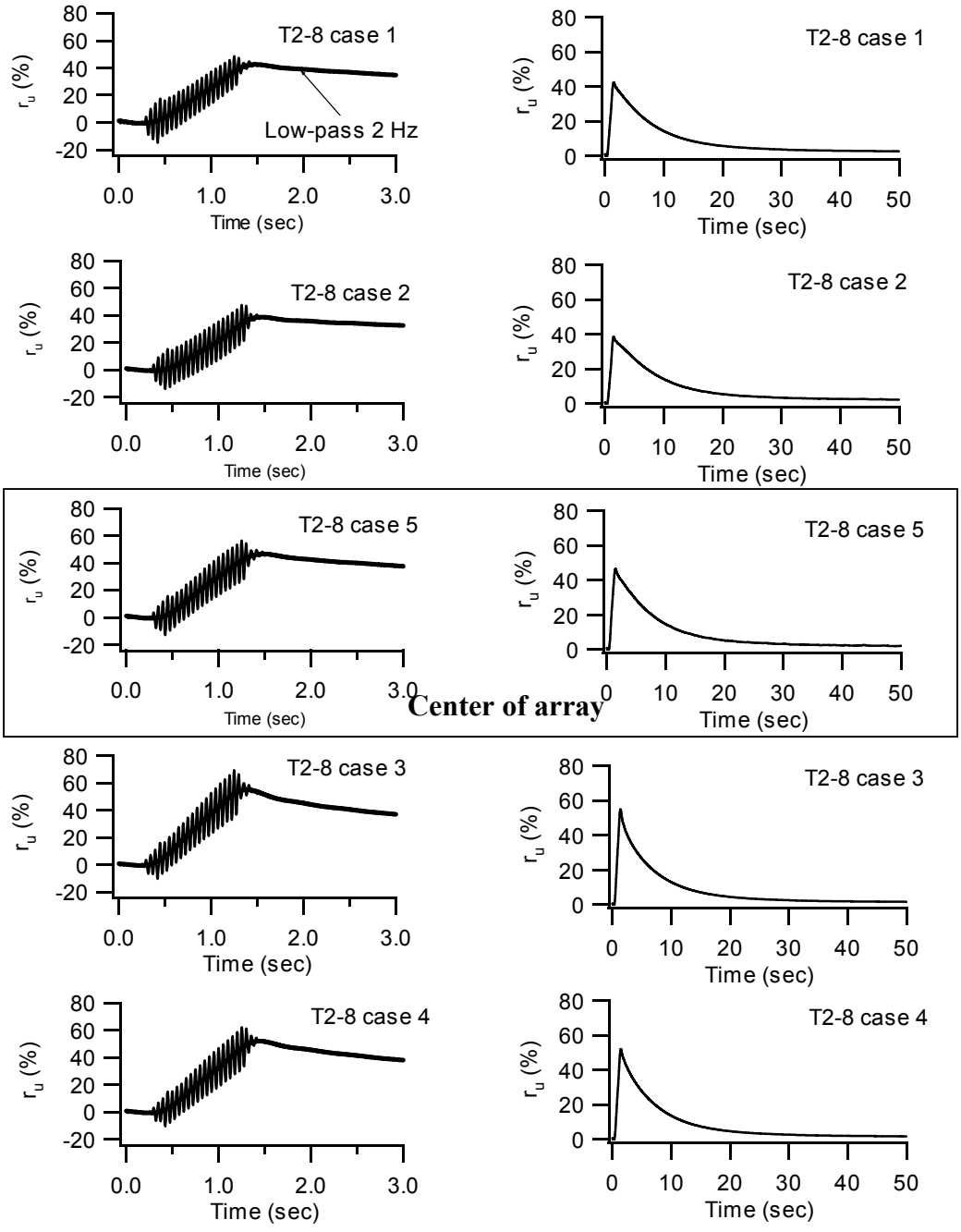

Figure 9-5 Pore pressure ratio-time histories for test T2-8 (large strain level test)

calculate the shear strains at the center of the array from the AW shear strains computed at the 4 sensors locations.

The mean shear strain amplitudes (γ_{xz}) from the different shear strain evaluation methods, the maximum excess residual pore pressure ($u_{r,max}$), and the excess pore pressure ratios (r_u) at the center of the array are summarized in Table 9-4. The relative density of the test specimen before each dynamic loading was estimated from the measured settlement induced by the previous tests, and is reported in Table 9-4 as well. The vertical effective stress was computed by assuming the total unit weight of the sand used for overburden was 17.3 kN/m^3 (110 pcf) and the water table remained at the top of the test specimen.

The pore pressure generation curves at the center of the array for test series T2 using the various shear strain evaluation methods are shown in Figure 9-6. The pore pressure generation curves with shear strain calculated by the SDM method for different loading cycles are shown in Figure 9-7. The data show little or no pore pressure generation at shear strains below 0.005%. Significant pore pressure is generated at shear strains above 0.01%. The maximum excess pore pressure ratio for this test series was 46.4%, and it occurred at a shear strain of about 0.015%. The permanent settlement after test T2-8 was 4.3 cm, which corresponds to 3.7% volumetric strain.

The pore pressure generation curves at the five sensor locations using the recorded excess pore pressure data and the shear strains calculated by the AW method are shown in Figure 9-8. All the pore pressure generation curves fall in a narrow range. The results reveal a unique relationship between the excess pore

Table 9-4 Summary results of induced shear strains and excess pore pressures at center of the array for test series T2

Test	SDM γ_{xz} (%)	PSW γ_{xz} (%)	PRW γ_{xz} (%)	AW γ_{xz} (%)	$\Delta u_{r,max}$ [1] (kPa)	r_u [2] (%)	Dr [3] (%)
T2-1	7.00E-04	6.62E-04	6.67E-04	5.11E-04	0.00	0.0	34.7
T2-2	1.00E-03	1.60E-03	1.64E-03	1.13E-03	0.09	0.5	34.7
T2-3	1.80E-03	2.68E-03	2.72E-03	1.75E-03	0.11	0.6	34.7
T2-4	2.30E-03	4.37E-03	4.29E-03	2.62E-03	0.15	0.8	34.7
T2-5	3.50E-03	6.24E-03	6.10E-03	3.82E-03	0.31	1.6	34.7
T2-6	5.50E-03	9.21E-03	8.83E-03	5.85E-03	0.62	3.2	34.7
T2-7	6.00E-03	1.04E-02	1.01E-02	6.85E-03	0.96	5.0	34.7
T2-8	1.40E-02	2.24E-02	2.20E-02	1.28E-02	8.96	46.4	38.5 [4]

Note: (1) Does not include the hydrodynamic component
(2) Initial vertical effective stress at center of array = 19.3 kPa
(3) Before loading
(4) Estimated from 0.05 cm settlement

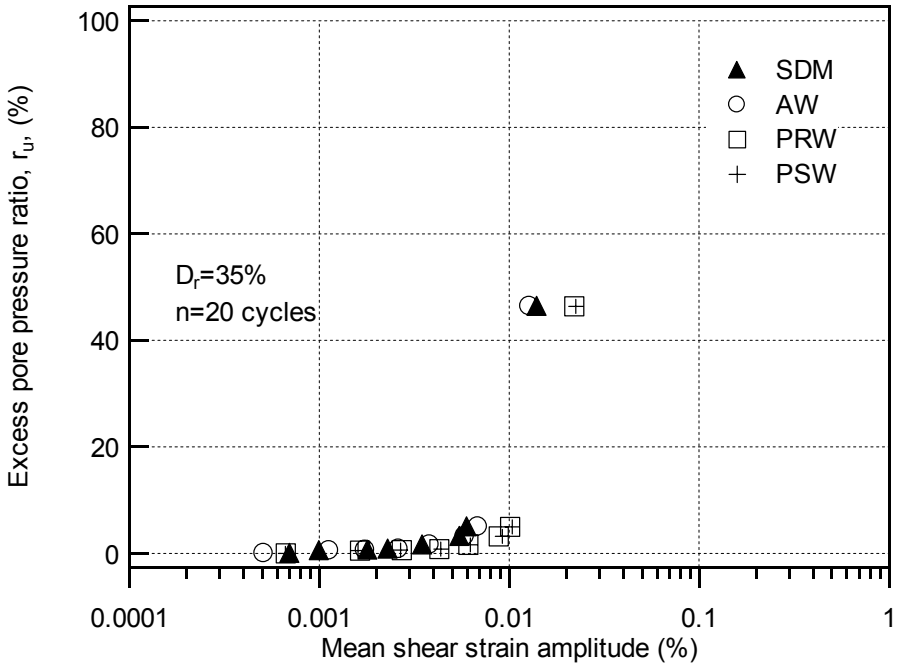

Figure 9-6 Pore pressure generation curves for test series T2

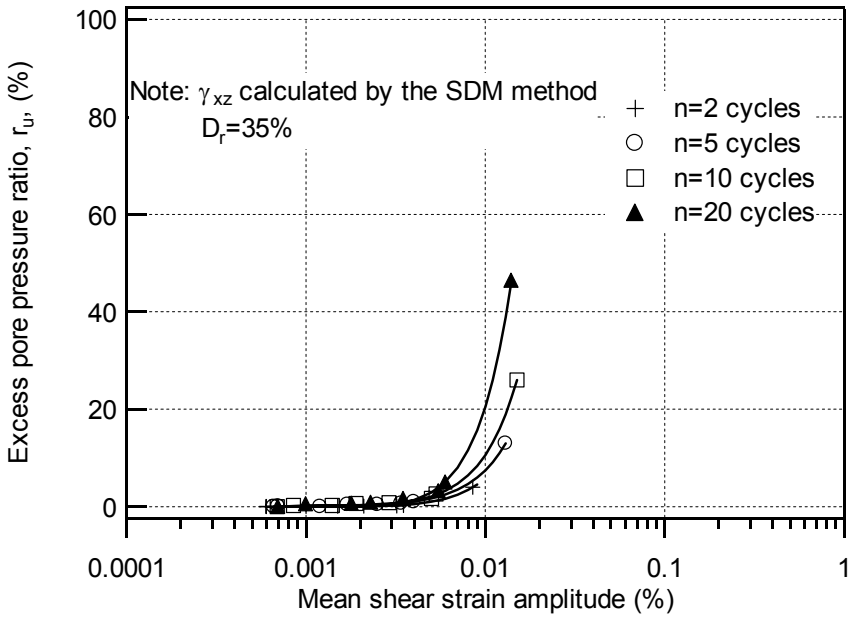

Figure 9-7 Pore pressure generation curves from Test series T2 for different numbers of loading cycles

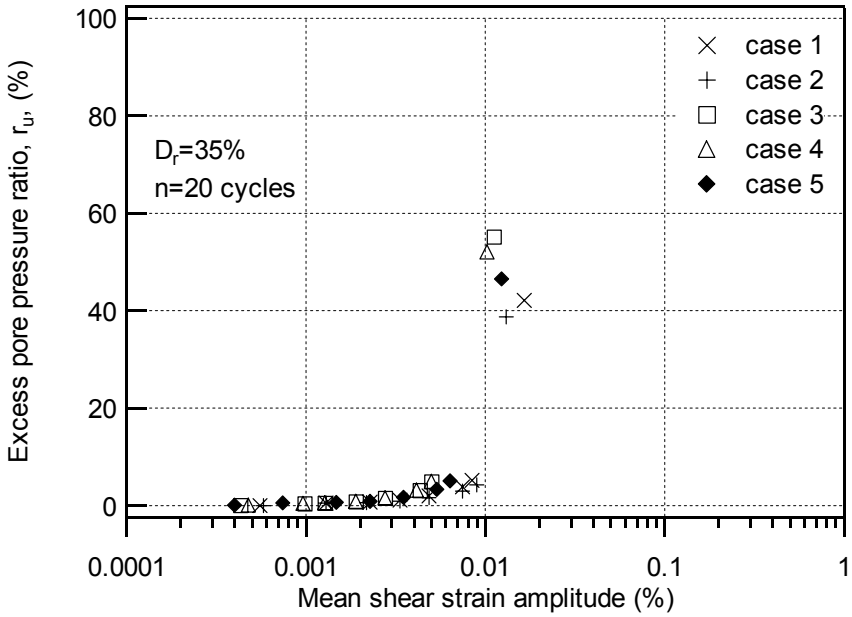

Figure 9-8 Pore pressure generation curves at 5 sensor locations for test series T2

pressure ratio and the induced shear strain which was first observed by Dobry et al. (1982). Further discussions of these data are presented in Chapter 11.

9.3 CHARACTERIZATION OF RECONSTITUTED TEST SEPCIMEN

To address the concerns regarding the physical properties of the reconstituted test specimen, especially the degree of saturation and the in situ density, small-strain seismic testing of P-wave velocity and direct in situ measurements of density were conducted in the test specimen. The P-wave velocity measurement was employed to verify the saturation of the test specimen. The saturation of the test specimen for test series T2 was a concern because the specimen was tested over a month after preparation. The direct in situ density measurements were used to evaluate the accuracy of the estimated in situ density.

9.3.1 Evaluation of saturation of the test specimen

The saturation of the test specimen for test series T2 was evaluated through measured P-wave velocities using the same equipment used for S-wave velocity measurements. For crosshole P-wave velocity measurements, the horizontal geophones were used as receivers. The P-wave measurements made before test T2-1 are shown in Figure 9-9. The signal-time histories from the receivers in cases 1 and 2 are shown in Figure 9-9(a) and the result from the receivers in cases 3 and 4 are shown in Figure 9-9(b). For saturated soil, the theoretical P-wave velocity is around 1500 m/s (5000 ft/s) and some high frequency waves are expected after the first arrival of the P-wave. The records

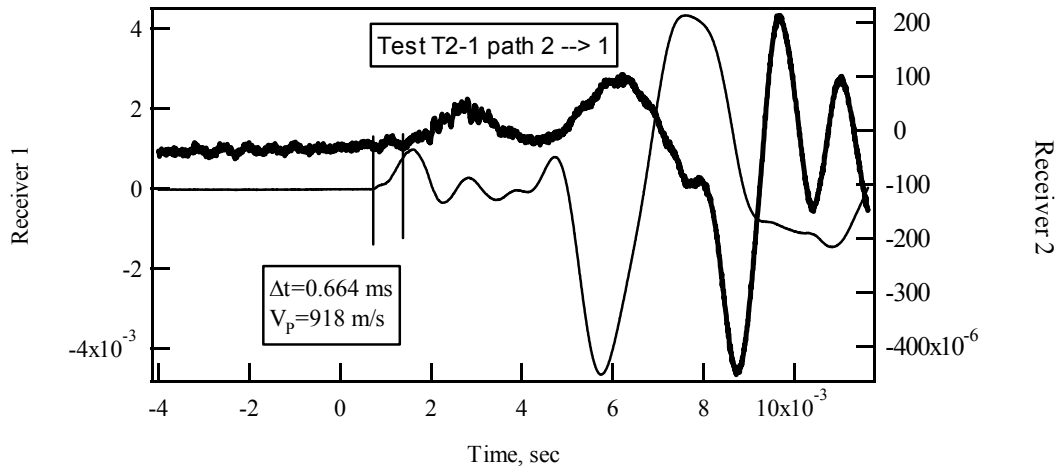

(a) Crosshole P-wave velocity measurement from case 2 to case 1

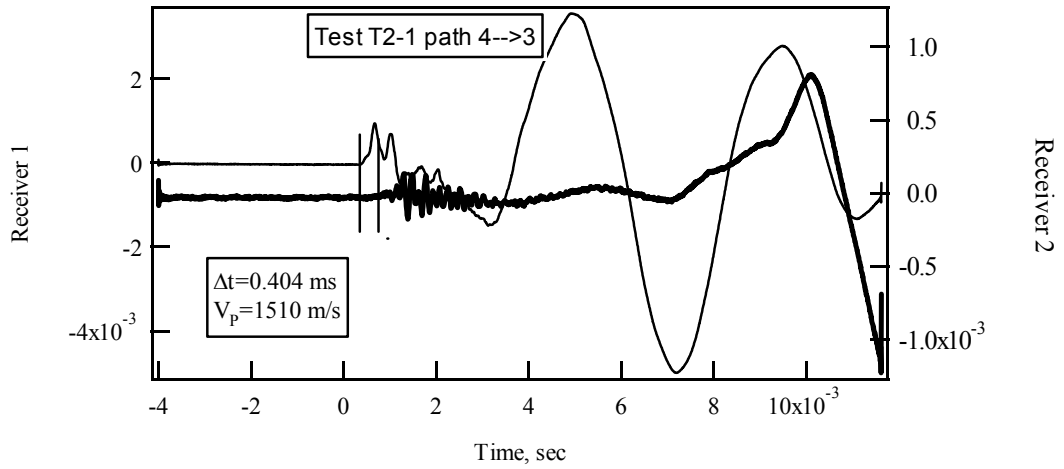

(b) Crosshole P-wave velocity measurement from case 4 to case 3

Figure 9-9 Crosshole signal-time histories for P-wave velocity measurement

from cases 3 and 4 (Figure 9-9(b)) indicate a P-wave velocity of 1510 m/s and high frequency waves are observed after the initial P-wave arrival. Based on these two criteria, the soil between cases 3 and case 4 is saturated. The P-wave velocity between cases 1 and 2 is relatively low (V_P=918 m/s) and no high frequency waves were observed, indicating less than full saturation. However, the soil between cases 1 and 2 may be very close to full saturation, because P-wave velocity drops off very quickly as saturation decreases. For a P-wave velocity of 900 m/s, the saturation level may be over 99.5% (Allen et al. 1980, Ishihara et al. 2001).

To further investigate the variation of P-wave velocity and saturation within the test specimen for test series T2, P-wave velocities were measured using the push-in geophone and source, as described in Section 6.7.2. The push-in source and receiver allow the P-wave velocity to be measured at many different depths and within different sections of the test specimen. These measurements were performed after test series T2 was completed because the push-in instrumentation disturbs the test specimen.

The distance between the push-in source and receiver was chosen as 0.3 m (1 ft). Because this small distance results in a very short travel time, a digital oscilloscope was used to measure the travel time. Four vertical profiles were selected to test the specimen saturation. The locations of the four profiles are shown in Figure 9-10 and the results are summarized in Table 9-5. The source is recorded by the instrumented hammer used to strike the top of the source rod and the wave arrival is recorded by the geophone in the push-in receiver. The travel

time is the difference between the two. However, the time, or delay, due to the wave traveling down to the bottom of the source rod must be substracted from the recorded travel time. The delay was measured in the laboratory as 0.35 ms. The corrected travel time from the bottom of the source rod to the receiver is listed in Table 9-5. The P-wave velocity is calculated from the distance between the source rod and the receiver (0.3 m) and the travel time.

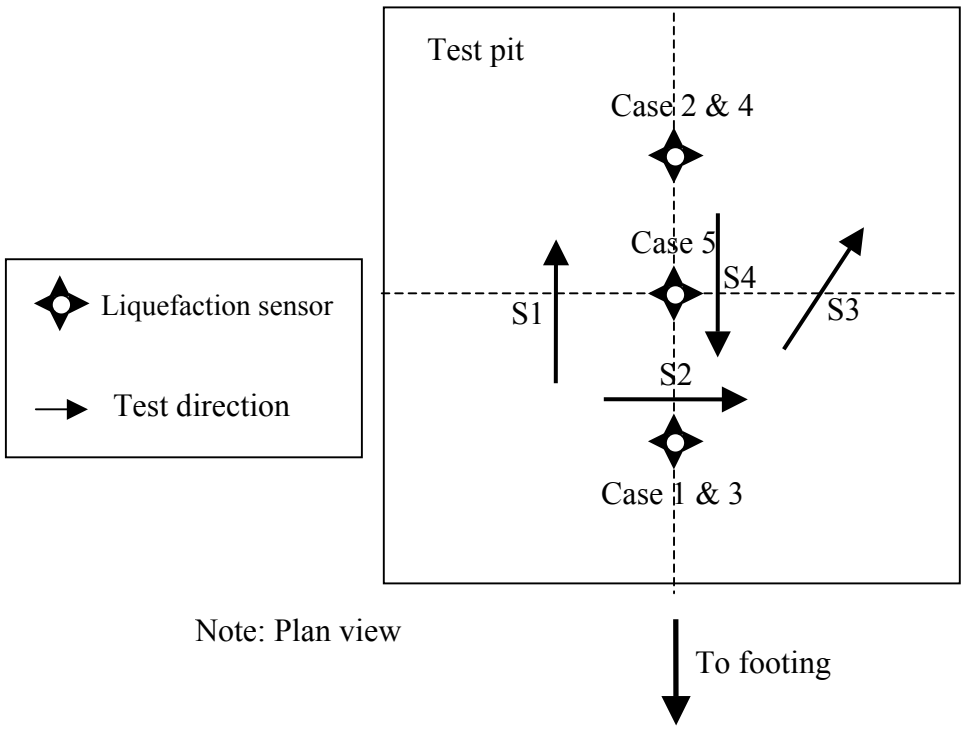

Figure 9-10 Locations of the saturation testing profiles

Table 9-5 Results of P-wave velocity measurement using movable P-wave receiver

Profile	S1		S2		S3		S4	
Depth (cm)	$\Delta t^{(1)}$ (ms)	$V_P^{(2)}$ (m/s)	Δt (ms)	V_P (m/s)	Δt (ms)	V_P (m/s)	Δt (ms)	V_P (m/s)
2.5	0.690	442	--- (3)	---	---	---	---	---
5.1	0.670	455	---	---	0.426	716	---	---
7.6	0.503	606	0.435	701	0.503	606	0.488	625
10.2	0.540	564	0.426	716	0.426	716	0.364	838
12.7	0.426	716	---	---	0.163	1876	0.390	782
15.2	0.285	1070	0.158	1929	0.163	1876	0.284	1074
17.8	0.297	1027	0.158	1929	---	---	0.284	1074
20.3	0.285	1070	---	---	0.162	1887	0.284	1074
22.9	0.285	1070	0.158	1929	---	---	0.281	1084
25.4	0.358	853	---	---	0.156	1929	0.274	1114
27.9	0.268	1137	0.158	1929	---	---	0.323	944
30.5	0.214	1428	---	---	0.156	1929	0.258	1181
33.0	0.166	1836	0.158	1929	---	---	0.204	1496
35.6	0.160	1905	---	---	0.156	1929	0.204	1496
38.1	0.160	1905	0.158	1929	---	---	---	---
40.6	0.160	1905	---	---	---	---	0.181	1682
43.2	0.160	1905	---	---	---	---	---	---
45.7	0.160	1905	---	---	---	---	---	---
48.3	0.160	1905	---	---	---	---	---	---
50.8	0.160	1905	---	---	---	---	---	---

Note: (1) Corrected for source rod delay
(2) Travel distance = 0.3 m (1 ft)
(3) No measurement data

Table 9-5 indicates saturation (V_P>1500 m/s) below about 30 cm for profiles S1 and S4. For profiles S2 and S3, saturation is observed below about 12 cm. Although the zone of partial saturation varied between the different profiles, the results indicate that the specimen is fully saturated below about 0.33 m (1.1

ft). Generally, the area within the instrumented array is close to saturation based on the P-wave measurements. It should be noted that if the soil surrounding the liquefaction sensors was significantly unsaturated, the hydrodynamic pressure response would be affected. However, the pore pressure-time histories show a strong hydrodynamic component. Therefore, it is concluded that the sample preparation procedure produces a saturated specimen and the PPTs are operating successfully.

9.3.2 In situ density measurement

As introduced in Chapter 6, the initial density of the reconstituted specimen is estimated from the measured weight of soil placed in the test pit and the known volume of the test pit. The initial void ratio and unit weight are estimated by assuming the prepared test specimen is saturated. To assess the accuracy of these estimated values, the in situ density was measured during the sensor retrieval process. Three in situ density measurements were conducted at different depths in the test specimen for test series T2. Because the in situ density was measured after the end of the test series, the measured values are the final density. The results are compared with the final density estimated from the initial density and the measured settlement. The results of the in situ density measurements are summarized in Table 9-6. The average relative density from the three samples was 61.6 %, and the estimated final relative density was 61.2 %. These values are very close and verify the estimated relative density.

Table 9-6 Results of in situ density measurements for test series T2

Depth (m)	Dry sand weight (g)	Sand[(1)] volume (cm^3)	Total volume (cm^3)	Void ratio e	Relative[(2)] density (D_r) (%)	Estimated [(3)] D_r (%)
0.15	1054.3	393.38	595.03	0.513	60.0	61.2
0.46	1056.3	394.14	595.03	0.510	61.4	61.2
0.76	1059.1	395.19	595.03	0.506	63.3	61.2

Note: (1) Gs=2.68

(2) e_{max}=0.64, e_{min}=0.43

(3) Corresponding to 4.3 cm settlement

9.4 SUMMARY

The test results from test series T2 are presented in this chapter. This test series was conducted under a more representative confining pressure by placing a layer of air-dried sand on top of the test specimen. Additionally, the liquefaction sensors were used in this test series, which resulted in five pore pressure transducers and 10 geophones. The test series was designed to measure pore pressure generation, evaluate the field performance of the liquefaction sensors, and compare the shear strain evaluation methods.

Eight tests were performed and the maximum excess pore pressure ratio induced was 46%. The corresponding maximum shear strain was about 0.015% at the center of the array, and the threshold shear strain was about 0.005%. The induced settlement was measured as 4.3 cm.

The pore pressure generation curves at the five sensor locations using the recorded excess pore pressure data and the shear strains calculated by the AW method show a unique relationship between the excess pore pressure ratio and the induced shear strain. This was first observed by Dobry et al. (1982) in laboratory tests.

P-wave velocity measurements were employed to verify the saturation of the test specimen. The results indicated that the area within the instrumented array was close to saturation based on the P-wave measurements. The evaluation of the saturation of the specimen, and the recorded hydrodynamic pore pressure response demonstrated that the sample preparation procedure produces a saturated specimen and that the PPTs are operating successfully.

The in situ density of the test specimen was directly measured to evaluate the accuracy of the estimated in situ density. The directly measured in situ density values were very close to the estimated values. The results verify the estimated relative density.

Chapter 10. Results from Test Series T3

10.1 INTRODUCTION

The pore pressure generation curve, represented by the induced shear strain level and the excess pore pressure ratio, is related to the number of loading cycles applied to the specimen. Because the maximum excess pore pressure in test series T2 was only about 50%, it was decided to increase the number of the loading cycles to generate larger excess pore pressure ratios. Also, this tests series allowed the pore pressure generation behavior for a long duration loading to be studied. The test results from test series T3 are presented in this chapter in a manner similar to test series T2 (Chapter 9). In addition, four settlement platforms were installed at different depths within this test specimen to observe the distribution of settlement versus depth. The measured settlement data are presented as well.

10.2 TEST RESULTS FROM TEST SERIES T3

In test series T3, the sensors and layout were similar to test series T2, except that three more settlement platforms were installed within the test specimen. The main goals for test series T3 are to study excess pore pressure behavior for a larger number of loading cycles and to observe the distribution of settlement versus depth. In test series T3, the vibroseis truck was operated for 3

seconds at a loading frequency of 20 Hz. Therefore, 60 loading cycles were applied to the test specimen.

10.2.1 Description of test series T3

The schematic layout for test series T3 is shown in Figure 10-1. The major modification is the installation of three more settlement platforms at different depths in the test specimen to measure settlement (i.e., vertical strain) inside the test specimen. In total, four settlement platforms were installed, three at depths of 0.96 m, 0.72 m, and 0.39 m, and one on top of the test specimen beneath the overburden. A 0.9-m layer of air-dried sand was placed on top of the test specimen as overburden to increase the stresses.

The same soil used in test series T1 and T2 was used for test series T3. The initial and final physical properties of the reconstituted test specimen for test series T3 are listed in Table 10-1. The final values are estimated based on 4.7 cm (1.7 in.) of settlement measured at the top of the specimen.

In this test series, 60 loading cycles were applied to the test specimen. To minimize the effect of multiple dynamic loadings, only five tests were conducted in test series T3.

Similar to test series T2, crosshole P-wave velocity measurements were performed to evaluate the saturation of the test specimen. The P-wave measurements made before test T3-1 are shown in Figure 10-2. The time histories from the receivers in cases 1 and 2 are shown in Figure 10-2(a) and the

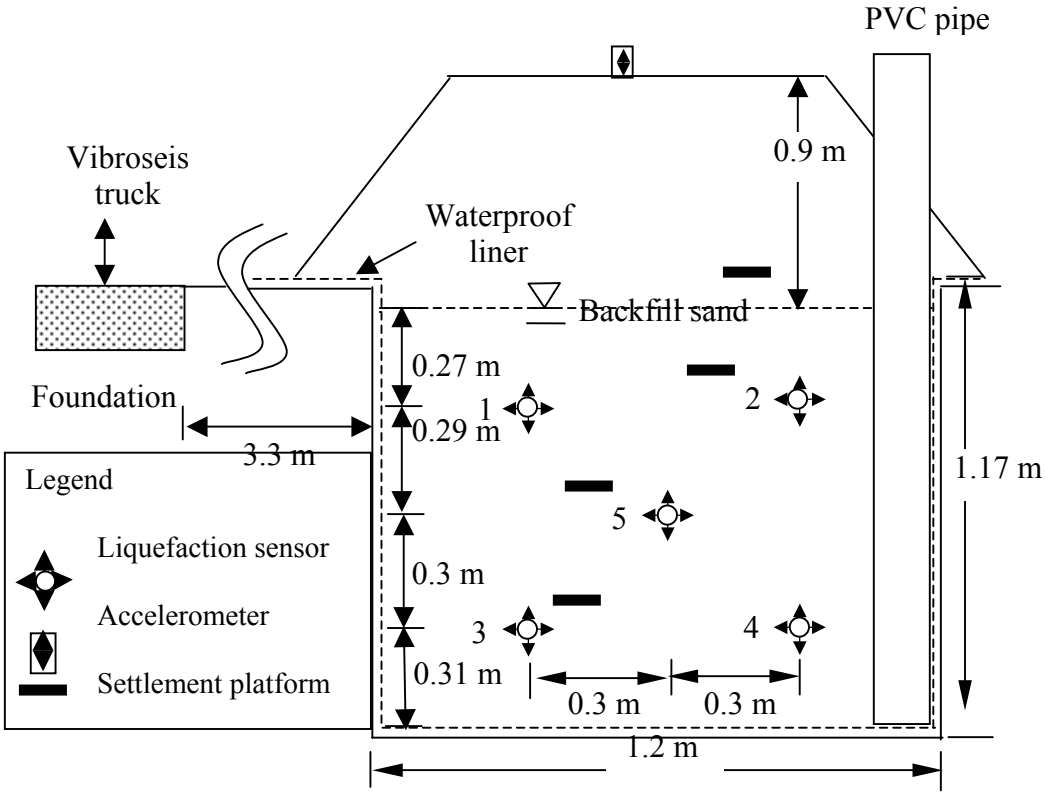

Figure 10-1 Schematic layout of test series T3

Table 10-1 Physical properties of the reconstituted specimen for test series T3

Soil Property		**Value**
Specific gravity (G_s)		2.68
Maximum void ratio (e_{max})		0.64
Minimum void ratio (e_{min})		0.43
Fines content		0.43%
Initial	Relative density (D_r,)	36.0%
	Water content (w)	21.0%
	Total unit weight (γ_t)	20.3 kN/m^3 (129.5 pcf)
Final[(1)]	Relative density (D_r,)	64.0%
	Water content (w)	18.8%
	Total unit weight (γ_t)	20.7 kN/m^3 (132.1 pcf)

Note: [(1)] These values are estimated from 4.3 cm (1.7 in.) settlement

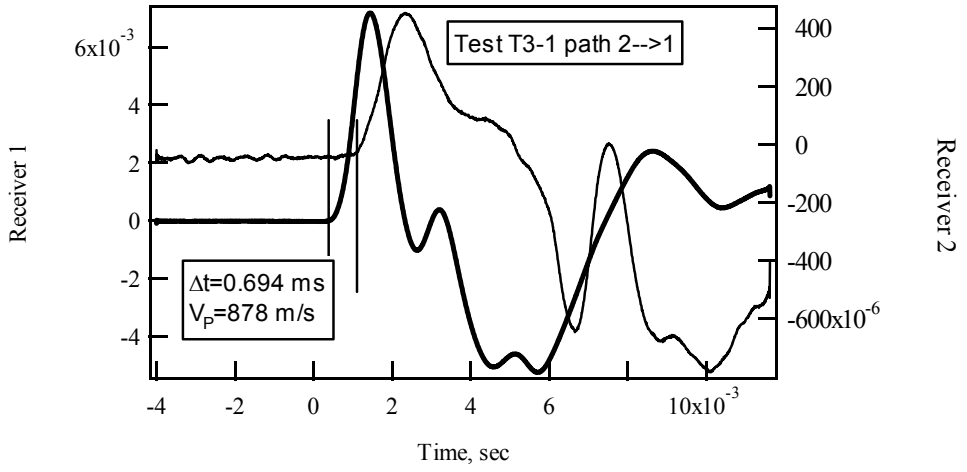

(a) Crosshole P-wave velocity measurement from case 2 to case 1

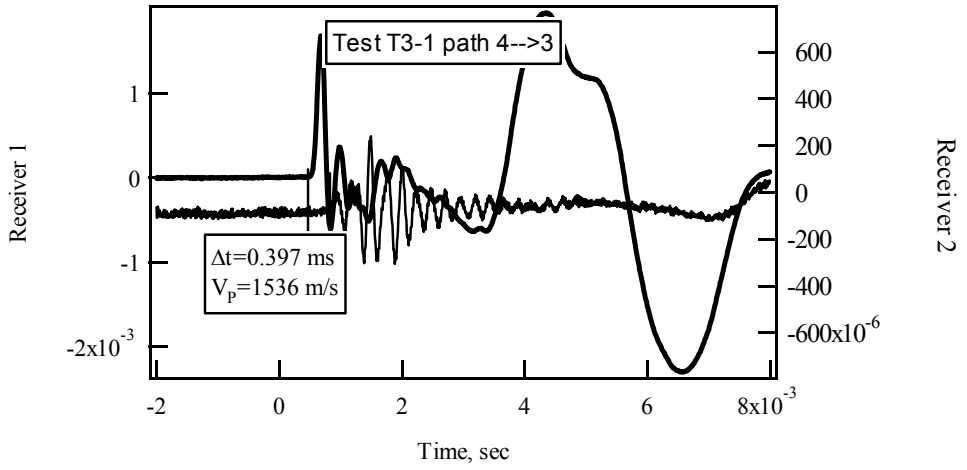

(b) Crosshole P-wave velocity measurement from case 4 to case 3

Figure 10-2 Crosshole signal-time histories for P-wave velocity measurement

results from the receivers in cases 3 and 4 are shown in Figure 10-2(b). The results indicate that the soil between cases 3 and 4 was saturated (V_P=1536 m/s) but the soil between cases 1 and 2 was not fully saturated (V_P=878 m/s). Although the P-wave velocity between cases 1 and 2 is relatively low and no high frequency waves were observed, the saturation level is still probably over 99.5% (Allen et al. 1980, Ishihara et al. 2001).

10.2.2 Geophone and accelerometer results

The recorded peak particle velocities for each test in test series T3 are summarized in Table 10-2. The maximum recorded vertical surface acceleration was 0.4 g and occurred during test T3-4. Similar to test series T2, the Fourier spectra of the velocity and surface acceleration data show a maximum response at 20 Hz, which coincides with the loading frequency. The measured velocities for a large strain level test (T3-4) are shown in Figure 10-3. Test T3-4 is chosen to display because significant excess pore pressure was observed, and significant vertical volumetric strain was induced. Again, the vertical velocities are larger and the horizontal velocity-time histories show varying amplitudes, as well as frequencies other than 20 Hz.

Table 10-2 Summary of the recorded peak particle velocities and surface acceleration for test series T3

Test #	H1 (cm/s)	V1 (cm/s)	H2 (cm/s)	V2 (cm/s)	H3 (cm/s)	V3 (cm/s)
T3-1	0.09	0.12	0.09	0.12	0.01	0.18
T3-2	0.18	0.30	0.20	0.27	0.04	0.18
T3-3	0.20	0.88	0.55	0.88	0.12	1.92
T3-4	0.82	2.07	0.85	1.52	0.70	1.92
T3-5	1.16	2.07	0.76	1.74	0.73	1.80

Test #	H4 (cm/s)	V4 (cm/s)	H5 (cm/s)	V5 (cm/s)	a_{max} (1) (g)
T3-1	0.02	0.18	0.04	0.10	0.02
T3-2	0.06	0.30	0.09	0.26	0.05
T3-3	0.23	0.88	0.24	0.79	0.24
T3-4	1.07	1.31	1.04	1.40	0.40
T3-5	0.82	1.52	1.04	1.65	0.36

Note: (1) Measured at the top of the overburden

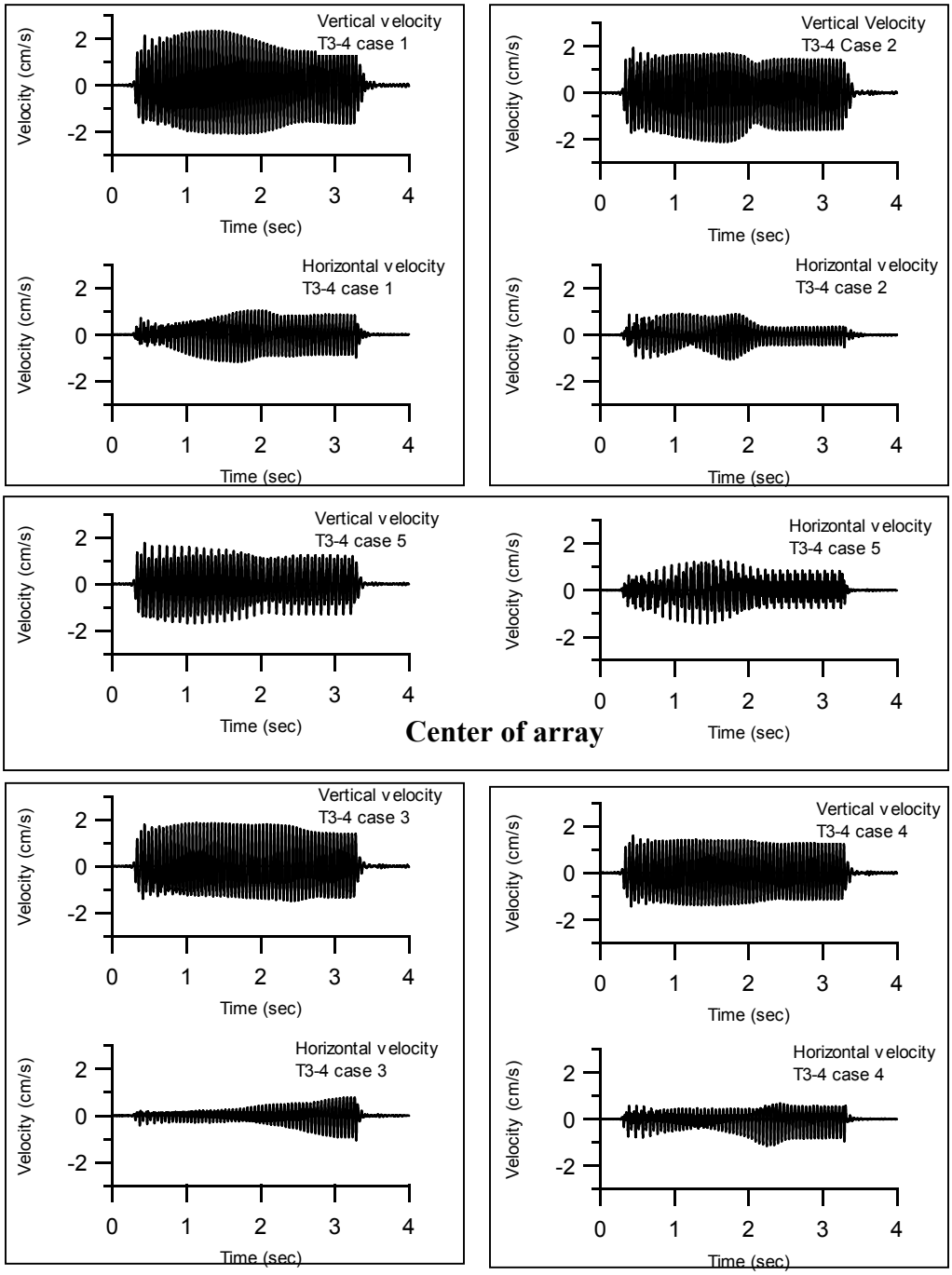

Figure 10-3 Measured velocity-time histories during test T3-4

10.2.3 Shear strain and pore pressure-time histories

The tests conducted in test series T3 are divided into two groups according to the induced mean shear strain levels. The low shear strain group includes tests T3-1 and T3-2, which had no or small excess pore pressure generated during the dynamic loading. The large shear strain level group includes tests T3-3 through T3-5, and these tests showed significant excess pore pressure and the shear strain amplitude varied during the dynamic loading.

To apply the wave propagation-based shear strain calculation methods, wave velocities are needed. Again, crosshole seismic tests were performed to measure the shear wave velocity before and after dynamic loading. The shear wave velocities measured before dynamic loading and the apparent wave velocities measured during dynamic loading are summarized in Table 10-3. The measured shear wave velocities are similar to those measured in test series T2. Again, the shear wave velocities measured throughout the test series vary within 10% of the initial values, with no observable trend. The apparent wave velocities tend to increase with each dynamic loading. This trend is discussed further in Chapter 11. The velocities listed in Table 10-3 are used in the PSW and AW strain evaluation methods. The Rayleigh wave velocity used in the PRW method is 152 m/s (500 ft/s), which is the same value used in test series T1 and T2. The ratio between the shear strain and the normalized vertical particle velocity ($\alpha_{v,}$) was taken as -1.767 and -1.454 for depths of 0.27 m and 0.86 m, respectively.

Table 10-3 Measured shear wave velocities and apparent wave velocities for test series T3

Test	Shear wave velocity[1] (m/s)		Apparent wave velocity[2] (m/s)	
	Path 2→ 1[3]	Path 4 → 3	Path 1→ 2	Path 3 → 4
T3-1	90	107	122	115
T3-2	85	107	123	145
T3-3	84	119	175	131
T3-4	80	97	175	161
T3-5	87	97	123	140
Final	88	97	---	---

Note: (1) Measured before each test
(2) Measured during dynamic loading
(3) Sensor number

The shear strain-time histories from test T3-2 are shown in Figure 10-4. The shear strains shown in this figure are calculated using the AW method at the 4 sensor points of the array and the shear strain-time histories at the center of the array are computed using the SDM method and the average of the AW strains at the four sensor points. For each time history, the shear strain amplitude remains approximately constant during the entire loading.

Test T3-4 experienced the largest mean shear strain level and the largest excess pore pressure ratio. The shear strain-time histories for test T3-4 are shown in Figure 10-5. The shear strain-time histories at the center of the array for test T3-4 are different than those from test T3-2. The strains are much larger for test T3-4 and the shear strain-time history computed at the center of the array using the SDM method shows a significant variation in amplitude over the loading cycles. The maximum strain is about 0.017% and occurs after about 15 cycles. After this point, the amplitude decreases and eventually reduces to less than half

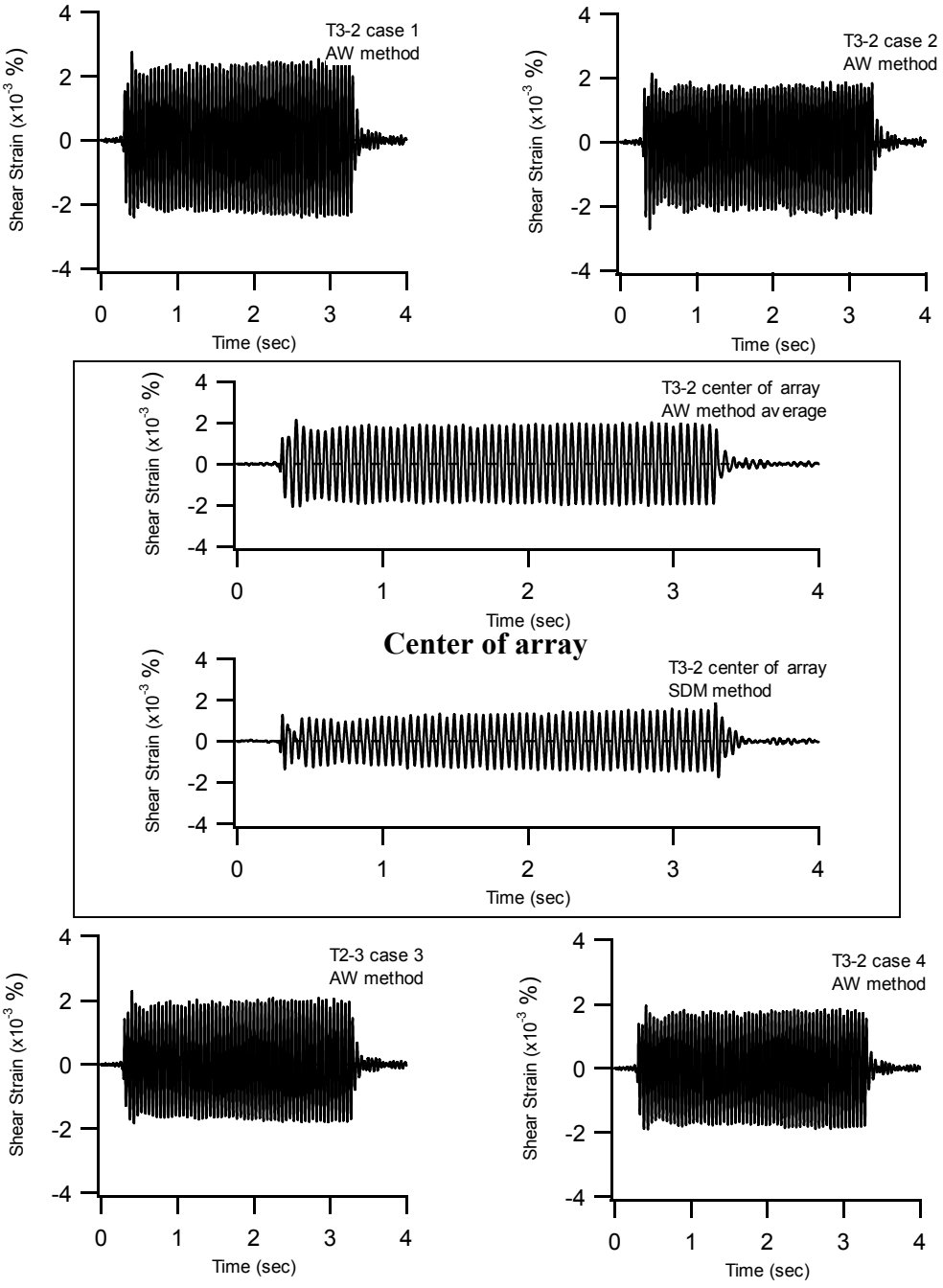

Figure 10-4 Shear strain-time histories at the 4 nodal points and at the center of the array for test T3-2 (low strain level test)

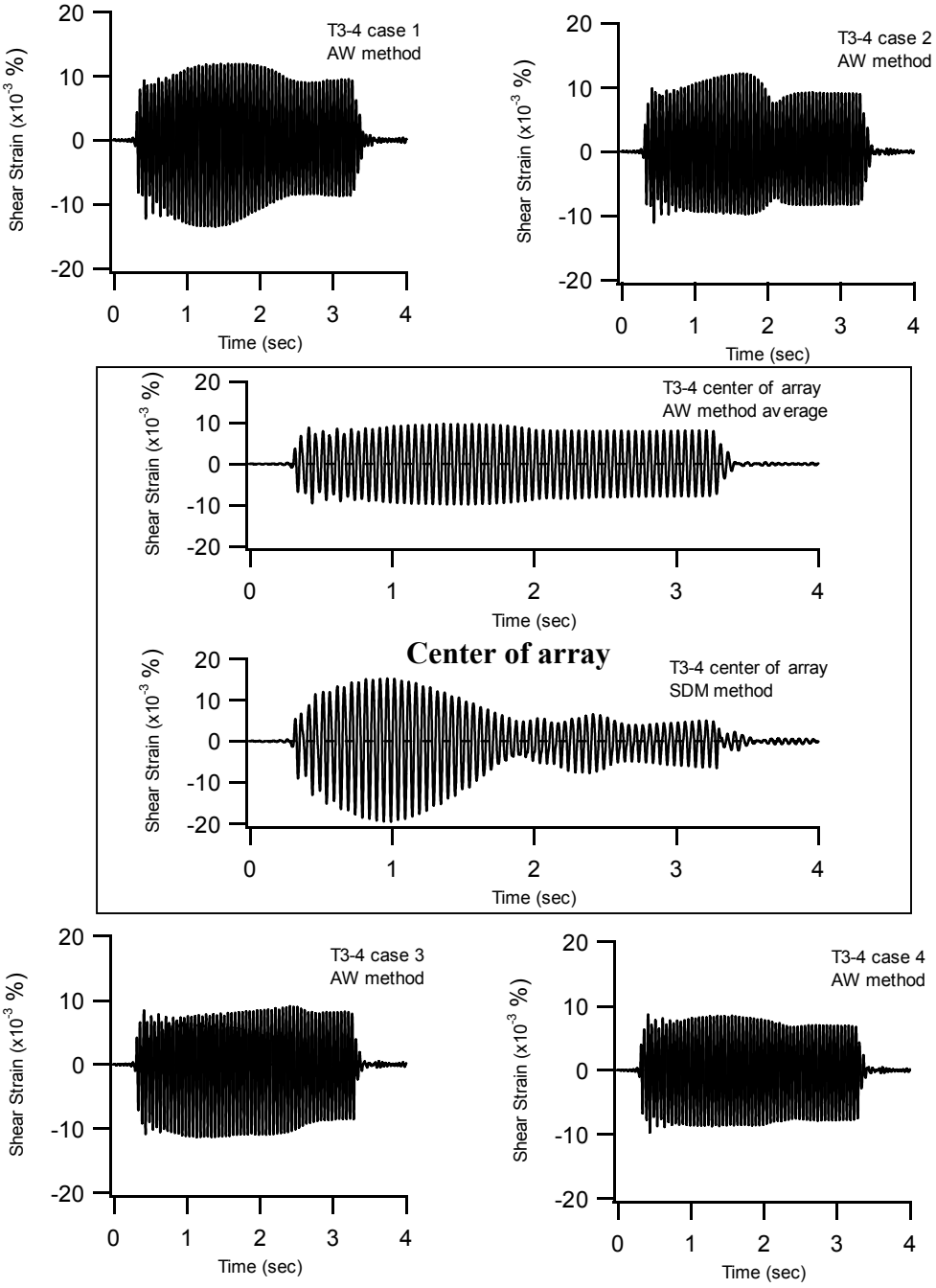

Figure 10-5 Shear strain-time histories at the 4 sensor points and at the center of the array for test T3-4 (large strain level test)

its peak value. Further discussions regarding the variation in shear strain amplitude are presented in Chapter 11.

The pore pressure ratio-time histories for test T3-4 are shown in Figure 10-6. Hydrodynamic pore pressure and residual pore pressures are again observed. For cases 1 and 2, the hydrodynamic peak to peak amplitude is about 20% and remains relatively constant. For cases 3, 4, and 5, the hydrodynamic peak to peak amplitude is about 30%. However, for these records the hydrodynamic amplitudes increase as the loading progresses. At the center of the array, the maximum residual pore pressure ratio is 62%. Slightly different values were reached at the four other sensors. Unlike the results from the 20 cycle tests (Test series T2), the pore pressures in Figure10-6 reach their maximum before the end of dynamic loading. These results are discussed further in Chapter 11.

10.2.4 Pore pressure generation curves

The mean shear strain amplitudes (γ_{xz}) from the different shear strain evaluation methods, the maximum excess residual pore pressure ($u_{r,max}$), and the excess pore pressure ratios (r_u) at the center of the array for this test series are summarized in Table 10-4. The vertical effective stress was computed by assuming the total unit weight of sand used as overburden was 17.3 kN/m^3 (110 pcf) and the water table remained at the top of the test specimen.

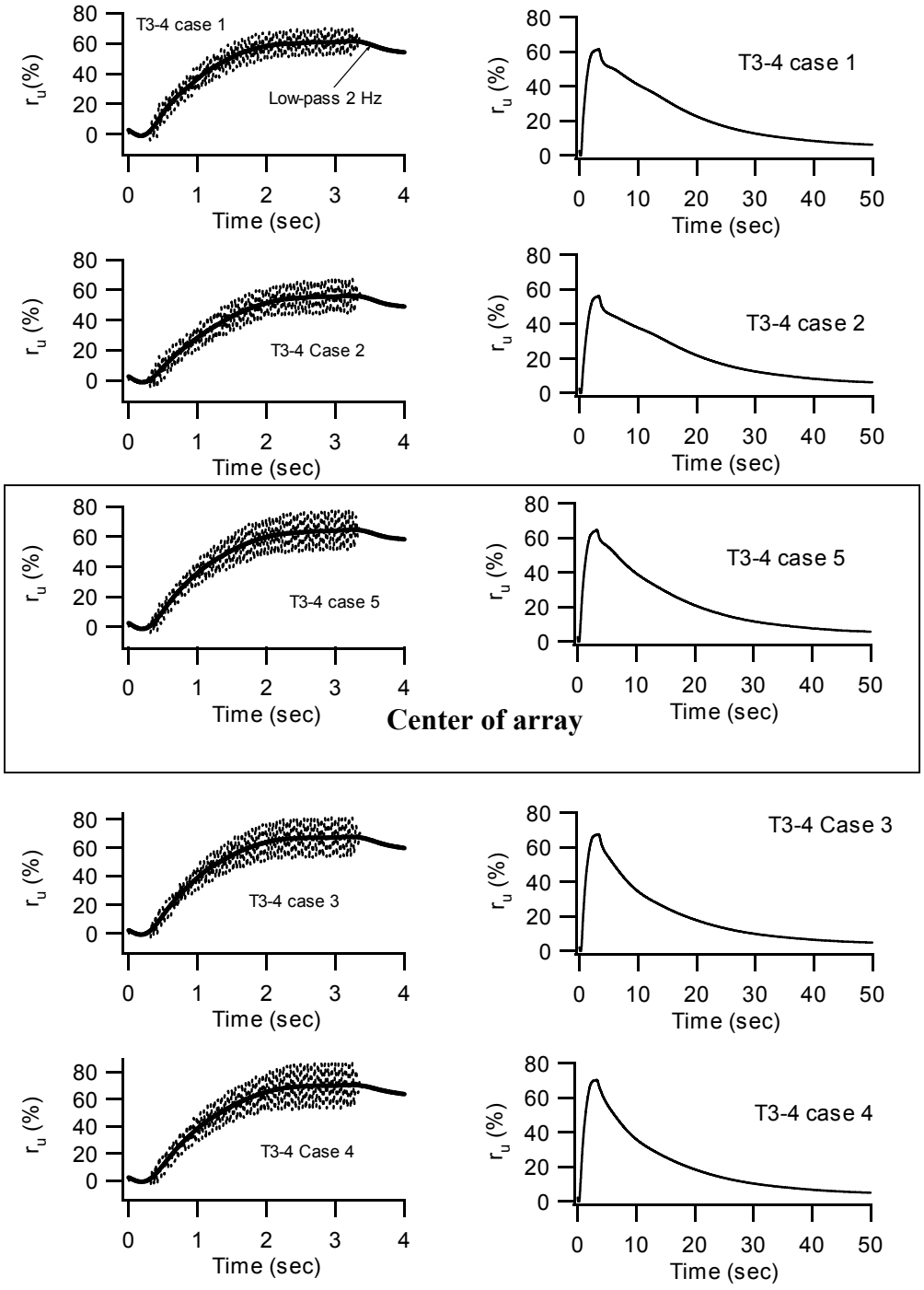

Figure 10-6 Pore pressure ratio-time histories for test T3-4 (large strain level test)

Table 10-4 Summary of results of induced shear strains and excess pore pressures at the center of the array for test series T3

Test	SDM γ_{xz} (%)	PSW γ_{xz} (%)	PRW γ_{xz} (%)	AW γ_{xz} (%)	$\Delta u_{r,max}$ [1] (kPa)	r_u [2] (%)	Dr [3] (%)
T3-1	1.60E-04	1.52E-03	1.56E-03	1.28E-03	0.00	0.0	36
T3-2	1.40E-03	2.84E-03	2.84E-03	2.02E-03	0.16	0.8	36
T3-3	7.50E-03	1.12E-02	1.18E-02	7.89E-03	3.24	15.4	36
T3-4	1.30E-02	1.63E-02	1.68E-02	9.38E-03	13.30	61.7	44[4]
T3-5	1.50E-02	1.95E-02	1.90E-02	1.37E-02	13.70	63.4	52[5]

Note: (1) Does not include the hydrodynamic component
(2) Initial vertical effective stress at center of array = 21.6 kPa
(3) Before loading
(4) With respect to 1.2 cm of total settlement
(5) With respect to 2.4 cm of total settlement

The pore pressure generation curve at the center of the array for test series T3 using the various shear strain evaluation methods is shown in Figure 10-7. The pore pressure generation curves with shear strain calculated by the SDM method for different loading cycles are shown in Figure 10-8. Only the first four tests were used to construct the pore pressure generation curve because the relative density changed significantly after test T3-4. However, it is interesting to note that a larger pore pressure ratio was generated in test T3-5, even though the specimen had already been densified somewhat during test T3-4. Little or no pore pressure was generated at shear strains less than 0.002%. No tests were performed at strain levels between 0.002% and 0.008%. At a shear strain level of 0.008%, a pore pressure ratio of 15% was experienced. The maximum recorded excess pore pressure ratio was 62 % and it occurred at a mean shear strain level of about

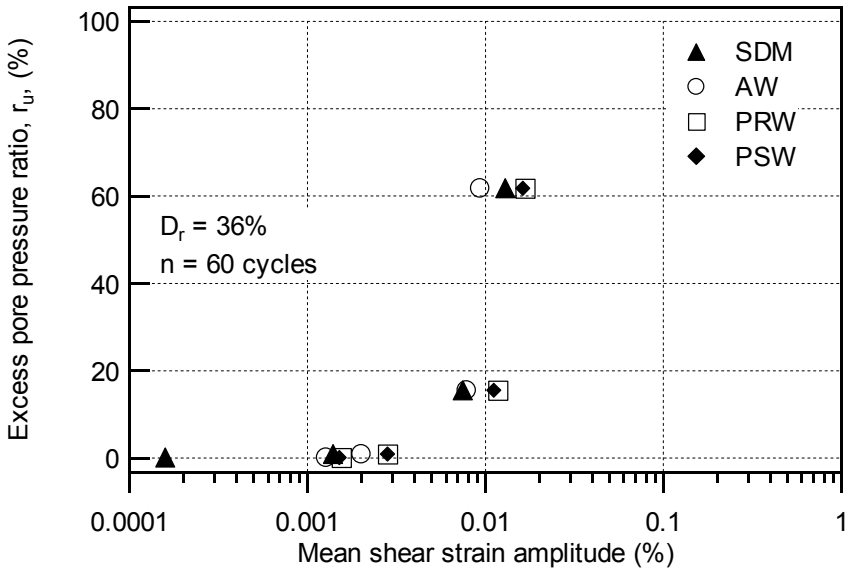

Figure 10-7 Pore pressure generation curves for test series T3 using different shear strain evaluation methods

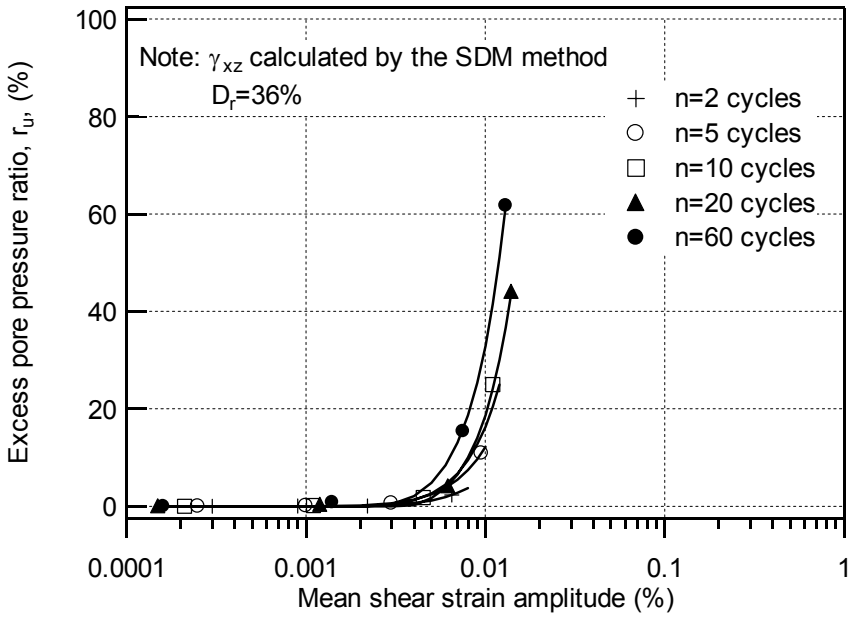

Figure 10-8 Pore pressure generation curves from Test series T3 for different numbers of loading cycles

0.01%. The permanent settlement after T3-5 was 4.3 cm, and that value corresponds to 2.6% volumetric strain.

The pore pressure generation curves at the five sensor locations using the recorded excess pore pressure data and the mean shear strains calculated by the AW method are shown in Figure 10-9. Again, all of the pore pressure generation curves fall in a narrow range. The results reveal a unique relationship between the excess pore pressure ratio and the induced shear strain for this test specimen which was first observed by Dobry et al. (1982) in laboratory tests.

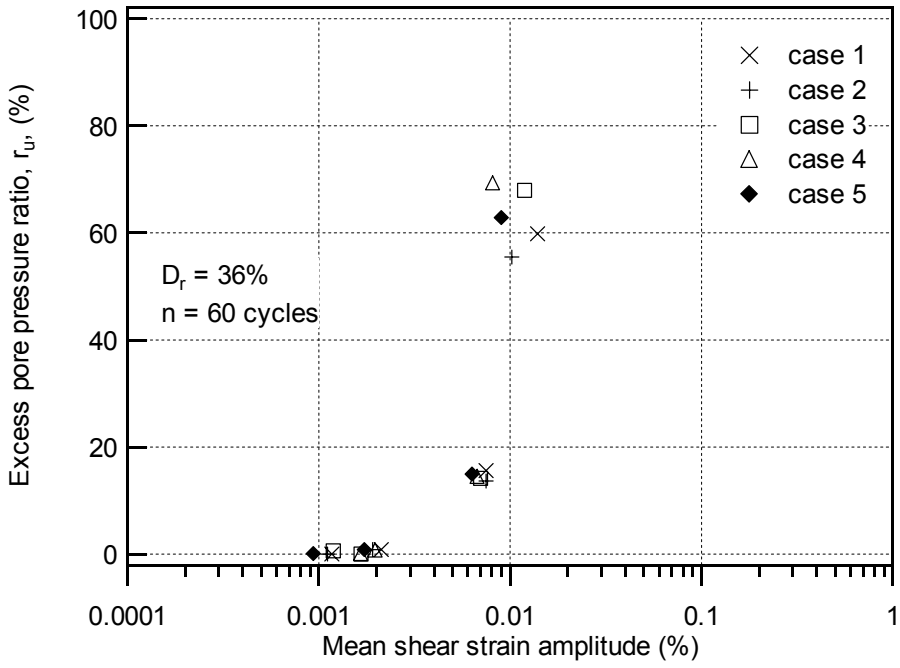

Figure 10-9 Pore pressure generation curves at 5 sensor points for test series T3

10.2.5 Settlement profile

In test series T3, four settlement platforms were installed at different depths to measure settlement versus depth. The measured settlement profile provides information regarding the induced settlement within the test specimen and the uniformity of the specimen. The settlement measurements at different depths during test series T3 are summarized in Table 10-5. The total settlement profiles after tests T3-3, T3-4, and at the final stage after test T3-5 are shown in Figure 10-10. It should be noted that the settlement is measured using an optical level and level rod with a resolution of 0.3 cm (0.01 ft). Therefore, very small settlements are hard to detect using the optical level and level rod. This is particularly important for settlement platforms SP-1 and SP-2, which are located at depth and experienced less settlement. At the final stage, a approximately linear relationship between total settlement and depth was observed. The linear relationship indicates that the induced vertical strain is uniform within the specimen.

10.3 SUMMARY

The third test series (T3) was conducted to study the excess pore pressure behavior for a large number of loading cycles and to observe the distribution of settlement versus depth. In test series T3, 60 loading cycles were applied to the test specimen at a loading frequency of 20 Hz. Five tests were performed and the maximum excess pore pressure ratio was about 60% at a shear strain level of about 0.013%.

Table 10-5 Summary of total settlement measurement for test series T3

Test #	SP-1 Depth=0.96 m Settlement[1] (cm)	SP-2 Depth=0.72 m Settlement (cm)	SP-3 Depth=0.39 m Settlement (cm)	SP-4 Depth=0 m Settlement (cm)
T5-1	0	0	0	0
T5-2	0	0	0	0
T5-3	0	0	0	0
T5-4	0.30	0.30	0.91	1.22
T5-5	0.91	0.91	2.13	2.44
Final	1.52	2.13	3.35	4.27

Note: (1) Measured after excess pore pressure dissipated

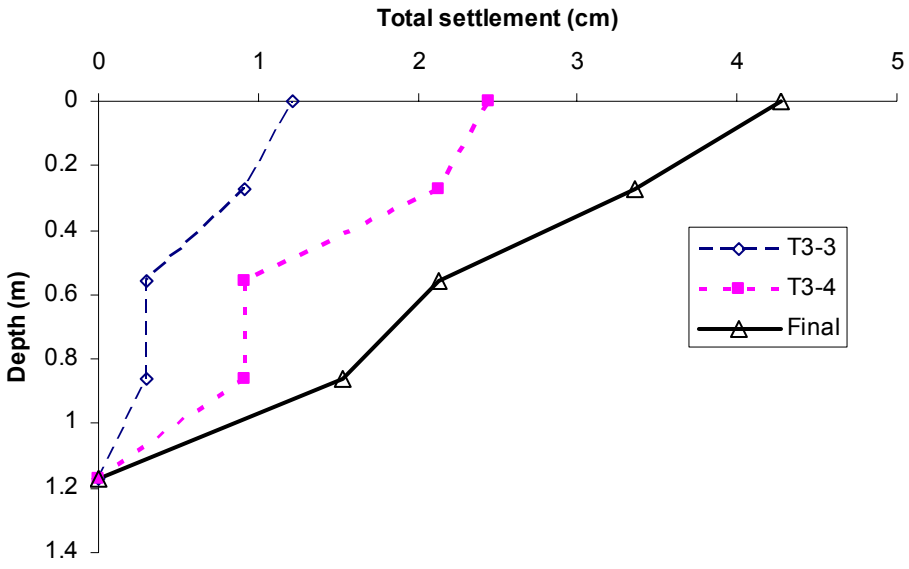

Figure 10-10 Total settlement profiles from test series T3

Crosshole P-wave velocity measurements were performed to evaluate the saturation of the test specimen. The results showed that the soil between cases 3 and 4 was saturated with V_P>1500 m/s. Although the P-wave velocity between cases 1 and 2 was relatively low (V_P=878 m/s), the saturation level is believed to be over 99.5%.

The shear strain-time history computed at the center of the array using the SDM method for test T3-4 showed a significant variation in amplitude over the loading cycles. Also, the pore pressure ratio-time history for test T3-4 reaches its maximum before the end of the dynamic loading, which is different from the observations from previous tests. Further discussions regarding the strain level variation during dynamic loading and the corresponding excess pore pressure behavior are presented in Chapter 11.

Four settlement platforms were placed at different depths within the test specimen to study the total settlement versus depth. A linear relationship between total settlement and depth was observed. The linear relationship indicates that the induced vertical strain was uniform within the test specimen.

Chapter 11. Discussion of Test Results

11.1 INTRODUCTION

This chapter presents discussions regarding several aspects of the test results. Specifically, the quality of the recorded particle motion and pore pressure data, the shear strain evaluation methods, the pore pressure generation curves, and pore pressure dissipation are discussed.

A qualitative assessment of the recorded data is presented in Section 11.2. This discussion includes the characteristics of the particle motion measured at the sensor points and the characteristics of the hydrodynamic pore pressure.

The shear strain-time histories computed by the SDM and AW methods are further discussed, with an emphasis on the variation in shear strain amplitude during large strain level tests. These discussions are provided in Section 11.3 and provide information regarding the applicability of these shear strain evaluation methods.

Observations regarding the pore pressure generation curves are presented in Section 11.4. The effects of confining stress and number of loading cycles, i.e. loading duration, on the pore pressure generation curves are investigated. Additionally, future laboratory experiments for validation of the collected data are introduced.

Finally, the dissipation characteristics of the excess pore pressure are described in Section 11.5. A comparison of the collected data and values calculated by Terzaghi's 1D consolidation theory is presented to verify the pore pressure dissipation behavior.

11.2 QUALITATIVE ASSESSMENT OF RECORDED DATA

The quality of the recorded data depends on the performance of the sensors and data acquisition systems. Two types of sensors were integrated into the liquefaction sensor, geophones and pore pressure transducers, and two data acquisition systems were employed to acquire the geophone and pore pressure transducer data. The qualitative assessment of the recorded data focuses on the recorded geophone and pore pressure transducer data.

The recorded geophone data are qualitatively evaluated through a comparison of the recorded particle motion with the particle motion predicted for the theoretical wave field. The discussions include the measured particle motion in the time domain, the frequency content of the particle velocities, and a comparison between the vertical and horizontal velocity amplitudes. The quality of the pore pressure data is assessed through the recorded hydrodynamic pore pressure. The hydrodynamic pore pressure is discussed with respect to the coupled behavior between the hydrodynamic pore pressure and wave propagation.

11.2.1 Assessment of recorded geophone data

For the current testing configuration, Rayleigh waves are the major wave type propagating through the instrumented test area. One of the unique characteristics of Rayleigh waves is retrograde elliptical particle motion near the ground surface. Because the liquefaction sensors contain two perpendicularly oriented geophones, the particle motion in the x-z plane (i.e., horizontal and vertical directions) can be displayed using displacement-time histories computed numerically from velocity-time histories. The particle motion at each liquefaction sensor during the 6th cycle of motion from test T2-3 is shown in Figure 11-1. Figure 11-1 shows retrograde elliptical particle motion inside the test specimen during this small strain level test. Also, the vertical displacements are always greater than the horizontal displacements, and the difference increases with depth. The inclined vertical axis of the ellipse in Figure 11-1 is due to the arrival of other wave types and reflected waves.

In contrast, more complicated wave motion was observed inside the test specimen during large-strain tests. The particle motion at each liquefaction sensor during the 6th cycle of motion during a large-strain test (T2-8) is shown in Figure 11-2. The particle motion traces at the five locations are significantly different than those from the small strain level test shown in Figure 11-1. For the first few cycles of motion (not shown in Figure 11-2), most of the sensors show retrograde elliptical motion. However, subsequent cycles show predominantly prograde elliptical motion (Figure 11-2). The reason is not quite clear at this point. A possible explanation is nonlinear wave propagation behavior and the presence of

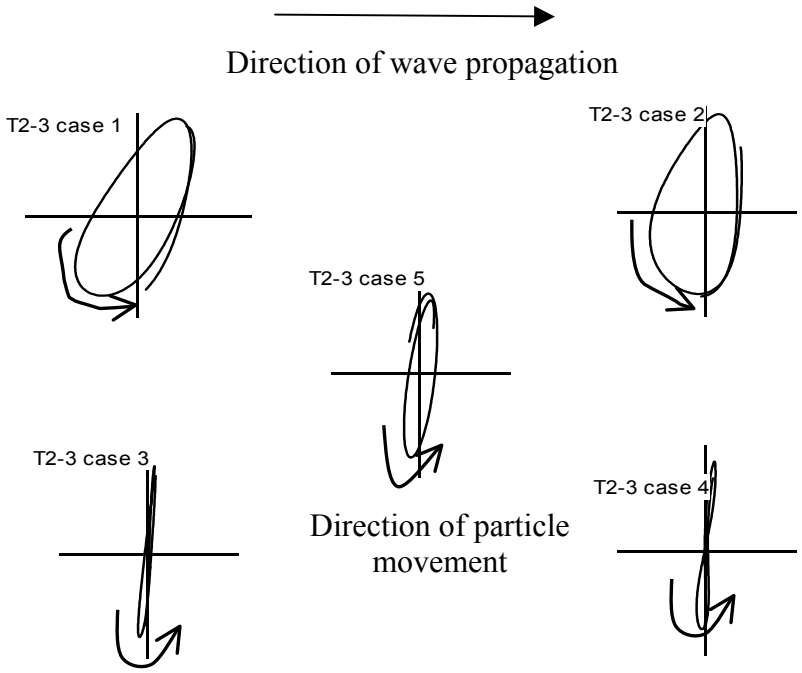

Figure 11-1 Retrograde elliptical displacement motion from test T2-3 (6^{th} cycle, small-strain test)

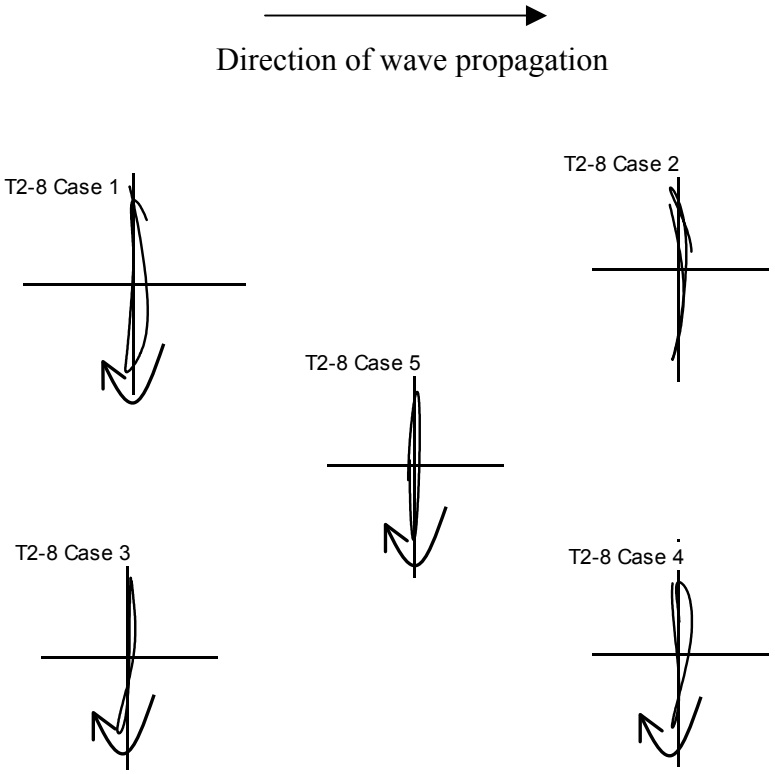

Figure 11-2 Particle motion for the 6th cycle in large-strain test T2-8

reflected waves. The irregularity in the particle motion during large-strain tests indicates that the wave propagation-based methods may have larger errors at larger strain levels.

The Fourier spectra of the measured velocity data from test T2-8 are shown in Figure 11-3. The dominant frequency for both the vertical and horizontal velocities is 20 Hz, which is coincident with the loading frequency. However, the Fourier spectra also show significant motion at 40 Hz. For

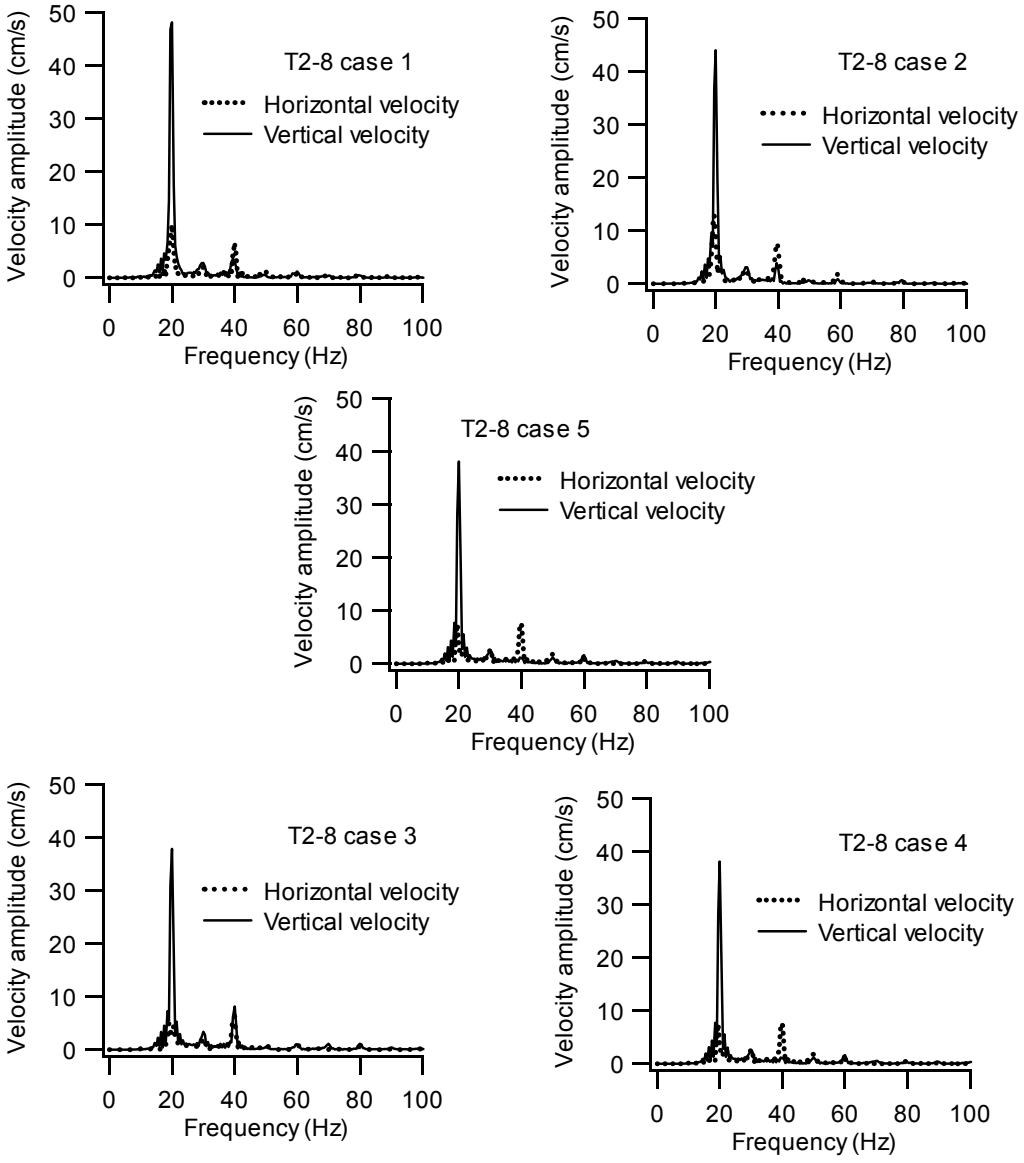

Figure 11-3 Fourier spectra of measured particle velocity from Test T2-8

horizontal motion, the 40 Hz motion can be as large as the 20 Hz motion. The 40 Hz motion may be a result of a higher mode of vibration of the source. At each measurement location, the vertical velocity is always greater than the horizontal velocity. In addition, the amplitude decreases with depth and distance from the dynamic source. These observations reveal that the measured particle velocities satisfy the general trends of wave propagation behavior. It should be noted that the Fourier spectra in Figure 11-3 are from a large strain level test (T2-8). The velocity records from the large strain level tests are more complicated than the records from the small strain level tests, as demonstrated in Figures 11-1 and 11-2. Even with this additional complication, the velocity data from the large-strain tests still agree with most of the expected trends for wave propagation.

11.2.2 Assessment of recorded pore pressure data

During dynamic loading, two types of excess pore pressure are generated: hydrodynamic and residual excess pore pressure. A well-designed and properly installed pore pressure transducer should be able to capture both components of pore pressure. As mentioned before, the major sources of error for an in situ pore pressure transducer are time lag and a reduced magnitude of measured pore pressure caused by trapped air between the filter and pressure-sensing diaphragm. For this study, it is proposed that these errors are small if the pore pressure transducer can capture the hydrodynamic pore pressure.

Scott and Hushmand (1995a) conducted a series of tests at Treasure Island, CA to calibrate previously installed USGS piezometers against a separate

push-in piezometer. The two criteria used to evaluate the performance of the USGS piezometers were the occurrence of pore pressure spikes that were relatively coincident with the acceleration records and the magnitude of the measured excess pore pressure. The pore pressure spikes in the Scott and Hushmand (1995a) study are analogous to the hydrodynamic pore pressure in this study and the acceleration is used to represent the passage of a dynamic disturbance. Similar criteria are addressed for the pore pressure transducers used in this study.

The evaluation of the field performance of the miniature pore pressure transducers (PPT) in the liquefaction sensors are assessed by looking at the hydrodynamic pore pressure time records. The hydrodynamic pore pressure is viewed as a response to the volumetric component of the wavefronts. This motion causes an increase in the mean stress that is transferred to water pressure due to the undrained condition. The magnitude and frequency of the hydrodynamic pore pressure should be closely related to the dynamic source. To study the hydrodynamic excess pore pressures separately, two digital filters are applied. A low-pass filter with a cut-off frequency of 2 Hz is used to highlight the residual pore pressure and a band-pass filter, preserving the signals between 15 Hz and 25 Hz, is used to highlight the hydrodynamic pore pressure. The pore pressure records from the center of the array (i.e., case 5) during test T2-8 are illustrated in Figure 11-4. The hydrodynamic excess pore pressure shows a dominant frequency of 20 Hz, which indicates that the hydrodynamic pressure is a result of wave passage from the source. The time histories of the vertical velocity measured at

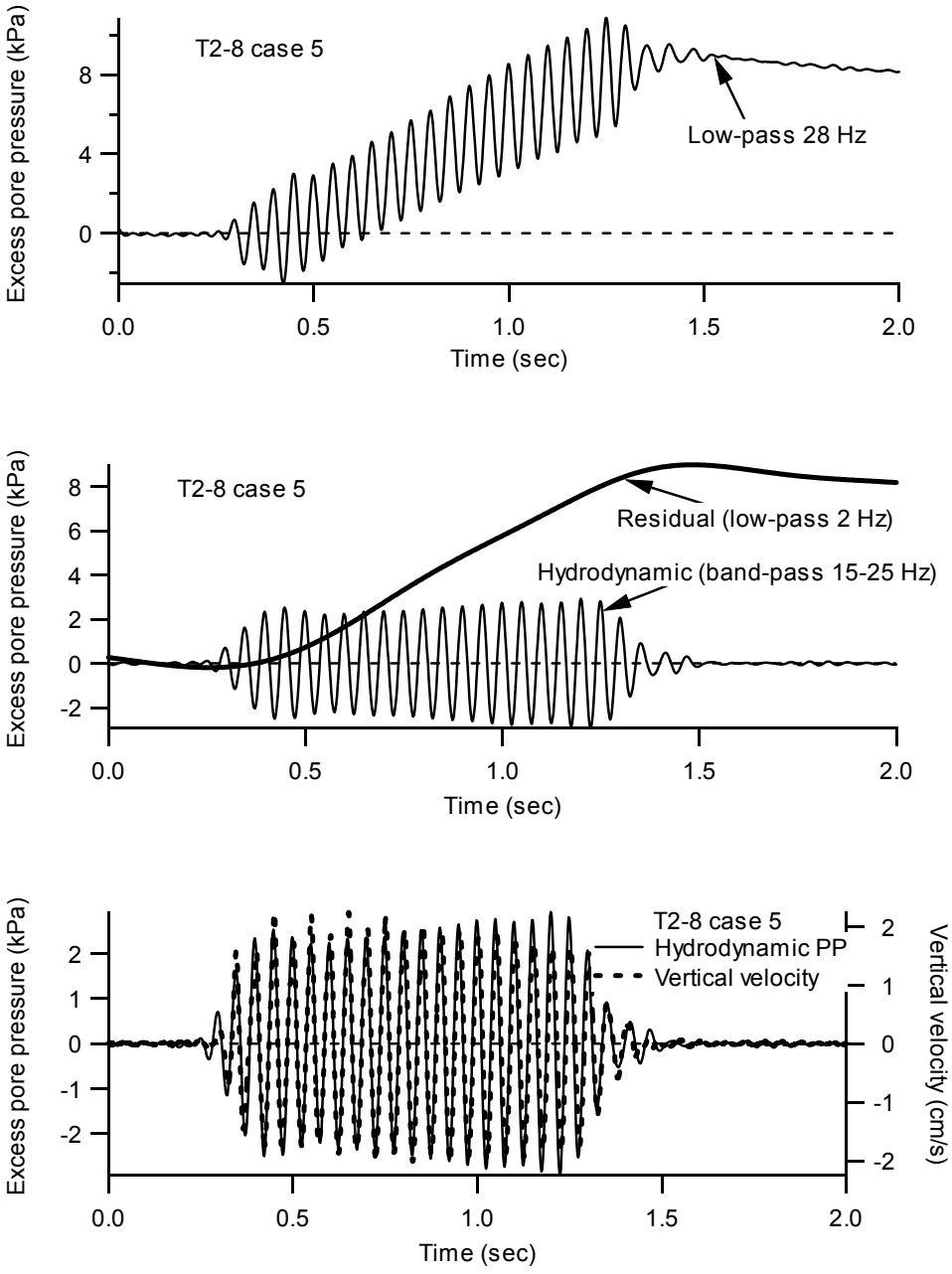

Figure 11-4 Hydrodynamic and residual pore pressure-time histories and the coupling of hydrodynamic pore pressure with vertical velocity (T2-8, case 5)

the same liquefaction sensor (case 5) are shown in the same figure, and these time records indicate that the hydrodynamic pore pressure is in phase with the vertical velocity measured at the same point. Other liquefaction sensors located at the measurement points show the same response.

Dobry et al. (1982) described the hydrodynamic pore pressure as an "elastic" pore pressure that should be proportional to the cyclic deviator stress in cyclic triaxial tests because the cyclic deviator stress is proportional to the increase in mean stress. Under undrained condition, this increase in mean stress is transferred to excess pore pressure. For the current test configuration, the stresses induced by propagating waves should be proportional to the amplitude of particle motion. The hydrodynamic pore pressures recorded at the center of the array and the measured horizontal and vertical particle velocity amplitudes from tests T2-1 through T2-8 are shown in Figure 11-5. A reasonably linear relationship exists between the measured hydrodynamic excess pore pressure and the particle velocities, particularly for horizontal velocity.

These data indicate that the pore pressure transducer in the liquefaction sensor is capable of capturing the hydrodynamic pore pressure, and therefore is operating correctly.

11.3 SHEAR STRAIN-TIME HISTORIES

In Chapter 5, the average shear strains computed by the various shear strain evaluation methods are compared. The results indicated that the SDM method and the AW method produce similar values of mean shear strain, when

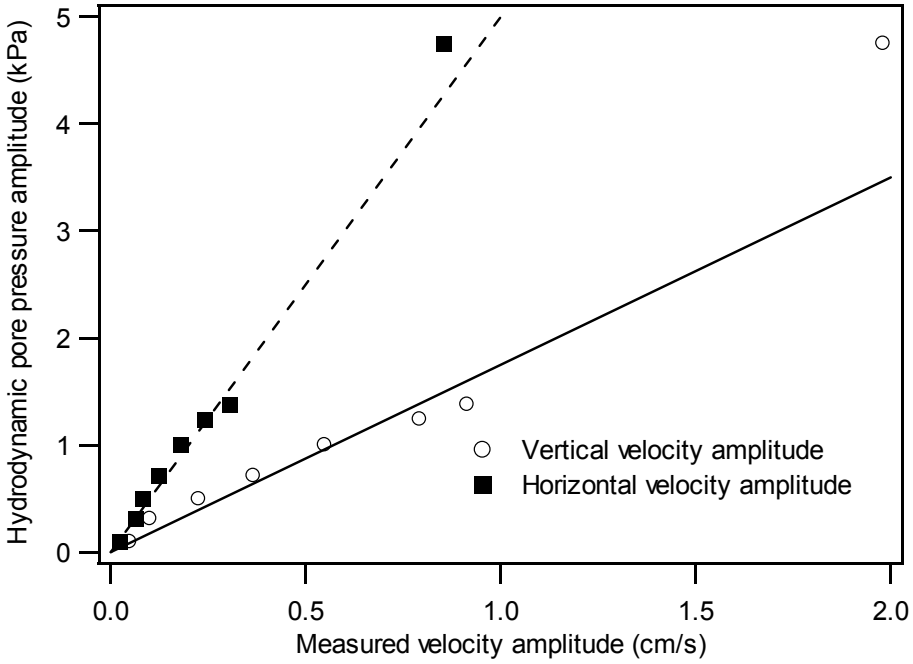

Figure 11-5 Relationship between measured hydrodynamic excess pore pressure and particle velocity amplitude (tests T2-1 to T2-8)

the shear strain-time histories are averaged over their entire length. A comparison of the full time histories is presented here. The shear strain-time histories computed by the AW and SDM methods at the center of the array for a small shear strain level test (T2-3) and a large shear strain level test (T2-8) are shown in Figure 11-6. The shear strains computed by the AW method in Figure 11-6 are calculated using the measured vertical particle velocities at the center vertical geophone in case 5.

In the small-strain test (T2-3), the shear strain-time histories computed by the AW and SDM methods are very similar throughout the dynamic loading and

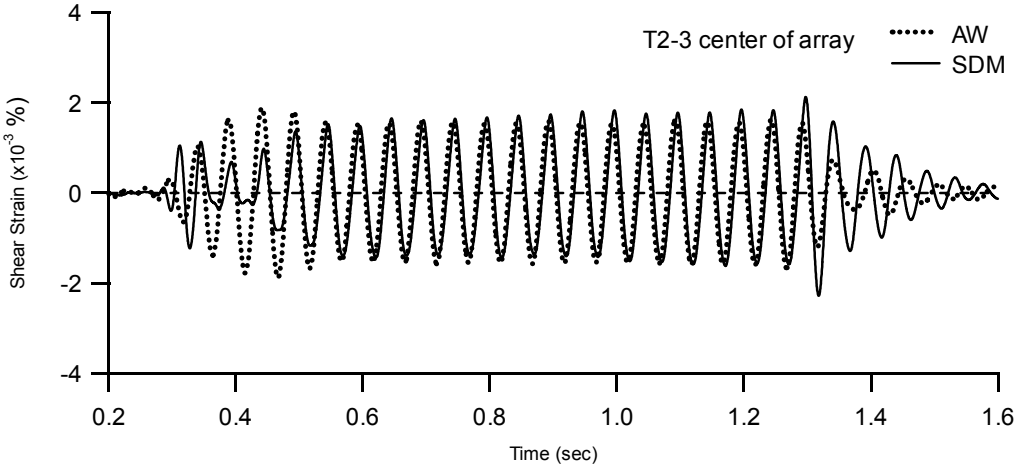

(a) Small-strain test (T2-3)

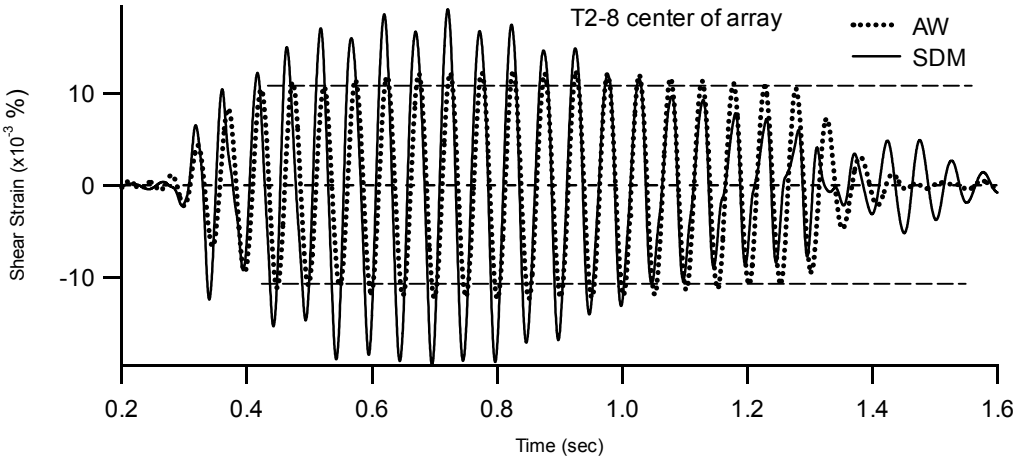

(b) Large-strain test (T2-8)

Figure 11-6 Comparison of shear strain-time histories at the center of the array calculated from the AW method and the SDM method

the shear strain amplitudes are relatively constant (Figure 11-6(a)). However, in the large-strain test (T2-8), the shear strain-time histories from the AW and SDM methods are significantly different after about the first three cycles (Figure 11-6(b)). The shear strain amplitudes computed by the SDM method vary considerably during the loading cycles, while the shear strain amplitudes computed by the AW method remain relatively constant. Although the average shear strain amplitudes from the AW and SDM methods are quite similar, the maximum shear strain and the large variation in amplitude between cycles are different.

The discrepancies between the shear strain-time histories computed by the SDM and AW methods during large strain tests (Figure 11-6(b)) raise questions about the shear strain evaluation methods. The two shear strain-time histories may represent different shearing mechanisms during dynamic testing. To assess which method more accurately represents the induced shear strains, several issues must be considered. These issues are the loading mechanism of the proposed testing technique, the effect of horizontal motion, the cycle-by-cycle shear strain calculation, and the coupled behavior between the induced shear strain and the generated excess pore pressure.

11.3.1 Effect of loading mechanism on induced shear strains

The shear strain-time histories computed by the AW method, which show a relatively constant shear strain amplitude (Figure 11-6), are similar to the results from cyclic strain-controlled tests. In a strain-controlled test, the applied strain

amplitude is constant and the stress applied to the soil element varies during cyclic testing in order to counterbalance soil softening at large strain levels due to soil nonlinearity and pore pressure generation. In contrast to cyclic strain-controlled tests, stress-controlled cyclic tests apply a constant stress amplitude to the soil specimen, resulting in a continuous increase in strain amplitude during cyclic loading due to soil nonlinearity and pore pressure generation at large strains.

The shear strain-time histories computed by the SDM method during larger-strain tests show that the shear strain amplitude increases first, and then decreases. This behavior is inconsistent with both strain-controlled and stress-controlled conditions. One possible explanation is that the cyclic stress applied to the specimen is relatively constant during the period when the shear strain is increasing. During this period, the test responds like a stress-controlled test. At some point, the pore pressure is large enough to change the wave propagation behavior within the test specimen, and the shear strain amplitude begins to decrease. This may be a result of smaller shear stresses being induced in the test specimen.

Based on these observations, the in situ dynamic liquefaction test cannot be described as solely a strain-controlled or stress-controlled test. Although constant cyclic loads are applied to the footing, the amplitude of the stress waves propagating through the instrumented test area vary because softening of the specimen changes the impedance contrast between the native soil and the reconstituted test specimen. The change in the transmitted energy is controlled by

the variation in the specimen stiffness. Excess pore pressure generation and soil nonlinearity both induce changes in the specimen stiffness.

11.3.2 Effect of horizontal particle motion on induced shear strain

The AW method only uses vertical particle velocity data to compute shear strain, while the SDM method uses both horizontal and vertical particle velocity data. To demonstrate the effect of horizontal motion on the shear strain computed by the SDM method, the shear strain was computed only using vertical or horizontal displacements. Figure 11-7 shows these shear strain-time histories, along with the shear strain-time history using both the horizontal and vertical motions. Figure 11-7 shows that the shear strain induced by the vertical motion is the dominant component and that this shear strain decreases as testing continues. The shear strain amplitude from the horizontal motion is less than half that from the vertical motion. Additionally, the shear strain from the horizontal motion actually increases somewhat as loading continues. After the dynamic loading ends at about 1.4 seconds, Figure 11-7(b) shows that the test specimen continues to vibrate in the horizontal direction.

The incorporation of horizontal motion in the SDM method for shear strain calculation increases the peak strain amplitude by about 25%. However, the horizontal motion does not contribute to the observed reduction in strain amplitude during later cycles of loading. Therefore, the difference between the shear-strain time histories computed by the SDM and AW methods cannot be explained by the incorporation of horizontal motion in the SDM method.

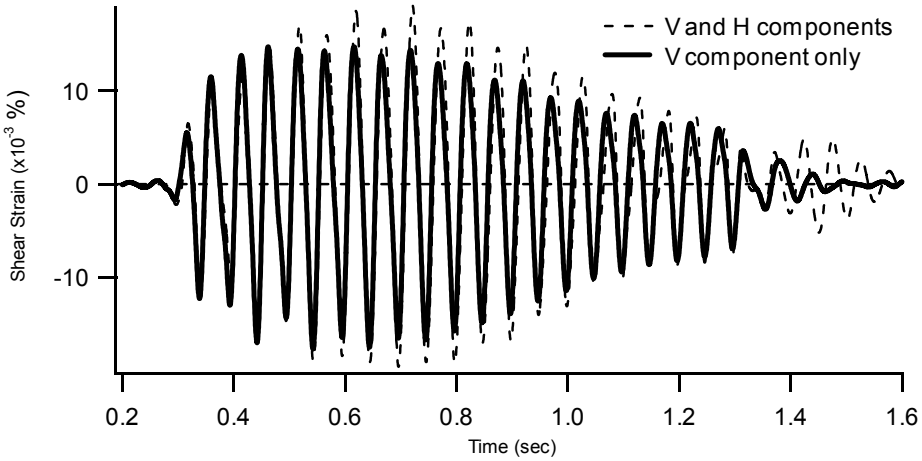

(a) Shear strain contribution from vertical particle motion (T2-8)

(b)

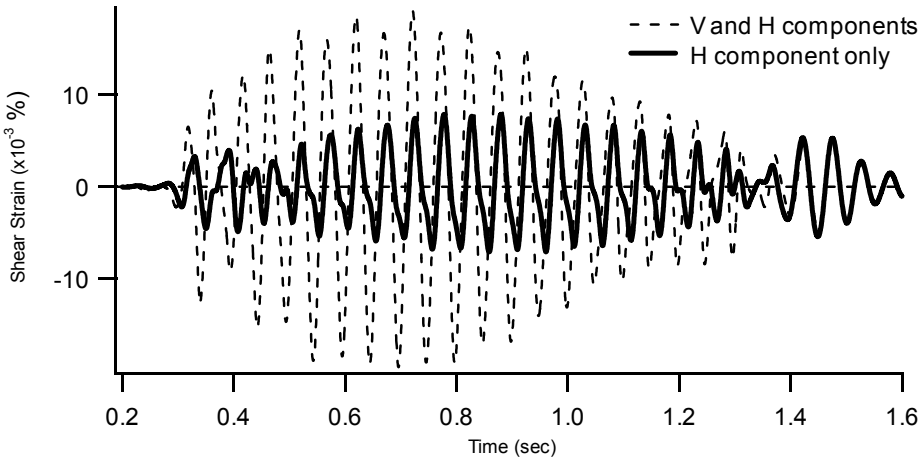

(b) Shear strain contribution from horizontal particle motion (T2-8)

Figure 11-7 Comparison of shear strain amplitudes contributed by vertical and horizontal components of motion in the SDM method (T2-8)

11.3.3 Effect of cycle-by-cycle shear strain evaluation

Another approach to consider when reconciling the shear strains computed by the AW and SDM methods is the variation in the apparent wave velocity from cycle to cycle. Previously, cross-power spectral analysis was used to calculate an average apparent wave velocity for the entire dynamic loading process, and this wave velocity was then used in the AW shear strain calculation. However, it is also possible to compute the apparent wave velocity for each cycle of motion and use these wave velocities in a cycle-by-cycle AW shear strain calculation.

The apparent wave velocities between cases 1 and 2 and cases 3 and 4 for each loading cycle are shown in Figure 11-8(a). Surprisingly, the apparent wave velocity increases with each cycle, particularly after cycle 10. For cases 1 to 2, the apparent wave velocity more than doubles during the dynamic loading. It should be emphasized that the apparent wave velocity is not equal to the shear wave velocity between the sensors, especially for the complicated wave field encountered in the developed testing technique. Therefore, the variation in the apparent wave velocities shown in Figure 11-8(a) does not represent the variation in the shear wave velocity or shear stiffness of the test specimen. It is not clear why the apparent wave velocity increases during dynamic loading. One possible explanation is that after a significant amount of pore pressure is induced (i.e., r_u~ 30% - 40%) an energy barrier is formed at the edge of the test pit. This energy barrier changes the wave propagation behavior, reduces the wave energy transmitted into the test specimen, and affects the apparent wave velocity. It

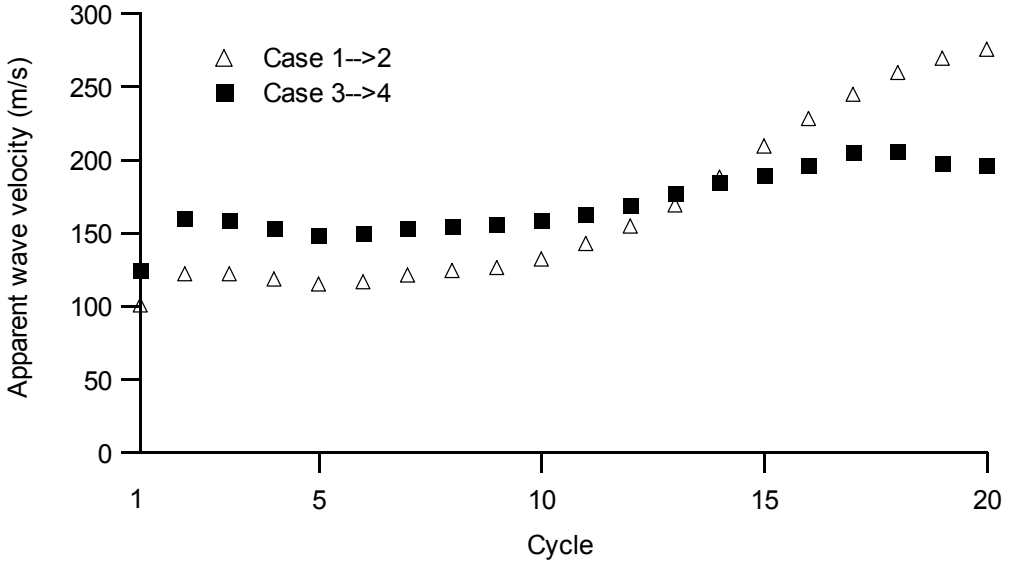

(a) Variation of apparent wave velocities during dynamic loading

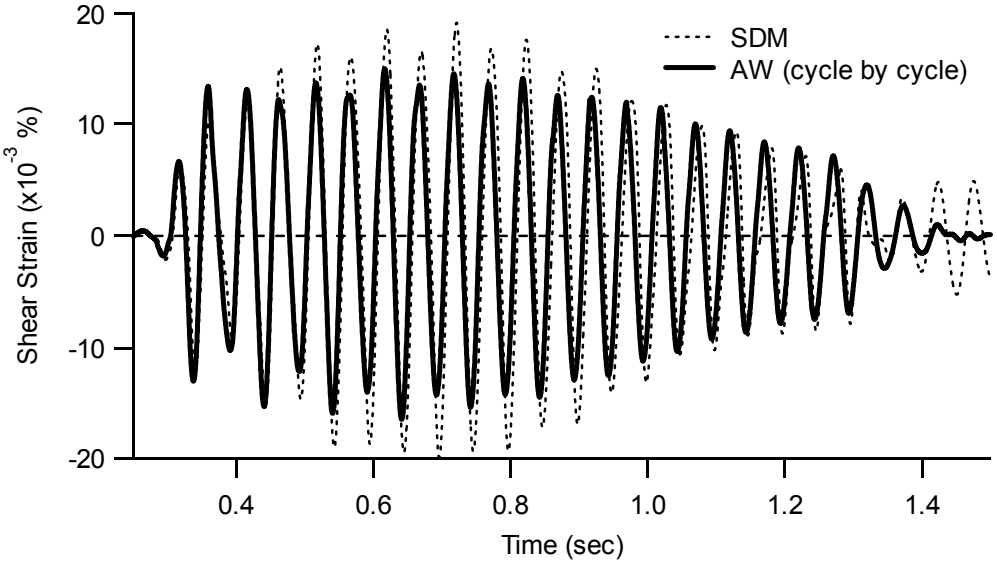

(b) Comparison of computed shear strain at the center of the array using cycle-by-cycle apparent wave velocity and the SDM method (T2-8)

Figure 11-8 Effect of variation of apparent wave velocity on the computed shear strain at the center of the array in a large strain test (T2-8)

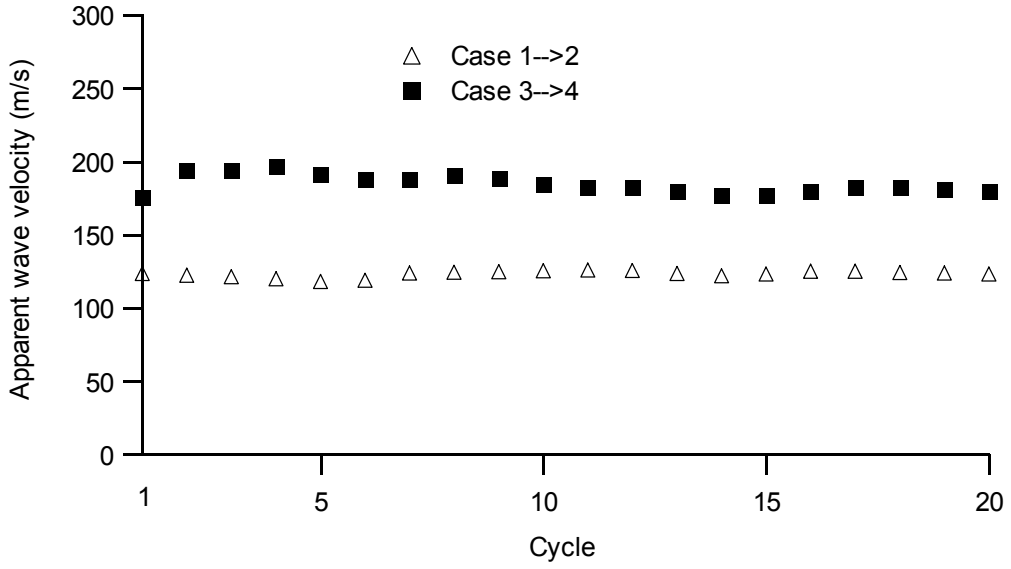

Figure 11-9 Variation of apparent wave velocities in small strain level tests (T2-3) during dynamic loading

should be noted that the apparent wave velocity does not change from cycle to cycle in the small shear strain level tests (Figure 11-9).

The apparent wave velocities in Figure 11-8(a) were used to compute shear strains on a cycle-by-cycle basis using the AW method. In this calculation, the shear strain at each sensor point was computed using the vertical particle velocity and the corresponding apparent wave velocity for that cycle. The shear strain at the center of the array was estimated by averaging the shear strains at the four nodal points. The shear strain-time history at the center of the array using the SDM method and the cycle-by-cycle AW method are shown in Figure 11-8(b). The results show better agreement between the two methods, with the AW

method showing a reduction in strain amplitude during later cycles due to the increased apparent wave velocity.

The overall apparent wave velocity represents the average apparent wave velocity for the entire loading process, so the computed AW shear strain using the overall apparent wave velocity represents the average shear strain throughout the dynamic loading. This statement is based on the observed small variation in the apparent wave velocity during small strain level tests, which show a fairly constant strain amplitude throughout the 20 loading cycles. Also, the shear strains computed by the AW method using the overall apparent wave velocity are fairly close to the mean shear strain amplitude computed by the SDM method for large strain level tests. Therefore, using the overall apparent wave velocity in the AW method should provide a good approximation of the average shear strain level. However, to closely investigate the coupled behavior between the induced shear strain and the generated excess pore pressure in the time domain, the shear strains computed by the SDM method are more appropriate. This is discussed further in the next section.

11.3.4 Coupled response between shear strain and excess pore pressure

Another observation that confirms the variation in shear strain amplitude during dynamic loading is the coupled behavior between the induced shear strain and the excess pore pressure. The shear strain-time histories and the excess pore pressure ratio-time history at the center of the array for the long vibration test T3-4 are shown in Figure 11-10. The shear strain-time histories in Figure 11-10 are

from (1) the AW method using the overall apparent wave velocity and the vertical particle velocity from case 5 in the center of the array (Figure 11-10(a)) and (2) the SDM method at the center of the array (Figure 11-10(b)). The pore pressure ratio-time history for test T3-4 can be divided into 4 phases. During the first phase, the excess pore pressure increases at a fast rate. During phase 2, the rate of excess pore pressure generation decreases, but the pore pressure is still increasing. During phase 3, excess pore pressure no longer develops and reaches a constant value, even though dynamic loading is still continuing. During phase 4, the dynamic loading stops and the excess residual pore pressure dissipates.

To explain this change in pore pressure generation behavior during dynamic loading, the shear strain-time histories are considered. The relatively constant shear strain amplitude computed by the AW method, as shown in Figure 11-10(a), is not sufficient to explain the change in pore pressure generation characteristics because a constant cyclic shear strain should induce a continuously increasing residual excess pore pressure. However, the variation in shear strain amplitude computed by the SDM method, as shown in Figure 11-10(b), can explain the pore pressure generation pattern. During phase 1, the shear strain amplitude increases while the excess pore pressure increases quickly. During phase 2, the shear strain amplitude decreases and the rate of pore pressure generation decreases. In phase 3, the shear strain amplitude is small and relatively constant, and no further residual pore pressure is generated. In general, during this phase the shear strain amplitude is about 0.005%, which is smaller than the threshold strain for pore pressure generation. In test T2-8, which is a large strain

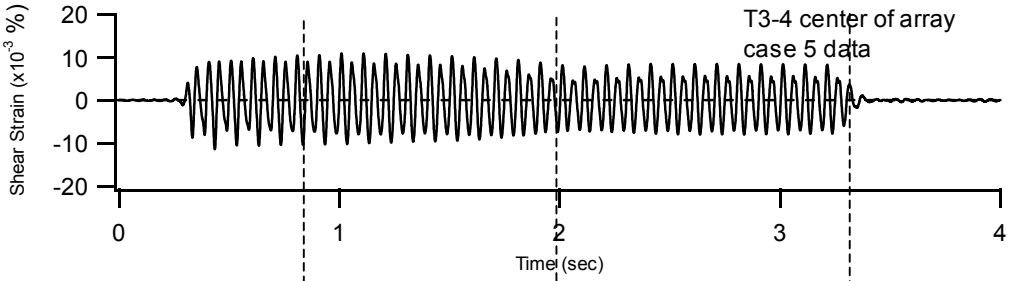

(a) Shear strain computed by AW method at the center of the array using case 5 and average apparent wave velocity

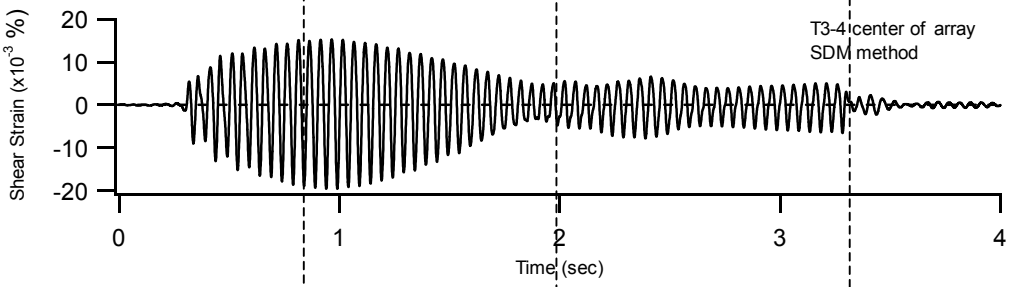

(b) Shear strain computed by SDM method at the center of the array

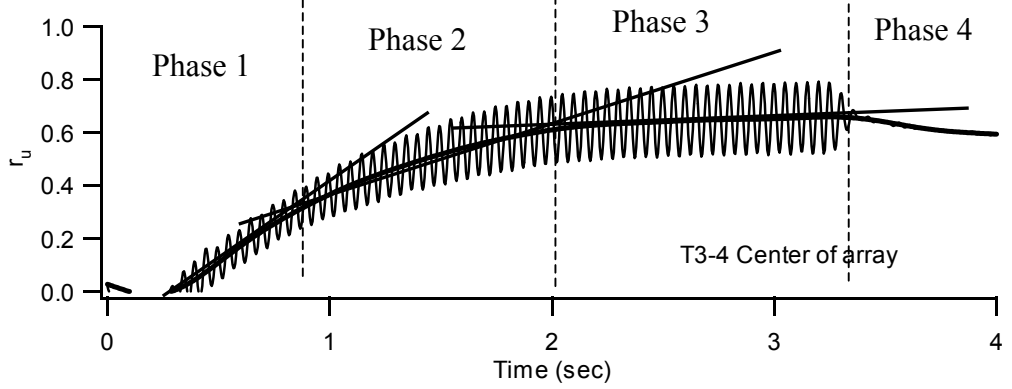

(c) Pore pressure ratio at the center of the array

Figure 11-10 Shear strains and pore pressure generation at the center of the array during the long-vibration, large-strain test (T3-4)

level, short vibration (20 cycles) test, only the first two phases were observed (Figures 9-4 and 9-5) because the vibration stopped before the specimen reached phase 3.

Based on these observations, shear strains computed by the SDM method agree best with the pore pressure generation patterns. Hereafter, the SDM method is the only method used when discussing shear strain evaluation.

11.4 OBSERVATIONS REGARDING PORE PRESSURE GENERATION CURVES

The pore pressure generation curves developed from the in situ dynamic liquefaction test are discussed here. The field measured pore pressure generation curves are compared with laboratory measured curves presented by Dobry et al. (1982). Additionally, the effects of confining stress and number of loading cycles (i.e., loading duration) on the field measured pore pressure generation curves are discussed. Future laboratory experiments for comparison with the field data are also introduced.

11.4.1 In situ pore pressure generation curves

The compiled mean shear strains and residual excess pore pressure ratios for different loading cycles from test series T2 and T3 are shown in Figure 11-11, along with pore pressure generation curves from Dobry et al. (1982). The Dobry et al. (1982) pore pressure generation curve is from strain-controlled cyclic triaxial tests on reconstituted Monterrey sand prepared at a relative density of 45% and performed at an effective confining pressure of 95.6 kPa. The field

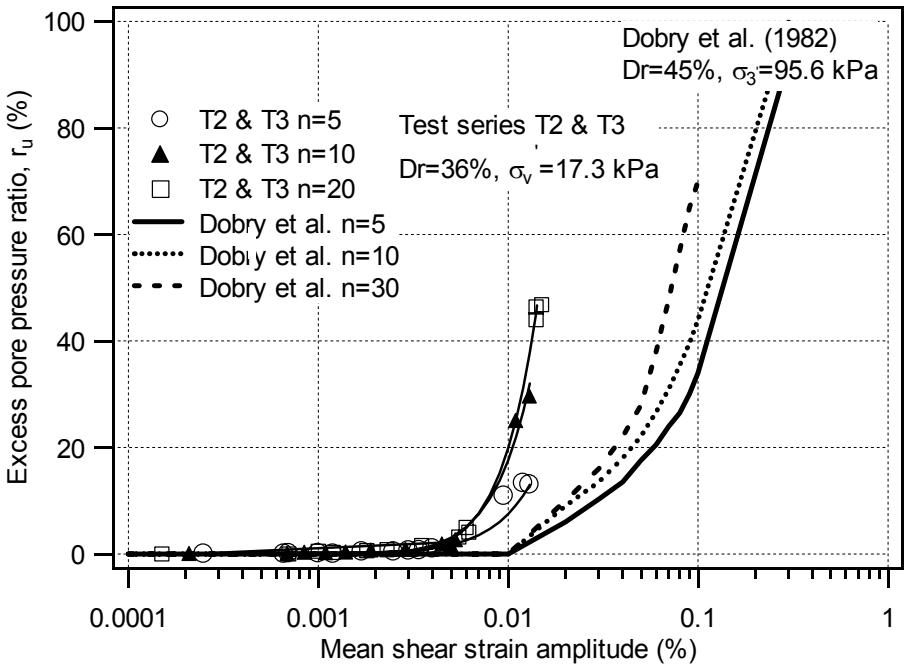

Figure 11-11 Comparison of field measured pore pressure generation curves with Dobry et al. (1982) results

measured pore pressure generation curves from this study are different from the Dobry et al. (1982) curves. The threshold shear strain for this study is smaller than the threshold shear strain from Dobry et al. (1982), and as a result, the field measured pore pressure ratios at specific strain levels are larger than those measured in the laboratory by Dobry et al. (1982).

The discrepancies may be due to differences in confining pressure, relative density, and/or loading mechanism. However, the in situ test data reflect that the residual pore pressure ratio increases quickly after the induced shear strain level

exceeds the threshold shear strain. This trend is consistent with the Dobry et al. (1982) data.

11.4.2 Effect of confining pressure on pore pressure generation

Threshold shear strain is defined as the strain level at which excess pore pressure begins to generate (Dobry et al. 1982). Below the threshold strain, no pore pressure is generated, even under a large number of loading cycles. Threshold shear strain is stress dependent and Dobry and Swiger (1979) proposed a relationship between threshold shear strain (γ_t) and confining stress ($\bar{\sigma}$):

$$\gamma_t(\%) = 1.75 \times 10^{-4} (\sigma)^{2/3} \quad \text{..... (11-1)}$$

where γ_t is in %, and σ in psf. This is a theoretical relationship developed from considering shear and volumetric strains within a cubically packed arrangement of Quartz spheres. Equation (11-1) predicts a threshold shear strain between 0.01% and 0.04% for stresses between 0.25 and 2 atm. Conventionally, the threshold strain for pore pressure generation is taken as 0.01%.

In test series T1, the vertical effective stress at the center of the array was 6.4 kPa (134 psf), which is below conventional stress levels. According to Equation (11-1), the threshold shear strain at the center of the array should be about 4.6×10^{-3} %. In test series T2, the vertical effective stress at the center of the array was 19.3 kPa (403 psf), and the corresponding threshold strain from Equation (11-1) is 9.7×10^{-3} %. The pore pressure generation curves from test series T1 and T2 are shown in Figure 11-12, along with the theoretical threshold strains from Equation (11-1). Both test series show a threshold shear strain of

about 0.005%, which agrees with Equation (11-1) for the stresses in test series T1, but does not agree with the stresses in test series T2.

Although the field-evaluated threshold strains indicated in Figure 11-12 do not agree with conventional values and do not indicate stress dependence, they are still considered reasonable. The theoretical relationship given in Equation (11-1) has not been verified for stresses below 100 kPa. In fact, there is almost no experimental data regarding the threshold strain for sand at confining pressures below 100 kPa. Therefore, a laboratory investigation of threshold strain at low confining pressures is recommended to verify the field measured threshold strains.

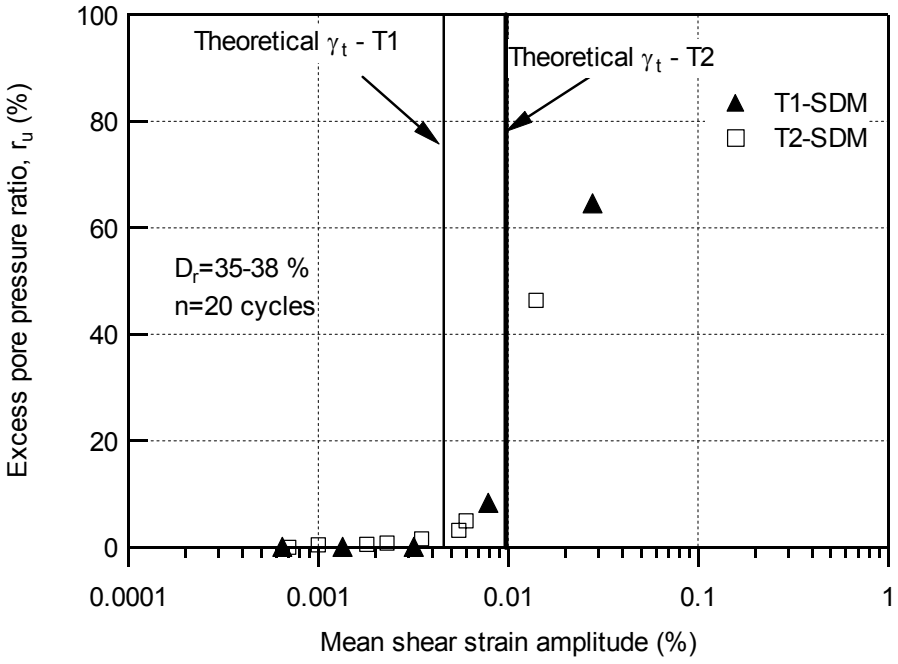

Figure 11-12 Field measured pore pressure generation curves and theoretical threshold shear strains

11.4.3 Effect of number of loading cycles on pore pressure generation

The number of cycles applied to a soil specimen is related to the duration of earthquake shaking. In strain-controlled cyclic laboratory tests, the amount of excess pore pressure generated for a specific shear strain level increases as the applied number of strain cycles increases (Dobry et al. 1982). In this study, test series T2 and T3 were prepared with similar stress levels and relative densities and tested with same instrumentation system. The compiled test data from test series T2 and T3 are used to show the effect of number of loading cycles on pore pressure generation. The pore pressure generation curves from both test series are shown in Figure 11-13. In Figure 11-13, the induced pore pressure increases as the number of loading cycle increases for same shear strain level, indicating the same trend as the laboratory data.

11.4.4 Ongoing laboratory testing plan

Ideally, the best way to verify the field measured pore pressure generation curves is to compare them with laboratory results performed on the same aggregate sand. The laboratory tests should be performed on specimens prepared with the same sample preparation technique as the field test specimen and the tests should be performed at confining stresses similar to those in the field. Two laboratory testing projects are in progress at UT to verify the pore pressure generation curves and associated properties measured by the in situ dynamic liquefaction test. These projects are discussed briefly below.

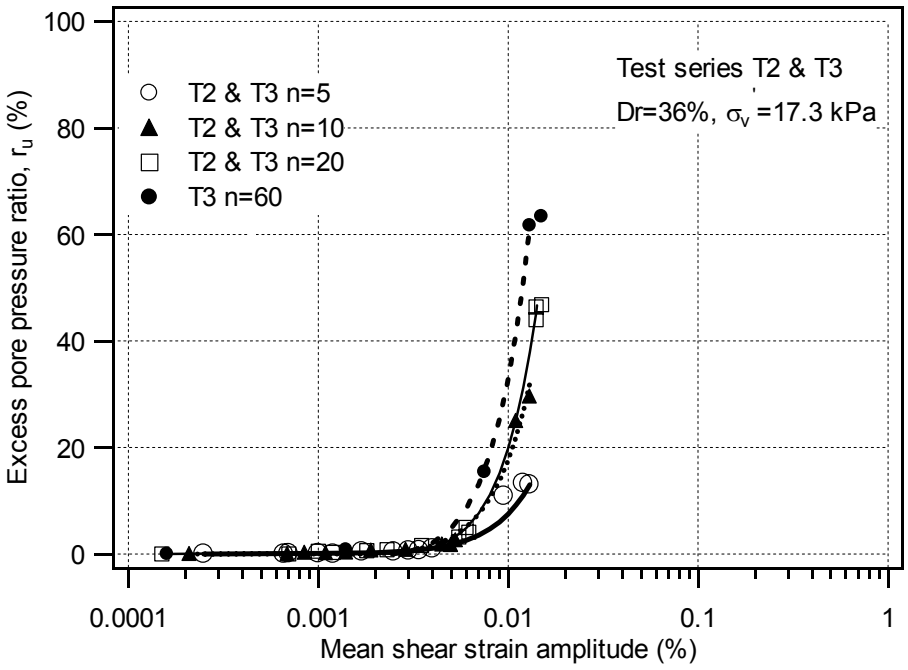

Figure 11-13 Effect of number of loading cycles on pore pressure generation

Because the developed testing technique is not truly a stress-controlled cyclic test nor a strain-controlled cyclic test, standard testing procedures must be modified to represent the field loading condition. As previously mentioned, the two principal parameters measured in the in situ dynamic liquefaction test are shear strain and pore pressure. A cyclic simple shear testing apparatus that is capable of conducting strain-controlled cyclic tests is one type of testing technique that can be used to measure the pore pressure generation induced at different shear strain levels. Conventional strain-controlled cyclic simple shear (CSS) tests apply a constant shear strain amplitude. However, the CSS apparatus at UT can apply non-uniform shear strain-time histories, such as those measured

in this study in the field. The laboratory-measured pore pressure-time histories induced by the field-measured shear strain-time histories will be compared with the in situ pore pressure-time histories collected in this study (Hazirbaba 2004, in progress).

Another ongoing laboratory study will utilize a stress-controlled torsional shear testing apparatus with bender elements at the top and bottom of the specimen (Valle 2003, in progress). The bender elements are used to measure the S-wave and P-wave velocities during the cyclic loading process. Therefore, the stiffness variation of the specimen during the cyclic loading process can also be monitored as well as the pore pressure generation characteristics. The torsional shear tests can also be used at very low stress levels (20 or 30 kPa) so that the effect of threshold shear strain will be studied. The laboratory-measured results will be compared with the field data collected in this study.

11.5 OBSERVATION REGARDING PORE PRESSURE DISSIPATION

Because the developed testing technique is capable of monitoring pore pressure during and after dynamic loading, pore pressure generation and dissipation both can be studied. The measured pore pressures at different depths during test T3-4 are presented here to illustrate the dissipation process.

Because five pore pressure transducers were installed at three different depths within the test specimen, the pore pressure profiles at different times after dynamic loading could be established. To simplify the two-dimensional test specimen into a one-dimensional system, a 1D vertical profile through the

location of liquefaction sensor 5 was chosen. The average pore pressure values from cases 1 and 2 were used to represent the excess pore pressure at a depth of 0.27 m below the water level. Similarly, the average pore pressure values from cases 3 and 4 were used to represent the excess pore pressure at a depth of 0.86 m. The pore pressure data from case 5 represented the pore pressure at a depth of 0.56 m. Because of the impervious liner placed around the test pit, one-dimensional vertical pore pressure dissipation through the drainage boundary at the top of the specimen is expected.

The pore pressure dissipation process for test T3-4 is shown in Figure 11-14. The peak residual pore pressures at each depth occurred at 3.5 seconds after the data acquisition systems started, which represents the end of the dynamic loading. Figure 11-14(a) shows excess pore pressure versus depth for t=3.5 to 7.5 s, while Figure 11-14(b) shows excess pore pressure versus depth for t=8.5 to 28.5 s. It should be noted that the values presented are excess pore pressures, with the initial static pore pressures already subtracted. The pore pressure profile at the end of dynamic loading (t=3.5 s) shows a linear variation of residual excess pore pressure with depth. A relatively constant excess pore pressure profile with depth was observed 10 seconds after the end of dynamic loading.

Numerical simulation of the consolidation process using finite difference modeling of Terzaghi's 1D consolidation theory was used to predict the excess pore pressure profiles after dynamic loading. In this analysis, a linearly increasing initial pore pressure profile was prescribed based on the measured pore pressure at the end of dynamic loading. A free drainage boundary was placed at the top of the

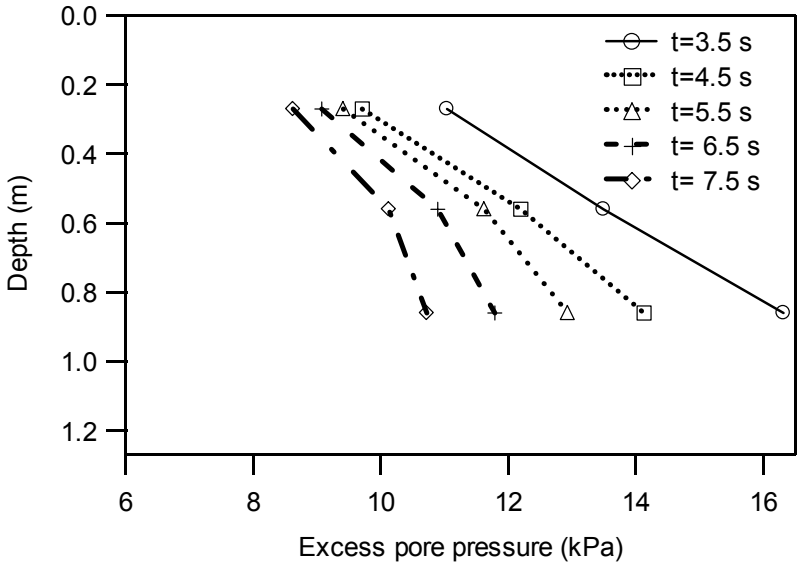

(a) Excess pore pressure dissipation during t=3.5 to 7.5 s (T3-4)

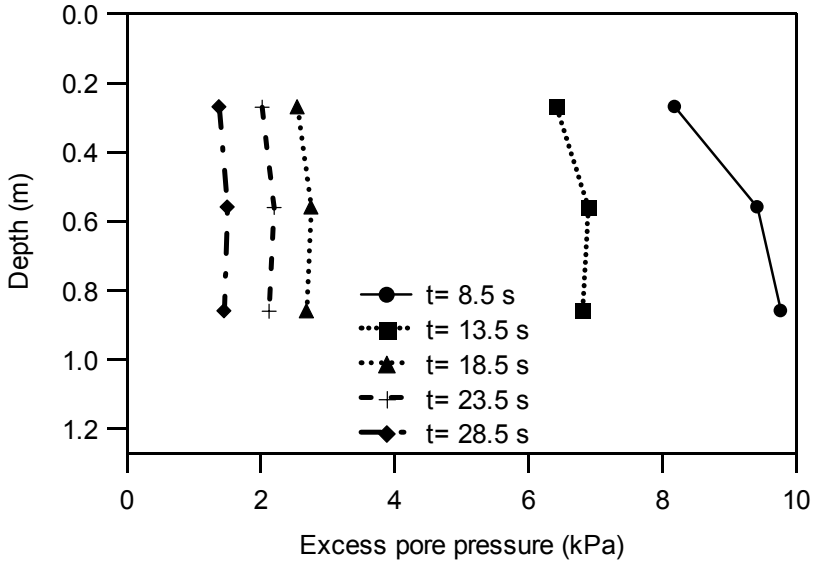

(a) Excess pore pressure dissipation during t=8.5 to 28.5 s (T3-4)

Figure 11-14 Pore pressure profiles during the dissipation process (T3-4)

specimen and the coefficient of consolidation (c_v) was taken as 0.033 m^2/sec. This value is chosen because it has the overall best fit to the measured pore pressure profiles at different times. It should be noted that the typical value of c_v for coarse sand is about 1.0~2.0 m^2/s (PHRI 1997). The computed excess pore pressure profiles and the measured profiles from test T3-4 are shown in Figure 11-15. The profiles in Figure 11-15 are plotted for five time intervals, from 1 second to 20 seconds after dynamic loading. The computed profiles dissipate more quickly than those measured in the field. Additionally, the computed pore pressure profiles are more curved at the top of the deposit, due to the immediate dissipation at the free drainage boundary at the top of the deposit. The discrepancies between the recorded and theoretical pore pressure profiles are most likely due to the existence of the overburden layer in the field. The overburden soil is unsaturated, and therefore provides some impedance to drainage that slows down the dissipation process.

11.6 SUMMARY

In this chapter, several specific aspects of the field-testing results are discussed. A qualitative assessment of the recorded geophone and pore pressure transducer data was presented. The recorded geophone data were qualitatively evaluated through a comparison of the recorded particle motion with the theoretical wave field. Based on the observed particle motion and the measured velocity Fourier spectra, the particle velocities satisfy the general trends of wave propagation behavior. The field performance of the miniature pore pressure

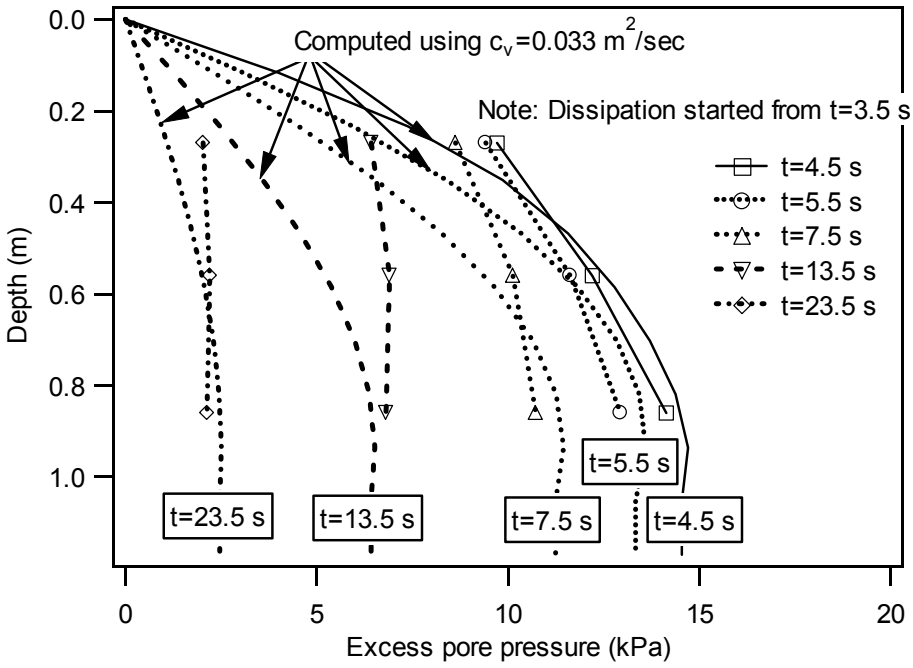

Figure 11-15 Measured and computed pore pressure profiles during dissipation process in test T3-4

transducers (PPT) in the liquefaction sensors was assessed based on the recorded hydrodynamic pore pressure. The observed hydrodynamic pore pressure amplitudes increased linearly with particle velocities, indicating that the pore pressure transducer in the liquefaction sensor is capable of accurately capturing the hydrodynamic excess pore pressure.

The shear strain-time histories computed by the AW and SDM methods were discussed further, with regard to the loading mechanism, the effect of horizontal particle motion, the effect of cycle-by-cycle shear strain evaluation, and the coupled behavior between the induced shear strains and pore pressures.

The results reveal that the shear strains computed from the SDM method agree the best with the pore pressure generation behavior. The AW method, which only considers the vertical particle velocity, provides a good estimate of the induced mean shear strain.

The pore pressure generation curves for the reconstituted test specimens were discussed with respect to three aspects: a comparison with data from Dobry et al. (1982), the effect of confining stress on threshold shear strain level, and the effect of the number of loading cycles on the induced pore pressure level. Although some discrepancies were observed between the measured pore pressure generation curves and the data from Dobry et al. (1982), the general trends still show good agreements. The measured field data indicated no confining pressure effect on threshold strain for the confining pressures tested. The field measured threshold strains were smaller than expected, but are still considered reasonable. Additionally, more pore pressure was generated when more cycles of loading were applied to the specimens. Two laboratory testing projects are in progress at UT to verify the pore pressure generation curves and associated properties measured by the in situ dynamic liquefaction test.

The pore pressure dissipation behavior was also presented in this chapter. Pore pressures dissipated quickly after the end of dynamic loading. The recorded excess pore pressure profiles during the dissipation process did not agree with those computed with a finite difference solution of Terzaghi's 1D consolidation theory. The main cause of the discrepancy is the overburden layer placed on top of the test specimen, which impeded drainage during the dissipation process.

Chapter 12. Summary and Conclusions

12.1 SUMMARY

In this dissertation, the development and initial test results from an in situ dynamic liquefaction test at the University of Texas at Austin are described. The research consists of five main components: (1) the setup and testing procedures for the in situ liquefaction test; (2) the analytical framework regarding ground response due to dynamic surface loads, numerical simulation of the testing setup, and data processing procedures; (3) issues regarding the sensors and data acquisition systems; (4) testing results and validation; and (5) implementation in fundamental soil liquefaction research.

12.1.1 Description of testing technique

The in situ soil liquefaction testing procedure under development at UT is one of the pioneering studies in this field. The distinct characteristic of this testing procedure is the in situ real-time measurement of ground response, particularly ground motions for shear strains calculations and pore water pressure. The in situ liquefaction test directly measures pore pressure generation in the field and avoids laboratory testing limitations related to sample disturbance and boundary conditions.

The essential components of the in situ liquefaction test are a dynamic loading source and an instrumentation system for simultaneously monitoring the ground response and pore pressure generation. The dynamic loading system consists of a vibroseis truck that applies dynamic loads at the ground surface. The dynamic loading system generates strong Rayleigh waves that propagate through the instrumented test area, strain the soil, and generate significant excess pore pressure. A liquefaction sensor was developed to monitor the coupled behavior between the soil skeleton and pore water pressure. Two data acquisition systems (one for short and one for long recording lengths) are employed in the developed testing technique to collect the signals from the liquefaction sensors. The measured response to dynamic loading is used to evaluate the pore pressure generation characteristics of the soil in terms of the induced shear strain and the generated excess pore pressure.

12.1.2 Analytical framework

For the developed liquefaction test, stress waves generated by the vertical, sinusoidal loads applied to the footing propagate through the native soil and then pass through the reconstituted test specimen. Particle motions in the soil during the test are governed by wave propagation theory. Analytical solutions for this loading source are beneficial in qualitatively assessing the measured particle motion data. However, the induced wave field for the current testing configuration is complicated due to variations in the soil properties, near-field

effects, and nonlinear soil behavior. Therefore, all theoretical approaches need to be justified to adequately interpret the field measurements.

Because of the complexity of the field conditions, the finite element method (FEM) was employed to simulate the dynamic soil motions and collect more insight into the soil response. FEM analyses were also conducted to validate the strain calculation from measured nodal displacements using the SDM method, as well as to evaluate the appropriateness of the array size and the effects of a layered system. The numerical results indicate that for the current test configuration, the induced shear strains are expected to be greater than the conventional threshold shear strain for pore pressure generation, 0.01 %. Also, the 0.6m-by-0.6m array was found to be appropriate for estimating the shear strain by the SDM method in a layered system.

The data analysis techniques involved in this research include signal processing, numerical algorithms, and computational methods for shear strain calculation. The collected signals from the embedded liquefaction sensors are processed in either the time domain or the frequency domain. Three types of analysis are performed in the time domain: numerical integration, baseline correction, and signal stacking. The major computations performed in the frequency domain are digital filtering using a linear filter and cross-spectral analysis for calculation of the phase velocity between two receivers.

The shear strain evaluation methods are classified into two categories: a displacement-based method and wave propagation-based methods. The displacement-based method uses the strain-displacement matrix from finite

element theory to calculate strain components at the center of the experimental array and is called the SDM method. Three wave propagation-based methods are presented, including the plane shear wave (PSW) method, the plane Rayleigh wave (PRW) method, and the apparent wave (AW) method. These wave propagation-based methods calculate the shear strain at the location of the sensor directly from the measured particle velocity.

12.1.3 Instrumentation system

To monitor the coupled response between soil particle motion and pore water pressure generation, a new sensor was developed. This sensor is called the liquefaction sensor. The liquefaction sensor consists of two perpendicularly oriented geophones that monitor horizontal and vertical particle velocities and one miniature pore pressure transducer. These three sensors were epoxied in an acrylic case for waterproofing and physical protection. Five liquefaction sensors were installed to form the embedded instrumentation array.

Two data acquisition systems, called the transient response data acquisition system (TRDAQ) and the long-term data acquisition system (LTDAQ), were employed in this research for different purposes and with different sensors. The TRDAQ is a dynamic signal analyzer that was used to record short duration signals, mainly from the geophones, without a time skew. The LTDAQ is a computer-based high speed data acquisition system consisting of a personal computer, an A/D board, and *LabView*® software. The LTDAQ was used to record long duration pore pressure signals, as well as velocity data from

the geophones at the center of the array. Both systems were operated at the same sampling rate, which allowed the data to be synchronized for future analyses and presentations. The two systems were synchronized after dynamic testing using a reference signal recorded by both systems.

Other instrumentation tools were used to characterize the reconstituted test specimen. These tools include a crosshole source for S-wave and P-wave velocity measurements, a push-in P-wave measurement receiver for saturation verification, settlement platforms for measuring settlements at different depths, and an in situ density measurement tool. The data collected by these tools provided useful information for verifying the test results.

12.1.4 Test results

Three test series (T1, T2, and T3) were performed on reconstituted test specimens with different confining stresses and loaded with a different number of loading cycles. The collected data were presented in terms of shear strain-time histories, pore pressure-time histories, and pore pressure generation curves.

The quality of the geophone data were assessed through the measured particle motion in the time domain, the frequency content of the particle velocities, and a comparison of the vertical and horizontal velocity amplitudes. The quality of the measured pore pressures was assessed through the recorded hydrodynamic pore pressure and the coupled response between the induced shear strain and the generated residual excess pore pressure. The results reveal that the

test design and the instrumentation system can effectively capture the soil liquefaction behavior of the reconstituted test specimen.

The physical properties of the reconstituted test specimens were evaluated through P-wave velocity measurements and in situ density measurements. These measurements were performed in response to concerns regarding the saturation of the test specimen and the procedures used to estimate the in situ density. The results demonstrated that the sample preparation procedure was able to create a saturated, loose specimen.

Pore pressure generation curves, which show the relationship between the induced shear strain and the excess pore pressure ratio for a specific number of loading cycles, were developed from the measured field data. The effect of confining pressure on the threshold shear strain and the effect of the number of loading cycles on the pore pressure generation curve were investigated. The testing results from test series T1 and T2 show that the threshold shear strains agree qualitatively with the theoretical values proposed by Dobry and Swiger (1979) and Dobry et al. (1982). However, a significant confining pressure effect on threshold strain was not observed for the confining pressures tested (7 kPa and 19 kPa). Future laboratory tests are planned to study threshold strains at these low confining pressures. Additionally, the generated excess pore pressure ratio increased as the number of loading cycles increased, which agrees with results from laboratory tests (Dobry et al. 1982).

To explain the observed coupled response between the induced shear strain and the excess pore pressure during long duration shaking, the pore

pressure generation process was divided into four phases based on the shear strain behavior and rate of pore pressure generation. At the beginning of loading, pore pressure generates relatively quickly and shear strain amplitudes increases. After reaching a pore pressure ratio of about 30-40%, the strain amplitudes start to decrease and the rate of pore pressure generation decreases. Eventually, the strain amplitude falls below the threshold strain amplitude and no further pore pressure is generated. Finally, at the end of the loading, the pore pressures start to dissipate. The observed excess pore pressure profiles during the dissipation process did not agree with those computed with a finite difference solution of Terzaghi's 1D consolidation theory. The main cause of the discrepancy is the overburden layer placed on top of the test specimen, which impeded drainage during the dissipation process.

12.2 FINDINGS

Based on the test results from the in situ dynamic liquefaction tests performed on reconstituted test specimens, several findings can be described.

12.2.1 In situ shear strain computation

Although four shear strain evaluation methods were proposed to compute the shear strain from the field test data, test results revealed that the AW and SDM methods are most suitable and accurate for the current test configuration. However, during large shear strain level tests, which showed significant excess pore pressure generation, only the SDM method provided shear strain-time

histories that corresponded with the measured variation in pore pressure generation.

The shear strains computed by the AW method using the overall apparent wave velocity represent the average shear strain during dynamic loading. This shear strain is similar to the mean average shear strain computed by the SDM method. The AW method provides accurate shear strain-time histories for small strain level tests and provides accurate values of average shear strain amplitude for large strain level tests. The SDM method is deemed the most suitable shear strain evaluation method for the complicated wave field in this test because it employ the fewest assumptions and best explains the measured pore pressure response.

12.2.2 Pore pressure generation curve

One of the main goals in the in situ liquefaction test is to establish a pore pressure generation curve for the instrumented test specimen. Although full liquefaction (i.e., zero effective stress) was not achieved in any of the test series performed in this study, important information was still developed. The threshold shear strains for the test specimens were determined from the pore pressure generation curves and were slightly smaller than the conventional threshold shear strain proposed by Dobry et al. (1982). The field-measured threshold strains most likely were smaller because of the low confining stresses used in this research. The shape of the full pore pressure generation curves shows that the residual

excess pore pressure ratio increases quickly after the induced shear strain level exceeds the threshold strain.

12.2.3 Coupled behavior between shear strain and excess pore pressure

During the long vibration, large strain test T3-4, the shear strain amplitude and rate of excess pore pressure generation varied during dynamic loading. When the excess pore pressure ratio was less than about 40%, the rate of excess pore pressure generation was the greatest and the shear strain amplitude increased with each loading cycle. After the excess pore pressure ratio reached about 40%, the shear strain amplitude started to decrease and the rate of excess pore pressure generation also decreased. Eventually, the shear strain amplitude reached a constant value, which was below the value of the threshold strain, and no further excess pore pressure was generated. A hypothetical explanation for this behavior is the formation of an energy barrier at the interface between the native soil and test specimen when pore pressures are elevated, which reduces the amplitudes of the stress waves that enter the test specimen. This issue needs further investigation.

12.2.4 Status of the in situ dynamic liquefaction test

The status of the proposed in situ dynamic liquefaction test is discussed below.

1. The results from the reconstituted test specimens show that the vibroseis truck can create enough energy to induce large shear strains

and generate significant excess pore pressure under the current test configuration.

2. The sample preparation procedure can produce a loose, uniform, saturated soil specimen and the properties of the test specimen can be accurately evaluated. Also, embedded sensors can be installed in specific locations within the sample during sample construction. The size of the instrumentation array is appropriate for strain evaluation using the SDM method.
3. The sensors and data acquisition systems are capable of capturing the dynamic coupled response between the soil skeleton and the excess pore pressure. The testing and data processing procedures are suitable for measuring the pore pressure generation curve.
4. The data reduction procedures have been computerized for future tests and applications. Also, the collected data can be analyzed in the field and used to make decisions regarding the next stage of the test.
5. The shear strain calculation methods have been validated using field measured data. The SDM method can be applied to the most complicated cases without losing important information. The AW method can provide an average shear strain level for the pore pressure generation curve, but does not capture the variation in shear strain amplitude during large strain tests. An advantage of the AW method is that it can reduce the sensor array to a point measurement.

Although the proposed testing technique was only applied to reconstituted test specimens, the testing configuration and testing procedure can be implemented at naturally occurring liquefiable sites without major modifications.

12.3 FUTURE WORK

Although the testing results showed qualitative agreement with previous research conducted in the laboratory, further laboratory studies will be crucial to quantitatively verify the field measured pore pressure generation curves. Also, some test refinements and modifications are needed to improve the performance of the in situ dynamic liquefaction testing technique.

12.3.1 Laboratory studies

To quantitatively verify the field pore pressure generation curves, strain-controlled, undrained, cyclic simple shear tests are required. The testing apparatus must be capable of applying the shear strain-time histories collected in the field and replicate the field conditions regarding the state of stress and sample preparation. Favorable agreement between the laboratory measured pore pressure-time histories and the pore pressure-time histories collected in this study will provide strong evidence for the credibility of the developed testing technique.

12.3.2 Refinement of the dynamic source

In the current testing configuration, the dynamic load generated by the vibroseis truck is vertically applied to a rigid footing near the ground surface. The

major advantage of this testing configuration is that it is easy to setup. However, it may not be optimal because this source generates mainly Rayleigh waves, which are complicated to analyze and are not the best wave type to shear the soil. A better dynamic source would generate large shear waves propagating through the instrumented test area. A possible solution is to build a vertical concrete wall underground and load it vertically to generate horizontally propagating and vertically polarized shear waves. Alternatively, a vibroseis truck that is capable of vibrating horizontally could be used. This source would generate vertically propagating (downward) horizontal shear waves.

Also, the vibroseis used in this study can only generate sinusodial waves between 15-100 Hz and the capacity is only 22.7 ton. To be more similar to earthquake loading, a lower loading frequency is preferred. To be able to reach the initial liquefaction state, a larger loading capacity will be essential.

A new vibroseis truck has been acquired by UT. This truck will be able to vibrate horizontally and will have larger load and lower frequency capabilities.

12.3.3 Modifications to the liquefaction sensor

To apply the proposed testing technique to naturally occurring liquefiable soil deposits, the liquefaction sensor needs to be modified so that it can be installed at a desired location. Because most liquefiable zones are located at least a few meters below the ground surface, a push-in liquefaction sensor is preferred. Some considerations for the push-in liquefaction sensor are discussed below.

1. A special mechanical design is required to maintain saturation of the pore pressure transducer during the transportation and installation process. Also, the push-in rod attached to the sensor needs to be detachable from the sensor after it is placed at the desired depth.
2. Special devices must be integrated into the sensor or the placement tool to ensure accurate orientation and verticality of the sensor.
3. The sensor must be retrievable after the test. The retrieval procedure should be taken into account when the sensor is modified. Alternatively, a disposable sensor could be used. The most expensive component in the liquefaction sensor is the miniature pore pressure transducer. If a cheap and reliable pressure transducer is available, a disposable sensor would be possible.
4. To push the sensor into the soil, the shape of the sensor case should be adjusted. A conical tip would aid in the push-in installation procedure.
5. After installation of the sensor, the hole above the sensor must be backfilled. The backfill procedure needs to be well designed to prevent an unwanted drainage path for excess pore pressures and any interference with the pore pressure measurement.

12.3.4 Refinements to the data acquisition system

Two data acquisition systems are employed in the current instrumentation system. To collect more data in the future, more sensors and more channels in the DAQ system are needed. The cost to expand the multichannel DSA is high, and

may even be impossible because the product has been discontinued by the manufacturer. An alternative is to use high speed A/D boards with analog triggers. To expand the number of available channels, two or more A/D boards can be installed in a single computer. These A/D boards can operate simultaneously with negligible time delay. By doing so, the synchronizing procedure used for the current two systems would not be necessary.

12.4 FUTURE APPLICATIONS

Although the short-term goal of this research was to develop a testing procedure to evaluate liquefaction in situ, it can open a window to advance the state of knowledge in several research areas. Specifically, the in situ liquefaction test can be used to study liquefaction of special soils (i.e., silts, gravels), liquefaction-induced deformation, in situ pore pressure generation, validation of numerical models, effectiveness of liquefaction remediation, and nonlinear soil properties. Several potential applications are described below.

1. This test could be used to improve the current empirical correlations used to evaluate liquefaction initiation. For example, issues related to long duration shaking, the location of the threshold line between liquefaction and nonliquefaction, the effect of fines content, and liquefaction of gravelly soils can be studied. The developed procedure can help gain insight into the parameters affecting liquefaction.
2. The deformations induced by liquefaction are a major concern because the majority of the damage associated with liquefaction is

due to excessive movement. The current testing procedure can measure strains and pore pressures simultaneously, which will provide a more accurate estimate of expected deformation and strain potential in liquefiable soils during a seismic event.

3. For decades, laboratory tests have been useful in understanding the mechanism of liquefaction and the factors affecting liquefaction. However, due to inevitable soil disturbance during sampling, it is extremely difficult to directly and accurately assess the liquefaction resistance of in situ soils in the laboratory. The developed in situ dynamic liquefaction test will overcome this limitation.
4. The developed testing technique can be implemented in a liquefaction study of gravelly soils. Gravelly soils are difficult to test in the laboratory and in situ test parameters (e.g., SPT, CPT) are less reliable for these soils because of their large particles.
5. More advanced and sophisticated numerical models have been developed to predict pore pressure generation and deformation induced in liquefiable soils during seismic events. However, these models require field validation and calibration. Several seismic monitoring arrays have been established around the world for this purpose. However, they all face the same difficulties such as the unpredictable occurrence of a large earthquake, reliability of the instrumentation after a significant time, lack of a standard procedure for data processing, and cost of maintenance. The developed testing

procedure avoid these problems and can be used to generate valuable data for numerical simulation and validation.

6. Because the developed test can measure pore pressure generation and dissipation induced by seismic motions, it can be adopted to assess the effectiveness of liquefaction remediation techniques. Currently, there are plans to evaluate the performance of a prefabricated, composite drain (Equake Drain^{TM}) that provides drainage for excess pore pressures, and thereby, avoids full liquefaction.
7. Nonlinear soil properties are important parameters when predicting the response of soil sites during earthquake loading. The in situ measurement of these properties has been recognized as an important research concern. The vibroseis truck with an embedded geophone array allows these large strain properties to be measured in situ.
8. The shear strain computation methods developed in this research can be implemented in future field seismic arrays and could be used to analyze previously recorded data.

The developed in situ liquefaction test has many applications in both engineering practice and academic research. The test not only establishes a new alternative for the evaluation of liquefaction susceptibility, but it also captures the coupled response between shear strain and excess pore pressure generation. Moreover, this test has the potential to advance the state of knowledge associated with liquefaction hazards and provide more effective strategies for liquefaction

remediation. Hence, this test potentially will have a great impact in the field of geotechnical earthquake engineering.

Bibliography

Allen, N. F., Richart, F. E., and Woods, R. D. (1980), "Fluid wave propagation in saturated and nearly saturated sands," *Journal of the Geotechnical Engineering Division*, ASCE, Vol. 106, No. GT3, pp. 235-254.

Andrus, R. D., Stokoe, K. H .II (2000), "Liquefaction resistance of soils from shear- wave velocity," *Journal of Geotechnical and Geoenvironmental Engineering*, ASCE, Vol. 126, No. 11, pp. 1015-1025

Anstey, N. A. (1991), *Vibroseis*, Prentice-Hall, Inc., NJ, 171 pp.

ASTM (2000) "Standard test methods for crosshole seismic testing," ASTM standard D4428/D4428M-00, American Society for Testing and Materials, PA.

Axtell, P. J. (2001), *In-Situ Measurements of Linear and Nonlinear Properties of a Near-Surface, Poorly Graded Sand*, M. S. Thesis, The University of Texas at Austin.

Bathe, K. –J. (1996), *Finite Element Procedures*, Prentice-Hall, Inc., NJ, 1037 pp.

Bay, J. A. (1997), "Development of a Rolling Dynamic Deflectometer for Continuous Deflection Testing of Pavements," *Ph.D. Dissertation*, University of Texas at Austin, pp.75-78.

Bay, J. A., Stokoe, K. H., II., McCullough, B. F., and Alexander, D. R. (1999), "Profiling Flexible Highway Pavement Continuously with Rolling Dynamic Deflectometer and a Discrete Points Falling Weight Deflectometer," *Transportation Research Record No. 1665*, 1999, pp.74-85.

Bay, J. A. and Stokoe, K. H., II (1999), "Continuous profiling of flexible and rigid highway and airport pavements with the rolling dynamic deflectometer," *Nondestructive Testing of Pavements and Backcalculation of Moduli: Third Volume, ASTM STP 1375*, S. D. Tayabji and E. O. Lukanen, Eds., American Society for Testing and Materials, Philadelphia, 1999, pp. 429-443.

Biot, M. A. (1955), "Theory of elasticity and consolidation for a porous anisotropy solid," *Journal of Apply Physics*, 26, pp. 182-185.

Casagrande, A. (1936), "Characteristics of cohensionless soils affecting the stability of slopes and earth fills," *Journal of the Boston Society of Civil Engineers*, reprinted in *Contributions to Soil Mechanics*, Boston Society of Civil Engineers, 1940, pp. 257-276.

Casagrande, A. (1976), "Liquefaction and cyclic mobility of sands: a critical review," *Harvard Soil Mechanics Series 88*, Harvard University, Cambridge, Massachusetts.

Castro, G. and Poulos, S. J. (1977), "Factors affecting liquefaction and cyclic mobility," *Journal of the Geotechnical Engineering Division*, ASCE, Vol. 106, No. GT6, pp. 501-506.

Celestino, V. (2003), Ph.D. dissertation, University of Texas, work in progress.

Channey, R. (1978), "Saturation effects on the cyclic strength of sands," *Earthquake Engineering and Soil Dynamics*, Vol. 1, pp. 342-358.

Charlie, W. A., Jacobs, P. J., and Doehring, D. O. (1992) "Blast-induced liquefaction of an alluvial sand deposit," Geotechnical Testing Journal, Vol. 15, No. 1, pp.14-23.

Chen, J. Y. (2001), *Borehole SASW Method: Numerical Simulation and Field Tests*, M. S. Thesis, The University of Texas at Austin.

Cooley, J. W. and Tukey, J. W. (1965), "An algorithm for the machine calculation of complex Fourier series," *Mathematics of Computation*, **19**, *90*, pp. 297-301.

Dobry, R., Ladd, R. S., Yokel, F. Y., Chung, R. M., and Powell, D. (1982), "Prediction of pore water pressure buildup and liquefaction of sands during earthquake by the cyclic strain method," *NBS Builing Science Series 138, National Bureau of Standards*, Gaithersburg, Maryland, 150 pp.

Dobry, R. and Swiger, W. F. (1979), "Threshold strain and cyclic behavior of cohesiobless soils," *Proceedings, 3rd ASCE/EMDE Specialty Conference*, Austin, TX, September 17-19, pp. 521-525.

Dunnicliff, J. (1988), *Geotechnical Instrumentation for Monitoring Field Performance*, John Wiley & Sons, Inc., New York, 577 pp.

EERI (2000), "The Izmit (Kocaeli), Turkey Earthquake of August 17, 1999," *Earthquake Spectrum Supplement A*, Vol. 16. No. 4.

EERI (2001), "The Chi-Chi, Taiwan Earthquake of September 21, 1999," *Earthquake Spectrum Supplement A,* Vol. 17. No. 1.

Elgamal. A. –W., Zeghal, M., Parra, E., Gunturi, R., Tang, H. T., and Stepp, J. C. (1996), "Identification and modeling of earthquake ground response – Site amplification," Soil Dynamic and Earthquake Engineering, Vol. 15, pp. 499-522.

Figliola, R. S., and Beasley, D. E., (2000), *Theory and Design for Mechanical Measurements*, 3rd edition, John Wiley & Sons, Inc., New York, 552 pp.

Finn, W. D. L., Lee, K. W., and Martin, G. R. (1977), "An effective stress model for liquefaction," *Journal of the Geotechnical Engineering Division,* ASCE, Vol. 103, No. GT6, pp. 517-533.

Foinquinos, R. and Roesset, J. M. (2000), "Elastic layered half-spaces subjected to dynamic surface loads," *Wave Motion in Earthquake Engineering*, Kausel, E. and Manolos, G. eds., WIT press, Ashurst, Southampton, UK, pp. 215-246.

Gohl, W. B., Howie, J. A., and Rea, C. E. (2001), "Use of controlled detonation of explosives for liquefaction testing," *Proceedings, 4st Int. Conf. on Recent Advances in Geotechnical Earthquake Geotechnical Engineering and Soil Dynamics and Symposium in Honor of Professor W. D. Liam Finn*, Paper No. 9.13, San Diego, CA, USA, March 26-31.

Harder, L. F. (1997), ''Application of the becker penetration test for evaluating the liquefaction potential of gravelly soils.'' *Proc., NCEER Workshop on Evaluation of Liquefaction Resistance of Soils*, National Center for Engineering Research, Buffalo, pp. 129–148.

Haskell, N. A. (1953), "The dispersion of surface waves in layered media," *Bull. Seism. Soc*. Am., 43, pp. 17-34.

Holzer, T. L., Youd, T. L., and Hanks, T. C. (1989), "Dynamics of liquefaction during the Supersition Hills Earthquake (M=6.5) of November 24,1987," *Science*, 244,April 7, pp. 56-59.

Hryciw, R. D., Vitton, S., and Thomann, T. G. (1990), "Liquefaction and Flow Failure During Seismic Exploration," *Journal of Geotechnical Engineering*, ASCE, Vol. 116, No. 12, pp. 1881-1899.

Hushmand, B. and Scott, R. F., and Crouse, C. B. (1992), "In–place calibration of USGS pore pressure transducer at Wildlife liquefaction site, California, USA," *Proceeding of 10th World Conference on Earthquake Engineering*, 3, pp. 1263-1267.

Hushmand, B., Scott, R. F., and Rashidi, H. (1993), "VELACS model no. 3: liquefaction in dense and loose sand columns," *Verification of numerical procedures for the analysis of soil liquefaction problems*," Arulanandan K., and Scott, R.F., eds., Vol. 1, Balkema, Rotterdam, The Netherlands, pp. 1415-1442.

Hvorslev, M. J. (1951), "Time lag and soil permeability in ground-water observation," U.S. Army Corps of Engineers, Waterway Experimental Station, Vicksburg, MS, Bull. No. 36.

Ishihara, K. (1970), "Approximate forms of wave equations for water-saturated porous materials and related dynamic modulus," Soils and Foundations, Vol. 10, No. 4, pp. 10-38.

Ishihara, K., Muroi, T., and Towhata, I. (1989), "In-situ pore water pressure and ground motions during the 1987 Chiba-Toho-Oki Earthquake," *Soils and Foundations*, 29(4), pp.75-90.

Ishihara, K. and Sherif, M. A. (1974), "Soil liquefaction by trosional simple shear device," *Journal of the Geotechnical Engineering Division*, ASCE, Vol. 100, No. GT8, pp. 871-888.

Ishihara, K., Shimizu, K., and Yamada, Y. (1981), "Pore water pressure measured in sand deposits during an earthquake," *Soils and Foundations*, 2(4), pp. 85-100.

Ishihara, K., Tsuchiya, H., Huang, Y., and Kamada, K. (2001), "Recent Studies on liquefaction resistance of sand-effect of saturation,' *Proceedings, 4st Int. Conf. on Recent Advances in Geotechnical Earthquake Geotechnical Engineering and Soil Dynamics and Symposium in Honor of Professor W. D. Liam Finn*, Keynote Lecture, San Diego, CA, USA, March 26-31.

Kayen, R. E. and Mitchell, J. K. (1997), "Assessment of liquefaction potential by Arias intensity," *Journal of Geotechnical and Geoenvironmental Engineering*, ASCE, Vol. 123, No. 12, pp. 1162-1174.

Kausel, E. and Roesset, J. M. (1981), "Stiffness matrices for layered soils," *Bull. Seism. Soc. Am.*, 71, No. 6.

Koga, Y. and Matsuo, O. (1990), "Shaking table tests of embankments resting on liquefiable sandy ground," *Soils and Foundations*, Vol. 30, No. 4, pp. 162-174.

Kramer, L. S. (1996), *Geotechnical Earthquake Engineering*, Prentice-Hall, Inc., NJ, 653 pp.

Ladd, R. S. (1974), "Specimen preparation and liquefaction of sand," *Journal of the Geotechnical Engineering Division,* ASCE, Vol. 100, No. GT10, pp. 1180-1184.

Lamb, H. (1904), "On the propagation of tremors over the surface of an elastic solid," *Phil. Tran. Roy. Soc.* A, 203, pp. 1-42.

Law, T. W., Cao, Y. L., and He, G. N. (1990), "An energy approach for assessing seismic liquefaction potential," *Canadian Geotechnical Journal*, Vol. 27, No. 3, pp. 320-329.

Martin, G. R., Finn, W. D. L., and Seed, H. B. (1975), "Fundamental of liquefaction under cyclic loading," *Journal of the Geotechnical Engineering Division,* ASCE, Vol. 101, No. GT5, pp. 423-438.

Miller, G. F. and Pursey, H. (1954), "The field and radiation impedance of mechanical radiators on the freee surface of a semi-infinite isotropic solid," *Proc. Roy. Soc. A*, 223, pp. 521-541.

Mitchell, J. K., Baxter, C. D. P., and Munson, T. C. (1995), "Performance of improved ground during earthquakes," *Soil Improvement for Liquefaction Hazaed Mitigation*, Geotech Special Pub. No. 49, ASCE, pp. 1-36.

Mitra, M. V. (1961), "Disturbance produced in an elastic half space by impulsive normal pressure," *Proc. Camb. Phil. Soc. Math. Phys. Sci*., 60, pp. 683-696.

Mulilis, J. P., Seed, H. B., Chan, C. K., Mitchell, J. K., and Arulanadan, K. (1977), "Effects of sample preparation on sand liquefaction," *Journal of*

the Geotechnical Engineering Division, ASCE, Vol. 103, No. GT2, pp. 91-108.

Oppenheim, A. V., Schafer, R. W., and Buck, J. R. (1999), *Discrete Time Signal Processing*, 2nd Edition, Prentice Hall, Inc, New Jersey, 870 pp.

Page, R. A., Boore, D. M., and Yerkes, R. F. (1995), "Reducing earthquake losses throughout the United States," U.S. Geological Survey Fact Sheet-096-95, January 1995

Phillips, R. D. (2000), *Initial Design and Implementation of an In Situ Test for Measurement of Nonlinear Soil Properties*, M.S. Thesis, The University of Texas at Austin.

Port and Harbour Research Institute (PHRI), Eds. (1997), *Handbook on liquefaction remediation of reclaimed land,* Balkema, Rotterdam.

Pieuchot, M. (1984), *Handbook of Geophysical Exploration, Section I. Seismic Exploration,* Vol. 2, Seismic Instrumentation, Geophysical Press, London, 71-89 pp.

Prevost, J. H. (1981), *DYNAFLOW: A Nonlinear Transient Finite Element Analysis Program*, Department of Civil Engineering, Princeton University, Princeton, New Jersey.

Pyke, R. M., Chan, C. K., and Seed, H. B. (1974), "Settlement and liquefaction of sands under multi-directional shaking," *Report No. EERC-74-2*, University of California, Berkeley.

Rayleigh, L. (1885), "On waves propagated along the plane surface of an elastic solid," *Proceedings of the London Mathematical Society*, Vol. 17, pp.4-11.

Reddy, J. N. (1984), *An Introduction to the Finite Element Method*, McGraw-Hill International Book Co., 495 pp.

Richart, F. E., Hall, J. R., and Woods, R. D. (1970), *Vibration of Soils and Foundations*, Prentice-Hall, Inc., New Jersey.

Robertson, P. K., Campanella, R. G., Gillespie, D, and Rice, A. (1985), "Seismic CPT to measure in-situ shear wave velocity," *Measurement and Use of Shear Wave Velocity for Evaluation Dynamic Soil Properties*, R. D. Woods editor. ASCE, pp. 35-49.

Robertson, P. K., and Wride, C. E. (1998), ‘‘Evaluating cyclic liquefaction potential using the cone penetration test,’’ *Can. Geotech. J.*, Ottawa, Vol. 35, No. 3, pp. 442–459.

Santamarina, C. S. and Fratta, D. (1998), *Introduction to Discrete Signal and Inverse Problems in Civil Engineering*, ASCE Press, Reston, Virginia, 327 pp.

Scott, R. F. and Hushmand, B. (1995a), "In situ calibration of dynamic pore pressure transducers," Cal. Inst. Of Tech., *Final Rep. To the U.S. Geology Survey*, Grant No. 1434-92-G-2169

Scott, R. F. and Hushamnd, B. (1995b), Discussion on technical paper 6044 of Geotechnical Engr. Jour., ASCE ("Piezometer performance at Wildlife liquefaction site, California" by T.L. Youd and T.L. Holzer). *Journal of the Geotechnical Engineering Division,* ASCE, Vol. 121, No. GT12, pp. 912-919.

Seed, H. B. (1979), "Soil liquefaction and cyclic mobility evaluation for level ground during earthquake," *Journal of the Geotechnical Engineering Division*, ASCE, Vol. 105, No. GT2, pp. 201-255.

Seed, H. B. and Brooker, J.R. (1977), "Stabilization of potentially liquefiable sand deposits using gravel drains," *Journal of the Geotechnical Engineering Division*, ASCE, Vol. 103, No. GT7, pp. 757-768.

Seed, H. B., and Idriss, I. M. (1967), "Analysis of soil liquefaction: Niigata Earthquake," *Journal of the Soil Mechanics and Foundations Division*, ASCE, Vol. 93, No. SM3, pp. 83-108.

Seed, H. B. and Idriss, I. M. (1971), "Simplified procedure for evaluation soil liquefaction potential," *Journal of the Soil Mechanics and Foundations Division*, ASCE, Vol. 107, No. SM9, pp. 1249-1274.

Seed, H. B. and Lee, K. L. (1966), "Liquefaction of saturated sands during cyclic loading," *Journal of the Soil Mechanics and Foundations Division*, ASCE, Vol. 92, No. SM3, pp. 105-134.

Seed, H. B., Mori, K., and Chan, C. K. (1975), "Influence of seismic history on the liquefaction characteristics of sands," Report No. EERC 75-25, Earthquake Engineering Research Center, University of California, Berkeley.

Seed, H. B., Mori, K., Idriss, I. M., and Makdisi, F. I. (1975), "The slides in the San Fernando Damsduring the earthquake of February 9, 1971," *Journal of the Geotechnical Engineering Division*, ASCE, Vol. 101, No. GT7, pp. 651-688.

Seed, H. B. and Peacock, W. H. (1971), "Test procedures for measuring soil liquefaction characteristics," *Journal of the Soil Mechanics and Foundations Division*, ASCE, Vol. 97, No. SM8, pp. 1099-1119.

Seed, H. B., Tokimatsu, K., Harder, L. F., and Chung, R. M. (1985), "Influence of SPT procedures in soil liquefaction resistance evaluations," *Journal of Geotechnical Engineering*, ASCE, Vol. 111, No. 12, pp.1425-1445.

Shen, C. K., et al. (1989), ''Chapter 25: Pore water pressure response measurements at Lotung site.'' *Proc., EPRI/NRC/TPC Workshop on Seismic Soil-Struct. Interaction Anal. Techniques Using Data from Lotung, Taiwan, Rep. No. EPRI NP-6154*, Electric Power Research Institute, Palo Alto, Calif., 2, 1–20.

Sheriff, R. E. and Geldart, L. P. (1995), *Exploration Seismology*, 2nd Edition, Cambridge University Press, 592 pp.

Stokoe, K. H., II., Bay, J. A., Rosenblad, B. L., Murphy, M. R., Fults, K. W., and Chen, D. H. (2000), "Super-Accelerated Testing of a Flexible Pavement with the Stationary Dynamic Deflectometer (SDD)," *2000 Annual Meeting of the Transportation Research Board*.

Stokoe, K. H. II and Hoar, R. J. (1978), "Generation and Measurement of Shear Wave In Situ," *Dynamic Geotechnical Testing*, ASTM STP 654, ASTM, Philadephia, pp. 3-29.

Stokoe, K. H. II and Nazarian, S. (1985), "Use of Rayleigh waves in liquefaction studies," *Measurement and Use of Shear Wave Velocity for Evaluation Dynamic Soil Properties*, R. D. Woods editor. ASCE, pp. 1-17.

Stokoe, K. H. II. and Woods, R. D. (1972), "In Situ Shear Wave Velocity by Crosshole-hole Method," *Journal of the Soil Mechanics and Foundations Division*, ASCE, Vol. 98, No. SM5, pp. 443-460.

Stokoe, K. H. II, Wright, S. G., Bay, J. A., and Roesset, J. M. (1994), "Characterization of geotechnical sites by SASW method," *Geophysical Characterization of Sites*, ISSMFE Technical Committee #10, Woods, R.D. ed, IBH Oxford Press, New Delhi, India, January, pp. 15-25.

Terzaghi, K., and Peck, R. B. (1967), Soil Mechanics in Engineering Practice, 2nd edition, Wiley, New York.

Valliappan, H. S., and Murti V. (1984), ‘‘Finite element constraints in the analysis of wave propagation problems,’’ *UNICIV Rep. No. R-218*, School of Civil Engineering, Univ. of New South Wales, New South Wales, Australia.

White, J. E. (1965), *Seismic Waves: Radiation, Transmission, and Attenuation*, McGraw-Hill Book Company, New York, 302 pp.

Wilson, D. W. (1998), *Soil-pile-superstructure interaction in liquefying sand*, Ph. D. dissertation, University of California, Davis.

Wood, D. M. (1990), *Soil Behaviour and Critical State Soil Mechanics*, Cambridge University Press, 462 pp.

Woods, R. D. (1968), “Screening of surface waves in soils,” *Journal of the Soil Mechanics and Foundations Division*, ASCE, Vol. 94, No. SM4, pp. 951-979.

Youd, T. L. (1984), “Geologic effects- liquefaction and associated ground failure,” *Proceedings, Geologic and Hydraulic Hazards Training Program*, Open File Report 84-760, U.S. Geological Survey, Menlo Park, CA, pp. 210-232.

Youd, T. L., and Holzer, T. L. (1994), “Piezometer performance at Wildlife liquefaction site, California,” *Journal of the Geotechnical Engineering Division*, ASCE, Vol.120, GT6, pp. 975-995.

Youd, T. L., and Wieczorek, G. F. (1984), “Liquefaction during the 1981 and previous earthquake near Westmorland, California,” *Open-File Report 81-680*, U.S. Geological Survey, Denver, CO.

Youd, T. L. et al. (2001), “Liquefaction resistance of soils: summary report from the 1996 NCEER and 1998 NCEER/NSF workshops on evaluation of liquefaction resistance of soils,” *Journal of Geotechnical and Geoenvironmental Engineering*, ASCE, Vol. 127, No. 10, pp. 817-833.

Zeghal, M. and Elgamal, A. W. (1994), “Analysis of Wildlife site using earthquake records,” *Journal of the Geotechnical Engineering Division*, ASCE, Vol.120, GT6, pp. 975-995.

Zienkiewicz, O. C., Chan, A. H. C., Pastor M., Paul, D. K., and Shiomi T. (1990), "Static and dynamic behaviour of geometerials – a rational approach to quantitative solutions, part-1 fully saturated problems," *Proc. Royal Society of London*, A429, pp. 285-309.

Zienkiewicz, O. C. and Taylor, R. L. (1989), The Finite Element Method, 4th Edition, Vol. 1: Basic formulation and linear problems, McGraw-Hill International Book Co., 648 pp.

Vita

Wen-Jong Chang was born on February 14, 1970 in Tainan, Taiwan, the son of Rong-Kuei Liu and Shaw Chang. He graduated from Provincial Taichung Fist High School in Taichung in June 1985. In September 1988, he entered National Chung-Hsing University in Taichung, Taiwan, and received his Bachelor and Master of Science in Civil Engineering in June 1992 and June 1994, respectively. He started his Ph.D. study at the University of Texas at Austin in January 1998 supervised by Dr. Ellen M. Rathje.

Permanent address: No. 125 Ming-Chi 5th St., Ching-Hsui
Taichung, Taiwan 436

This dissertation was typed by the author